ISSN (p) 1857-1727
ISSN (e) 2345-1688

Volume 10 No. 1, 2015

CHEMISTRY
JOURNAL OF MOLDOVA

General, Industrial and Ecological Chemistry

NCAA national scientific journals ranking: Category B

Academy of Sciences of Moldova
Institute of Chemistry
State University of Moldova

Academy of Sciences of Moldova, Institute of Chemistry
State University of Moldova, Faculty of Chemistry and Chemical Technology

CHEMISTRY JOURNAL OF MOLDOVA
General, Industrial and Ecological Chemistry

Universal Impact Factor 0.135 for year 2014

Editorial office address:
Institute of Chemistry of Academy of Sciences of Moldova, 3, Academiei Str., Chisinau, MD-2028, Republic of Moldova
Tel: + 373 22 725490; Fax: +373 22 739954; e-mail: chemjm@asm.md, chemjm@gmail.com
Web: www.cjm.asm.md

ISSUE CONTENTS LIST WITH GRAPHICAL ABSTRACTS

CHEMISTRY JOURNAL OF MOLDOVA.

General, Industrial and Ecological Chemistry

was awarded

The GOLD MEDAL

at

TECHNICAL-SCIENTIFIC, ARTISTIC AND LITERARY BOOK SALON
"EUROINVENT"

May 14-15, 2015, Iasi, Romania

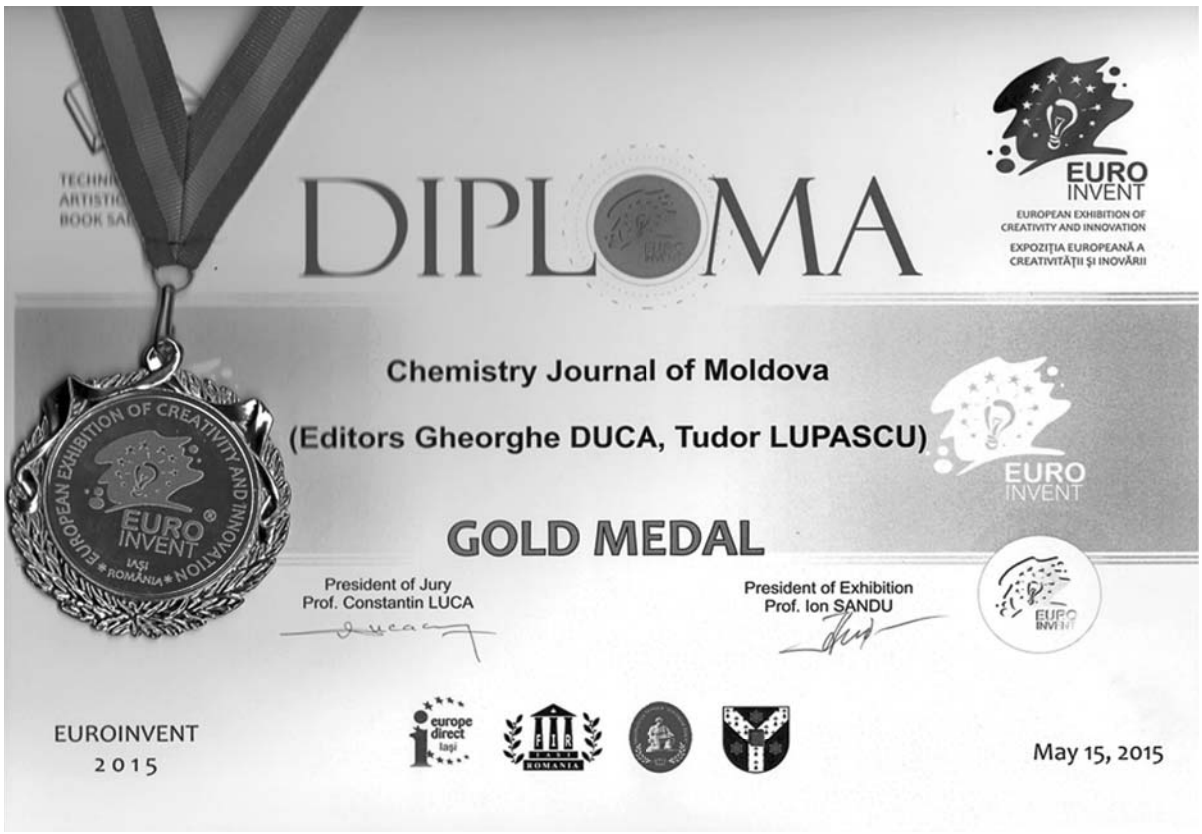

THE XVIIIth INTERNATIONAL CONFERENCE "PHYSICAL METHODS IN COORDINATION AND SUPRAMOLECULAR CHEMISTRY"

PMCSC-XVIII
October 8-9, 2015,
Chisinau, Republic of Moldova

The Organizing Committee is pleased to invite you to participate at the XVIIIth International Conference "Physical Methods in Coordination and Supramolecular Chemistry". The conference will be organized in Chisinau, Republic of Moldova in October, 2015.

Scientific program

The Conference program will include Plenary Lectures, Oral Communications and Poster Presentations on a range of interdisciplinary topics connected with the study of coordination and supramolecular compounds by physical methods including optical, γ–resonance and radio-spectroscopy, diffraction methods, magnetochemistry, quantum-chemical methods. The special attention will be paid to the compounds with the library of useful properties, e.g., molecular magnets, MOFs, sensors, biologically important compounds, and nanomaterials.

The Conference will be focused on the following topics:

- Study of coordination compounds in the solid state and in solution by EPR, NMR, Mössbauer, laser and X-ray photoelectron spectroscopy;
- Diffraction methods in study of coordination and supramolecular compounds,
- Relationship structure – property and quantum-chemical methods for the compounds with the library of useful properties (bioactive compounds, materials for molecular electronics);
- Magnetochemistry and single-molecule magnets (SMMs).

The official Conference language will be **English.** No translation will be provided.

DEADLINE FOR REGISTRATION	**JULY 1, 2015**
DEADLINE FOR ABSTRACT SUBMISSION	**AUGUST 1, 2015**
DEADLINE FOR FULL PAPER SUBMISSION	**SEPTEMBER 15, 2015**

All participants of the conference are also invited to present a full paper of their communications to be published in ***Chemistry Journal of Moldova*** after peer-reviewing process. Please follow the *Instructions for authors* and *paper template* provided on the journal web page *http://www.cjm.asm.md*.

Full information about PMCSC-XVIII is available on the Conference web page *http://chem.asm.md/pmcsc/*.

CORESPONDENCE ADDRESS

Conference Secretariat
Institute of Chemistry of Academy of Sciences of Moldova
3, Academiei str.,
Chisinau MD-2028, Republic of Moldova
Phone: (+373 22) 739722
Fax: (+373 22) 739954
e-mail: pmcsc2015@gmail.com

SYNTHETIC TRANSFORMATIONS OF *ENT*-KAURENOIC ACID

Olga Morarescu

Institute of Chemistry of Academy of Sciences of Moldova, 3, Academiei str., Chisinau MD-2028, Republic of Moldova
e-mail: olea_chetraru@yahoo.com; phone: (+373-22) 73 97 75; fax: (+373-22) 73 97 75

Abstract. This paper presents a review on kaurane diterpenes, covering various aspects of chemical and microbiological transformations of native *ent*-kaurenoic acid, namely, its reactions *via* COOH groups, double bonds and rearrangements of the carbon skeleton that lead to a wide range of natural and synthetic derivatives with potential biologic activities and can present convenient synthons for the syntheses of other native *ent*-kauranes.

Keywords: diterpenes, *ent*-kaur-16-en-19-oic acid, synthesis, biological activity.

Received: March 2015/ Revised final: April 2015/ Accepted: April 2015

Introduction

Ent-kaur-16-en-19-oic acid **1** is a natural *ent*-kaurane-type diterpenoid that can be isolated in a good yield from many plants, such as *Wedelia* [1], *Mikania* [2], *Annona* [3], *Xylopia* [4] and *Helianthus* genera, especially from sunflower (*Helianthus annuus* sp) [5-16]. A wide spectrum of bioactivities of *ent*-kaur-16-en-19-oic acid **1** and its derivatives has been reported, including the following effects: trypanocidal [2], embryotoxic [17], cytotoxic [12, 17] anti-HIV, anti-inflammatory, anti-fertility, antibacterial, antifungal, molluscicidal [18], anti-feedant [19], anti-platelet aggregation [20], anti-cancer [21], anti-plasmodic and relaxant activities [22], anti-Alzheimer and antioxidant [23]; acid **1** was also used as remedy for the treatment of type 2 diabetes and obesity [24].

Ent-kaur-16-en-19-oic acid **1** is one of the intermediate compounds, which is involved in the biosynthesis of diverse *ent*-kaurane diterpenes, including gibberellins, a group of growth phyto-hormones. Therefore, it is not surprising that many *ent*-kauranes and their derivatives act as growth regulators in plants [25].

The broad spectrum of presented by the *ent*-kaurane diterpenes biological activities has motivated countless studies of structural modifications of the skeleton, aiming at obtaining the new potentially bioactive substances. These structural transformations have been achieved either chemically or microbiologically, by using microorganism cultures.

Chemical transformation of *ent*-kaur-16-en-19-oic acid

Chemical transformation of natural substances is an important and promising direction in medicinal chemistry. However, there are at least three factors that hinder investigations in this direction. The first factor is the afore-mentioned extremely low content of most of the diterpenoids in the natural sources. The second one is the presence of several reactive centers in these molecules, which complicates the course of chemo- and regioselective synthesis. The third factor is the susceptibility of *ent*-kauranes to skeletal rearrangements. Nevertheless, the huge structural variety in the class of the isolated *ent*-kaurane diterpenoids and relatively large content of some of these compounds in the available natural sources make them a very attractive basis for further chemical transformations.

Functionalization of carboxy group in ent-kaur-16-en-19-oic acid

In *ent*-kauranes the carboxy group at C_4 is sterically screened by methyl groups of C_{18} and C_{20}, being, hence, less reactive than the analogous group in carboxylic acids. It should be noted that functionalization of a carboxyl group of *ent*-kauranes can significantly change the biological activity of the initial metabolite, but in some cases this appeared to be necessary for expression the biological activity.

In early investigations, the carboxyl group in *ent*-kaurane diterpenoids was esterified by diazomethane [26] and the resulting ester was reduced to a reactive primary hydroxyl group, which could then be readily modified. One of the first works [27] that employed this scheme for the transformation of *ent*-kaurane diterpenoids was reported in 1964, in which *ent*-kaur-16-en-19-oic acid **1**, 16α-*ent*-kauran-17,19-dioic acid **2** and other isolated from *Ricinocarpus stylosus* kauranes were subjected to sequential methylation, reduction, oxidation, and olefination, to yield a broad array of derivatives **3** - **9** etc. (Figure 1).

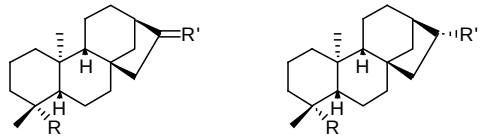

1 R = COOH; R' = CH_2
3 R = $COOCH_3$; R' = CH_2
4 R = CH_2OH; R' = CH_2
5 R = COOH; R' = O

2 R = R' = COOH
6 R = R' = $COOCH_3$
7 R = COOH; R' = $COOCH_3$
8 R = CHO; R' = $COOCH_3$
9 R = COOH; R' = CH_2OH

Figure 1. Structures of *ent*-kaurenoic acid 1, *ent*-kaurandioic acid 2 and their derivatives [27].

The reaction of a carboxyl group of *ent*-kauranes with toxic and explosive diazomethane is by no means the best esterification method and this group is more frequently functionalized using the chloroanhydride pathway. According to this, the chloroanhydrides of carboxylic acids are typically obtained by using $POCl_3$, PCl_3 or $SOCl_2$. However, the interaction of these reactants with polyfunctional kaurenoids is frequently accompanied by undesired side reactions. For example, the preparation of chloroanhydride of *ent*-kaur-16-en-19-oic acid **1** may be accompanied by hydrochlorination of the double bond, resulting with the *ent*-kaur-16β-methoxy-19-oic acid **10** (Scheme 1) [28].

At the same time, the chloroanhydrides of carboxylic acids that contain labile in acidic media fragments can softly be obtained by using a CCl_4–PPh_3 mixture [29]. By means of this approach the chloroanhydride of *ent*-kaur-16-en-19-oic acid **1** was originally synthesized in 1974 in a good yield, being then used in obtaining of a series of esters [30].

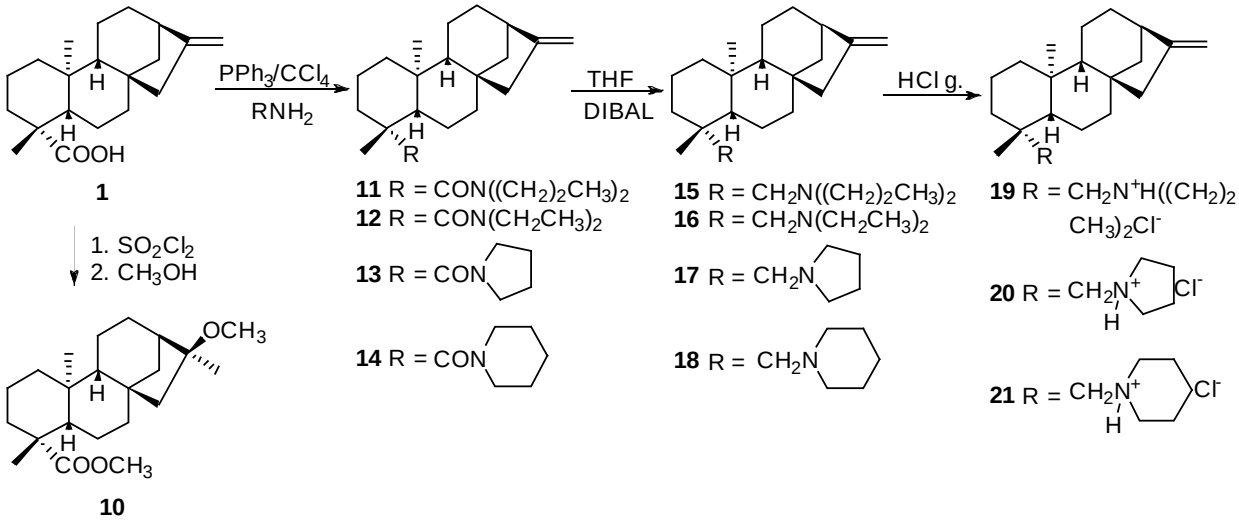

Scheme 1. Synthesis of the *ent*-kaurane derivatives [28, 31].

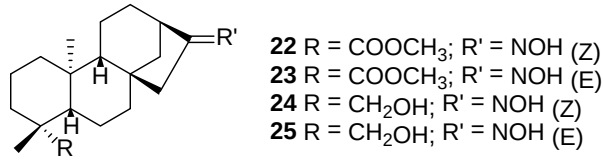

Figure 2. Structures of the synthesized from *ent*-kaurenoic acid 1 isomeric oximes [31].

In recent years, this method has also been successfully used to synthesize a large series of *ent*-kaurenoic derivatives. Intending to reduce or eliminate the lytic effect of *ent*-kaur-16-en-19-oic acid **1** on erythrocytes of the infected blood that are usually used in the *in vitro* assays against trypomastigote forms of *Trypanosoma cruzi*, Vieira et al. [31] succeeded in synthesis of a series of derivatives **11** – **21**, with amine or amide functions at C_{19}, (Scheme 1) and containing an oxime group at C_{16} kaurane derivatives **22 - 25** (Figure 2). From all the mentioned compounds, only oxime **22** was more active than **1**, presenting trypanosomicidal activity in all the tested concentrations (2.27 – 0.57 μM), along with a slight lysis of the red cells. Although hydrochloride **20** was the only product that did not produce haemolysis, its trypanosomicidal activity was comparable to that of the *ent*-kaur-16-en-19-oic acid **1**. Derivatives **23**, **24** and **25** were as active as **1**, presenting, however, a slight lysis of erythrocytes.

The same research centre, headed by Boaventura [32], reported on the preparation of novel monoamides **26** – **33** in good yields. They were obtained from the reaction of *ent*-kaur-16-en-19-oic acid **1** with monoamines and symmetrical diamines, by using a modified protocol for monoacylation (Figure 3). The activity of novel monoamides on seed germination and growth of radicle and shoot of *Lactuca sativa* (lettuce) has been tested. Amides from symmetrical diamines showed significant inhibitory activity at higher concentrations.

The abundance of *ent*-kaur-16-en-19-oic acid **1** in some plant species, along with the lack of a general method for the synthesis of alkyl kaurenoates, has motivated Boeck and collaborators [28] to carry out the chemical modification of this diterpene in order to synthesize new kaurane derivatives and to evaluate their potential pharmacological activities. As a result, a simple method was developed for preparing *ent*-kauranic esters **3, 34** – **39** (Figure 3), through the alkylation of the acid **1** with alkyl halides, in a KOH-acetone system, avoiding the use of anhydrous conditions and establishing a reproducible method for this reaction. Moreover, it was observed that only *ent*-kaur-16-en-19-oic acid **1** and its derivatives, containing a free carboxyl group, showed moderate antifungal activity against the assayed dermatophytes, suggesting that the presence of hydrophilic groups can be essential for the observed antifungal activity.

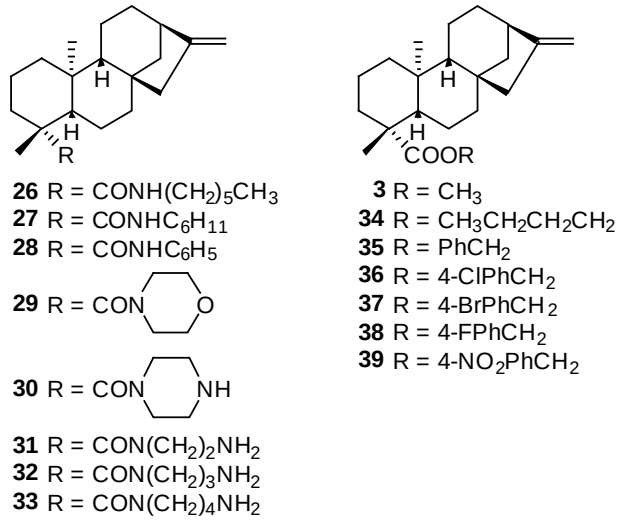

Figure 3. Monoamides and alkyl halide esters of *ent*-kaurenoic acid 1 [28, 32].

Functionalization of double bonds in ent-kaurenoic acid

One of the first reported chemical transformations of *ent*-kaurene diterpenoids was the reduction of C_{16}-C_{17} double bond by hydrogen, which was originally used in 1948 to reduce *ent*-kaurene to *ent*-kaurane [33]. In 1964, this method was applied to reduce *ent*-kaur-16-en-19-oic acid **1** [27]. It should be mentioned, that in *ent*-kaurenoids the double bond plays a significant role in manifestation of their biological activity.

Oxidation of double bonds is an attractive direction in functionalization of *ent*-kaurenes for obtaining the new promising synthones. As a rule, this reaction is carried out by using *meta*-chloroperbenzoic acid (MCPBA) and this approach was used for the synthesis of many epoxy derivatives, including *ent*-kaur-16-en-19-oic acid epoxide **40** [34] (Scheme 2). Alternatively, the oxidation can be conducted by hydroxylation and ozonolysis, but the latter is frequently accompanied by undesired side reactions.

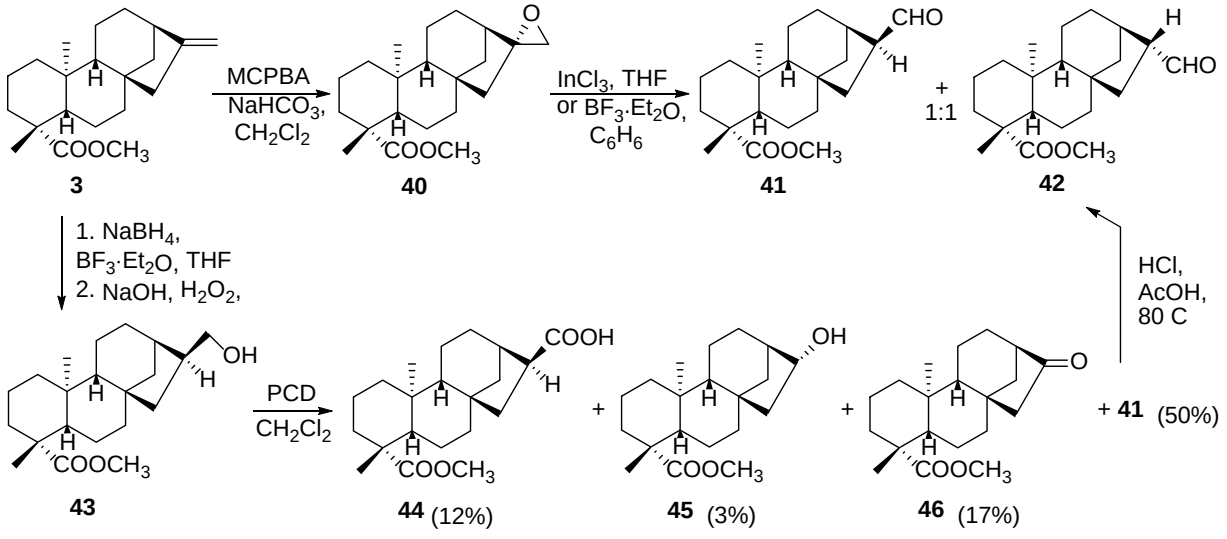

Scheme 2. Products of oxidation of *ent*-kaurenoic acid 1 [35].

In the same line of research, Batista et al. [35] synthesized *ent*-kaurane aldehydes, methyl 16S,17-oxo-*ent*-kauran-19-oate **41** and methyl 16R,17-oxo-*ent*-kauran-19-oate **42**, important as semisynthetic coupling intermediates, starting from *ent*-kaur-16-en-19-oic acid **1** and its methyl ester **3**. Additionally they described, for the first time, synthesis of the *ent*-kaurane and *ent*-norkaurane derivatives **41, 44 - 46** under pyridinium dichromate (PDC) conditions. The initial oxidation of **43** afforded the expected aldehyde **41**, which in the presence of the chromate underwent further oxidation to the acid **44**. The latter can be considered the precursor of *ent*-norkauranes, methyl 16α-hydroxy-17-*ent*-norkauran-19-oate **45** and methyl 16-oxo-17-*ent*-norkauran-19-oate **46** (Scheme 2).

Synthesis of steviol by Cook and Knox [36-38] involves a series of oxidative transformations, starting with *ent*-kaur-16-en-19-oic acid **1** (Scheme 3). Conversion of methyl *ent*-kaur-16-en-19-oate **3** to nor-ketone **46** and subsequent Baeyer-Villiger oxidation afforded γ-lactone **47**, which was converted by hydrolysis, methylation and oxidation into the keto-diester **48**. Treatment of **48** with sodium-liquid ammonia gave the acyloin-like cyclization product, diol-acid **49**, which was oxidized to **50**. Silyl ether protection of **50** and subsequent Wittig reaction with methylenetriphenylphosphorane, followed by a dilute acid work-up, gave steviol **51**.

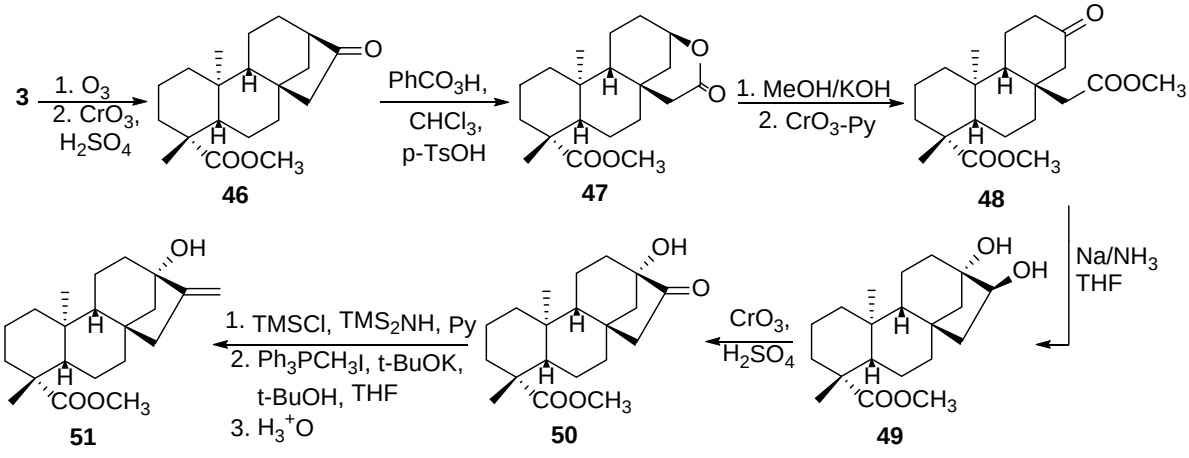

Scheme 3. Synthesis of steviol from *ent*-kaurenic acid 1 [36-38].

Recently, it has been reported that hydroformylation of the $C_{16} = C_{17}$ bond in *ent*-kaur-16-en-19-oic acid **1** [39] and *ent*-kaur-16-en-19-ol **4** [40] was performed by the use of rhodium catalysts. Substrates, such as methyl *ent*-kaur-16-en-19-oate **3** and trimethylsilyl-*ent*-kaur-16-en-19-ol ether **52** have been hydroformylated by using unmodified Rh catalysts, as well as Rh/PPh_3 and Rh/*tris*-(*o*-*t*-butylphenyl) phosphite catalytic systems. It should be noted, that formation of the corresponding aldehydes **53**, **54** and **55**, **56,** respectively, was accompanied by the isomerization of substrates into derivatives **57** and **58** with endo-cyclic double bonds (Scheme 4).

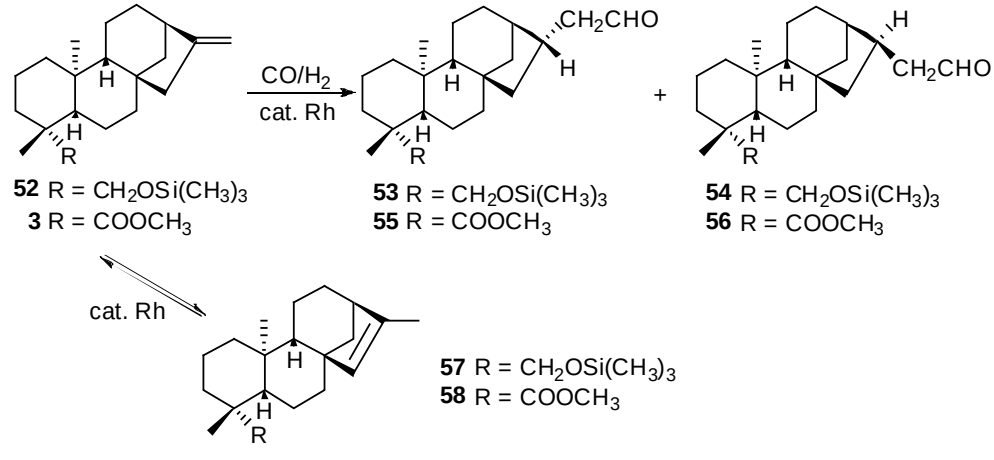

Scheme 4. Rh/PPh_3 hydroformylation of *ent*-kaurenic acid 1 [40].

Usage of the same hydroformylation rhodium catalytic systems led to the development of processes for *tandem* sequential hydroxyaminomethylation (hydroformylation followed by hydrogenation *in situ*) [41]. Thus, the rhodium precursor $[Rh(acac)(CO)_2]$ and a 15-fold excess of PPh_3 ligand were introduced into the reactor. The substrate, methyl *ent*-kaur-16-en-19-oate **3,** and dissolved in toluene piperidine were subsequently introduced into the reactor. The reaction was maintained at 100°C at a total pressure ($CO:H_2$ = 1:1) of 20 bar for 48 hours to ensure that any formed imine was transformed by hydroxyaminomethylation. As a result, the diastereoisomers **59** and **60** have been obtained, as potential biologically active compounds (Scheme 5). The GC-analysis after 48 hours showed the 84% conversion with a diastereomeric ratio **59** / **60** = 61:39.

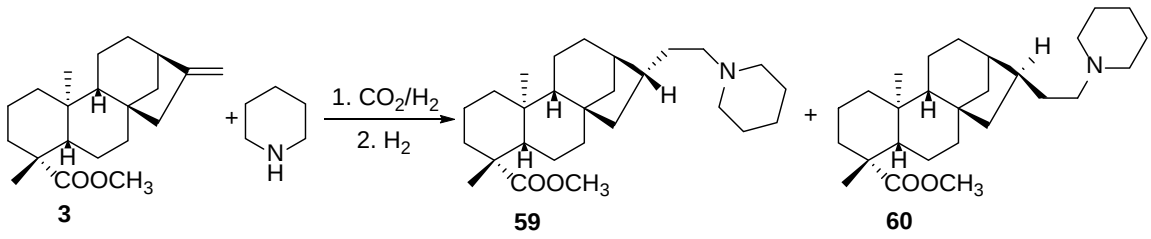

Scheme 5. Rhodium catalytic hydroxyaminomethylation of *ent*-kaurenoic acid 1 [41].

To study the cytotoxicity of *ent*-kauranes with respect to some human cancer cells, derivatives **61 - 63** were recently synthesized by electrophilic addition at the double bond of *ent*-kaur-16-en-19-oic acid **1** [44]. It was established, that this modification (Scheme 6) led to the complete disappearance of the anticancer effect.

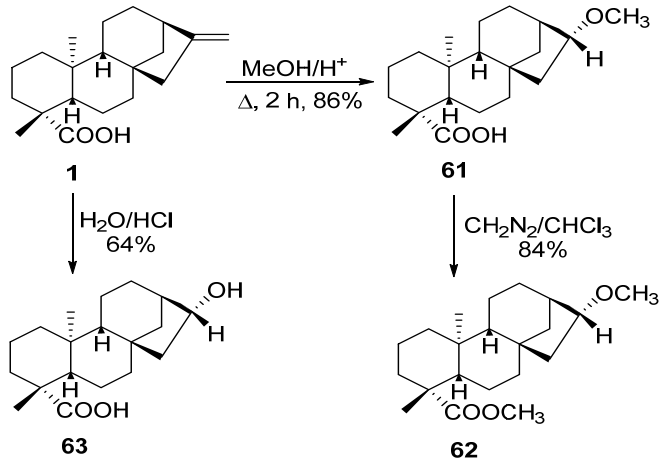

Scheme 6. Electrophilic addition at a double bond of *ent*-kaurenoic acid 1 [44].

Aparicio et al. [42] described the allylic oxidation of *ent*-kaur-16-en-19-oic acid **1**, methyl *ent*-kaur-16-en-19-oate **3** and *ent*-kaur-16-en-19-ol **4** with SeO_2/H_2O_2 (Scheme 7). The reaction was run in a dioxan solution at room temperature at stirring for 4 hours. Treatment of acid **1** afforded 56% of 15α-hydroxy-*ent*-kaur-16-en-19-oic acid (grandifloric acid) **64**. However, treatment of methyl ester **3** furnished two products: methyl 15α-hydroxy-*ent*-kaur-16-en-19-oate **65** (34% yield) and methyl 15α,16α-epoxi-17-hydroxy-*ent*-kauran-19-oate **67** (59% yield). In a similar way, treatment of *ent*-kaur-16-en-19-ol **4** rendered two products: 15α,19-dihydroxy-*ent*-kaur-16-ene **66** (57% yield) and 15α,16α-epoxi-17,19-dihydroxy-*ent*-kaurane **68** (34% yield). In the same direction, 15α-hydroxy-*ent*-kaur-16-en-19-oic acid **64** was synthesized with a better yield by using SeO_2/EtOH system, starting with *ent*-kaur-16-en-19-oic acid **1** and by saponification of the 15α-angeloyl-*ent*-kaur-16-en-19-oic acid **69** [43].

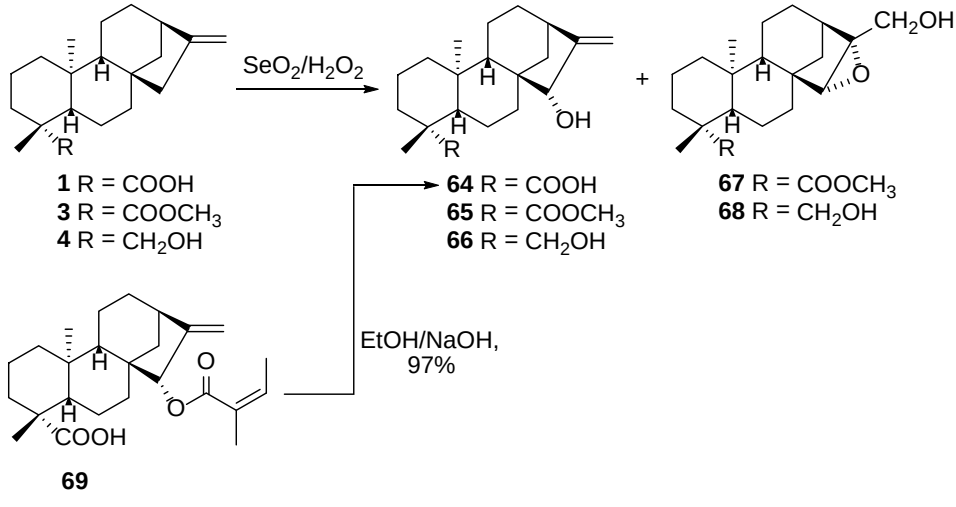

Scheme 7. Allylic oxidation of *ent*-kaurenoic acid 1 [42, 43].

Due to a continuing interest in the evaluation of biological potential of natural diterpenes, Hueso-Falcónin et al. [44] reported a study on the preparation of *ent*-kaurane derivatives from the natural *ent*-kaur-16-en-19-oic acid **1** (Scheme 8). These compounds were tested for their ability to induce apoptosis of signaling pathway in mouse and human cancer cells and some conclusions about structure–activity relationships have been made. The most active compounds were investigated and they were able to induce apoptosis with methyl 15-oxo-e*nt*-kaur-16-en-19-oate **75** being the best inducer.

Presence of the α-oxo methylene moiety seems to play an important role in expressing the bio-activity and this fragment can act as Michael acceptor for nucleophilic residues, especially cysteine sulfhydryl groups [45]. Replacement of the oxo group or double bond in compounds **75** leads to the loss of the cytotoxic activity. Thus, such natural compounds as: acetate **78**, alcohol **79** or in the case of 15-oxo-*ent*-kaurene derivatives, α-phenylethylketone **76** and α-oxopyrazoline **80** exhibit no such activity. Moreover, the cytotoxic activity of methyl 15-oxo-e*nt*-kaur-16-en-19-oate **75** is 35 times greater, than that of initial acid **77** [44].

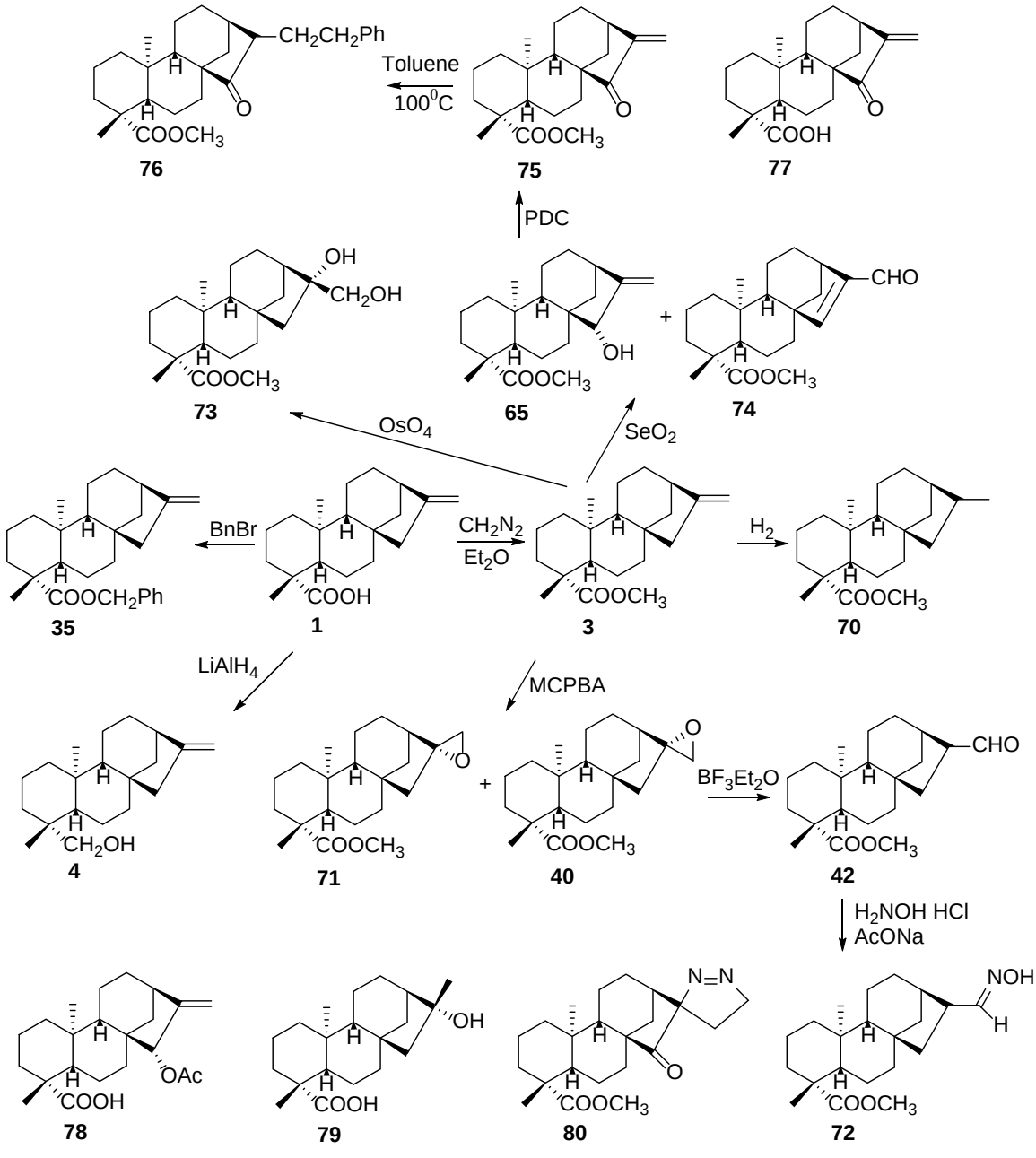

Scheme 8. Preparation of *ent*-kaurane derivatives from the *ent*-kaurenoic acid 1 [44].

Carbon skeleton rearrangements in ent-kaur-16-en-19-oic acid

Many isoprenoids, particularly diterpenoids, are characterized by susceptibility to skeletal rearrangement - a process accompanied by changes in the carbocyclic framework. These reactions play a special role in the functionalization of *ent*-kauranes, making possible the synthesis of compounds with rather unusual structures that cannot be obtained by other methods.

Photooxygenation is one of the first rearrangement reactions of *ent*-kaur-16-en-19-oic acid **1** [46]. The oxygenation of olefins containing allylic hydrogen atoms in the presence of a suitable sensitizer and visible light gives allylic hydroperoxides, the process being invariably accompanied by a shift of the double bond. The dissolved in pyridine methyl *ent*- kaur-16-en-19-oate **3** was irradiated with fluorescent tubes and hematoporphyrin was employed as a sensitizer. The resulting hydroperoxide was not isolated, being directly reduced in an ethanol solution with sodium iodide and acetic acid. The chromatography of the product over silica gel afforded the allylic alcohol **81** in a 30% yield (Scheme 9).

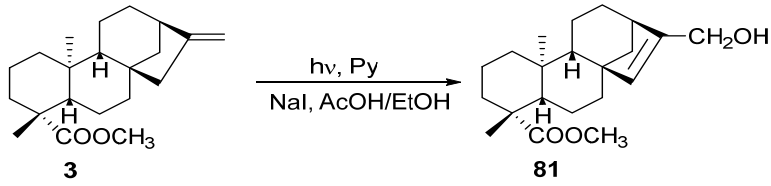

Scheme 9. **Photooxygenation reactions of *ent*-kaurenoic acid 1 [46].**

The rearrangements of *ent*-kaurane diterpenes under the action of different reagents have been reported [47]. Most of the examples report on the reactions that involve formation of the non-classical carbocation. It is well-known from the work of Olah et al. [48], that superacids are very convenient generators of these species, in particular, fluorosulfonic acid (FSO_3H) is known as an efficient promoter of cyclizations and rearrangements of terpenoids.

Recently [49] an efficient one-step, retro-biomimetic procedure for the synthesis of natural products having the atisane structure has been reported (Scheme 10), which are natural components of medicinal plants and possess a relevant biological activity.

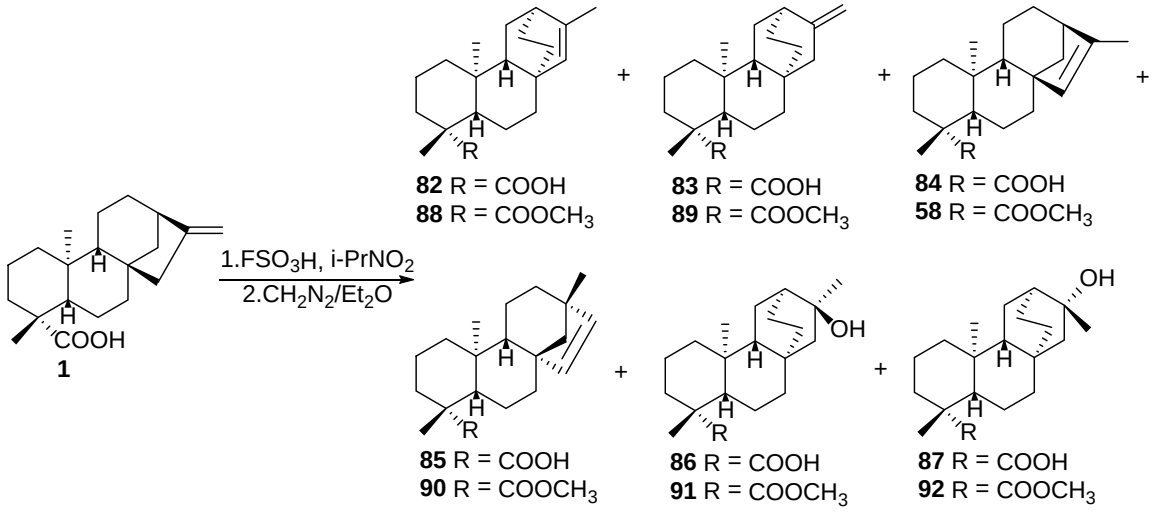

Scheme 10. Rearrangements of *ent*-kaurenoic acid 1 [49].

Treatment of *ent*-kaur-16-en-19-oic acid **1** with fluorosulfonic acid under mild reaction conditions allowed carbonium ion generation and skeletal rearrangement to occur. The reaction product included: *ent*-atis-15-en-19-oic acid **82** (8%), *ent*-atis-16-en-19-oic acid **83** (22%), recovered starting material **1** (18%), *ent*-kaur-15-en-19-oic acid **84** (17%), *ent*-beyer-15-en-19-oic acid **85** (7%), 16β-hydroxy-*ent*-atisan-19-oic acid **86** (5%) and 16α-hydroxy-*ent*-atisan-19-oic acid **87** (4%). Treatment of the individual acids **82** – **87** with an Et_2O solution of diazomethane led to the corresponding esters: methyl *ent*-atis-15-en-19-oate **88**, methyl *ent*-atis-16-en-19-oate **89**, methyl *ent*-kaur-15-en-19-oate **58**, methyl *ent*-beyer-15-en-19-oate **90**, methyl 16β-hydroxy-*ent*-atisan-19-oate **91** and methyl 16α-hydroxy-*ent*-atisan 19-oate **92**.

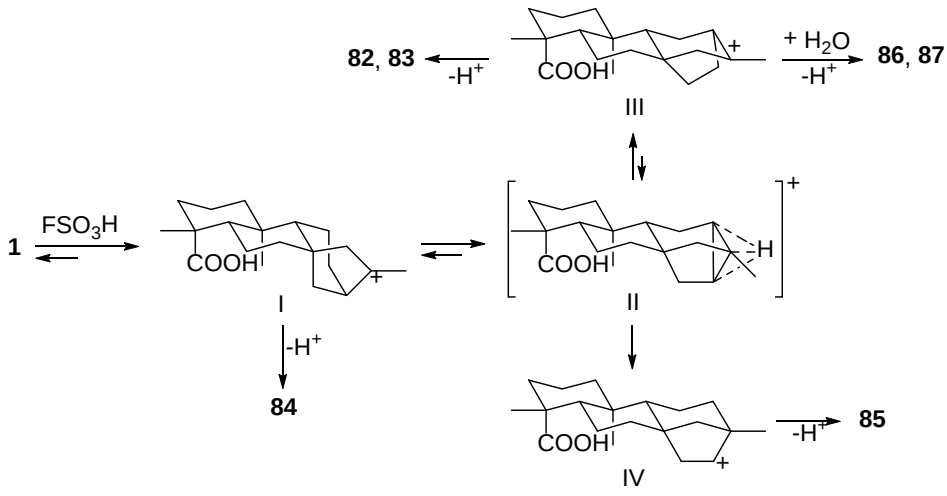

Scheme 11. The proposed reaction course for superacid-promoted isomerization of *ent*-kaurenoic acid 1 [49].

Thus, the superacid-promoted rearrangement of *ent*-kaur-16-en-19-oic acid **1** led predominantly to tetracyclic *ent*-atisane diterpenoids (see: **82**, **83**, **86** and **87**), with an overall yield of 39%. Taking into account the recovered starting material **1**, the combined yield of atisane-type compounds amounted to ca. 62%.

The transformation of *ent*-kaur-16-en-19-oic acid **1** into *ent*-atisane-type compounds takes place by the formation of carbonium ion **I**, which rearranges *via* the nonclassical pentacyclic ion **II** to the *ent*-atisane carbonium ion **III** (Scheme 11). The latter undergoes a H-atom loss either from C_{15} or C_{17}, to form the double bond isomeric *ent*-atis-15-en-19-oic acid **82** and *ent*-atis-16-en-19-oic acid **83**. The hydroxylated *ent*-atisanoic acids **86** and **87** are formed by quenching the cabocation **III** with a water molecule. On loss of one H-atom from C_{15} of *ent*-kauranoic acid carbonium ion **I**, the *ent*-kaur-15-en-19-oic acid **84** is obtained. The *ent*-beyer-15-en-19-oic acid **85** is formed after transformation of the nonclassical carbonium ion **II** to the *ent*-beyeranoic acid cation **IV** and subsequent H-atom loss from C_{16}.

Microbiological transformation of ent-kaur-16-en-19-oic acid

Microorganisms are able to transform a huge variety of organic compounds, such as hydrocarbons, terpenoids, steroids, alkaloids, antibiotics and amino-acids. Hydroxylation of inactivated carbons remains the most explored area in the microbial transformation of organic compounds. This reaction makes possible the preparation of countless novel diterpenoid derivatives that are inaccessible by chemical means.

Microbiological transformations of *ent*-kaur-16-en-19-oic acid **1** with *Calonectria decora*, *Rhizopus nigricans* ans *Aspergillus ochraceous* have been investigated by Ghisalberti et al. affording the following hidroxy derivatives: 7α-hydroxy-*ent*-kaur-16-en-19-oic acid **93**, 7β-hydroxy-*ent*-kaur-16-en-19-oic acid **94** and 16α,17-dihydroxy-*ent*-kauran-19-oic acid **95** [50] (Figure 4).

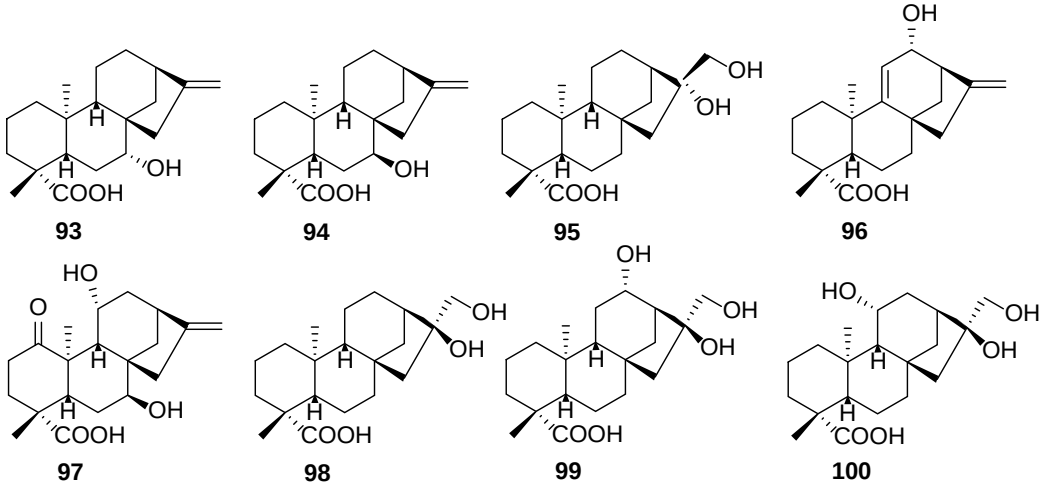

Figure 4. The obtained by microbiological transformation derivatives of *ent*-kaurenoic acid 1 [50-53].

As a part of the program of transformation the diterpenoids by microorganisms, Silva et al. [51] carried out the transformation of *ent*-kaur-16-en-19-oic acid **1**, by using *Rhizopus stolonifer.* Results of the incubations indicate that the obtained in the microbial transformation products were formed by hydroxylation in the B, C and D rings.

The incubation of **1** with *R. stolonifer* for seven days yielded compounds: 7β-hydroxy-*ent*-kaur-16-en-19-oic acid **94** and 12α-hydroxy-*ent*-kaur-9(11),16-dien-19-oic acid **96**, the former being the major product (~ 5%). The incubation of **1** with *R. stolonifer*, under the same conditions, for a longer period (for 15 days), led to the formation of a third metabolite, 16α,17-dihydroxy-*ent*-kauran-19-oic acid **95** (Figure 4).

Punnapayak et al. [52] reported generation of an interesting compound, 7β,11α-dihydroxy-l-oxo-*ent*-kaur-16-en-19-oic acid **97** that was obtained by fermentation of *ent*-kaur-16-en-19-oic acid **1** with *Aspergillus niger* for 7 days (Figure 4).

J. Pechwang et al. [53] described the biotransformation by *Psilocybe cubensis* of *ent*-kaur-16-en-19-oic acid **1** to produce its derivatives, along with *in vitro* evaluation of cytotoxic activity of all metabolites against human tumor cells. After two days of incubation the *ent*-kaur-16-en-19-oic acid **1**, 16β,17-dihydroxy-*ent*-kauran-19-oic acid **98** was isolated. After a further incubation for nine days, two novel metabolites, 12α,16β,17-trihydroxy-*ent*-kauran-19-oic acid **99** and 11α,16β,17-trihydroxy-*ent*-kauran-19-oic acid **100**, were obtained (Figure 4).

Conclusions

This paper reviewed the occurrence and biological activities of *ent*-kaur-16-en-19-oic acid, but especially the synthetic and semisynthetic methods that offer a wide range of natural and synthetic *ent*-kaurane derivatives. The accumulation of *ent*-kaur-16-en-19-oic acid and other naturally occurring kaurane diterpenes in some plant species make them important sources of these compounds, which are thus available as starting materials in the synthesis of new derivatives for biomedical and industrial research. Indeed, in the last few years, a growing number of publications have reported the use of *ent*-kaurane diterpenes for the synthesis of novel sweetening, antimicrobial, cytotoxic and trypanocidal agents, and this synthetic approach is still far from being fully exploited by the natural products chemistry community.

Acknowledgments

The author is very grateful to Dr. hab. Nicon Ungur and Dr. Veaceslav Kulciţki for assistance in the preparation of the manuscript.

References

1. Batista, R.; Chiari, E.; Oliveira, A.B. Trypanosomicidal kaurane diterpenes from Wedelia paludosa. Planta Medica, 1999, 65, pp. 283-284.
2. Alves, T.M.A.; Chaves, P.P.G.; Santos, L.M.S.T.; Nagem, T.J.; Murta, S.M.F.; Ceravolo, I.P.; Romanha, A.J.; Zani, C.L. A diterpene from Mikania obtusata active on Trypanosoma cruzi. Planta Medica, 1995, 61, pp. 85-87.
3. Oliveira, B.H.; Sant'ana, A.E.; Bastos, D.Z.L. Determination of the diterpenoid kaurenoic acid in Annona glabra by HPLC. Phytochemical Analysis, 2002, 13, pp. 368-371.
4. Melo, A.C.; Cota, B.B.; Oliveira, A.B.; Braga, F.C. HPLC quantitation of kaurane diterpenes in Xylopia species. Fitoterapia, 2001, 72, pp. 40-45.
5. Pyrek, J.St. New pentacyclic diterpene acid trachyloban-19-oic acid from sunflower. Tetrahedron, 1970, 26, pp. 5029-5032.
6. Elliger, C.A.; Zinkel, D.F.; Chan, B.G.; Waiss, A.C. Diterpene acids as larval growth inhibitors. Experientia, 1976, 32, pp. 1364-1366.
7. Morris, B.D.; Foster, S.P.; Grugel, S.; Charlet, L.D. Isolation of the diterpenoids, ent-kauran-16a-ol and ent-atisan-16a-ol, from sunflowers, as oviposition stimulants for the banded sunflower moth, Cochylis hospes. Journal of Chemical Ecology, 2005, 31, pp. 89-102.
8. Mitscher, L.A.; Rao, G.S.R.; Veysoglu, T.; Drake, S.; Haas, T. Isolation and identification of trachyloban-19-oic and (−)-kaur-16-en-19-oic acids as antimicrobial agents from the prairie sunflower, *Helianthus annuus*. Journal of Natural Products, 1983, 46, pp. 745-746.
9. Mullin, C.A.; Alfatafta, A.A.; Harman, J.L.; Everett, S.L.; Serino, A.A. Feeding and toxic effects of floral sesquiterpene lactones, diterpenes, and phenolics from sunflower on western corn rootworm. Journal of Agricultural and Food Chemistry, 1991, 39, pp. 2293-2299.
10. Gao, Y.; Zheng, C.-D.; Li, Y.; Fan, C.; Tu, G.-H.; Gao, J.-M. Chemical constituents from leaves of allelopathic cultivar sunflower in China. Chemistry of Natural Compounds, 2008, 44, pp. 773-775.
11. Macías, F.A.; López, A.; Varela, R.M.; Torres, A.; Molinillo, J.M.G. Helikauranoside A, a new bioactive diterpene. Journal of Chemical Ecology, 2008, 34, pp. 65-69.
12. Suo, M.R.; Tian, Z.; Yang, J.S.; Lu, Y.; Wu, L.; Li, W. Diterpenes from *Helianthus annuus* and their cytotoxicity in vitro. Acta Pharmacologica Sinica, 2007, 42, pp. 166-172.

13. Bohlmann, F.; Jakupovic, J.; King, R.M.; Robinson, H. New ent-atisirenic- and ent-kaurenic acid-derivatives from *Helianthus* species. Phytochemistry, 1980, 19, pp. 863-868.
14. Herz, W.; Kulanthaivel, P.; Watanabe, K. Ent-kauranes and other constituents of three *Helianthus* species. Phytochemistry, 1983, 22, pp. 2021-2025.
15. Herz, W.; Kulanthaivel, P. Ent-pimaranes, ent-kauranes, Heliangolides and other constituents of three *Helianthus* species. Phytochemistry, 1984, 23, pp. 1453-1459.
16. Ungur, N.; Grinco, M.; Kulciţki, V.; Barba, A.; Bîzîcci, T.; Vlad, P.F. Isolation of ent-kaur-16-en-19-oic and ent-trachiloban-19-oic acids from the sunflower *Helianthus annuus L.*dry waste. Chemistry Journal of Moldova, 2008, 4, pp. 105-108.
17. Costa-Lotufo, L.V.; Cunha, G.M.A.; Farias, P.A.M.; Viana, G.S.B.; Cunha, K.M.A.; Pessoa, C.; Moraes, M.O.; Silveira, E.R.; Gramosa, N.V.; Rao, V.S.N. The Cytotoxic and embryotoxic effects of kaurenoic acid, a diterpene isolated from Copaifera langsdorffii oleo-resin. Toxicon, 2002, 40, pp. 1231-1234.
18. Ghisalberti, E.L. The biological activity of naturally occurring kaurane diterpenes. Fitoterapia 1997, 68, pp. 303-325.
19. Bruno, M.; Rosselli, S.; Pibiri, I.; Piozzi, F.; Bondi, M.L.; Simmonds, M.S.J. Semisynthetic derivatives of ent-kauranes and their antifeedant activity. Phytochemistry, 2001, 58, pp. 463-474.
20. Yang, Y.L.; Chang, F.R.; Wu, C.C.; Wang, W.Y.; Wu, Y.C. New ent-kaurane diterpenoids with anti-platelet aggregation activity from *Annona squamosa*. Journal of Natural Products, 2002, 65, pp. 1462-1467.
21. Zhang, Y.H.; Peng, H.Y.; Xia, G.H.; Wang, M.Y.; Han, Y. Anticancer effect of two diterpenoid compounds isolated from *Annona glabra* Linn. Acta Pharmacologica Sinica, 2004, 25, pp. 937-942.
22. Tirapelli, C.R.; Ambrosio, S.R.; de Costa, F.B.; Coutinho, S.T.; de Oliveira, D.C.; Oliveira, A.M. Analysis of the mechanisms underlying the vasorelax- ant action of kaurenoic acid in the isolated rat aorta. European Journal of Pharmacology, 2004, 492, pp. 233-241.
23. Jung, H.A.; Lee, E.J.; Kim, J.S.; Kang, S.S.; Lee, J.-H.; Min, B.-S.; Choi, J.S. Cholinesterase and BACE1 inhibitory diterpenoids from *Aralia cordata.* Archives of Pharmacal Research, 2009, 32, pp. 1399-1408.
24. Na, M.K.; Oh, W.K.; Kim, Y.H.; Cai, X.F.; Kim, S.H.; Kim, B.Y.; Ahn, J.S. Inhibition of protein tyrosine phosphatase 1B by ursane-type triterpenes isolated from *Symplocos paniculata*. Bioorganic & Medicinal Chemistry Letters, 2006, 16, pp. 3061-3064.
25. Vieira, H.S.; Takahashi, J.A.; Pimenta, L.P.S.; Boaventura, M.A.D. Effects of kaurane diterpene derivatives on germination and growth of *Lactuca sativa* seedlings. Zeitschrift für Naturforschung C: A Journal of Biosciences, 2005, 60C, pp. 72-78.
26. Baddeley, G.V.; Jarvips, M.W.; Jefferies, P.R.; Rosich, R.S. The diterpenes from a *Beyeria* sp. Australian Journal of Chemistry, 1964, 17, pp. 578-586.
27. Henrick, C.A.; Jefferies, P.R. The diterpenes of *Ricinocarpus stylosus* Diels. Australian Journal of Chemistry, 1964, 17, pp. 915-933.
28. Boeck, P.; Sa, M.M.; Souza, B.S.; Cercena, R.; Escalante, A.M.; Zachino, S.A.; Filho, V.C.; Yunes, R.A. A Simple synthesis of kaurenoic esters and other derivatives and evaluation of their antifungal activity. Journal of the Brazilian Chemical Society, 2005, 16, pp. 1360-1366.
29. Lee, J.B. Preparation of acyl halides under very mild conditions. Journal of the American Chemical Society, 1966, 88, pp. 3440-3441.
30. Croft, K.D.; Ghisalberti, E.L.; Jefferies, P.R.; Knox, J.R.; Mahoney, T.J.; Sheppard, P.N. Chemical and microbiological syntheses of intermediates in gibberellin biosynthesis. Tetrahedron, 1974, 30, pp. 3663-3667.
31. Vieira, H.S.; Takahashi, J.A.; de Oliveira, A.B.; Chiari, E.; Boaventura, M.A.D. Novel derivatives of kaurenoic acid: preparation and evaluation of their trypanocidal activity. Journal of the Brazilian Chemical Society, 2002, 13, pp. 151-157.
32. Boaventura, M.A.D.; Pereira, R.G.; Oliveira-Freitas, L.B.; Reis, L.A.; Silva-Vieira, H. Preparation and phytotoxicity of novel kaurane diterpene amides with potential use as herbicides. Journal of Agricultural and Food Chemistry, 2008, 56, pp. 2985-2988.
33. Briggs, L.H.; Cawley, R.W. The identity of kaurene with podocarprene. Journal of the Chemical Society, 1948, 70, pp. 1888-1889.
34. Bohlman, F.; Adler, A.; Schuste, A.; Gupta, R.K.; King, R.M.; Robinson, H. Diterpenes from Mikania species. Phytochemistry, 1981, 20, pp. 1899-1902.
35. Batista, R.; Garcia, P.A.; Castro, M.A.; Miguel Del Corral, J.M.; Feliciano, A.S.; Oliveira, A.B. iso-Kaurenoic acid from *Wedelia paludosa* D.C. Journal of the Brazilian Chemical Society, 2007, 18, pp. 622-627.
36. Cook, I. F.; Knox, J. R. A synthesis of steviol. Tetrahedron Letters, 1970, 11, pp. 4091-1493.
37. Cook, I. F.; Knox, J. R. The synthesis of 13-hydroxylated ent-kaur-16-ene derivatives using an acyloin-like cyclization of keto esters. Tetrahedron, 1976, 32, pp. 363-367.

38. Cook, I. F.; Knox, J. R. Bridged-ring products from the acyloin-like cyclization of diterpenoid keto-esters. Tetrahedron, 1976, 32, pp. 369-375.
39. Peixoto, A.F.; Melo, D.S.; Fernandes, T.F.; Fonseca, Y.; Gusevskaya, E.V.; Silva, A.M.S.; Contreras, R.R.; Reyes, M.; Usubillaga, A.; Santos, E.N.; Pereira, M.M.; Bayon, J.C. Rhodium catalyzed hydroformylation of kaurane derivatives: A route to new diterpenes with potential bioactivity. Applied Catalysis A-General, 2008, 340, pp. 212-219.
40. Peixoto, A. F. Development of new transition metal catalysts. Ph.D. Thesis, University of Coimbra, Coimbra, Portugalia, 2010 (in Portuguese).
41. Cavalcanti, B.C.; Bezerra, D.P.; Magalhaes, H.I.F.; Moraes, M.O.; Lima, M.A.S.; Silveira, E.R.; Camara, C.A.G.; Rao, V.S.; Pessoa, C.; Costa-Lotufo, L.V. Kauren-19-oic acid induces DNA damage followed by apoptosis in human leukemia cells. Journal of Applied Toxicology, 2009, 29, pp. 560-568.
42. Aparicio, R.; Bahsas, A.; Usubillaga, A. Allylic oxidation of ent-kaurenic acid, ent-kaurenic acid methyl ester and ent-kaurenol. Avances en Química. 2007, 2, pp. 3-8.
43. Grinco, M.; Chetraru, O.; Kulciţki, V.; Barba, A.; Boico, A.; Vlad, P.; Ungur, N. C15 functionalized derivatives of ent-kaur-16-en-19-oic acid: isolation from the sunflower *Helianthus annuus* L. and synthesis. Chemistry Journal of Moldova, 2010, 5, pp. 106-108.
44. Hueso-Falcón, I.; Girón, N.; Velasco, P.; Amaro-Luis, J.M.; Ravelo, A.G.; Heras, B.; Hortelano, S.; Estevez-Braun, A. Synthesis and induction of apoptosis signaling pathway of ent-kaurane derivatives. Bioorganic & Medicinal Chemistry, 2010, 18, pp. 1724-1735.
45. Lyss, G.; Knorre, A.; Schmidt, T.J.; Pahl, H.L.; Merfort, I. The anti-inflammatory sesquiterpene lactone helenalin inhibits the transcription factor NF-kappaB by directly targeting p65. Journal of Biological Chemistry, 1998, 273, pp. 33508-33516.
46. Banerjee, A.K.; Martin, A.; Nakano, T. Photosensitized oxygenations of some derivatives of kaurenes. Journal of Organic Chemistry, 1973, 38, pp. 3807-3811.
47. Ungur, N.; Barba, A.N.; Vlad, P.F. Molecular rearrangement of tetra- and pentacyclic diterpenoids formed with the participation of pimarane intermediates. Chemistry of Natural Compounds, 1991, 27, pp. 3-16 (in Russian).
48. Olah, G.A.; Prakash, G.K.S.; Molnar, A.; Sommer, J. Superacid Chemistry. Wiley, New Jersey, 2009, 867 p.
49. Ungur, N.; Kulcitki, V.; Chetraru, O.; Grinco, M.; Vlad, P.F. Synthesis of natural atisane-type diterpenoids by retro-biomimetic transformations. Helvetica Chimica Acta, 2013, 96, pp. 864-871.
50. Ghisalberti, E.L.; Jefferies, P.R.; Sefton, M.A. Sheppard, P. N. Microbiological transformations of 19-oxygenated ent-kauranes. Tetrahedron, 1977, 33, pp. 2451-2456.
51. Silva, E.A.; Takahashi, J.A.; Boaventura, M.A.D.; Oliveira, A.B. The biotransformation of ent-kaur-16-en-19-oic acid by *Rhizopus stolonifer*. Phytochemistry, 1999, 52, pp. 397-400.
52. Punnapayak, H.; Pechwang, J.; Chaichit, N.; Jaiboon, N.; Pornpakakul, S.; Petsom, A. Crystal structure of ent-(7 beta, 11 alpha)-dihydroxy-1-oxo-kaur-16-en-19-oic acid, C20H28O5. Zeitschrift für Kristallograhic, 2002, 217, pp. 603-604.
53. Pechwang, J.; Sihanonth, P.; Pornpakakul, S.; Muangsin, N.; Piapukiew, J.; Vangnai, A.; Chaichit, N.; Chuchawankul, S.; Petsom, A. Biotransformation of ent-kaur-16-en-19-oic acid by Psilocybe cubensis. Natural Product Research, 2010, 24, pp. 905-914.

DETERMINATION OF STRONTIUM IONS IN WATERS WITH A HIGH CONTENT OF SODIUM IONS

Tatiana Mitina*, Nadejda Bondarenco, Diana Grigoras, Elena Botizat, Tudor Lupascu

Institute of Chemistry of Academy of Sciences of Moldova, 3 Academiei str., Chisinau MD-2028, Republic of Moldova
**e-mail: mitina_tatiana@mail.ru; phone / fax (+373 22) 73 99 77*

Abstract. This paper reports on the influence of sodium ions on experimental determination of strontium ions concentration in waters with a high content of sodium ions by using emission flame photometry and atomic absorption spectroscopy. For the method of emission flame photometry it was shown that at a wavelength of 460.7 nm (spectral emission line of strontium) the emission is linearly dependent on the concentration of sodium ions. The greatest impact of high concentrations of sodium ions on the result of determination the strontium ions concentration has been registered at low levels of strontium. The influence of nitric acid on the results is also discussed. In the case of using atomic absorption spectroscopy method no influence of sodium ions and nitric acid on the results of determination the strontium ions concentration was revealed. The metrological characteristics of both methods are evaluated.

Keywords: water analysis, strontium ions, emission flame photometric method, atomic absorption spectroscopy.

Received: June 2014/ Revised final: October 2014/ Accepted: November 2014

Introduction

Strontium is a micro-component of waters. The negative effects of elevated strontium on human health are well established. Being close to the chemical properties of calcium, strontium sharply differs in its biological action. Excess levels of this element in water cause the substitution of calcium in the bones, liver and brain. This pathology is a reflection of the competitive relations of strontium and calcium in their distribution in the body [1]. Despite the fact that strontium content in drinking water is not regulated by the Governmental Decision No. 934 from 15.08.2007, according to GOST 2874-82 strontium content must not exceed 7 mg/L. The US EPA (United States Environmental Protection Agency) has set three health advisory levels for strontium: a Lifetime Health Advisory Level (Lifetime HAL), a one-day Health Advisory Level (One-Day HAL), and at ten-day Health Advisory Level (10-Day HAL). HALs serve as an estimate of acceptable levels in drinking water [2]. They are used by Federal, State, and local officials, when making decisions about the safety of the drinking water supply. The HALs for strontium are defined as:

- Lifetime HAL = 4 mg/L: a person drinks this level (or lower) their entire life and is not expected to develop any health problems related to strontium exposure.
- One-Day HAL = 25 mg/L: the level for which a child, drinking 1 L of water in a day, would not be expected to develop any related to strontium exposure health problems.
- Ten-Day HAL = 25 mg/L: the level for which a child, drinking 1 L of water per day for ten days, would not be expected to develop any related to strontium exposure health problems.

The evaluation of strontium content in drinking water, especially in Moldova, is necessary because its content in groundwater in some areas exceeds the permissible concentration [3]. In order to determine the strontium in water, the following standardized methods are used: emission flame photometric method [4], the method using capillary electrophoresis [5] and the method of atomic emission spectroscopy with inductively coupled plasma [6, 7]. One of the most affordable and widely used methods is emission flame photometric strontium determination. However, this method is applied to drinking water and does not take into account the influence of sodium ions on the determination of strontium from its spectral emission line (λ = 460.7 nm).

Evidence of water micro-components on the background of high concentrations of its major components is always associated with the possibility to get doubtful results, due to the occurrence of spectral and matrix effects. We have studied the effect of sodium ions on the result of determination the strontium ions concentration, by using emission flame photometry. As known, sodium is a macro-component of water and its content in drinking water in Moldova is limited to a concentration of 200 mg/L. The results of our research show that concentration of sodium in the waters of Moldova is highly variable and can range from small values to concentrations far exceeding the maximum permissible value. In the present study we have evaluated the use of flame emission photometry method for determining the concentration of strontium ions in water in the presence of various concentrations of sodium ions.

Experimental

All experimental work on the determination of strontium ions concentration by flame photometry were performed on an atomic absorption spectrometer AAS-1 (mode-emission) in a flame of propane-butane-air at a wavelength of λ = 460.7 nm [4].

Model solutions containing strontium ions with concentrations of 1.0, 2.5, 5.0, 7.5, 10 mg/L were prepared from a standard sample ISS 0148:200, certified mass concentration of strontium ions 1 mg/cm^3 and a relative error of less than

1% with a probability of 0.95% (Ukraine). The background is a solution containing sodium ions with concentrations of 0, 23, 46, 92, 230, 575 and 1150 mg/L, prepared from a standard of 0.1 M NaCl. In these solutions we have added nitric acid 1:5 (1 mL to 100 mL of sample) and lanthanum buffer (2.5 mL La^{3+} 100 mg/L to 100 mL of sample).

The graphs of the emission intensity as function of strontium ions concentration coincide at given sodium ions concentrations of 0, 23, 46 and 92 mg/L.

Results and discussion

The influence of sodium ions begins at a concentration of 230 mg/L. Figure 1 shows the effect of sodium ions on the intensity of strontium emission.

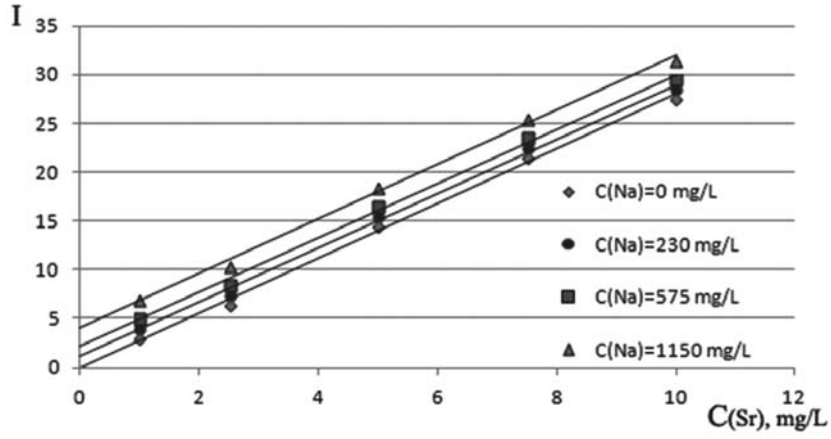

Figure 1. Dependence of emission intensity of strontium ions upon their concentration at various sodium contents.

The dependence of emission intensity of strontium ions concentration is linear for different sodium contents and is described by the equation $y = a \cdot x$, when the background solution contains sodium ions at a concentration of less than 230 mg/L and by the equation $y = a \cdot x + b$ in the case, when sodium ions are presented at concentrations above 230 mg/L. The correlation coefficient ranged from 0.997 to 1.

Figure 1 shows that increase of sodium ion concentration enhances the strontium ions emission intensity.

Figure 2 shows the dependence of the emission intensity on the concentration of sodium ions at a wavelength $\lambda = 460.7$ nm. The graph is linear over the sodium concentration range 0-1150 mg/L.

According to Figures 1 and 2, the presence of sodium ions in model solutions increases the emission intensity that was measured at strontium spectral emission line ($\lambda = 460.7$ nm).

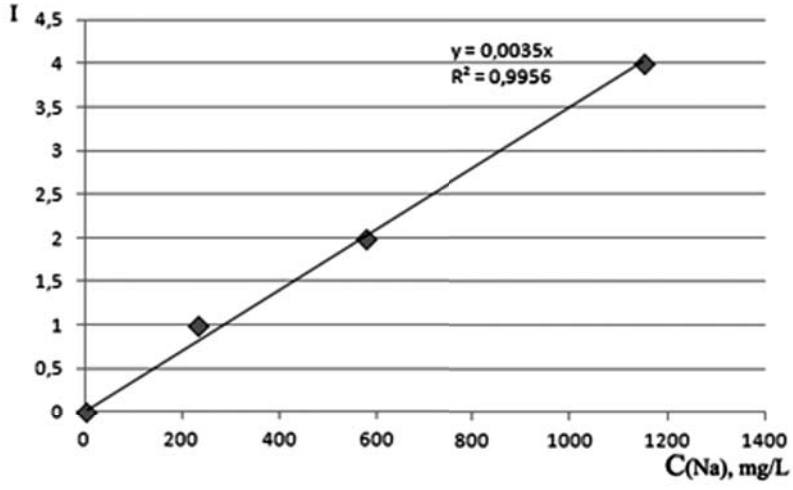

Figure 2. Emission intensity of sodium ions at $\lambda = 460.7$ nm.

Figure 3 shows dependence of the total emission intensity to the intensity of radiation of strontium ions at various sodium ions concentrations.

Figure 3 demonstrates that sodium ions at concentrations above 200 mg/L have a marked effect on the result of determination the strontium ions concentration. It should be noted, that this effect greatly increases at low strontium concentrations. Thus, the detected signal for strontium (concentration 1.0 mg/L) increases by 1.33 times in the presence of sodium ions concentration of 230 mg/L, increases by 1.66 times when the concentration of sodium ions is 575 mg/L and by 2.33 times at a concentration of sodium ions of 1150 mg/L.

Thus, the effect of sodium, which is caused by nonspecific radiation, augments with decreasing the strontium concentrations.

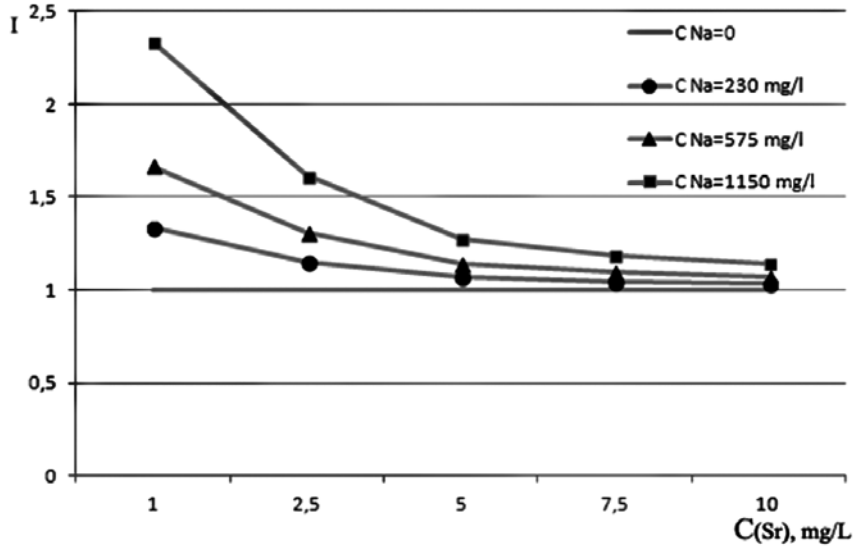

Figure 3. Dependence of the total emission intensity to the emission intensity of strontium ions at various concentrations of sodium ions.

Besides model solutions, in order to study the effect of sodium ions in the determination of strontium ions concentration by flame photometry, the natural mineral water Soroca was used, with a sodium content of 1.5 g/L. Strontium in this sample was determined: 1) without considering the background, 2) taking into account the background and 3) using the method of supplementation. Using the calibration graph plotted from reference solutions containing no sodium ions, strontium concentration was found 1.8 mg/L. At the same time, if we consider the background emission (sodium ion concentration of 1.5 g/L), the content of strontium in the test water is less than 0.5 mg/L.

In order to assess the correctness of strontium ions determination, the method of additions was used. The graphs for the addition method were plotted with and without taking into account the background radiation (Figures 4 and 5).

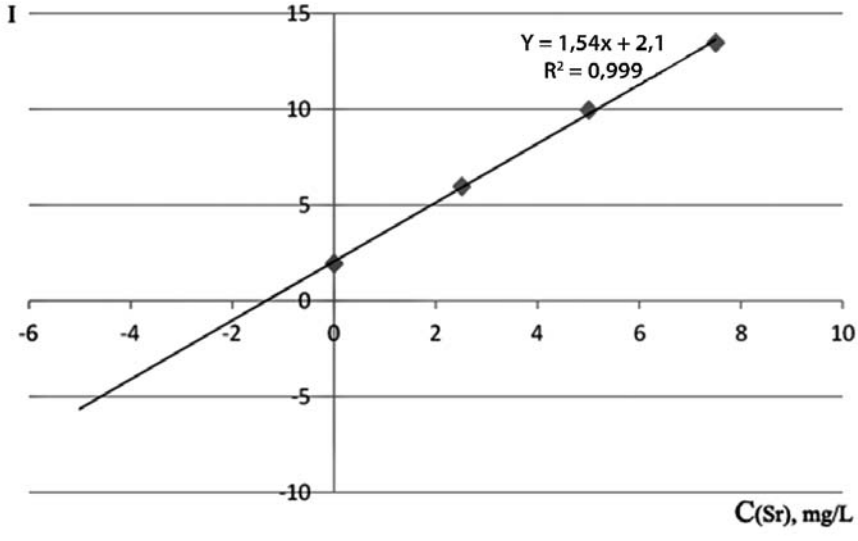

Figure 4. Method of additions without considering the background (water Soroca).

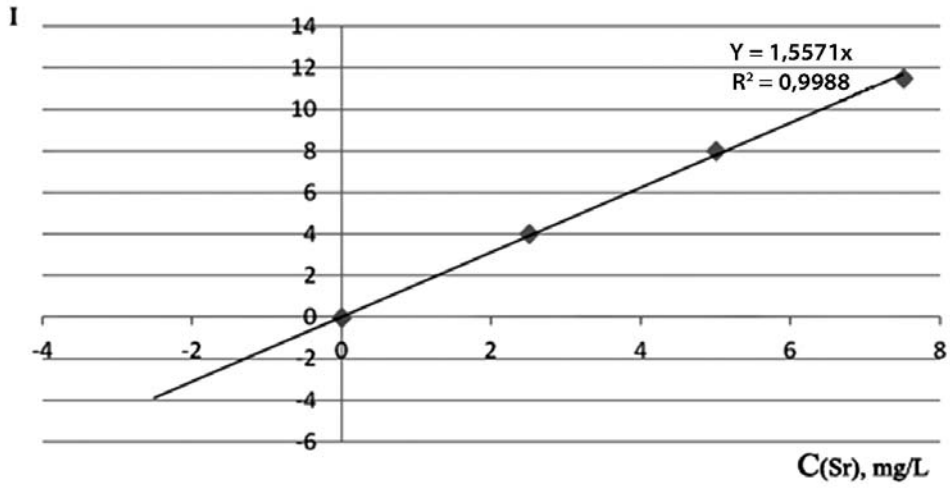

Figure 5. Method of additions taking into account the background (water Soroca).

Strontium ions content that was determined by excluding the background is 1.3 mg/L, as opposed to 0.5 mg/L, when the background is considered.

Thus, in the case of interfering effect that was caused by a non-selective emission of sodium ions, the method of addition may be applied, if the background emission is taken into account. The results of determination the strontium ions concentration, which were obtained by direct determination, are in good agreement with the results obtained by the addition method, taking into account the background.

In addition, we have shown the effect of nitric acid on the results of determination the strontium ions concentration by flame photometry. According to GOST 23950-88, nitric acid is added in standard solutions and samples (1:5, 10 mL per one liter of sample), *i.e.* its concentration is 0.03 N.

Increasing the nitric acid concentration by 0.04 N (to 0.07 N) leads to the suppression of strontium signal by 20%, while increasing the nitric acid concentration by 0.05 N (up to 0.075 N) leads to the suppression of the signal by 21%. Hence, using the method of flame photometry it is important to align the content of nitric acid in the samples and standards. This is particularly important in the determination of strontium ions concentration in the conserved waters, where 5 mL of concentrated nitric acid per 1 L of sample are usually added, to achieve a pH <2. Nitric acid concentration in these samples is 0.075 N.

Besides the method of flame photometry, we have employed the method of atomic absorption determination of strontium ions in water, which is not standardized [8].

Assays were performed with an atomic absorption spectrometer AAS-1N in the flame of acetylene-air at a wavelength of λ = 460.7 nm and 5 mA current of the hollow cathode lamp.

In the analysis of model solutions with different concentrations of sodium and natural mineral water Soroca, no effect of sodium on strontium absorption was found. Analogically, we observed no effect of nitric acid on the result of strontium ions determination.

The concentration of strontium ions in the mineral water Soroca, which was determined by atomic absorption spectrometry, was less than 0.5 mg/L, as in the case of flame photometric method, when the background was taken into account.

Metrological parameters of both methods were determined on model solutions with the content of sodium ions of 1150 mg/L and the content of strontium ions of 2 mg/L and 5.0 mg/L [9]. The accuracy of obtained by both methods results is presented in the Table 1.

Table 1

The accuracy in determining the strontium ions concentration by flame photometry, considering the background emission, and by atomic absorption spectrometry.

Strontium concentration, mg/L	*Flame photometry, considering the background emission*		*Absorption spectrometry*	
	Found, mg/L	*Divergence, %*	*Found, mg/L*	*Divergence, %*
2.0	1.97	1.50	2.03	1.49
5.0	5.11	2.17	5.07	1.39

The variation coefficient of flame photometry for the determination of strontium in water is 6.3%, of atomic absorption - 4.5%, the detection limit for both methods is 0.5 mg/L. Thus, for the determination of strontium by flame

photometry it's necessary to consider the background emission and align the concentration of nitric acid in the sample solutions and standards. To determine strontium in waters of unknown composition and water samples preserved with nitric acid, it's preferably to use atomic absorption spectrometry.

Conclusions

The influence of sodium ions and nitric acid on experimental determination of strontium ions concentration in waters by using emission flame photometry and atomic absorption spectroscopy has been investigated, being also evaluated metrological characteristic of both methods.

The evaluation of the use of flame emission photometry method for determining the concentration of strontium ions in water, the following remarks can be outlined: high sodium content in water leads to an overestimation of the results of determination strontium; at wavelength of 460.7 nm (spectral emission line of strontium) the emission is linearly dependent on the concentration of sodium ions; obtained results showed suppressing influence of nitric acid on the determination of strontium ions.

In the case of using atomic absorption spectroscopy method no influence of sodium ions and nitric acid on the results of determination the strontium ions concentration was revealed.

In conclusion, for the determination of strontium by flame photometry it is necessary to consider the background emission and align the concentration of nitric acid in the sample solutions and standards. To determine strontium in waters of unknown composition and preserved with nitric acid water samples, it is preferably to use atomic absorption spectrometry.

References

1. Sudia, D.A.; Lastkov, D.O. Problem toxicological actions of stable strontium salts on the organism. Modern problems of toxicology of food and chemical safety, 2013, 62(3), pp. 55-60 (in Russian).
2. The Potential Regulatory Implications of Strontium. American Water Works Association, http://www.awwa.org/Portals/0/files/legreg/documents/2014AWWAStrontiumBriefingPaper.pdf
3. Mitina, T.; Bondarenco, N.; Bunciuc, O. The study of chemical composition and evaluation of groundwater quality in some regions of Moldova. Chemistry Journal of Moldova, 2012, 7(2), pp. 89-92.
4. GOST 23950-88. Drinking water. Emission flame photometric method for the determination of strontium. (in Russian).
5. GOST R 31869:2012. Water. Methods for the determination of cations (ammonium, barium, potassium, calcium, lithium, magnesium, sodium, strontium) using capillary electrophoresis (in Russian).
6. ISO/WD 11885:2003 Water Quality. Determination of 33 elements by inductively coupled plasma atomic emission spectroscopy (ICP-OES) (Revision of ISO 11885:1996)
7. GOST R 51309-99 Determination of elements by atomic spectroscopy (method of atomic emission spectroscopy with inductively coupled plasma). (in Russian).
8. Poluektov, N.S; Mishcenko, V.T. Analytical chemistry of strontium. Nauka: Moskow, 1978, 223 p. (in Russian).
9. ISO 5725-(1-6)-2002 Accuracy (trueness and precision) of determination methods and results.

IMPROVEMENT OF COAGULATION PROCESS FOR THE PRUT RIVER WATER TREATMENT USING ALUMINUM SULPHATE

Larisa Postolachi*, Vasile Rusu, Tudor Lupascu, Alexei Maftuleac

Institute of Chemistry of Academy of Sciences of Moldova, 3 Academiei str., Chisinau, MD-2028, Republic of Moldova
**e-mail: larisa.postolachi@gmail.com; phone: (+373 22) 73 97 31; fax: (+373 22) 73 99 54*

Abstract. The aim of presented research was to optimize the treatment process of the Prut River water. In order to realize the proposed goal, there were studied the following factors which can improve the process of coagulation: (i) the influence of stirring speed during coagulation and (ii) the influence of the concentration of the coagulant solution added in the process of coagulation. The optimal conditions of coagulation were established using the *Jar-test* method. Application of the recommended procedure contribute to the reduction of the coagulant dose, the contact time, the aluminum concentration in water and the expenses for water treatment.

Keywords: coagulation, aluminum sulphate, *Jar-test* method.

Received: February 2015/ Revised final: April 2015/ Accepted: April 2015

Introduction

Natural water is a heterogeneous medium due to the presence of particulate materials and micro-bubbles of gas. The particulate materials of natural waters are distinguished by their size. The particles with sizes of less than 10μ have a sedimentation velocity less than 0.01 cm/s, and are evenly distributed throughout the water horizon [1]. With decreasing of particle size, the time required for settling has increased. Due to very small dimensions, the only way to separate the particles is their agglomeration into bigger ones that settles easier. Rejecting electrostatic forces prevent the particles to reach each other, and the suspension is stable [2].

For removal of fine-dispersed and colloidal impurities, the methods of coagulation and flocculation are often applied. Coagulation is based on the interaction of colloid and fine-dispersed particles with aggregates formed upon adding of coagulants. This method was first used at the beginning of XX century [1]. Coagulation can be used both on treatment of drinking water [3-7] and on the purification of waste water [8-10].

The role of coagulation is to overcome the factors that contribute to the stability of the given system. It is achieved using the suitable chemical substance, typically aluminum or iron salts, so-called coagulants. The coagulation process takes place in two distinct steps. The first step is the adding of coagulant; as a result, the destabilization of colloidal suspension occurs and the flocs are formed. During second step, the formation of agglomerates, large agglomerates, takes place, which can easily be separated by gravitational sedimentation [2].

The most widely used coagulant is the aluminum sulphate, which has been used for water treatment [2] applied in a number of countries since the early 1900 [11]. It, usually, is obtained by reaction of bauxite with sulphuric acid [2, 12].

Coagulation is the main reaction stage for the removal of natural organic matter and other contaminants in water treatment processes. The choice of a coagulant has a major influence on the performance of the coagulation process [13]. The aluminum sulphate is used at the purification of water with high turbidity. This coagulant is characterized by relatively low cost, good solubility, no special requirements for the use of dry and dissolved product. It was demonstrated the high efficacy at the removal of humic substances, using the aluminum sulphate [14]. Its application ensures the satisfactory effect in the pollutants removal without adding any additive agents [6].

The beneficial effects of the use of aluminum as a coagulant in water treatment are recognized. However, according to the World Health Organization [15], the excess of aluminum is a risk factor for the development or acceleration of Alzheimer's disease. The contribution of drinking-water to the total oral exposure to aluminum is usually about 5% of the total intake. Taking this into account, a practicable level is derived, based on optimization of the coagulation process in drinking-water plants, to minimize aluminum levels in water at final stage. Several approaches are available for minimizing residual aluminum concentrations in treated water. These include (i) use of optimum pH in the coagulation process, avoiding excessive aluminum dosage, (ii) good mixing at the point of application of the coagulant, (iii) optimum paddle speeds for flocculation and (iv) efficient filtration of the aluminum flocs.

The goal of this paper was to perform the coagulation tests, establishing the influence of different factors in the laboratory conditions and at the Water Treatment Plant, Municipal Company "Apa-Canal", town Ungheni (Republic of Moldova).

Experimental

The efficiency of the coagulation process depends on raw water quality, the coagulant used and operational factors, including mixing conditions, coagulation dose and pH. The required coagulant dose and pH can be determined by using small-scale batch coagulation tests, often termed *Jar-test* (tests with the volume of water of the order of 1 L

and above) [15]. *Jar test* is a pilot-scale test of the treatment chemicals used in a particular water plant. It simulates the coagulation/flocculation process in a water treatment plant and helps operators determine if they are using the right amount of treatment chemicals, and, thus, improves the plant's performance [16].

Increasing doses of coagulant are applied to raw water samples that are stirred and allowed to settle. The optimum dose is selected as that which achieves adequate removal of turbidity; the optimum pH can be selected in a similar manner. These tests have to be conducted at a sufficient frequency to keep pace with changes in raw water quality and hence coagulant demand [15].

In our research, the optimal conditions of coagulation were established using the *Jar-test* method [16,17]. During experiment there was used the modelled water (MW, tap water with turbidity modified with aquatic sediments) and the natural water from the Prut River (town Ungheni). The coagulation process was studied using the raw water with turbidity between 33-109 nephelometric turbidity units (NTU). As coagulant, the aluminum sulphate ($Al_2(SO_4)_3 \cdot 18H_2O$) was used, the working solutions being of 1, 10 and 25%. The different coagulant doses were studied, i.e. from 3.7 to 35 mg/L.

In the sample of raw water (800mL) the required amount of coagulant has been added slowly [18]. Then the sample was subjected to rapid mixing (500 rpm) for 2 minutes, followed by a slow mixing (120 rpm) for 20 minutes. After mixing the samples have been left for sedimentation. At the end of the settling period, the supernatant is withdrawn for analyses. During the *Jar-testing* the dynamics of turbidity and value of pH have been determined (Table 1).

Table 1

Monitored parameters during tests of coagulation.

Analyzed parameter	*Raw water*	*Water after 20 minutes of settling*	*Water after 40 minutes of settling*	*Water after 60 minutes of settling*
pH	+	+	+	+
Turbidity	+	+	+	+

The turbidity has been determined in accordance with standard GOST 3351-74 [19]. The turbidity removal (R_T, %), which expresses the efficiency of the process, was calculated using the following Eq.(1) [20]:

$$R_T = \frac{T_i - T}{T_i} \cdot 100\%, \quad (1)$$

where: T_i – initial turbidity, NTU;
T – residual turbidity, NTU.

In order to optimize the process of coagulation there were studied the following factors: (i) the influence of mixing speed and (ii) the influence of the concentration of coagulant added in the process of coagulation.

This paper presents a study regarding the water treatment with aluminum sulphate, aiming to obtain drinking water with turbidity values lees than 5 NTU, according the existing criteria. The existing drinking water criteria for studied parameters are presented in Table 2.

Table 2

The limit values of studied parameters according to different criteria for drinking water.

Parameter	*Directive 98/83/EC (European Union) [21]*	*Law 458/2002 (Romania) [22]*	*Order 934/2007 (Republic of Moldova) [23]*
pH	6.5-9.5	6.5-9.5	6.5-9.5
Turbidity	≤1 NTU	≤5 NTU	≤5 NTU

Results and discussion

The main stages applied in the potabilization technologies of natural waters

The water quality from surface sources (rivers, lakes) often does not correspond to the drinking water criteria, because of the high turbidity, the high content bacteria or dangerous dissolved substances. In order to be consumed, the natural water would be processed, so as to meet the existing criteria for drinking water.

The role of treatment plant is to "correct" the raw water quality to achieve user requirements [24]. The main stages applied in the potabilization technologies of natural waters are presented in Figure 1 and include the following:

- *pre-oxidation* is the permanent process that should ensure the optimal operation of subsequent processes, removing the organic matter presented in water, the analyzed parameters being the biochemical oxygen demand;

- the process of *water clearness* consisting of coagulation and flocculation processes - in order to obtain a performance at this stage the choice of coagulant is essential, the analyzed parameters being turbidity and pH value;

- *decantation* for retain the coagulated suspensions (flocs);

- *filtration* for finishing of the clearness process;
- *water conditioning* which consists of oxidation with ozone, followed by adsorption on granular activated carbon in order to remove the toxic chemical compounds;
- *water disinfection* for the total removal of viruses, bacteria and other micro-organisms from the water.

For the coagulation of particulate materials, the aluminum sulphate is the most commonly used, which by hydrolysis and the formation of oligomers with complex structures into a wide range with high loads (from $[Al_2(OH)_2(H_2O)_8]^{4+}$ to $[Al_{28}(OH)_{70}(H_2O)_{28}]^{14+}$) facilitates the aggregation and sedimentation of particulate materials from water [25].

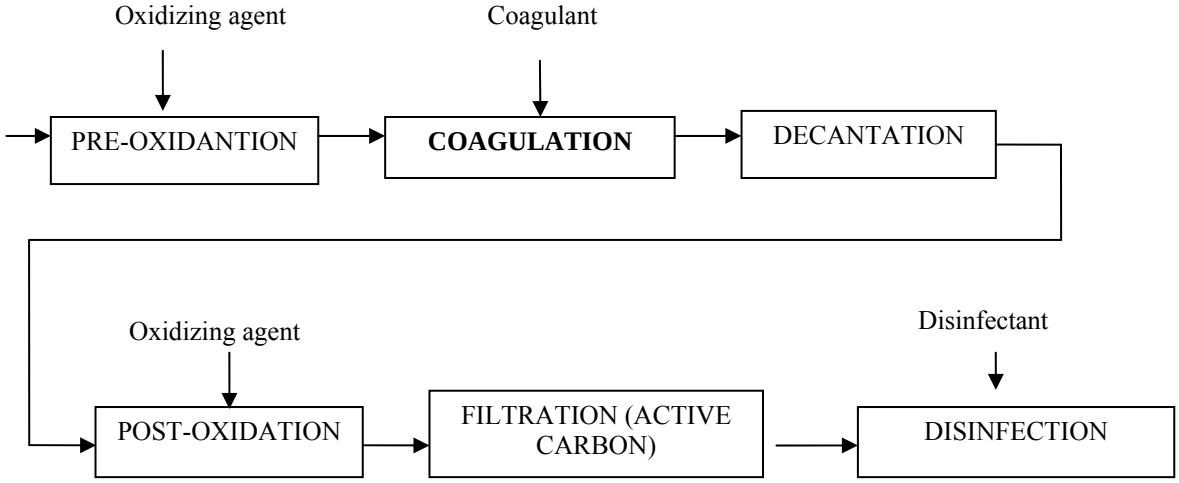

Figure 1. The main steps of potabilization technologies applied for natural waters [24].

Jar-testing performed on MW

The turbidity removal during the coagulation process depends on the colloids type, temperature, the pH value and chemical composition of the water, the type and dosage of coagulant, and the contact time provided for the formation of agglomerates [26].

Numerous *Jar-tests* were carried out in order to establish a practical understanding of the coagulation performance for this application. Initially, the coagulation process was studied on MW with turbidity between 33 and 40 NTU (Figures 2 and 3).

Experiments were carried out to determine the optimum dose of aluminum sulphate. During *Jar-testing* it was founded that during rapid mixing (Figure 2) the coagulation process was less efficient in comparison with the results obtained in conditions of the regular mixing (Figure 3). It was also established that in the conditions of the regular mixing at doses of coagulant in the range from 3.7 to 9.8 mg/L the turbidity of water falls below 5 NTU.

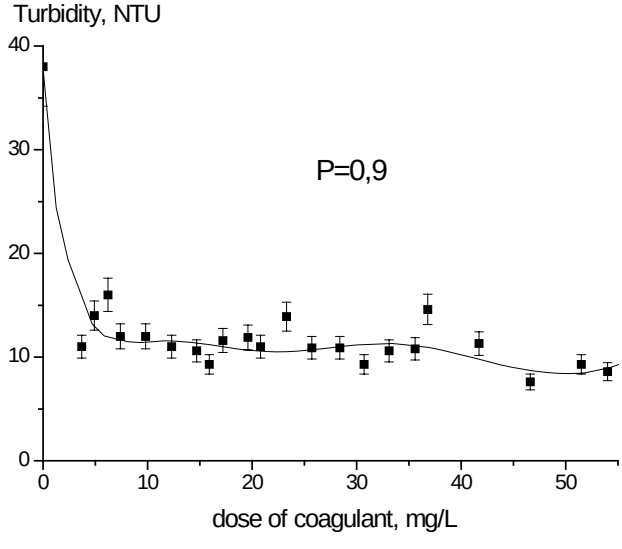

Figure 2. Residual turbidity for MW as function of coagulant dose, in conditions of rapid mixing (coagulant concentration of 1%). P – probability level.

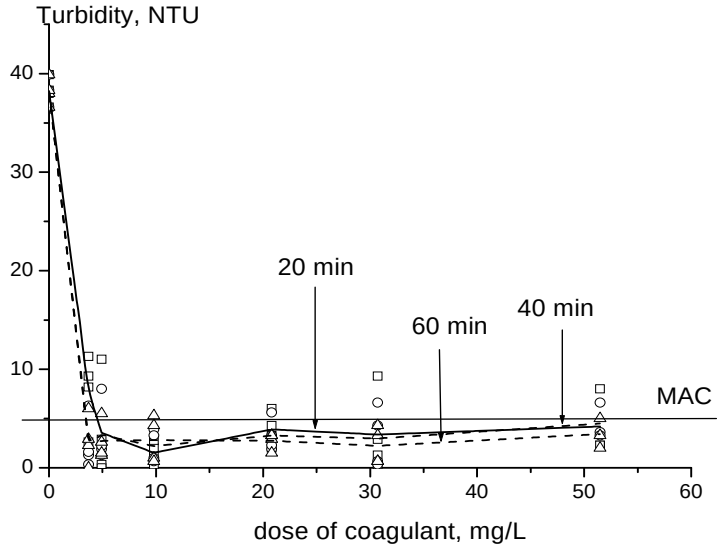

Figure 3. Residual turbidity for MW as function of coagulant dose, in conditions of regular mixing (coagulant concentration of 1%). MAC - maximal admissible concentration.

The concentration of the coagulant solution is an important factor in the coagulation process [18]. In this paper there has been studied the effectiveness of different dosages of the coagulant during the coagulation process in MW, being used the aluminum sulphate solution at various concentrations (10 and 25%) (Figures 4 and 5). The highest values of turbidity removal (83-93%) were obtained using more concentrated solution of the coagulant (25%).

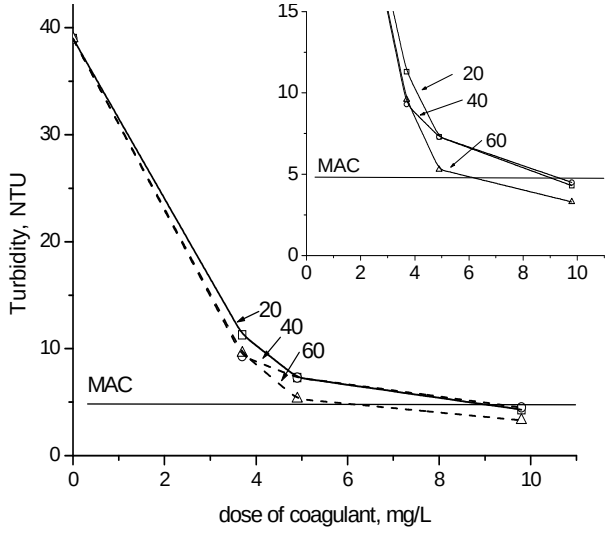

Figure 4. Residual turbidity for MW as function of coagulant dose (coagulant concentration of 10%) for different settling time (20, 40, and 60 minutes).

During the coagulation process, at the adding of coagulant the pH value of water has decreased [18]. Depending on the dose of coagulant (Figure 6), the pH value in water has decreased up to 7.5, which framing in limits of the accepted standards (Experimental, Table 2).

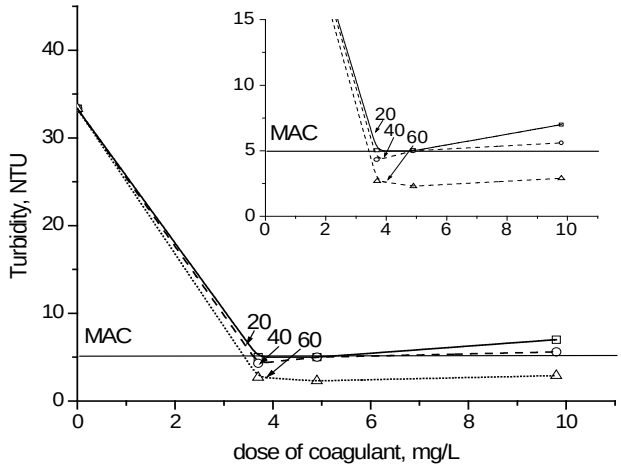

Figure 5. Residual turbidity for MW as function of coagulant dose (coagulant concentration of 25%) for different settling time (20, 40, and 60 minutes).

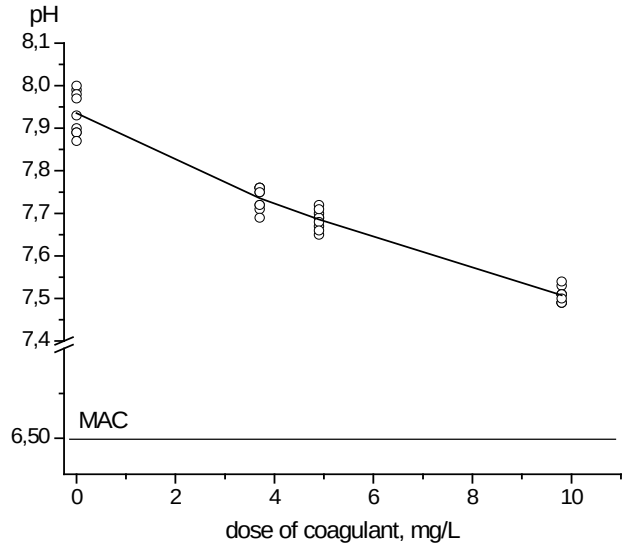

Figure 6. The variation of pH value in MW as function of added coagulant dose.

Jar-testing performed on natural water

The role of the coagulant agent depends on many factors including speciation of the hydrolysis products, quantity and reactivity of complexing ligands, and the rate of mass transfer between these components. The pH value of raw water is an important factor in determining the physical and chemical properties of the water as well as the hydrolyzates or the stability of coagulants. The efficiency of the pH is relative with the molecular structure of coagulants. The aluminum sulphate would generate various hydrolyzates such as $[Al_2(OH)_2]^{4+}$, $[Al_3(OH)_4]^{5+}$, $Al(OH)_3$, and $Al(OH)_4^-$ corresponding to different pH values of water. Those different hydrolyzates would exert a different effect on colloidal particles so that the mechanism and efficiency of the coagulation would be changed. When the solution pH is lower than 6, the positive hydrolyzates such as $[Al_2(OH)_2]^{4+}$ and $[Al_3(OH)_4]^{5+}$ could easily neutralize the colloidal particles with negative charges and further destabilize the colloids. Those positive hydrolyzates also generated the physical and/or chemical adsorption of the destabilized colloids [13].

In order to establish the optimal conditions of coagulation, the tests of coagulation on the raw water of the Prut River at the Water Treatment Plant of Municipal Water Company, Ungheni were carried out. As a coagulant the aluminum sulphate is used at Water Treatment Plant. The turbidity of natural water during the research period was in the range 50-109 NTU. The dose of coagulant was varied from 3.7 to 35 mg/L.

During of coagulation tests conducted on raw water at doses of coagulant in the range 3.7 – 9.8 mg/L, the turbidity have been decreased below value of 5 NTU (Figures 7-9).

Studying the efficiency of different doses of coagulant in coagulation process, the coagulant concentrations of 10 and 25% have been used (Figures 8 and 9). During the coagulation tests, the maximal values of the turbidity removal (89-98%) were obtained using more concentrated solution of coagulant (25%).

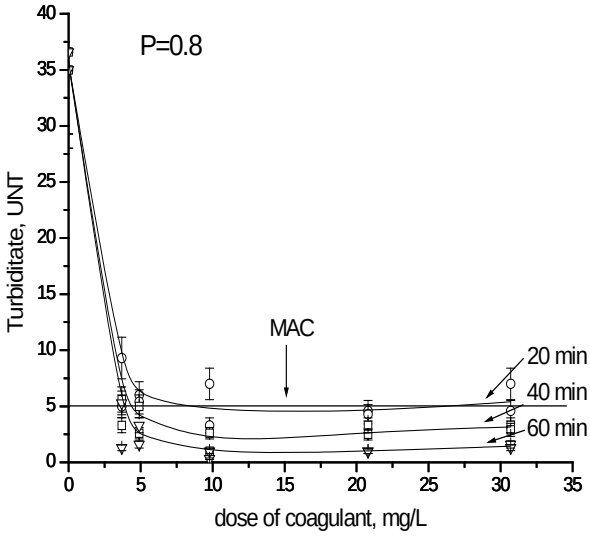

Figure 7. Residual turbidity for raw water, as function of coagulant dose (coagulant concentration of 1%). P – probability level. MAC - maximal admissible concentration.

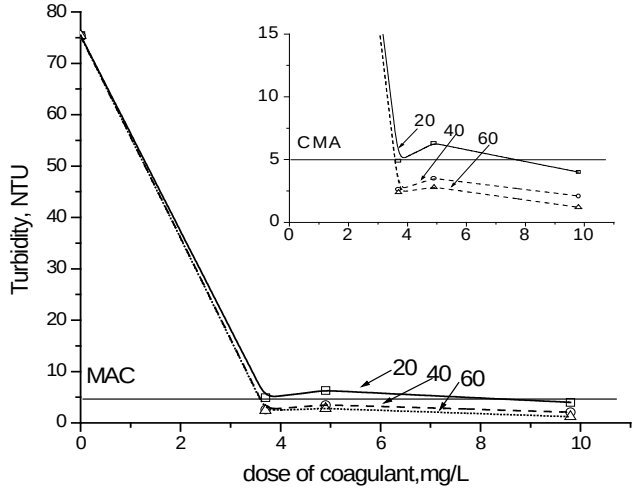

Figure 8. Residual turbidity for raw water as function of coagulant dose (coagulant concentration of 10%) for different settling time (20, 40, and 60 minutes).

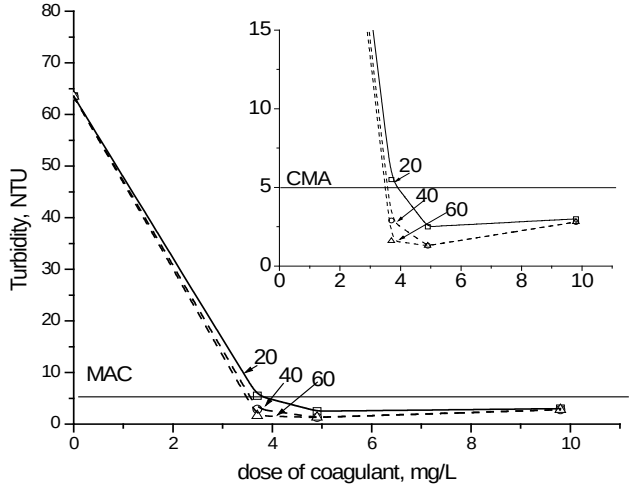

Figure 9. Residual turbidity for raw water as function of coagulant dose (coagulant concentration of 25%) for different settling time (20, 40, and 60 minutes).

During the *Jar-testing*, the pH value of raw water decreased (Figures 10 and 11). Depending of the coagulant dose, the pH value have been decreased until 7.2; value that didn't exceed the established standards (Table 2).

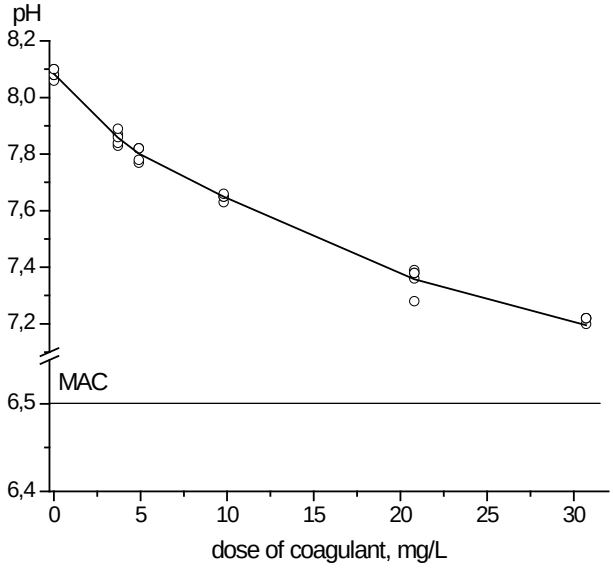

Figure 10. The variation of pH value in raw water, as function of added coagulant dose. MAC - maximal admissible concentration.

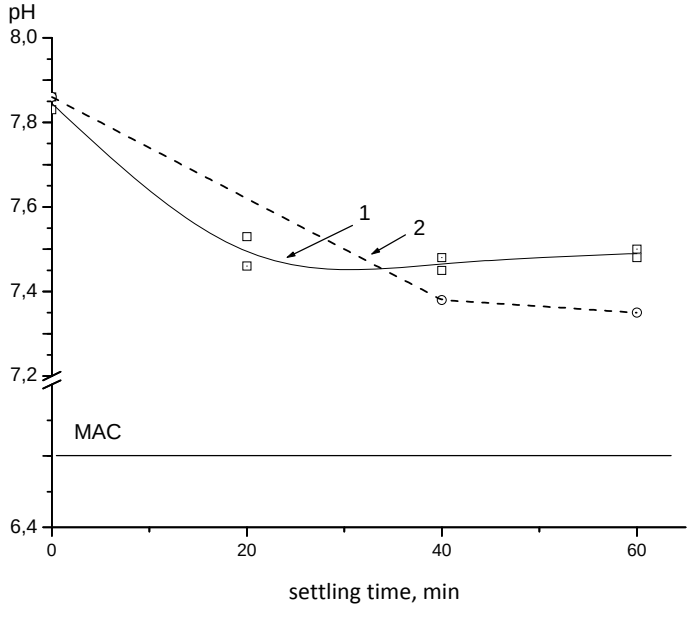

Figure 11. The variation of pH value in raw water, as function of added coagulant dose (1 - 4.9 mg/L, 2 – 9.8 mg/L). MAC - maximal admissible concentration.

Conclusions

Based on laboratory studies at the Water Treatment Plant, Municipal Enterprise, Ungheni, it was established that in conditions of regular mixing (rapid stirring for 2 minutes, followed by slow stirring for 20 minutes) the optimal dose of coagulant could be reduced to approximately 10 mg/L, being registered the decreasing of the turbidity value less than 5 NTU. The residual pH value is framing in limits of the accepted standards.

It was established that the use of concentrated solutions of the coagulant improves the coagulation process, the optimum concentration of aluminum sulphate being of 25%.

Application of the recommended procedure contribute to the reduction of the coagulant dose, the contact time, the aluminum concentration in water and the expenses for water treatment.

Acknowledgments

Thanks to Ms. Natalia Bors, deputy-director of the Municipal Water Treatment Company "Apa-Canal" of town Ungheni, for her kind support in achievement of this study.

References

1. Duca, Gh.; Scurlatov, Y.; Misiti. A.; Macoveanu, M.; Surpateanu, M. Ecological chemistry. Matrix Rom: Bucuresti, 1999, 305 p. (in Romanian).
2. Tzoupanos, N.; Zouboulis, A. Coagulation-flocculation processes in water/wastewater treatment: the application of new generation of chemical reagents. Heat Transfer, Thermal Engineering and Environment (HTE'08). Rhodes, Greece, 2008, pp. 309–317.
3. Grisin, B.; Bikunova, M.; Titov, E. et al. Experimental studies of water purification from Sura reservoir using aluminum-coagulants. Water treatment, 2010, 7, pp. 23–29 (in Russian).
4. Vlaicu, I.; Radovan, C. Application of several aluminum prehydrolysed coagulants to a surface water treatment for potable use. Environmental Engineering and Management Journal, 2009, 8(6), pp. 1371–1376.
5. Meghzili, B.; Medjram, M.; Zoubida, M. Tests of Coagulation - Flocculation by Aluminum Sulphate and Polycations Al13 on Raw Waters of the Station of Treatment Skikda (Algeria). European Journal of Scientific Research, 2008, 23(2), pp. 268–277.
6. Wira, D.; Wira J. Influence of flocculating agents onto the water coagulation course. Baltic Coastal Zone, 2006, 10, pp. 147–166.
7. Zamfiroiu, E.; Masu, S. Aspects Regarding the Efficiency of Coagulation Process for Some Surface Waters. Chemical Bulletin of Polytechnic University of Timisoara, 2007, 52(66), pp. 1–2.
8. Aygun, A.; Yilmaz, T. Improvement of Coagulation-Flocculation Process for Treatment of Detergent Wastewaters Using Coagulant Aids. International Journal of Chemical and Environmental Engineering, 2010, 1(2), pp. 97–101.
9. Klimiuk, E.; Filipkowska, U.; Libecki, B. Coagulation of Wastewater Containing Reactive Dyes with the Use of Polyaluminum Chloride (PAC). Polish Journal of Environmental Studies, 1999, 8(2), pp. 81–88.
10. Zaleschi, L.; Teodosiu, C.; Cretescu, I.; Rodrigo, M. A comparative study between electrocoagulation and chemical coagulation applied for wastewater treatment. Environmental Engineering and Management. Book of abstracts, Bahatonalmadi, Hungary, 2011, pp. 123–124.
11. Jalba, K.; Bucur, A. Residual aluminum—quality criteria for drinking water. Hydrotechnics, 1987, 32(4), pp. 14–19 (in Romanian).
12. Manual for testing of water and wastewater treatment chemicals (Final Report), Water Research Commission, http://www.wrc.org.za/Knowledge%20Hub%20Documents/Research%20Reports/1184%20web.pdf.
13. Zhang, Z.; Wu, C.; Wu, Y.; Hu, C. Comparison of coagulation performance and floc properties of a novel zirconium-glycine complex coagulant with traditional coagulants. Environmental Science and Pollution Research, 2014, 21, pp. 6632–6639.
14. Babenkov, E. Water treatment using the coagulants. Nauka: Moskva, 1977, 356 p. (in Russian).
15. Guidelines for Drinking-water Quality. World Health Organization: Geneva, 4th Edition, 2011, 541 p.
16. Satterfield, Z. Jar Testing. Technical Brief, 2005, 5(1), pp. 1–4.
17. Pask, D. Jar Testing: Getting started on a low budget. On Tap, 1993, 2(2), pp. 4–6.
18. Stumm, W.; Morgan, J. Chemical aspects of coagulation. Journal of the American Water Works Association, 1962, 54, pp. 971–992.
19. GOST 3351-74 Drinking water. Methods for determination of turbidity. Gosstandart Rossii: Moskva, 1992 (in Russian).
20. Stefan, D.; Costache, C.; Ruxandu, V.; Balas, M.; Stefan, M. Comparative study on surface water treatment using aluminum sulphate and polyaluminum chlorides as coagulant reagents. Environmental Engineering and Management Journal, 2009, 8(4), pp. 859–863.
21. EC Directive, Directive 98/83/EC of the European Parliament and of the Council of 3 November 1998, on the quality of water intended for human consumption. Official Journal of the European Communities, L 330/32, 5.12.1998, Brussels.
22. Law no. 458/2002 of 07 August 2002 on drinking water quality. Official Journal of Romania, Part I, 29.07.2002, no. 552 (in Romanian).
23. Governmental Decision no. 934 of 15 August 2007 regarding the establishment of automated information system "State Register of natural mineral and drinking waters and soft bottled drinks". Official Journal of the Republic of Moldova, 24.08.2007, no. 131-135 (970) (in Romanian).
24. Toma, P. Considerations regarding the operation of water treatment plants. Journal of Environmental Research and Protection, 2012, 32, pp. 27-34 (in Romanian).
25. Rusu, V.; Lupascu, T. Chemistry of aquatic sediments. Properties of surface. Physicochemical models. Elena V.I.: Chisinau, 2004, 272 p. (in Romanian).
26. Cical, E.; Burtica, G.; Gasparik, G.; Negrea, A.; Lupa L. Contributions regarding the combined use of the coagulation reagents. Environmental Engineering and Management Journal, 2006, 5(6), pp. 1263–1266.

EQUILIBRIUM AND KINETIC PARAMETERS FOR THE SEDIMENTATION OF TARTARIC SALTS IN YOUNG WINES

Ecaterina Covaci[a*], Gheorghe Duca[b], Rodica Sturza[c]

[a]*Institute of Chemistry of Academy of Sciences of Moldova, 3, Academiei str., Chisinau MD-2028, Republic of Moldova*
[b]*Academy of Sciences of Moldova, 1, Stefan cel Mare str., Chisinau MD-2001, Republic of Moldova*
[c]*Technical University of Moldova, 168, Stefan cel Mare str., Chisinau MD-2004, Republic of Moldova*
[*]*e-mail: covaci_ecaterina@yahoo.com; phone: (+373) 69 305 475*

Abstract. In young wines potassium hydrogen tartrate is always present in supersaturating concentration and crystallizes spontaneously. The aim of this study is to obtain kinetic parameters, which explain the stability of young wines during the stabilization treatments. The kinetic and equilibrium parameters were evaluated and discussed. The heating factor has a decisive influence on the reaction rate of potassium hydrogen tartrate precipitation in young wines. An increase of temperature leads to a decrease in efficiency of stabilization process and to an enhancement of the activation energy of the system. According to the obtained experimental results, the optimal regime for production and stabilization of young wines has been established.

Keywords: kinetic parameters, young wines, crystalline stabilization, Arrhenius plots.

Received: February 2015/ Revised final: April 2015/ Accepted: April 2015

Introduction

The presence of tartaric salts, potassium hydrogen tartrate (KHT) and calcium tartrate (CaT) is one of the main causes of wines instability. The wine differs in the retention capacity for tartaric salts in solution. If the holding capacity is exceeded, these salts will precipitate, resulting in the formation of *tartrate casse* or tartaric precipitation [1]. Generally, the solubility of potassium hydrogen tartrate primarily depends on the alcohol content, the value of pH, the temperature of the wine, the presence of colloids and the interactive effects of various cations and anions. In young wines, KHT is always present in supersaturating concentrations and crystallizes spontaneously [2].

Nowadays, several treatments are used prior to wine bottling in order to prevent the precipitation of tartaric salts. Physical treatments consists in promoting the crystallization by cooling the wine to – 4°C and subsequent removal of tartaric salts by filtration or elimination of the potassium and tartaric ions by electro-dialysis or by the use of ion-exchange resins [3, 4]. The used for the treatment of young wines cooling techniques have found a commercial application. These techniques are characterized by long term (weeks), the wine conservation being carried out at temperature below freezing, to encourage the tartrates to crystallize and precipitate out of the wine [5].

The precipitation of KHT in wine follows a second-order kinetics reaction between the bitartrate ion (HT^-) and the potassium ion (K^+), briefly expressed in kinetic notations [6]:

$$\underset{A}{HT} + \underset{B}{K^+} \leftrightarrow \underset{X}{KHT} \quad (1)$$

The KHT crystallization process occurs in two stages: nucleation phase and growing of nucleus into crystals. In the second stage crystal growth occurs, when the KHT ions migrate to the active sites on the surface of the seed crystals and are incorporated into a crystal lattice. If, for some reason, the active sites on the crystal surface are blocked (due to adsorption of colloids), crystal growth is impeded. Certain present in wine phenolic compounds and polysaccharides have been shown to impede crystal growth. Also, it is important to note that nucleation occurs in a supersaturated solution with the KHT concentration at a critical level. Below this level (such as *e.g.* in the case of slightly supersaturated wine) nucleation will be slow. It is because of the thermodynamics involved, that it requires a long time for the solution to change from supersaturation to a reasonably stable state [7]. Thus, the efficiency of cold stabilization (the wine cooling performed in interval – 4 to – 10 ºC) is caused by decrease of the tartaric salts solubility, which determines the creation of an interface between the two phases, a process that requires a lot of interface energy [8]. This step can be accelerated by the addition of cream of tartar (crystal of potassium tartrate), which has the role of crystallization initiator. The addition of KHT crystals eliminates the nuclei induction phase and this speeds up the time that is required to stabilize the wine. Once formed, the crystals grow and then can be removed by filtration leaving a stable towards KHT wine [9].

The KHT precipitation may be elucidated by using a thermodynamic model [10], but a kinetic model is another useful tool to explain the mechanism of processes. The present contribution is aimed at determination the equilibrium and kinetic parameters of the tartaric precipitation in young wines in order to elucidate the mechanism of KHT precipitation at different concentration of colloidal systems. To the best of our knowledge, this is the first report about the use of potassium hydrogen tartrate for study of kinetic parameters for the precipitation from a natural solution (white and red young wines). These parameters describe the kinetics of stabilization, the precipitation process at different temperature and the KHT concentrations are evaluated and discussed.

Experimental

Investigations have been conducted on two young wines that were obtained from *Chardonnay* and *Pinot Noir* varieties of vintage 2014. Experiments were carried out during September-December 2014, at the Oenology Research Centre of Technical University of Moldova and the National Audit Centre of Alcoholic Products, Chisinau, Republic of Moldova. The presence of proteins and polyphenolic compounds can exhibit a holding capacity for tartaric acid, thus inhibiting KHT formation, as set forth in Introduction [7]. In order to minimize the influence of complex agents and colloidal substances on KHT precipitation, the wine should be clarified by fining agents and filtration, before chilling and cold storage. Fouling of KHT crystals occurs when, during the crystallization processes, certain colloidal substances occupy the active sites on the crystal surface and, as a result, halt crystal growth. The fouling substances include certain pigments, polyphenols, proteins, and polysaccharides. The extent of crystal fouling depends on the amount and types of present in wine colloidal substances. Pre-treatment of wine, such as clarification, fining and filtration reduce the level of colloidal material and thus minimize the fouling of KHT crystals that is important for its reuse [11]. For this purpose, the *Chardonnay* grapes variety was vinified by two technological schemes: the classical scheme (sample 1) and the application of gluing treatments before fermentation with bentonite and cryo-maceration of the marc (sample 2). The similar treatments were also carried out for the *Pinot Noir* grape variety, such as classic winemaking (sample 3) and carbonic maceration of grains (sample 4).

Application of bentonite (0.3 g/kg grapes) and cryo-maceration of the marc allowed the reduction of oxidative enzyme activity by an average of 20 %, as well as decrease of protein and phenolic substances content [12]. Moreover, these products have medium color intensity, high content of varietal and secondary aromas and organoleptic characteristic of the variety. During carbonic maceration the intracellular maceration of integral grains in normal atmosphere occurs, which promotes the major diffusion of the substances from the peel to the core by changing the permeability of tissues and cell wall (biological phenomena) [13].

After the completion of alcoholic fermentation, the wine samples have been decanted and settled in order to ensure the colloidal stability. Then tartaric stabilization of the wines samples was performed by two methods: conventional cold stabilization or chill-proofing and static contact seeding with 5 g/L KHT at the temperature of –5°C [14]. The gluing agent for white wine was bentonite of Super type [15] at doses 0.75 g/L and gelatin of Pulviclar S type [16] at 0.35 g/L. After the stabilization by the above-mentioned procedures, the wine samples were filtrated at the seeding temperature, to avoid resolubilization of potassium bitartrate crystals into wine. Physico-chemical analyses of the wine have been evaluated by the alcohol content, the total acidity, the pH value, the content of tartaric acid, potassium and others, using the presented in national and international standards methods [17]. The content of cations in wines before and after the tartaric stabilization were determined *via* the recommended by International Organization of Vine and Wine (IOVV) method, using atomic absorption spectrometry and the content of organic acids - by capillary electrophoresis. The obtained data were used to calculate the progress, the rate and the Arrhenius parameters of the reaction, according to the proposed by methodology [18, 19].

Results and discussion

The data of the main wine composition characteristics, before and after the stabilization, are presented in Tables 1 and 2. According to them, the color intensity and the total polyphenol index diminished in the limits of 23 ÷ 40 % of initial values, during the tartaric stabilization of wine samples.

Table 1

Physico-chemical characteristics of white wines.

Parameters	*Sample 1 of white wine*			*Sample 2 of white wine*		
	Initially	*Stabilized by chill-proofing*	*Stabilized by contact seeding*	*Initially*	*Stabilized by chill-proofing*	*Stabilized by contact seeding*
Ethanol (± 0.06% v/v)	12.62	12.48	12.48	12.42	12.22	12.22
pH (± 0.01)	3.13	3.08	3.06	3.27	3.13	3.11
Total acidity in tartaric acid, (± 0.04 g/L)	7.82	6.80	6.72	7.94	6.90	6.86
Content of tartaric acid (± 0.01 g/L)	2.60	1.62	1.58	2.25	1.46	1.41
Content of potassium (± 0.002 g/L)	0.920	0.713	0.682	0.846	0.643	0.613
Color intensity, $A_{420\ nm}$ (± 0.001)	0.092	0.048	0.042	0.089	0.054	0.052
Total polyphenol index (TPI) (± 0.02 mg/L)	148.8	86.3	82.5	132.5	88.1	86.4
Conductivity at 20 °C (± 1 μS/cm)	1988	1670	1620	1813	1510	1530
Organoleptic analysis (± 0.1 points)	7.7	7.8	7.8	8.0	8.0	8.1

The content of tartaric acid and potassium ions in samples has also decreased in the following order: 37.64% and 25 % for samples of white wines and 26.24 % and 41.14 % for red ones, correspondingly. The electrical conductivity during the stabilization has diminished an average of 15.9 % and the treatments of young wines enhance the aroma expression, the flavor persistence and specific color for this type of wine in organoleptic terms.

Table 2

Physico-chemical characteristics of red wines.

Parameters	*Sample 3 of red wine*			*Sample 4 of red wine*		
	Initially	*Stabilized by chill-proofing*	*Stabilized by contact seeding*	*Initially*	*Stabilized by chill-proofing*	*Stabilized by contact seeding*
Ethanol (± 0.06% v/v)	10.25	10.20	10.20	10.15	10.00	10.00
pH (± 0.01)	3.30	3.20	3.22	3.12	3.04	3.05
Total acidity in tartaric acid (± 0.04 g/L)	8.43	7.62	7.61	7.85	7.0	7.1
Content of tartaric acid (± 0.01 g/L)	2.07	1.48	1.46	2.0	1.52	1.54
Content of potassium (± 0.002 g/L)	1.071	0.612	0.614	0.734	0.454	0.432
Color intensity (± 0.001)	1.483	1.121	1.134	0.864	0.612	0.642
Total polyphenol index (TPI) (± 0.02 mg/L)	1498.1	1158.3	1142.7	692.7	422.6	411.5
Conductivity at 20 °C (± 1 μS/cm)	2066	1735	1702	1920	1800	1770
Organoleptic analysis (± 0.1 points)	7.8	7.9	7.9	8.0	8.1	8.1

The applied schemes have a positive impact upon the KHT precipitation, compared to the traditional method of winemaking in examined wine samples. This effect is described by reducing the content of ions HT^- by 14.29 % and 8.09 % of K^+ for sample 2 and 3.62 % and 31.39 % for the sample 4, respectively. The comparative analysis of the two procedures revealed that decrease of all parameters is more significant in the case of contact seeding procedure, in comparison with conventional cold stabilization.

The determination of equilibrium and kinetic parameters for the sedimentation of tartaric salts was possible through the study of the reaction rate at different temperatures and stabilization time, which allowed describing the process by Arrenius equation for the studied wines.

Effect of stabilization time on the kinetic parameters

The solubility of KHT diminishes essentially at lower temperature that facilitates its crystallization and precipitation into wines. The KHT precipitation rate is dependent on the chemical composition of the reaction medium and the duration of treatment. On the basis of the tartaric acid and potassium ions content at a temperature of 268 K, the kinetic parameters which describe the process of KHT precipitation in all wine samples there were calculated. The terms, which are used in the calculation of rate constant (k) and the reaction rate ($dCx/d\tau$), are the following:

$$k = \frac{1}{\tau(Ca - Cb)} \ln \frac{Cb\ (Ca - Cx)}{Ca\ (Cb - Cx)} \tag{2}$$

$$-\frac{dCx}{d\tau} = k(Ca - Cx)(Cb - Cx) \tag{3}$$

In order to find the prevalent compounds at the equilibrium stage, the equilibrium constants of reaction (1) were calculated, whose values are in the range 17.75 – 22.48 for the white samples and 18.96 – 29.63 for the red samples, respectively. The dominance of the reaction products in the system at equilibrium stage is marked by a higher value of k to unity, allowing the subsequent calculation of the evolution of kinetic parameters at different temperatures and stabilization time. The value of parameters that describe the reaction progress and the rate for two samples of wine are given in Table 3. Calculations were carried out at different steps of the reaction, until obtaining the constant values of the studied parameters.

From the Table 3, the amount of precipitated KHT is almost the same for the white wine samples by an average of 3.42 $mol^2 \cdot L^{-2} \cdot 10^5$ and 4.61 – 2.24 $mol^2 \cdot L^{-2} \cdot 10^5$ for the red ones, respectively. The positive impact of technological schemes was achieved by the increase of KHT rate precipitation with an average of 4.8 % for studied wine samples.

Table 3

The concentrations of reactants species and the rate of process at different stages of the reaction (T = 268 K, the process of conventional cold stabilization).

Type of wine	*The reaction step*	*Average concentrations of reactants species*			*The reaction rate,* $mol \cdot L^{-1} \cdot h^{-1} \cdot 10^7$
		HT^-, $mol \cdot L^{-1} \cdot 10^2$	K^+, $mol \cdot L^{-1} \cdot 10^2$	KHT, $mol^2 \cdot L^{-2} \cdot 10^5$	
Sample 1 of white wine	τ_0	1.75	2.35	-	-
	$\tau_{1/4}$	1.60	2.26	0.131	0.35
	$\tau_{1/2}$	1.37	2.06	1.089	1.05
	$\tau_{2/3}$	1.19	1.92	2.352	3.35
	τ_{eq}	1.07	1.84	3.495	4.44
Sample 2 of white wine	τ_0	1.5	2.16	-	-
	$\tau_{1/4}$	1.40	2.14	0.026	0.75
	$\tau_{1/2}$	1.27	2.05	0.268	1.11
	$\tau_{2/3}$	1.13	1.84	2.172	3.59
	τ_{eq}	1.04	1.49	3.349	4.64
Sample 3 of red wine	τ_0	1.38	2.74	-	-
	$\tau_{1/4}$	1.27	2.36	0.431	2.16
	$\tau_{1/2}$	1.13	2.18	1.409	3.48
	$\tau_{2/3}$	1.08	1.98	2.294	4.64
	τ_{eq}	0.99	1.57	4.606	5.73
Sample 4 of red wine	τ_0	1.33	1.88	-	-
	$\tau_{1/4}$	1.29	1.83	0.019	1.21
	$\tau_{1/2}$	1.19	1.59	0.389	2.04
	$\tau_{2/3}$	1.13	1.381	0.998	3.48
	τ_{eq}	1.01	1.17	2.241	5.89

With the aim of elucidation the optimal method of stabilizing both the processes (conventional cold and contact seeding stabilization), the comparative evolution of kinetic parameters has been studied in wine samples under the same conditions of stabilization. Evolution of reaction and its rate for young white and red wine are similar, as representatively shown for sample 2 in Figure 1.

From the presented in Figure 1 diagram it is evident that the level of KHT precipitation process is practically constant (with slight variations) for both applied processes throughout the stabilization. A growth of 0.1 to $0.25 \cdot 10^{-5}$ $mol \cdot L^{-1}$ occurs at the contact process, in comparison with the classic one. The second calculated parameter, the rate of reaction, is strongly influenced by the contact process that determines a major difference between the two applied methods. At the beginning of contact stabilization, the rate of formation and KHT precipitation in wine is by 4-5 times higher compared to the classical process at 268 K, and then halve in the final stages. This can be explained by the addition of cream of tartar, which initiates formation of KHT micro-crystals in wine volume. As a result, the period of wine stabilization is significantly reduced, as representatively displayed in Figure 2.

Using the contact method of stabilization, the reduction of stabilization period with 30 hours for sample 1 and 23 hours for sample 3 was obtained, in comparison with chill-proofing stabilization method (Figure 2). Samples 2 and 4 require a stabilization period of 8 and 15 hours, respectively, which is shorter as compared to control samples (samples 1 and 3), using the same stabilization method. This fact may be explained by the presence of macromolecules that inhibit the tartaric salts agglomeration in the wine. Thus, the produced by two technological schemes wines (samples 2 and 4) contain 18 – 23 % less protein and colloidal substances, when compared to the control sample, which explains the increasing trend of the reaction rate.

In conclusion, we recommend the cryo- and carbonic maceration as technological schemes for the production of young wines and stabilization by contact seeding, in order to achieve young wines with pronounced organoleptic characteristics.

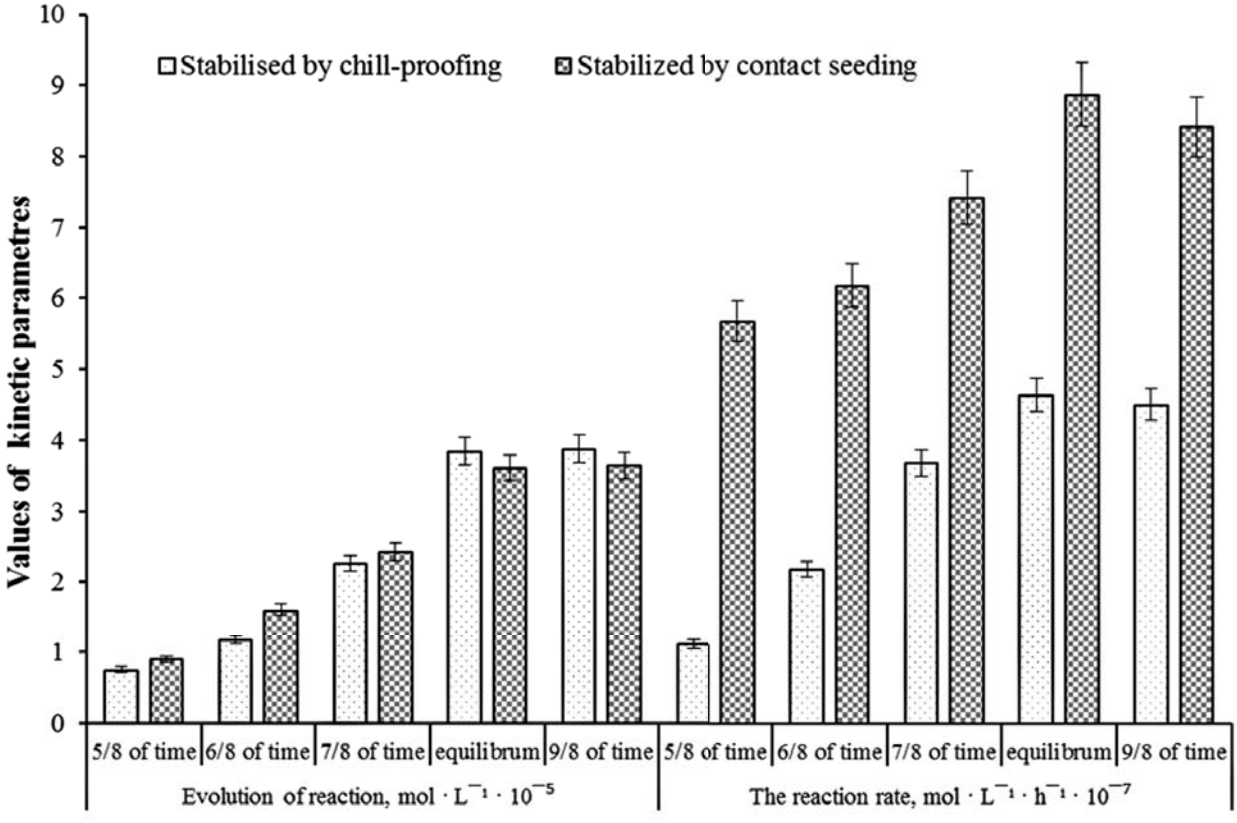

Figure 1. Evolution of reaction and its rate as a function of stabilization time (sample 2, T=268 K).

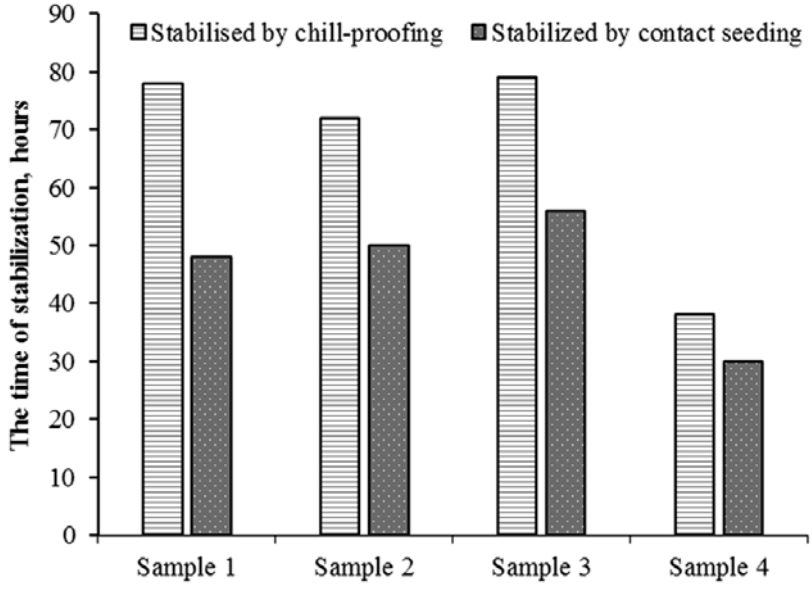

Figure 2. Time of stabilization the wine samples, depending on the applied process (T=268 K).

Effect of temperature on the kinetic parameters

As it is well known, temperature and storage time that is necessary to stabilize a wine, depend on the kind of wine. The thermal factor is determinative on the process for KHT precipitation in wine, because it determines its solubility. The kinetic parameters of precipitation the potassium hydrogen tartrate at temperatures of 268, 273 and 278 K are presented in Figure 3.

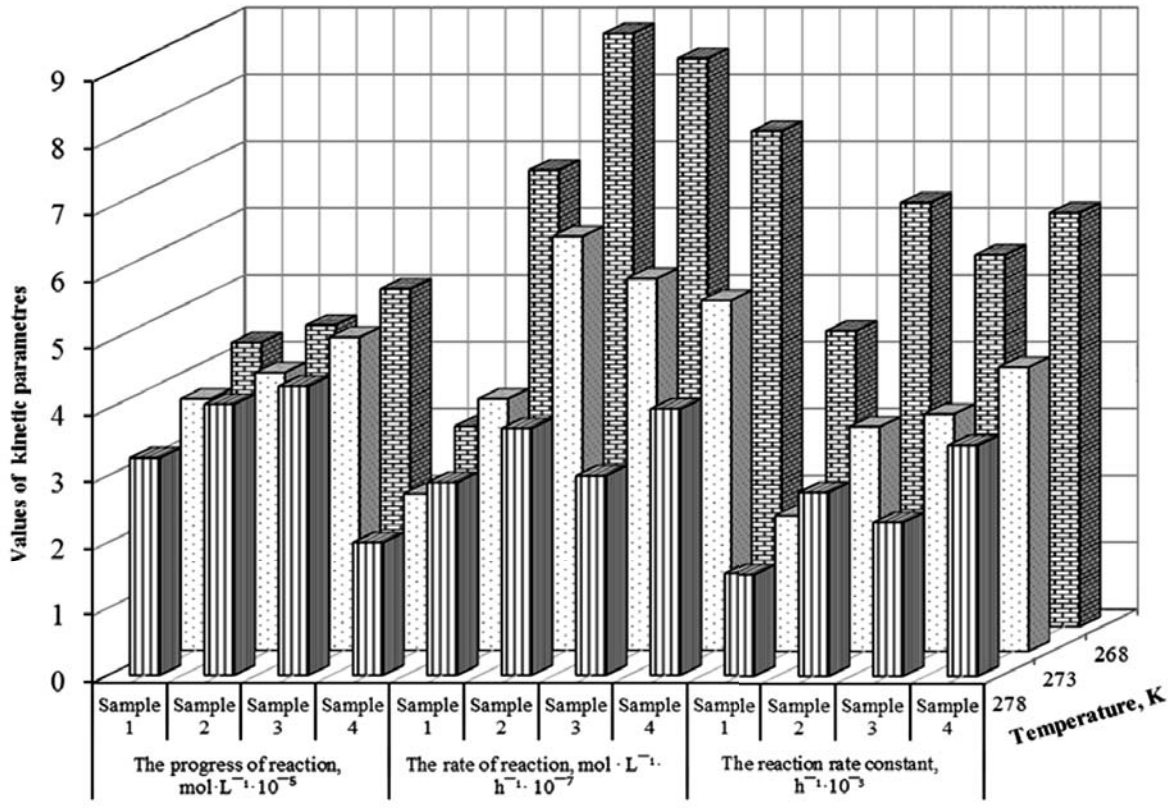

Figure 3. Values of the kinetic parameters of potassium hydrogen tartrate precipitation at different temperatures (sample 1 is stabilized by contact seeding).

From the presented in Figure 3 diagram, the increase of temperature causes significant decreasing of kinetic parameter values, such as rate and rate constant, and for reaction advancing the amendment is minor. Temperature fluctuations during cold stabilization have a significant effect for reducing the rate of KHT precipitation, due to the effect on the speed of nuclei formation. The temperature dependence of the parameters was determined, through the mathematical calculations [20]. The increasing of temperature with ratio 5 (arithmetic progression) determines the regression with ratio 3 of rate reaction in examined wine samples.

In order to optimize the tartaric stabilization process, we studied at the same time both the influence of temperature and stabilization time on the values of reaction rate in wine samples. The correlation between reaction rate and stabilization time at different temperatures for sample 2 is shown in Figure 4.

The presented in Figure 4 histogram shows a relative rising trend up to 62.5 % of the stabilization time, followed by a significant increasing until reaching the final equilibrium and a slight decreasing of values at the end of process. Throughout the stabilization, the reaction rate has maximum values at 268 K and minimum at 278 K. Taking into account the afore-presented considerations (Figures 2 and 3), sample 2 can be stabilized by contact seeding at 273 K to preserve its native character and to reduce the financial costs of the wine stabilization.

Mathematical processing of the results, according to Jäntschi L. [21], allowed determining the dependence of the reaction rate on both factors (Table 4). Rate of the process linearly depends by a polynom of 4 orders on the treatment temperature and stabilization time. In the achieved calculations, Pearson correlation coefficient (R^2) has values within the limits 0.9866 ÷ 0.9975, which shows the correctness of selected functions and that the variance of y is attributed to the relation existing between x and y.

Table 4

The regression equation and the correlation coefficient of precipitation rate constant for sample 2, stabilized by conventional cold stabilization method.

Temperature, K	*The regression equation*	*The correlation coefficient*
268	$Y=-3E-07x^4+6E-05x^3-0.0034x^2+0.0612x-0.0189$	0.9947
273	$Y=-3E-07x^4+6E-05x^3-0.0036x^2+0.0603x-0.0078$	0.9975
278	$Y=-1E-07x^4+3E-05x^3-0.0012x^2+0.0175x-0.0088$	0.9866

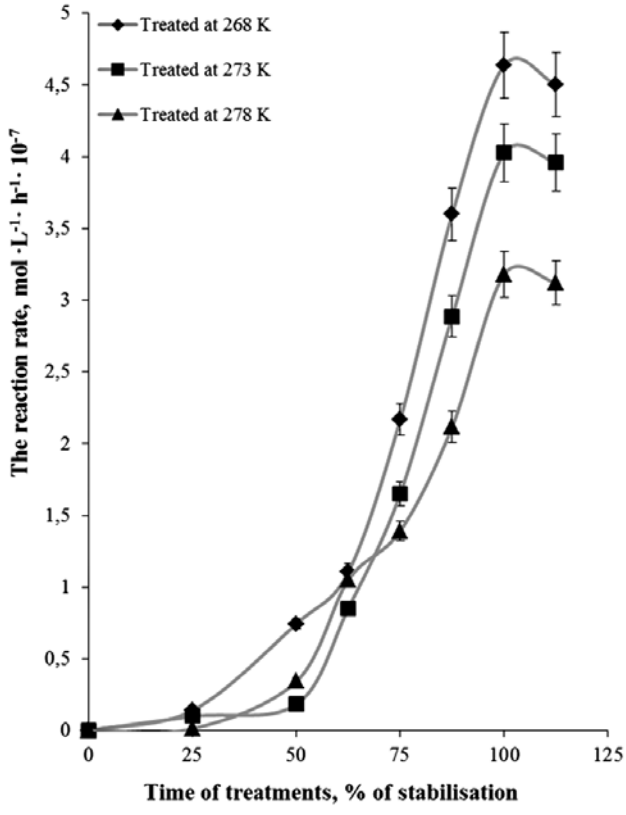

Figure 4. Values of the potassium hydrogen tartrate precipitation rate at different temperatures (sample 2 stabilized by conventional cold stabilization).

In conclusion, the values of kinetic parameters diminish with increasing of temperature, indicating on the exothermic character of KHT precipitation and this trend is presented for all samples of wine. Temperature and wine composition have a major influence on the reaction rate. The rate of KHT precipitation is greater at lower temperatures than at higher temperatures in the examined wines containing 10 – 12 % alcohol.

Kinetic parameters of activation

The KHT precipitation can be summarized by a reversible process, which may be elucidated by using a kinetic model for explanation the mechanism that occurs during this process. In order to determine the Arrhenius parameters of the reaction, graphics of dependence ln$k$ = f(1000/T) at 268, 273 and 278K temperatures were built (Figure 5). In the achieved calculations, the reaction rate constant (k) logarithm is represented as a straight line function of 1/T of KHT precipitation in acid medium and its correlation coefficients were observed to be highest (R^2 = 0.9842 – 0.9867) in examined white wine.

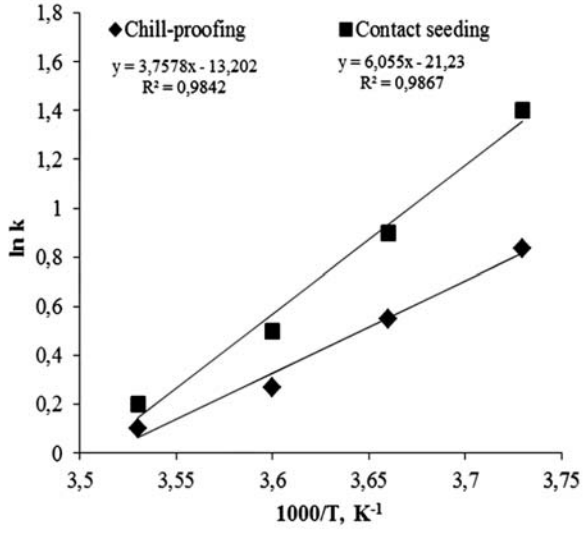

Figure 5. Arrhenius plots of precipitation rate constant for sample 1.

From the slope of the exposed in Figure 5 dependence, there has been graphically calculated and analytically determined the value of activation energy (E_a) by the relationship (4) and by Eq.(5). The KHT precipitation may be expressed by the Arrhenius Eq.(6) as follows:

$$tg\alpha = \frac{E_a}{R} \tag{4}$$

$$\frac{\ln k_2}{\ln k_1} = -\frac{E_a}{R}\left(\frac{1}{T_2} - \frac{1}{T_1}\right) \tag{5}$$

$$\ln k = \ln A - \frac{E_a}{RT} \tag{6}$$

where: E_a - apparent activation energy (kJ·mol^{-1}),
$tg\alpha$ - tangent of the angle on the dependence ln k = f(1000/T),
R - universal gas constant (8.314 J·mol^{-1}·K^{-1}),
k - reaction rate constant at T_2 and T_1 (h^{-1}),
A - pre-exponential factor or the frequency factor (h^{-1}),
T - absolute temperature (K).

As notion, the activation energy (E_a) is the minimum amount of energy that is required for initiation of a chemical reaction, while A represents the frequency of active interaction and can be treated as a constant for a given reacting system over fairly wide temperature range. The results of Arrhenius parameters for the studied samples of wine are listed in Table 5.

According to these data, the value of pre-exponential factor (A) and the values of E_a augment with the temperature, due to the exothermic character of the precipitation process. A higher content of tartaric acid and potassium caused highest values of A factor in red wines, as compared to the white ones. Comparative analysis of obtained by different technological schemes wine samples reveals that applied pre-fermentation operations lead to a reduced content of proteins and colloids into wines, which in turn caused the decrease of the activation energy of the studied process. The average values of this reduction constituted 19.14 % for white sample and 23.19 % for red ones, respectively. The values of activation energy were calculated by the analytical and graphical method for the KHT precipitation and the difference of them does not exceed 8 %.

Table 5

Value of Arrhenius parameters for KHT precipitation in stabilized by chill-proofing wine samples.

Type of wine	*Absolute temperature, T, K*	*Pre-exponential factor, A h^{-1}, 10^{-8}*	*Activation energy, E_a, kJ·mol^{-1}*
Sample 1 of white wine	268	7.31	74.40 ± 0.84
	273	11.21	77.28 ± 0.62
	278	10.14	79.26 ± 0.78
Sample 2 of white wine	268	5.31	58.09 ± 0.72
	273	6.95	63.62 ± 0.91
	278	10.46	65.03 ± 0.78
Sample 3 of red wine	268	$0.86 \cdot 10^4$	91.49 ± 0.88
	273	$2.04 \cdot 10^4$	97.41 ± 0.67
	278	$4.28 \cdot 10^4$	99.08 ± 0.92
Sample 4 of red wine	268	$2.07 \cdot 10^3$	68.76 ± 0.53
	273	$4.15 \cdot 10^3$	72.77 ± 0.48
	278	$5.03 \cdot 10^3$	79.83 ± 0.80

The results show that the precipitation reaction of KHT in wine is characterized by medium activation energy and a high frequency factor, which explains the significant reaction rate of these compounds in young white and red wines. In addition, the reaction of KHT precipitation is limited by the kinetics factors, but not by diffusion ones.

Conclusions

This study on stabilization methods allowed us to obtain the necessary data for explaining physico-chemical phenomena, which influence the stability or instability during young wines stabilization treatments, related to the precipitation of tartaric salts. Kinetic parameters suggested that the KHT precipitation process is influenced by the temperature changes, therefore the increase of temperature leads to a decrease of stabilization process efficiency and an augment of the activation energy in the studied system. The kinetic factors limit the reaction of KHT precipitation, but not the diffusion ones. Also, the pre-fermentative treatments (cryo-maceration of the marc and carbonic maceration of grains) reduce significantly the content of compounds with inhibitory effect on the KHT precipitation. The optimal regime for production and stabilization of young wines was established in economic and technological reasons. The contact seeding is recommended as an efficient method for the tartaric stabilization of young white and red wines.

References

1. Boiret, M.; Marty, A.; Fabrega, C.; Guittard, A.; Tixier, A.; Schaeffer, A.; Schlewltz, A. Tartaric stability index of wines and the risk of precipitation. Revue Française d′Oenologie, 1991, 128, pp. 53-58 (in French).
2. Vallée, D.; Bagard, A.; Blay, C.; Bourde, L. Tartaric stability assessment of wines by the saturation temperature - influence of time factor on stability. Revue Française d′Oenologie, 1990, 126, pp. 51-61 (in French).
3. Cotea, V. D.; Zănoagă, C.; Cotea, V.V. Treaty of oenochimie. Romanian Academy: Bucharest, 2009, 750 p. (in Romanian).
4. Covaci E.; Duca Gh.; Sturza R. The influence of applied stabilization method on the crystalline stability of young white wines. Chemistry Journal of Moldova, 2013, 8(2), pp. 73-77.
5. Maujean, A. Artificial cold treatment of wines in relation to their stabilization against the crystalline tartaric troubles. In: Recent acquisitions in the physical treatment of the wine. Lavoisier Tec & Doc:Paris, 1994, 830 p. (in French).
6. Novak, J.; Labik, St.; Malijevsky, A. Physical chemistry in brief. Institute of Chemical Technology: Prague, 2005, 466 p., http://www.old.vscht.cz/fch/en/tools/breviary-online.pdf
7. Maujean, A.; Sausy, L.; Vallee, D. Determination of potassium bitartrate supersaturation of a wine. Quantification of protective colloids effects. Revue Française d′Oenologie-cahier scientifique, 1985, 100(4), pp. 39-49 (in French).
8. Gerbaud, V.; Gabas, N.; Blouin, J.; Pellerin, P.; Moutounet, M. Influence of wine polysaccharides and polyphenols on the crystallisation of potassium hydrogen tartrate. Journal International des Sciences de la Vigne et du Vin, 1997, 31(2), pp. 65-83 (in French).
9. Rhein, O.; Nersdt, F. Tartrate stabilization by the contact process. American Journal of Enology and Viticulture, 1997, 4, pp. 265-266.
10. Covaci E. Thermodynamic parameters of potassium bitartrate during the young wines cold stabilization. Chemistry Journal of Moldova, 2015, 10(1), pp. 41-44.
11. Puig-Deu, M.; López-Tamames, E.; Buxaderas, S.; de la Torre-Boronat, M. Quality of base and sparkling wines as influenced by the type of fining agent added pre-fermentation. Food Chemistry, 1999, 66, pp. 35-42.
12. Marangon, M.; Pocock, K.; Waters, E. The addition of bentonite at different stages of white winemaking and its effect on protein stability. Australian & New Zealand Grapegrower & Winemaker, 2012, pp. 71-73.
13. Vidal, J. Vinification technique by carbonic maceration of grapes and its installation. EP Patent, 1987, No. 0217683 A1 (in French).
14. Droux, F.; Vialatte, C. The study of tartaric precipitation in wines using "*mini-contact*" procedure. Revue d'Oenologie, 1983, 29, pp. 13-14 (in French).
15. Bentonita oenological (Bentonit super), http://www.protectvit.ro/cumpara/bentolit-super-bentonita-sodica/Super.htm.
16. Gelatin oenological de tip Pulviclar S, http://shop.carolinawinesupply.com/Pulviclar/PulS1.htm.
17. International Organisation of Vine and Wine. International Code of Oenological Practices. Official Edition, Paris, 2012, 298 p. (in French).
18. Zarrouk, A.; Hammouti, B.; Zarrok, H.; Al-Deyab, S.S.; Messali, M. Temperature effect, activation energies and thermodynamic adsorption studies of L-cysteine methyl ester hydrochloride As Copper Corrosion Inhibitor In Nitric Acid 2M. International Journal of Electrochemical Science, 2011, 6, pp. 6261-6274.
19. Cruz, C.; da Costa, A.; Henriques, A. Kinetic modeling and equilibrium studies during cadmium biosorption by dead Sargassum sp. Biomass. Bioresource Technology, 2004, 91, pp. 249-257.
20. Agresti, A.; Yongyi, M. On small-sample confidence intervals for parameters in discrete distributions. Biometrics, 2001, 57(3), pp. 963-971.
21. Jäntschi L. Presentation and processing of the experimental data. UTPress: Cluj-Napoca, 2013, 70p. http://www.lori.academicdirect.org/books/press/PPDE_total.pdf (in Romanian).

THERMODYNAMIC PARAMETERS OF POTASSIUM BITARTRATE DURING THE YOUNG WINES COLD STABILIZATION

Ecaterina Covaci

Institute of Chemistry of Academy of Sciences of Moldova, 3, Academiei str., Chisinau MD-2028, Republic of Moldova
e-mail: covaci_ecaterina@yahoo.com; (+373) 69 305 475

Abstract. The present work was undertaken to study the effect of the treatment temperature on the potassium bitartrate stability and composition of young wines. The thermodynamic parameters, namely $\Delta G°$, $\Delta H°$, $\Delta S°$ were calculated to predict the nature of potassium hydrogen tartrate (KHT) precipitation. According to the achieved results, the exothermal nature and thermodynamical feasibility of KHT precipitation in young wines were established. Based on thermodynamics, negative $\Delta G°$, $\Delta H°$ values and positive $\Delta S°$ value give a spontaneous KHT process at lower temperatures.

Keywords: cold stabilization, tartaric salts, thermodynamic parameters, young wines.

Received: February 2015/ Revised final: April 2015/ Accepted: April 2015

Introduction

Wine is a complex chemical mixture and its stability depends on the activity of microorganisms and the changes in its environment. Less than half of the found in grapes tartaric acid is free standing, the majority of it being presented as potassium acid salt (KHT, etc.). Once bottled, a wine may cause cloudiness, formation and precipitation of tartaric crystals. Under certain conditions, *e.g.* storage at low temperature, the dissolved form of KHT become insoluble forming small crystals, which settle to the bottom [1-3]. As it is known, for the commercial distribution of wines in bottles, the wine must not only be clear at the time of bottling, but also must remain in this condition over the time.

Numerous efficient treatment methods for the stabilization of wines are known up to now: cooling [4], cationic exchange [5-6], reverse osmosis, electro-dialysis [7] and the addition of selected additives [8-9]. From the above-mentioned techniques, cooling alone has found commercial application for the tartaric stabilization of young wines. This method involves cooling the wine near its freezing point to encourage the tartrates to crystallize and precipitate out of the wine before bottling.

The present study was conducted in order to study the variation of thermodynamic parameters of KHT during the cold treatment of white and red young wines. Our efforts were also directed to the determination of some thermodynamic parameters, which describe the precipitation process at the equilibrium, such as: equilibrium constant, entropy change ($\Delta H°$), enthalpy change ($\Delta S°$) and Gibbs free energy ($\Delta G°$) of KHT precipitation.

Materials and methods

Investigations have been conducted on two young wines obtained from *Chardonnay* and *Merlot* varieties of vintage 2014. Experiments were carried out during September - December 2014, at the Oenology Research Centre of Technical University of Moldova. The tartrate precipitation is induced by such essential factors, as: the concentration of tartaric acid, cations and anions, pH value and presence of various complexing agents. The studied grapes varieties were vinified by classical technological schemas and after the alcoholic fermentation, wine samples were decanted and fined to ensure their colloidal stability. The used gluing agents for white wine was bentonite of Super type [10] at doses 0.5 g/L and gelatin of Pulviclar S type [11] at 0.4 g/L for the red wine, respectively. After the gluing treatment, wine samples were subjected to membrane filtration and tartaric stabilization by conventional cold stabilization at the temperature of minus 5°C (filtration at the seeding temperature, to avoid resolubilization of potassium bitartrate crystals into wine). Physico-chemical characteristics of the wine were evaluated by the alcohol content, total acidity, pH value, conductivity, content of phenolic compounds and others, using the methods presented in national and international standards [12-13] at the National Audit Centre of Alcoholic Products (Chisinau, Moldova). The content of components of studied reaction at the equilibrium – tartaric acid and potassium ions, was determined by atomic absorption spectrometry and capillary electrophoresis methods. The obtained data were used to calculate the equilibrium constant of the reaction, according to the proposed methodology [14-17].

Results and discussion

Data on the main wine composition characteristics before and after the tartaric stabilization are presented in Table 1. Colour intensity, content of tartaric acid and total polyphenol index of wine samples diminished within the limits of 23÷40 % of the initial values during the stabilization. Content of tartaric acid and potassium has also decreased in the following order: 37.7 % and 22.5 % for white wine sample and 28.5 % and 42.86 % - for the red one, respectively. Comparative analyses of these two young wines reveal that values of all parameters decrease more significantly in the

case of white sample. In terms of organoleptic analysis, treatment of young wines enhances the aroma expression, the flavour persistence and specific colour for the certain type of wine. The decrease in conductivity depends on the wine type, varying in our case from 318 to 331 μS (Table 1).

Table 1

Physico-chemical characteristics of the wine samples.

Parameters	*Sample 1 of White wine*		*Sample 2 of Red wine*	
	Initially	*Stabilized*	*Initially*	*Stabilized*
Ethanol (± 0.06% v/v)	12.62	12.50	10.25	10.20
pH (± 0.01)	3.13	3.08	3.30	3.20
Total acidity in tartaric acid (± 0.04 g/L)	7.82	6.80	8.43	7.62
Content of tartaric acid (± 0.01 g/L)	2.60	1.62	2.07	1.48
Content of potassium (± 0.002 g/L)	0.920	0.713	1.071	0.612
Colour intensity A_{420} nm (± 0.001)	0.092	0.048	1.483	1.121
Total polyphenol index (TPI) (± 0.02 mg/L)	148.8	86.3	1498.1	1158.3
Conductivity at 20°C (± 1 μS/cm)	1988	1670	2066	1735
Organoleptic analysis (± 0.1 points)	7.7	7.8	7.8	7.9

In our opinion, in order to gain an insight into KHT precipitation process, it is absolutely necessary to take into account the thermodynamic parameters of the process such as: enthalpy, entropy and free energy. The precipitation of potassium bitatrate can be summarized by the following reversible process, which represents a heterogeneous equilibrium:

$$HT^- + K^+ \leftrightarrow KHT \tag{1}$$

For determining the thermodynamic parameters of the process (1), the value of equilibrium constant of reaction is initially calculated by Eq.(2). The free energy of a precipitation process is a function of state, which is related to the equilibrium constant by the classical Van't Hoff Eq.(3):

$$K_{eq} = \frac{C_{prod}}{C_{reac}} \tag{2}$$

$$\Delta G° = -RT \ln K_{eq} \tag{3}$$

where: C_{prod} - concentration of reaction products at equilibrium,
C_{reac} - concentration of reactants in solution at equilibrium,
$\Delta G°$ - Gibbs free energy change (kJ mol^{-1}),
R - ideal gas constant (8.314 J mol^{-1} K^{-1}),
T - absolute temperature (K).

Subsequently, the equilibrium constant is expressed in terms of enthalpy change of precipitation ($\Delta H°$) and entropy change ($\Delta S°$), as functions of temperature, following the Eq.(4):

$$\ln K_{eq} = \frac{\Delta S°}{R} - \frac{\Delta H°}{RT} \tag{4}$$

The determined thermodynamic parameters for the wine samples are presented in Table 2. For sample 1 the following $\Delta G°$ values for the KHT precipitation processes at 268, 273 and 278 K were obtained: -6.36, -5.35 and -1.33kJ·mol^{-1}, respectively. These negative $\Delta G°$ values indicate that precipitation of KHT compound onto wine is thermodynamically feasible and spontaneous. The augment of temperature induces a significant diminution of K_{eq} and $\Delta G°$ values. On the contrary, the entropy changes are well-correlated with the temperature of the system and positive entropy describes an irreversible heat flow through a system during KHT precipitation.

Table 2

Thermodynamic parameters change of the KHT precipitation reaction *versus* temperature for the wine samples.

Type of sample	*Temperature of treatment, K*	*Thermodynamic parameters of KHT precipitation*		
		Equilibrium constant, K_{eq}	*Gibbs free energy, $\Delta G°$, kJ·mol^{-1}*	*Entropy, $\Delta S°$, J·mol^{-1}·K^{-1}*
White wine	268	17.37	-6.36±0.74	985.74
	273	10.54	-5.35±0.51	978.46
	278	1.33	-1.33±0.27	977.88
Red wine	268	20.90	-6.77±0.73	627.05
	273	12.14	-5.67±0.42	641.52
	278	3.17	-2.67±0.17	604.19

Temperature dependence of the KHT precipitation is associated with the studied thermodynamic parameters. In order to define the significant dependence of these parameters as a function of temperature, the Pearson correlation coefficient (R^2) was determined according to the reported method [18]. For that, graphics of dependence: lnK_{eq}= f(1000/T) and $\Delta G°$=f(T) at the 268, 273 and 278 K temperatures were built (Figures 1 and 2).

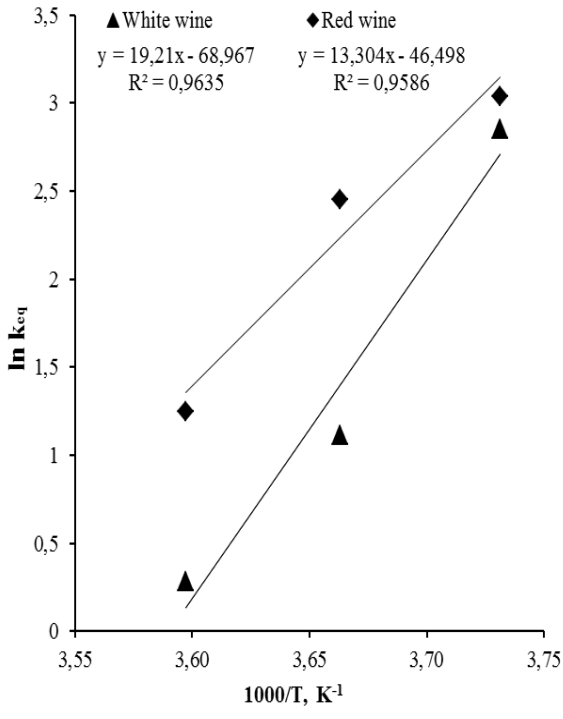

Figure 1. Van't Hoff plots for KHT precipitation at different temperatures in wine samples.

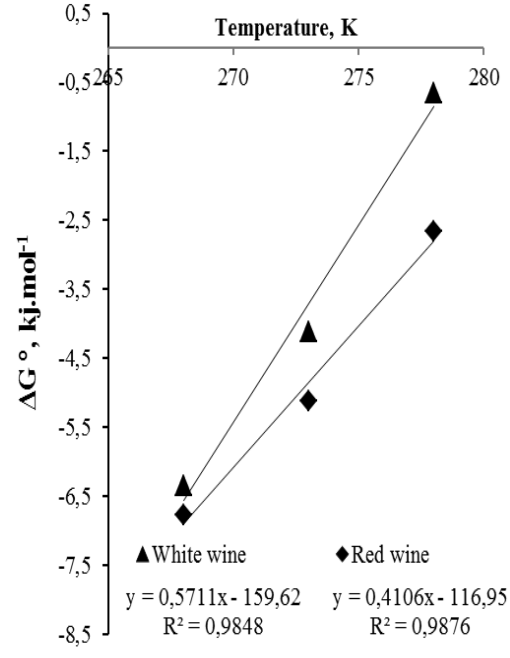

Figure 2. Gibbs plots for KHT precipitation at different temperatures in wine samples.

The values of $\Delta H°$ were determined by using the Van't Hoff Eq. (4), the average value constituting –263.6 ± 6.9 kJ·mol^{-1} for the white wine and –165.4 ± 6.9 kJ·mol^{-1} for that red one, respectively. A negative value of $\Delta H°$ expresses that the precipitation process for KHT is exothermic and the positive value of $\Delta S°$ shows the increased randomness at the solid/solution interface during the precipitation.

The Gibbs free energy indicates on the degree of spontaneity of the KHT process and the higher negative value reflects a more energetically favourable precipitation. As depicted in Figure 2, the increase in temperature determines a significant decrease of the $\Delta G°$ value. Also, the high value of R^2 (within the limits 0.9848 and 0.9876) shows correctness of the selected functions and that the variance of issue parameter is attributed to the relation existing between the temperature (x) and free energy or equilibrium constant logarithm (y).

Conclusions

Cold stability is often considered an essential step in producing of qualitative wine. A lot of production methods are used in industry as means to cold stabilization. Often, winemakers are looking for more economical or efficient solutions for cold stabilization of wines. The study of the temperature influence on the solubility and the forms of potassium bitatrate from wines, allowed to obtain data necessary for explaining physico-chemical phenomena, which influence the stability or instability during the cold stabilization treatments, related to the precipitation of tartaric salts. Thermodynamic parameters suggested that the KHT precipitation process is spontaneous and exothermic. Also, the negative $\Delta G°$ and $\Delta H°$ values and positive $\Delta S°$ values give a spontaneous process at lower temperatures with an easier KHT precipitation.

To our knowledge this is the first report on the thermodynamic study of the precipitation of potassium bitatrate in a real system (such as wine) and not in an aqueous solution.

Acknowledgment

I would like to acknowledge and express my gratitude to my scientific advisers Acad. Gheorghe Duca and Dr. hab. Rodica Sturza for the encouragement and continuous support throughout my scientific research.

References

1. Boiret, M.; Marty, A.; Fabrega, C.; Guittard, A.; Tixier, A.; Schaeffer, A.; Schlewltz, A. Tartaric stability index of wines and the risk of precipitation. Revue Française d′Oenologie, 1991, 128, pp. 53-58 (in French).
2. Dunsford, P.; Boulton, R. The kinetics of potassium bitartrate crystallization from table wines. American Journal of Enology and Viticulture, 1981, 32, pp. 106-110.
3. Mínguez, S.; Hernández, P. Tartaric stabilization of red, rose and white wines with L(+)- calcium tartrate crystal seeding. American Journal of Enology and Viticulture, 1998, 49 (2), pp. 177-182.
4. Ferenczi, S.; Asvany, A.; Erczhegyi, L. Cold stabilization of wines against tartaric precipitations. Bulletin de l′OIV, 1982, 613, pp. 203-220 (in French).
5. Mira, H.; Leite, P.; Ricardo-Da-Silva, R.; Curvelo-Garcia, A. Use of ion exchange resins for tartrate wine stabilization. Journal International des Sciences de la Vigne et du Vin, 2006, 440, pp. 223-246.
6. Benitez, P.; Castro, R.; Barroso, C. Removal of iron, copper and manganese from white wines through ion exchange techniques: effects on their organoleptic characteristics and susceptibility to browning. Analytical Chimica Acta, 2002, 458, pp.197-202.
7. Gómez-Benítez, J.; Palacios-Macías, V.; Szekely-Gorostiaga, P.; Veas-López, R.; Pérez-Rodríguez, L. Comparison of electrodialysis and cold treatment on an industrial scale for tartrate stabilization of sherry wines. Journal of Food Engineering, 2003, 58, pp. 373-378.
8. Feuillat, M.; Charpentier, C. The yeast mannoproteins: a potential enological adjuvant. Bulletin de l′OIV, 1998, 813-814, pp. 945-951 (in French).
9. Moine-Ledoux, V.; Dubourdieu, D. The role of yeast mannoproteins in the tartaric stabilization of wines. Bulletin de l′OIV, 2002, 857-858, pp. 471-482 (in French).
10. Bentonit oenological (Bentonit super). http://www.protectvit.ro/cumpara/bentolit-super-bentonita-sodica / Super.htm.
11. Gelatin oenological, tip Pulviclar S. http://shop.carolinawinesupply.com/Pulviclar/PulS1.htm.
12. International Organization of Vine and Wine. International Code of Oenological Practices. Official Edition, Paris, 2012, 298 p. (in French).
13. Gerjicovoi, V. Methods of technological control in winemaking. Tavrida: Simferopol, 2009, 304 p. (in Russian).
14. Cruz, C.; Da Costa, A.; Henriques, A. Kinetic modeling and equilibrium studies during cadmium biosorption by dead Sargassum sp. Biomass. Bioresource Technology, 2004, 91, pp. 249-257.
15. Sevim, A.; Hojiyev, R.; Gül, A.; Celik, M. An investigation of the kinetics and thermodynamics of the adsorption of a cationic cobalt porphyrazine onto sepiolite. Dyes and Pigments, 2011, 88, pp. 25-38.
16. Kumar, U.; Jyotikusum, A. Thermodynamics of the Adsorption of Pb (II) from Aqueous Solution on NCRH. International Journal of Chemical Engineering and Applications, 2011, 2 (6), pp. 416-420.
17. Sethu, V.; Kua, Y.; Quek, W.; Lim, K.; Andresen, J. Adsorption thermodynamics of Cu (II) ions from waste water using Neem-leaf based bisorbents. Journal of Environmental Research and Development, 2011, 6, pp. 26-33.
18. Agresti, Al.; Yongyi, M. On small-sample confidence intervals for parameters in discrete distributions. Biometrics, 2001, 57 (3), pp. 963-971.

SONOCHEMICAL SYNTHESIS OF HEMATITE NANOPARTICLES

Mihail Iacob

"Petru Poni" Institute of Macromolecular Chemistry, 41A, Grigore Ghica Voda Alley, Iasi, Romania
Institute of Chemistry of the Academy of Sciences of Moldova, 3, Academiei str., 2028 Chisinau, Republic of Moldova
e-mail: iacob.mihai@icmpp.ro

Abstract. Hematite nanoparticles were prepared by a procedure consisting in sonication of μ_3-oxo trinuclear iron(III) acetate of composition $[Fe_3O(OOCCH_3)_6(H_2O)_3]NO_3 \cdot 4H_2O$, $\{Fe_3O\}NO_3$ as iron source, in strong basic conditions followed by thermal treatment at 600˚C. The formation of the hematite was confirmed by IR spectroscopy, X-ray powder diffraction and Raman spectroscopy while, the shape and size of the nanoparticles and their agglomeration were evidenced and estimated on the basis of the images taken with TEM techniques.

Keywords: hematite, nanoparticles, iron oxides, sonochemistry.

Received: July 2014/ Revised final: September 2014/ Accepted: September 2014

Introduction

Iron oxide based nanomaterials attracted attention of researchers due to their interesting properties and large applicability in various areas such as: diagnostic agents in magnetic resonance imaging (MRI) [1,2], magnetic hyperthermia [2], drug delivery [3], immunoassay [4], magnetic separation [5], and magneto-caloric refrigeration [6].

There are various forms of iron oxides [7]. They differ in composition, in the valence of Fe and, above all, in crystal structure. The most stable and wide spread oxide phase of iron is α-Fe_2O_3, where Fe has the lower Gibbs free energy [8]. Hematite has hexagonal structure of the corundum type with a close-packed oxygen lattice in which two-thirds of the octahedral sites are occupied by Fe(III) ions. Bulk hematite is antiferromagnetic till Morin temperature (TM) (~260 K). Between TM and Neel temperature (TN) (~ 950K) it is weak ferromagnetic and above TN the hematite is paramagnetic [9,11]. These transitions are influenced by particle size, shape and crystallinity [9-11]. Particles smaller than 16 nm have a superparamagnetic behaviour at room temperature [12].

Hematite nanoparticles proved to be effective catalyst in numerous reactions such as the decomposition of soot and NO_x in diesel exhausts [13], oxidation of CO [14], photocatalytic degradation of salicylic acid [15], and Fischer-Tropsch synthesis [16]. An iron-based solid catalyst is also normally used as a Lewis acid catalyst and/or support in homogeneous and heterogeneous catalysis [17]. Hematite nanoparticles could be applicable in water treatment technology for removing metal [18]. Hematite has a bandgap of 2-2.2 eV thus being semiconductor suitable for photo-catalytic water-splitting with hydrogen formation [19].

The hematite nanoparticles could be obtained by different routes: co-precipitation [20], microemulsion method [20,21], thermal decomposition [20,22], sol-gel method [23], ball milling [24], green synthesis method [25], sonochemical synthesis [26], forced hydrolysis [20,27,28], hydrothermal and solvothermal method [17,20,29].

Different iron sources for hematite nanoparticles are reported in literature: iron(III) chlorides ($FeCl_2$ and $FeCl_3$) [21, 23, 27-29], ferrocene [22], iron(III) nitrate [17, 25], ferrous sulfate [30], iron pentacarbonyl [26], etc.

Our approach in this study is to obtain hematite nanoparticles using μ_3-oxo homotrinuclear $\{Fe_3O\}NO_3$ acetate as an iron source and easy sonochemical route as a synthesis procedure. The obtained product was characterized by adequate techniques (FTIR, energy-dispersive X-ray spectroscopy, Raman spectroscopy, wide angle X-ray spectroscopy, transmission electron microscopy), in order to evaluate the formed structure.

Experimental

Materials

μ_3-oxo trinuclear iron(III) acetate ($[Fe_3O(CH_3COO)_6(H_2O)_3]NO_3 \cdot 4H_2O$) was prepared through an already reported procedure [31] by using $Fe(NO_3)_3 \cdot 9H_2O$ (Sigma-Aldrich) and sodium acetate (CH_3COONa) (Sigma-Aldrich), glacial acetic acid (Chemical Company), and distilled water. Structure of the compound was verified by FTIR (Figure 1, IA) and XRD (literature [31]: a = 15.69(3), b = 11.77(2), c = 15.32(4) Å); obtained: a = 15.65, b = 11.765, c = 15.31 Å)

FTIR ν_{max} (KBr), cm^{-1}: 420vw, 468vw, 527w , 613s, 662s, 822w, 835w, 898vw, 951w, 1035m, 1292s, 1385vs, 1450vs, 1589vs, 1688s, 2545vw, 2636vw, 3413s.

Equipments

An Energy Dispersive X-Ray system (EDX) available on Environmental Scanning Electron Microscope (ESEM) type Quanta 200 was also used for qualitative analysis and elemental mapping.

The infrared spectra were registered on a Bruker Vertex 70 FT-IR instrument, in transmission mode, in the 300-4000 cm^{-1} range (resolution 2 cm^{-1}, 32 scans), at ambient temperature.

The Raman spectra were recorded with a Renishaw InVia Reflex spectrometer, equipped with a 632.8 nm HeNe laser as excitation source. A 50x objective lens with NA= 0.75 of a Leica DM 2500M microscope was used to

focus the laser beam on the sample and collect the backscattered Raman signal. The investigated spectral region was 100-1000 cm^{-1}, at low incident laser power selected in order to avoid sample degradation. For a high signal to noise ratio, the exposure time and accumulation number were optimized.

Transmission Electron Microscopy (TEM) investigation was made with Hitachi High-Tech HT7700 Transmission Electron Microscope operated at 100 kV accelerating voltage in high contrast mode. The samples were prepared on carbon coated copper grids of 200 mesh size. Microdrops of the nanoparticles dispersed in water (0.1 %) were placed on the grids, and then solvent was removed in vacuum.

Scanning electron microscope (SEM) images were acquired with an electronic microscope (ESEM) type Quanta 200 operating at 30 kV with secondary and backscattering electrons in high vacuum mode.

Wide Angle X-rays Diffraction (WAXD) was performed on a Bruker-AXS D8 ADVANCE diffractometer, with Bragg Brentano parafocusing goniometer. Scans were recorded in step mode using Ni-filtered Cu Kα radiation λ =0.1541 nm. The working conditions were 40 kV and 30 mA tube power. The Bruker computer software Eva 11 and Topaz 3.1 were used to plot and process the data.

Preparation of hematite nanoparticles (NPs)

The μ_3-oxo heterotrinuclear $\{Fe_3O\}$ acetate ($[Fe_3O(CH_3COO)_6(H_2O)_3]NO_3 \cdot 4H_2O$) (1.00 g, 1.38 mmol) was dissolved in 5 mL distilled water and ultrasonicated for 5 min at room temperature. To this, 5 mL of 25 M NaOH solution was added. The obtained mixture was ultrasonicated for another 30 min (UTR200, 200w, 24KHz). The purification of the product was done by washing with distilled water until the pH reaches neutral value. After that it was calcinated for 10 h at 600 ºC. The final product was obtained as a red fine-crystalline mass.

Results and discussion

Iron oxide, NPs, have been prepared by a procedure consisting in the decomposition of μ_3-oxo trinuclear iron(III) acetate, $\{Fe_3O\}NO_3$, by sonication in strong alkaline aqueous medium (pH=11.7), followed by neutralization and calcination, as is illustrated in Scheme 1. The water molecules are eliminated and acetate groups are decomposed. It is assumed that during these processes the Fe-O bonds in iron(III) oxide molecules are preserved. The oxide molecules are agglomerated in nanoparticles (NPs) of different sizes.

Scheme 1. A graphical representation of the pathway leading to iron oxide nanoparticles.

The infrared spectrum of nanoparticles, NPs, as compared with that for $\{Fe_3O\}NO_3$ cluster, (Figure 1) reveals the almost complete disappearance of acetate and nitrate anions, water, and iron-ligand vibrations present in the spectrum of iron acetate. The bands at 552, 474, 446, 384 cm^{-1} could be assigned to Fe-O vibrations, characteristic for hematite according to literature data [32].

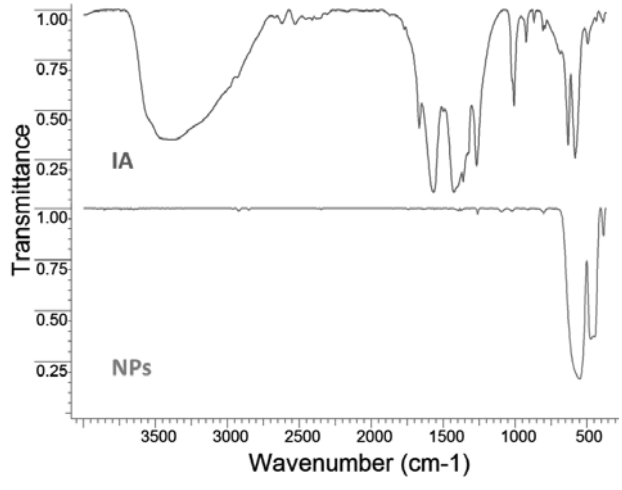

Figure 1. FTIR spectra of $\{Fe_3O\}NO_3$ acetate (IA) and obtained nanoparticles (NPs).

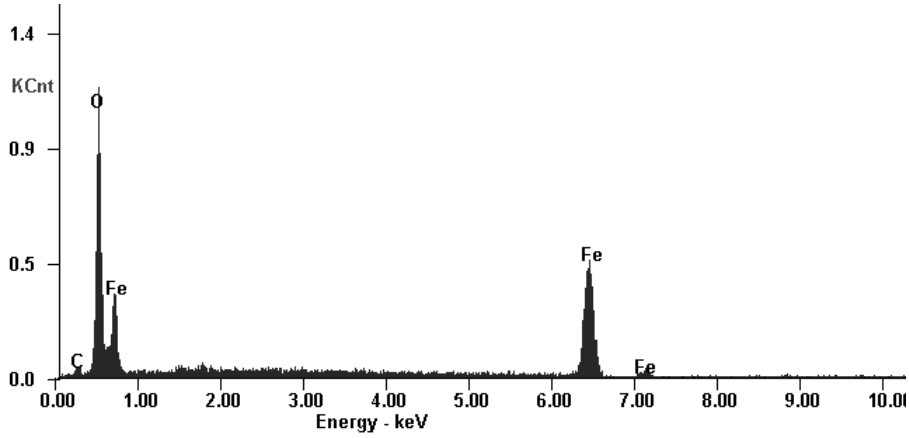

Figure 2. EDX spectrum for NPs.

The presence of iron and oxygen in the prepared material is clearly revealed by EDX analysis (Figure 2). The peak with a low intensity which corresponds to carbon, is attributed to the substrate.

TEM images (Figure 3) were taken on water-dispersed nanoparticles sprayed on carbon coated copper grid and glass substrate, respectively. From Figure 3a it can be observed that particles have irregular shape. Images were processed with ImageJ 3.0 [33] to obtain the derived histogram (Figure 3b) and, according to these, the agglomerated particles size are in the range 10 – 40 nm with the main diameter of about 20 nm.

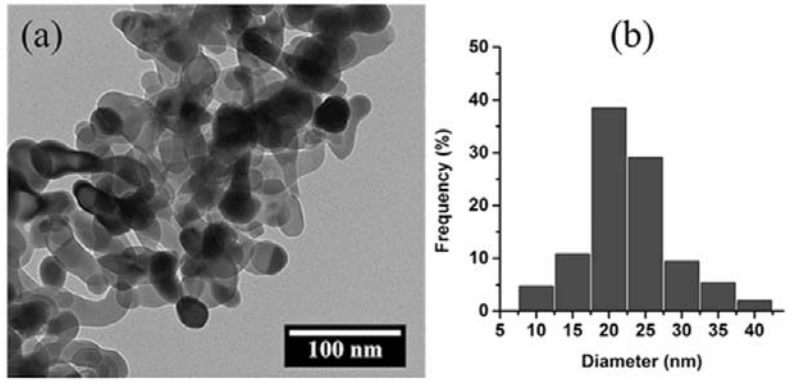

Figure 3. TEM images of nanoparticles (a) and size distribution of nanoparticles (histogram) (b).

Wide Angle X-ray powder diffraction was measured on the obtained material at room temperature in the range 20 – 70 (2θ °). The found XRD patterns (Figure 4) revealed good crystallinity and the peak assignment made according to literature data corresponds to well established structure of hematite as shown in Table 1 [34]. Appling Scherrer formula [35], the crystallite size was calculated as being 15 nm.

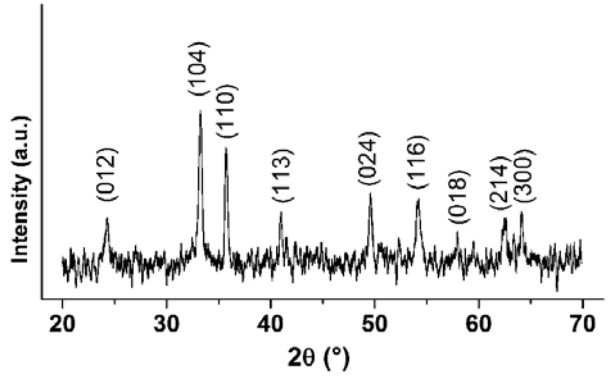

Figure 4. X-ray powder diffraction pattern of nanoparticles.

Table 1

The peak assignment of NPs in comparison with literature data [34].

NPs		*Literature data*	
2θ(°)	*d(Å)*	*2θ(°)*	*d(Å)*
24.27	3.67	24.17	3.68
33.25	2.69	33.19	2.70
35.71	2.51	35.67	2.52
40.91	2.21	40.91	2.21
49.54	1.84	49.52	1.84
54.34	1.69	54.13	1.70
57.96	1.59	57.66	1.60
62.45	1.49	62.51	1.49
64.04	1.45	64.08	1.45

The Raman spectrum of nanoparticles is shown in Figure 5. In this spectrum the signatures specific for hematite are visible: there are two A_{1g} modes (222 and 493 cm^{-1}) and four E_g modes (241, 289, 404, 607 cm^{-1}), and longitudinal optical (LO) E_u mode (656 cm^{-1}) [36,37]. Thus, the data from the Raman spectrum confirmed the presence of α-Fe_2O_3 (hematite) as it was identified through WAXD.

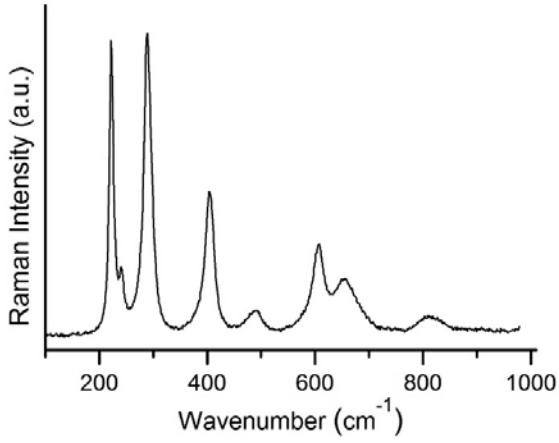

Figure 5. Raman spectrum of nanoparticles.

Conclusions

Sonochemistry followed by thermal decomposition has been proved to be an efficient route to iron oxide nanoparticles starting from μ_3-oxo trinuclear iron(III) acetate as a metal source. The chemical nature of the reaction medium (basic pH) together with some physical factors (e.g., temperature), favored the formation of the hematite species of the iron oxide as has been demonstrated by WAXD analysis and confirmed by Raman and FTIR spectroscopy. The size of agglomerated nanoparticles estimated on the basis of TEM images was found to be in the range 10-40 nm, but applying Scherrer formula, the crystallite size was calculated as being 15 nm.

Acknowledgments

This work was supported by a grant of the Ministry of National Education, CNCS – UEFISCDI, Program PN-II-Capacities, Modul III, Romania - Moldova Bilateral Cooperation (Project ComSilBio, Contract 690/16.04.2013), national project number No. 14.518.02.05A and project No. 11.817.08.24A.

References

1. Xu, F.; Cheng, C.; Chen, D.-X.; Gu, H. Magnetite Nanocrystal Clusters with Ultra-High Sensitivity in Magnetic Resonance Imaging. ChemPhysChem, 2012, 13, pp. 336 – 341.
2. Maity, D.; Chandrasekharan, P.; Yang, C.-T.; Chuang, K.-H.; Shuter, B.; Xue, J.-M.; Ding, J.; Feng, S.-S. Facile synthesis of water-stable magnetite nanoparticles for clinical MRI and magnetic hyperthermia applications. Nanomedicine, 2010, 5(10), pp. 1571–1584.

3. Guo, M.; Yan, Y.; Liu, X.; Yan, H.; Liu, K.; Zhang, H.; Cao, Y. Multilayer nanoparticles with a magnetite core and a polycation inner shell as pH-responsive carriers for drug delivery. Nanoscale, 2010, 2, pp. 434–441.
4. Zhang, G.; Liu, Y.; Zhang, C.; Hu, W.; Xu, W.; Li, Z.; Liang, S.; Cao, J.; Wang, Y. Aqueous immune magnetite nanoparticles for immunoassay. Journal of Nanoparticle Research, 2009, 11, pp. 441–448.
5. Sayin, S.; Ozcan, F.; Yilmaz. M. Two novel calixarene functionalized iron oxide magnetite nanoparticles as a platform for magnetic separation in the liquid–liquid/solid–liquid extraction of oxyanions. Materials Science and Engineering C, 2013, 33, pp. 2433–2439.
6. Hariharan, S.; Gass J. Superparamagnetism and Magneto-Caloric Efect (MCE) in Functional Magnetic Nanostrucutres. Reviews on Advanced Materials Science, 2005, 10, pp. 298-402.
7. Schwertmann, U.; Cornell, R.M. Iron Oxides in the Laboratory. Preparation and Characterization. Second, Completely Revised and Extended Edition. Wiley-VCH: Weinheim, 2000, 188p.
8. Schmid, G. Nanoparticles from Theory to Application. Second Edition. Wiley-VCH: Weinheim, 2010, 522p.
9. Zysler, R.D.; Vasquez-Mansilla, M.; Arciprete, C.; Dimitrijewits, M.; Rodriguez-Sierra, D.; Saragovi, C. Structure and magnetic properties of thermally treated nanohematite. Journal of Magnetism and Magnetic Materials, 2001, 224, pp. 39-48.
10. Can, M.M.; Fırat, T.; Özcan, Ş. Interparticle interaction effects on magnetic behaviors of hematite (α-Fe_2O_3) nanoparticles. Physica B: Condensed Matter, 2011, 406, pp. 2483–2487.
11. Tadić, M.; Marković, D.; Spasojević, V.; Kusigerski V.; Remškar M.; Pirnat J.; Jagličić Z. Synthesis and magnetic properties of concentrated α-Fe_2O_3 nanoparticles in a silica matrix. Journal of Alloys and Compounds, 2007, 441(1-2), pp. 291-296.
12. Cornell, R.M.; Schwertmann, U. The Iron Oxides: Structure, Properties, Reactions, Occurrences and Uses. John Wiley & Sons, 2003, 695p.
13. Wagloehner, S.; Kureti, S. Study on the mechanism of the oxidation of soot on Fe_2O_3 catalyst. Applied Catalysis B: Environmental, 2012, 125, pp. 158-165.
14. Khedr, M.H.; Abdel Halim, K.S.; Nasr, M.I.; El-Mansy, A.M. Effect of temperature on the catalytic oxidation of CO over nano-sized iron oxide. Materials Science and Engineering: A, 2006, 430 (1-2), pp. 40-45.
15. Gu, J.; Li, S.; Wang, E.; Li, Q.; Sun, G.; Xu, R.; Zhang, H. Single-crystalline α-Fe_2O_3 with hierarchical structures: Controllable synthesis, formation mechanism and photocatalytic properties. Journal of Solid State Chemistry. 2009, 182(5), pp. 1265-1272.
16. Mahajan, D.; Gütlich, P.; Stumm, U. The role of nano-sized iron particles in slurry phase Fischer–Tropsch synthesis. Catalysis Communications, 2003, 4(3), pp. 101-107.
17. Nguyen, D.C.; Nguyen, D.H.; Tran, T.H.; Dinh, Q.K.; Duong, T.Q.; Vu V. Q.; Nguyen, V.H. Nanoporous hematite nanoparticles: Synthesis and applications for benzylation of benzene and aromatic compounds. Journal of Alloys and Compounds, 2014, 585(5), pp.83-87.
18. Covalev, V.V.; Turta K.I.; Band, M.I. Investigation of the phase composition of the precipitate formed in electrochemical cleaning hot wastewater. Izvestie AN MSSR, Biological and Chemical Engineering Sciences, 1985, 2, pp. 42-48 (in Russian).
19. Le Formal, F.; Grätzel, M.; Sivula K. Controlling Photoactivity in Ultrathin Hematite Films for Solar Water-Splitting. Advanced Functional Materials, 2010, 20, pp. 1099-1107.
20. Abdulkadir, I.; Aliyu, A.B. Some wet routes for synthesis of hematite nanostructures. African Journal of Pure and Applied Chemistry, 2013, 7(3), pp. 114-121.
21. Han, L.-H.; Liu, H.; Wei, Y. In situ synthesis of hematite nanoparticles using a low-temperature microemulsion method. Powder Technology, 2011, 207, pp. 42–46.
22. Bhattacharjee, A.; Rooj, A.; Roy, M.; Kusz, J.; Gutlich, P. Solventless synthesis of hematite nanoparticles using ferrocene. Journal of Materials Science, 2013, 48, pp. 2961–2968.
23. Woo, K.; Lee H.J. Synthesis and magnetism of hematite and maghemite nanoparticles. Journal of Magnetism and Magnetic Materials, 2004, 272-246, pp. E1155-E1156.
24. Borzi, R.A.; Stewart, S.J.; Punte, G.; Mercader, R.C.; Vasquez-Mansilla, M.; Zysler, R.D.; Cabanillas, E.D. Magnetic interactions in hematite small particles obtained by ball milling. Journal of Magnetism and Magnetic Materials, 1999, 205, pp.234-240.
25. Ahmmad, B.; Leonard, K.; Islam, Md. S.; Kurawaki, J.; Muruganandham, M.; Ohkubo, T.; Kuroda, Y. Green synthesis of mesoporous hematite (α-Fe_2O_3) nanoparticles and their photocatalytic activity. Advanced Powder Technology, 2013, 24, pp. 160–167.
26. Bang, J.H.; Suslick, K.S. Sonochemical Synthesis of Nanosized Hollow Hematite. Journal of the American Chemical Society, 2007, 129, pp. 2242-2243
27. Marinović-Cincović, M.; Wang, G.; Fedoroff, M.; Šaponjić, Z.V.; Milonjić, S.K.; Nedeljković, J.M. Ferricoxychloride and Hematite Nanoparticles: Synthesis and Phase Transformation. Materials Science Forum, 2006, 518, pp. 63-66.

28. Oćwieja, M.; Adamczyk, Z.; Morga, M.; Bielanska, E.; Wegrzynowicz, A. Hematite nanoparticle monolayers on mica preparation by controlled self-assembly. Journal of Colloid and Interface Science, 2012, 386, pp. 51–59.
29. Zhu, M.; Wang, Y.; Meng, D.; Qin, X.; Diao, G. Hydrothermal Synthesis of Hematite Nanoparticles and Their Electrochemical Properties. The Journal of Physical Chemistry C, 2012, 116, pp. 16276−16285.
30. Sreeram, K.J.; Nidhin, M.; Nair, B.U. Synthesis of aligned hematite nanoparticles on chitosan–alginate films. Colloids and Surfaces B: Biointerfaces, 2009, 71, pp. 260–267.
31. Turta, K.I.; Shova, S.G.; Spatari, E.A.; Mazus, M.D.; Malinovskii, T.I. Crystal and molecular structure, electron structure of iron(III) carboxylate. Zhurnal Strukturnoi Khimii, 1994, 35, pp. 112-120 (in Russian).
32. Rendon, J.L.; Serena, C. J. IR spectra of powder hematite: effects of particle size and shape. Clay Minerals, 1981, 16, pp. 375-381.
33. Abramoff, M.D.; Magalhaes, P.J.; Ram, S.J. Image Processing with ImageJ. Biophotonics International, 2004, 11(7), pp. 36-42.
34. Downs, R.T. The RRUFF Project: an integrated study of the chemistry, crystallography, Raman and infrared spectroscopy of minerals. Program and Abstracts of the 19th General Meeting of the International Mineralogical Association in Kobe, Japan, 2006, O03-13.
35. Patterson, A.L. The Scherrer formula for X-Ray particle size determination. Physical Review, 1939, 56, pp. 978-982.
36. Jubb, A. M.; Allen, H. C. Vibrational spectroscopic characterization of hematite, maghemite, and magnetite thin films produced by vapor deposition. Applied Materials & Interfaces, 2010, 2(10), pp. 2804-2812.
37. de Faria, D.L.A.; Silva, S.V.; de Oliveira M.T. Raman microspectroscopy of some iron oxides and oxyhydroxides. Journal of Raman Spectroscopy, 1997, 28, pp. 873-878.

CRYSTAL STRUCTURE OF $\{[La_2(CNCH_2COO)_6(H_2O)_4]\cdot H_2O\}_n$ COMPLEX

Ana Lazarescu[a*], Elena Melnic[b], Sergiu Shova[a], Victor Kravtsov[b], Constantin Turta[a]

[a]*Institute of Chemistry of Academy of Sciences of Moldova, 3, Academiei str., Chisinau MD-2028, Republic of Moldova*
[b]*Institute of Applied Physics of Academy of Sciences of Moldova, 5, Academiei str., Chisinau, MD-2028, Republic of Moldova*
[*]e-*mail: analazarescu@yahoo.com; phone: (+373 22) 73 97 22; fax:* (*+373 22) 73 99 54*

Abstract. The lanthanum(III) cyanoacetate complex of formula $\{[La_2(CNCH_2COO)_6(H_2O)_4]\cdot H_2O\}_n$ (**1**), has been prepared and characterized by X-ray diffraction analysis. Compound crystallizes in the triclinic centrosymmetric space group *P*-1 (No.2), *a*=8.997(5) Å, *b*=9.251(5) Å, *c*=9.728(5) Å, α=67.849(5)°, β=84.224(5)°, γ=81.351(5)°. Single-crystal X-ray diffraction study reveals that crystals of **1** exhibits one-dimensional coordination polymer structure, which is composed of cyanoacetate bridged lanthanum(III) ions. The O_9 coordination surrounding of La cation is completed by oxygen atoms of six carboxylate ligands that are coordinated in the bidentate bridging and tridentate-chelating bridging mode and two water molecules. The cations are bridged in a polymeric chain by four exo-bidentate cyanoacetate ligands or through μ_2-O function of two other chelato-bridgind cyanoacetate ligands. The La···La separation along the polymer is equal to 4.754(3) Å and 4.608(2) Å.

Keywords: coordination polymers, lanthanum (III), cyanoacetic acid, crystal structure.

Received: November 2014/ Revised final: January 2015/ Accepted: February 2015

Introduction

The synthesis of functional rare-earth coordination polymers with various N- and / or O-donor ligands has attracted increasing interest, due to their various topologies [1-3] and potential applications as optical, electronic and magnetic materials [4-7].

The carboxylate ligands are attractive candidates for construction of the polymeric networks due to their versatile functions as bridges or terminal groups, which lead to generation of dimers [8, 9], 1D chains [10], 2D-layers [11], and 3D- polymeric structures [12].

However, investigation of lanthanide complexes with cyanoacetic acid anion as ligand is very scarce [13,14]. Our previous investigations of 3*d* and 4*f* metal complexes with cyanoacetate anions have demonstrated that copper(II) ion has $\{O_4^{(carbox.)}N^{(CN)}\}$ coordination node, while neodymium(III) ion – $\{O_7^{(carbox.)}O_2^{(H_2O)}\}$, respectively [15, 16]. The study of magnetic properties of gadolinium(III) cyanoacetate complex has shown that external magnetic field induces two slow relaxation processes, while heat capacity and direct current susceptibility measurements at very low temperatures has indicated strong single ion anisotropy, due to the Kramer's doublet of the ground state [17].

In continuation of our research on the use of cyanoacetic acid with both O- and N- potential donor atoms as a ligand for 4*f* cations [16, 17] and *d*-block transition metal [15], we have synthesized and structurally characterized the $\{[La_2(CNCH_2COO)_6(H_2O)_4]\cdot H_2O\}_n$ compound by single crystal X-ray method.

Experimental

Synthesis

All reagents of analytical grade were commercially purchased and used without further purification. Elemental analyses (C, H, N) were performed on a Elemental Analyzer vario EL(III). The lanthanum content in the complex was determined gravimetrically as stable oxide by precipitating lanthanide (III) ions with ammonium hydroxide [18].

$\{[La_2(CNCH_2COO)_6(H_2O)_4]\cdot H_2O\}_n$ (**1**). Solution of cyanoacetic acid (0.51 g, 6 mmol) in water (10 mL) was added to La_2O_3 (0.32 g, 1 mmol). After stirring the resulting solution was passed through a glass filter. The filtrate was stored at room temperature for some weeks, whereupon the suitable for X-ray analysis colorless crystals of the product appeared. The crystals were collected by filtration, dried under reduced pressure and kept in desiccator. Yield: 52 %. Anal. found (calc.)%: for $\{C_9H_{12}N_3O_9La\}_n$, C, 23.99 (24.29); H, 2.43 (2.69); N 9.07 (9.45); La, 30.89 (31.22). IR data (Nujol, cm^{-1}): 3545br, 3430br, 3250br, 2265sh, 1705s, 1600vs, 1580s, 1545s, 1410s, 1264m, 1195m, 955w, 930m, 915m, 700m, 570m, 515m.

Physical measurements

IR spectrum of polycrystalline sample was recorded on Perkin Elmer spectrum 100 FT IR Spectrometer in the range of 4000-400 cm^{-1}.

X-ray crystallography

The X-ray data for **1** were collected at room temperature on an Oxford Diffraction Xcalibur diffractometer equipped with CCD area detector and a graphite monochromator utilizing MoKα radiation. The crystals were placed at 40 mm from the CCD detector. The data were processed using the CrysAlis package of Oxford Diffraction [19]. The final unit cell dimensions were obtained and refined on an entire data set. The structures were solved by direct methods using SHELX-97 program package [20] and refined with full-matrix least squares method with anisotropic thermal parameters for the non-hydrogen atoms. The C(sp^2)-bound H atoms were placed in calculated positions and were treated

using a riding model approximation with Uiso(H) = 1.2Ueq(C), while the hydrogen atoms of water molecules were refined with isotropic displacement parameter Uiso (H) = 1.5Ueq(O) using DFIX restrain instruction. The figures were produced using MERCURY [21]. The X-ray data and details of the refinement for **1** are summarized in Table 1, the selected geometric parameters are given in Table 2 and the hydrogen-bonding geometry is given in Table 3. CCDC 1032624 contains the crystallographic data for **1**. These data can be obtained free of charge from The Cambridge Crystallographic Data Centre via www.ccdc.cam.ac.uk/data_request/cif.

Table 1

Crystal and structure refinement data for 1.

Parameter	*Value*
Compound	**1**
Empirical formula	$C_9H_{12}N_3O_9La$
Formula weight	445.13
T (K)	293(2) K
Crystal system	*Triclinic*
Space group	*P*-1
Z	2
a, Å	8.997(5)
b, Å	9.251(5)
c, Å	9.728(5)
α, (º)	67.849(5)
β, (º)	84.224(5)
γ, (º)	81.351(5)
V, Å^3	740.5(7)
D_{calc} (g cm^{-3})	1.996
μ(mm^{-1})	2.934
F(000)	432
Crystal size (mm)	0.30 x 0.20 x 0.15
θ_{min}, θ_{max} (º)	2.62 - 25.99
Reflections collected/unique	5555 / 2899
Reflections with [$I > 2\sigma(I)$]	2810
Data/restraints/parameters	2899 / 9 / 217
Goodness-of-fit (GOF)on F^2	1.000
$R1$, $wR2$ [$I > 2\sigma(I)$]	0.0182, 0.0464
$R1$, $wR2$ (all data)	0.0190, 0.0468
$\Delta\rho_{max}$, $\Delta\rho_{min}$, (e×Å^{-3})	0.416, -0.689

Table 2

Selected bond lengths (Å) and angles (º) in coordination metal environment in 1.

Bond	*d, (Å)*	*Bond*	*d, (Å)*
La-O(1)	2.511(2)	La-O(3)^{ii}	2.804(2)
La-O(2)	2.456(2)	La-O(6)^{i}	2.490(2)
La-O(3)	2.525(2)	La-O(1*w*)	2.578(2)
La-O(4)	2.451(2)	La-O(2*w*)	2.667(2)
La-O(5)	2.639(2)	-	-
Angle	*ω, (deg)*	*Angle*	*ω, (deg)*
O(1)-La-O(2)	117.39(7)	O(3)-La-O(3)^{ii}	60.38(6)
O(1)-La-O(3)^{ii}	121.23(5)	O(3)-La-O(1*w*)	74.69(7)
O(1)-La-O(3)	79.09(6)	O(3)-La-O(2*w*)	78.71(6)
O(1)-La-O(4)	75.31(7)	O(4)-La-O(3)^{ii}	114.09(6)
O(1)-La-O(5)	138.55(7)	O(4)-La-O(5)	77.08(6)
O(1)-La-O(6)^{i}	73.48(7)	O(4)-La-O(6)^{i}	117.37(7)
O(1)-La-O(1*w*)	143.16(6)	O(4)-La-O(1*w*)	138.48(7)
O(1)-La-O(2*w*)	67.33(6)	O(4)-La-O(2*w*)	68.49(7)
O(2)-La-O(3)	141.97(6)	O(5)-La-O(3)^{ii}	47.66(5)
O(2)-La-O(3)^{ii}	120.81(7)	O(5)-La-O(6)^{i}	147.68(6)
O(2)-La-O(4)	73.24(7)	O(5)-La-O(1*w*)	75.17(7)
O(2)-La-O(5)	82.64(7)	O(5)-La-O(2*w*)	74.06(6)
O(2)-La-O(6)^{i}	75.29(7)	O(6)^{i} -La-O(3)^{ii}	128.54(6)
O(2)-La-O(1*w*)	73.10(7)	O(1*w*)-La-O(3)^{ii}	65.62(6)

Continuation of Table 2

Angle	*ω, (deg)*	*Angle*	*ω, (deg)*
O(2)-La-O(2*w*)	138.57(6)	O(1*w*)-La-O(2*w*)	130.08(6)
O(3)-La-O(4)	144.14(6)	O(1*w*)-La-O(6)^{i}	75.99(7)
O(3)-La-O(5)	108.01(6)	O(2*w*)-La-O(3)^{ii}	64.55(6)
O(3)-La-O(6)^{i}	77.77(6)	O(2*w*)-La-O(6)^{i}	137.25(6)

Symmetry code: ^{i} *-x+1, -y, -z+1;* ^{ii} *-x+1, -y+1, -z+1*

Table 3

Geometric parameters of hydrogen bonds (Å, deg) in 1.

D–H···A	*d(H···A)*	*d(D···A)*	*Ð(DHA)*	*Symmetry transformation for acceptor*
O1*w*-H1*w*1···N3	2.28(2)	3.106(4)	168(3)	*x, y, z*
O1*w*-H2*w*1···O2*w*	1.92(2)	2.771(3)	161(3)	-*x*+1, -*y*+1, -*z*+1
O2*w*-H2*w*2···O3*w*	1.90(2)	2.770(3)	164(3)	*x, y, z*
O2*w* -H1*w*2···O3*w*	2.02(2)	2.809(3)	153(2)	-*x*+1, -*y*+1, -*z*
O3*w* -H1*w* 3···N1	2.29(3)	2.951(4)	136(3)	-*x*+2, -*y*+1, -*z*
O3*w* -H2*w*3···N2	1.95(2)	2.802(3)	176(3)	*x*, *y*+1, *z*

Results and discussion

The reaction of lanthanum(III) oxide with cyanoacetic acid in a molar ratio of 1:3 in water solution leads to polymeric complex with the composition $\{[La_2(CNCH_2COO)_6(H_2O)_4]\times H_2O\}_n$ (**1**). The complex is a colorless, air hygroscopic crystalline solid, readily dissolves in water, but is insoluble in organic solvents, such as methanol, acetone and acetonitrile. The IR spectrum shows the absorption band at 2265 cm^{-1}, which is characteristic to the ν(C≡N) vibrations of the ligand.

Here we report the results of X-ray study of the lanthanum(III) compound with cyanoacetate ligands, which is a linear polymer of composition $\{[La_2(CNCH_2COO)_6(H_2O)_4]\times H_2O\}_n$. Compound crystallizes in the triclinic centrosymmetric space group *P*-1, a = 8.997(5) Å, b = 9.251(5) Å, c = 9.728(5) Å, α = 67.849(5)°, β = 84.224(5)°, γ = 81.351(5)°, V = 740.5(7) Å^3 and is isostructural to the reported earlier Nd analog [16]. The inversion centers related to La cations are linked in 1D structure by carboxylic groups of cyanoacetate ligands, which exhibit different binding modes (Figure 1).

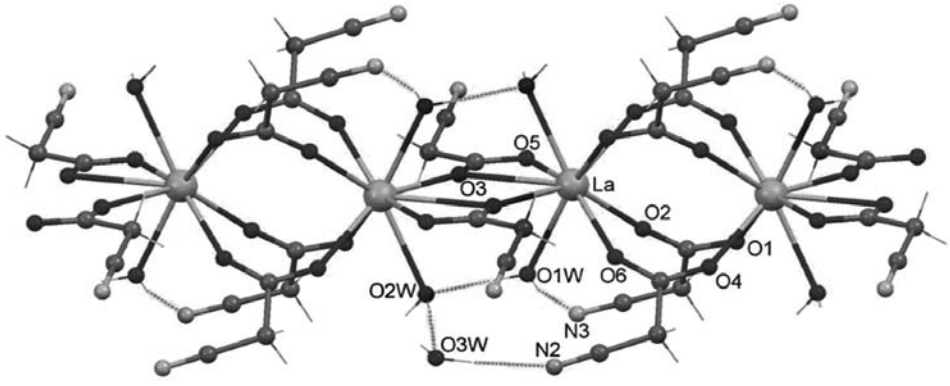

Figure 1. View of polymeric chain.

The La cation is linked to the center of symmetry related neighboring La cations either by four cyanoacetic ligands, acting as *syn–syn* (c-2-c) bidentate bridges (La–O2, 2.455(2); La–O6, 2.490(2); La–O1', 2.511(2); La–O4', 2.450(2) Å), or through two tridentate (3_2-c) chelate-bridging ligands with the La – O3 bond lengths of 2.524(2) and 2.806(2) Å, respectively.

Two different La···La separations in the polymer chain alternate and are equal to 4.755 and 4.608 Å, respectively. The shorter of the La···La distance is related with monoatomic bridging function of carboxylic group in the second case. The coordination surrounding of lanthanum is completed to nine by two coordinated water molecules O(1w) and O(2w) (La–O(1w), 2.579(2) and La-O(2w), 2.664(2) Å). The coordination polyhedron of lanthanum is a monocapped tetragonal antiprism. The comparison of average La-O distances for acting as *syn–syn* (c-2-c) bidentate bridges (2.477 Å) ligands, chelate-bridging ligands (2.525, 2.639 and 2.804 Å) and coordinated water molecules (2.623 Å) in **1** with the corresponding values in related Nd analog [16] (2.420, 2.463, 2.587 Å and 2.831, 2.590 Å) revealed well agreement

with the difference in ionic radii of nine coordinated La^{III} (1.36 Å) and Nd^{III} (1.30 Å) [22]. The cyano group of the cyanoacetate ligands does not coordinate to the lanthanide cation. The coordinated water molecules are involved in intra- and inter-chain hydrogen bonds (Table 3).

In the crystal, the parallel polymer chains run along a crystallographic axis and are united into a three-dimensional network through a system of hydrogen bonds involving water molecules and nitrogen atoms of cyanoacetic ligands (Figure 2).

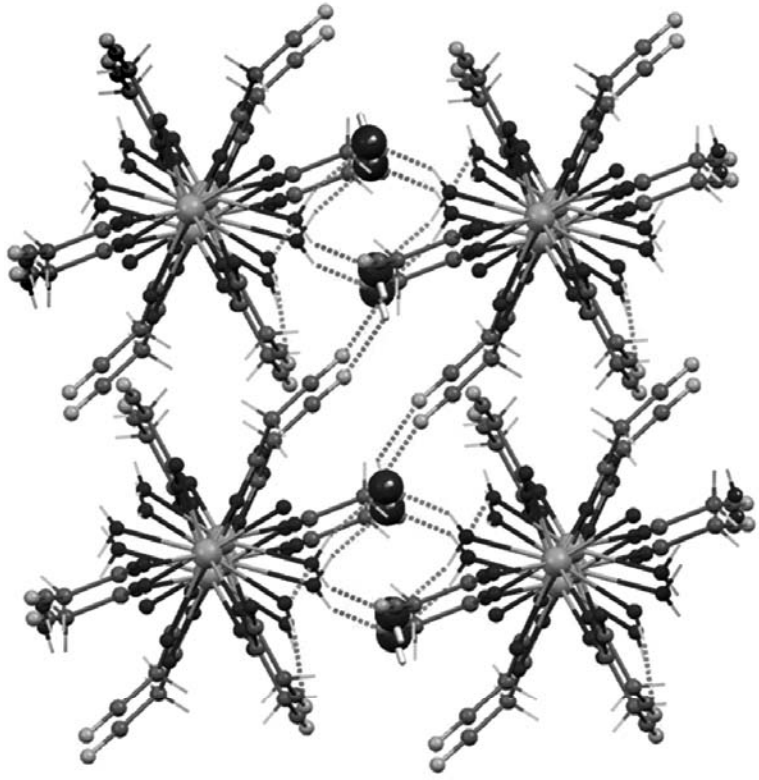

Figure 2. Hydrogen bonded parallel polymer chains in the crystal structure of $\{[La_2(CNCH_2COO)_6(H_2O)_4]\cdot H_2O\}_n$. Solvent water molecules O3*w* are shown by bigger radii red spheres.

Conclusions

The lanthanum(III) cyanoacetate polymer of formula $\{[La_2(CNCH_2COO)_6(H_2O)_4]\cdot 2H_2O\}_n$ **(1)** has been synthesized and characterized by single-crystal X-ray diffraction. The complex was found to be isostructural to Nd analog. The cyano-group of the ligand is not coordinated to the lanthanide ion.

References

1. Decadt, R.; Van Hecke, K; Depla, D; Leus, K; Weinberger, D; Van Driessche, I.; Van Der Voort, P; Van Deun, R. Synthesis, crystal structures, and luminescence properties of carboxylate based rare-earth coordination polymers. Inorganic Chemistry, 2012, 51, pp. 11623-11634.
2. Qin, C.; Wang. X.I.; Wang, E.B.; Su, Z.M. A Series of three-dimensional lanthanide coordination polymers with rutile and unprecedented rutile-related topologies. Inorganic Chemistry, 2005, 44, pp. 7122-7129.
3. Gai, Y.-Li; Xiong, K.-C.; Chen, L.; Bu, Y.; Li, X.-J.; Jiang, F.-L.; Hong, M.-C. Visible and NIR Photoluminescence Properties of a Series of Novel Lanthanide–Organic Coordination Polymers Based on Hydroxyquinoline–Carboxylate Ligands. Inorganic Chemistry, 2012, 51, pp. 13128-13137.
4. Liu, C.M.; Xiong, M.; Zhang, D.Q.; Du, M.; Zhu, D.B. Two-and three-dimensional lanthanide-organic frameworks constructed using 1-hydro-6-oxopyridine-3-carboxylate and oxalate ligands. Dalton Transactions, 2009, 29, pp. 5666-5672.
5. Hasegawa, Ya.; Nakagawa, T.; Kawai, T. Recent progress of luminescent metal complexes with photochromic units. Coordination Chemistry Review, 2010, 254, pp. 2643-2651.
6. Cidália, M.G.dos Santos; Harte, A.J.; Quinn, S.J.; Gunnlaugsson, T. Recent developments in the field of supramolecular lanthanide luminescent sensors and self-assemblies. Coordination Chemistry Review, 2008, 252, pp. 2512-2527.

7. Cunha-Silva, L.; Lima, S.; Ananias, D.; Silva, P.; Mafra, L.; Carlos, I.D.; Pillinger, M.; Valente, A.A.; Almeida Paz, P.A.; Rocha, J. Multi-functional rare-earth hybrid layered networks: photoluminescence and catalysis studies. Journal of Materials Chemistry, 2009, 19, pp. 2618- 2632.
8. Rohde, A.; Urland, W. Synthesis, crystal structures and magnetic behaviour of dimeric and tetrameric gadolinium carboxylates with trichloroacetic acid. Journal of Chemical Society, Dalton Transactions, 2006, 24, pp. 2974-2978.
9. Yi-Shan, S.; Bing, Y.; Zhen-Xia, C. Different crystal structure and photophysical properties of lanthanide complexes with 5-bromonicotinic acid. Journal of Solid State Chemistry, 2004, 177, pp. 3805-3814.
10. Chen, C.; Zhang, S.-Y.; Song, H.-B.; Shi, W.; Zhao, B.; Cheng, P. One-dimensional lanthanide coordination polymers as promising luminescent materials. Inorganica Chimica Acta, 2009, 362, pp. 2749-2745.
11. Mahata, P.; Ramya, K.V.; Natarajan, S.; Reversible water intercalation accompanied by coordination and color changes in a layered metal-organic framework. Inorganic Chemistry. 2009, 48, pp. 4942-4951.
12. Lu, W.-G.; Jiang, L.; Feng, X.-L.; Lu, T.-B. Three-dimensional lanthanide anionic metal-organic frameworks with tunable luminescent properties induced cation exchange. Inorganic Chemistry, 2009, 48, pp. 6997-6999.
13. Starynowicz P. Structure and electron spectroscopy of potassium triaquadecakis(cyanoacetato)trineodymate hexahydrate. Polish Journal of Chemistry, 1994, 68, pp. 621-629.
14. Starynowicz, P. *Catena*-Poly[{aqua(cyanoacetato-κO)(N,N-dimethylformamide-κO)neodymium}-di-μ-cyano-acetato-κO,κO':κO']monohydrate. Acta Crystallographica, Sect.C: Crystal Structure Communications, 1993, 49, pp. 1621-1623.
15. Novitskii, G.; Shova, S.; Voronkova, V.; Korobcenko, L.; Gdanets, M.; Simonov, Iu.; Turta, C. Copper(II) cyanoacetate polymer: synthesis and structure. Russian Journal of Coordination Chemistry, 2001, 27, pp. 839-844 (in Russian).
16. Shova, S.G.; Simonov, Yu.A.; Gdaniec, M.; Novitskii, G.V.; Lazarescu, A.; Turta, K.I. Synthesis and Structure of catena-{Bis(μ-cyanoacetato(O,O,O¢))tetrakis(μ-cyanoacetato(O,O¢))dineodymium(III*)*. Russian Journal of Inorganic Chemistry, 2002, 47, pp. 946-952 (in Russian).
17. Arauzo, A.; Lazarescu, A.; Shova, S.; Bartolomé, E.; Cases, R.; Luzón, J.; Bartolomé, J.; Turta, C. Structural and magnetic properties of some lanthanide (Ln= Eu(III), Gd(III) and Nd(III)) cyanoacetate polymers: Field-induced slow magnetic relaxation in the Gd and Nd substitutions. Dalton Transactions, 2014, 43, pp. 12342-12356.
18. Charlot G. Methods of Analytical Chemistry. The Quantitative Analysis of Inorganic Compounds. Chemistry: Leningrad, 1965, 975 p. (in Russian).
19. *CrysAlis*PRO, Oxford Diffraction /Agilent Technologies UK Ltd, Yarnton, England.
20. Sheldrick, G.M. A short history of SHELX. Acta Crystallographica, 2008, A64, pp. 112-122.
21. Edgington, P.R.; McCabe, P.; Macrae, C.F.; Pidcock, E.; Shields, G.P.; Taylor, R.; Towler, M.; Van de Streek, J. Mercury: visualization and analysis of crystal structures. Journal of Applied Crystallography, 2006, 39, pp. 453-457.
22. Vainshtein, B.K., Indenbom, V.L.; Fridkin, V.M. Modern crystallography. Crystal structure. Science: Moscow, 1979, V. 2, pp. 77-78 (in Russian).

IRIDOID GLYCOSIDES FROM *LINARIA GENISTIFOLIA* (L.) MILL. IN BIOLOGICAL CONTROL OF SOIL-BORNE FUNGAL PATHOGENS OF WHEAT AND SOME STRUCTURE CONSIDERATIONS

Natalia Mashcenko[a*], Angela Gurev[a], Galina Lupascu[a], Elena Gorincioi[b]

[a]*Institute of Genetics and Plant Physiology of Academy of Sciences of Moldova, 20, Padurii str., Chisinau MD-2002, Republic of Moldova*
[b]*Institute of Chemistry of Academy of Sciences of Moldova, 3, Academiei str. Chisinau MD-2028, Republic of Moldova,*
[*]*email: mne4747@mail.ru; tel: (+373 22) 55 52 59; fax: (+373 22) 55 61 80*

This article is dedicated to the memory of Prof. Pavel Kintia

Abstract. Biological activity of the iridoid glycosides extract from *Linaria genistifolia* (L.) Mill. has been investigated, namely its influence on the resistance of the winter wheat Odesschi 51 plant to the caused by the *Fusarium oxysporum* and *Helminthosporium avenae* pathogenic fungi root rot. Our results indicate that summary iridoid glycosides from this plant, containing four major known compounds: 5-O-allosylantirrinoside, antirrinoside, linarioside and 6-β-hidroxiantirride, can be successfully employed in biological control of the afore-mentioned wheat pathogens: it stimulates wheat grains germination and embryonic root growth in conditions of fungal infection. ^{1}H and ^{13}C NMR characteristics of 5-O-allosylantirrinoside in Py-d_5 are for the first time presented. Structures of two conformers of 5-O-allosylantirrinoside in D_2O and Py-d_5 solutions are proposed, based on the experimental NMR evidence and molecular modelling studies.

Keywords: *Linaria genistifolia* (L.) Mill., iridoid glycosides, bioactivity, 5-O-allosylantirrinoside, NMR, molecular modelling.

Received: February 2015/ Revised final: April 2015/ Accepted: April 2015

Introduction

More than 200 species of genus *Linaria* (Scrophulariaceae) are representatives of wild flora, constituting a rich source of biologically active substances, such as flavonoids, iridoids, alkaloids, diterpenoids, glycosides and others. A series of beneficial physiological activities characterizes these medicinal plants of repute, explaining their wide application in folk and traditional medicine, as well as in homeopathic practice. Thus, different *Linaria sp*. have been used as tonics, antiscorbutics, laxatives, antidiabetics and diuretics, spasmolytics, cholagogic drugs, as well as for treatment of wounds, bladder catarrhs, haemorrhoids and vascular disorders [1-3].

The iridoid composition of *L. dalmatica* (L.) Mill., *L. genistifolia* (var. *genistifolia* and var. *euxina*) (L.) Mill., *L. simplex* (Wild.), *L. pelisseriana, L. vulgaris* and *L. peloponnesiaca* Bois & Heldr., which occur in Bulgaria, has been in depth examined and reported by N. Handjieva, S. Popov et al. [4-6]. Structure elucidations have been carried out mainly by spectral methods and the data of pioneering studies on molecular mechanics calculations in this field were published [4]. An iridoid glycoside has been found amongst the chemical constituents of *L. aucheri* that is characteristic for the flora of Turkey [7]. The iridoid composition of *L. japonica* M_{IQ}., a Japanese folk medicine known as laxative and diuretic, has been investigated, detailed proton magnetic resonance examinations on the found iridoid glycosides and their derivatives being presented [8].

We have previously presented the results of our studies on biologically active compounds from *Linaria vulgaris* Mill. [9]. As an extension of this study we have now investigated the other species of *Linaria*, namely *L. genistifolia* (L.) Mill. that is widely distributed on the territory of Republic of Moldova, for the biological activity against soil-borne fungal pathogens of wheat *F. oxysporum* and *H. avenae*. These fungi are very spread, being known by severe affection of some vital processes in wheat plant, such as: seed germination, growth and development of the embryonic root and also infecting the grains with micro toxins, as well as reduction of the crop quantity and quality [10,11].

Results and discussion

This study was carried out with an objective of investigation the antifungal activity potential of the iridoid glycosides extract (IGE) from *L. genistifolia* (L.) Mill. We have studied the properties of IGE from *L. genistifolia* (L.) Mill. on the resistance of the winter wheat Odesschi 51 plant to the root rot that is caused by the *F. oxysporum* and *H. avenae* pathogenic fungi. Our results indicate that summary iridoid glycosides from this plant can be successfully employed in biological control of the afore-mentioned wheat pathogens: it stimulates wheat grains germination and embryonic root growth in conditions of fungal infection.

In IGE four major known iridoids were identified, after chromatographic separation, their presence in *L. genistifolia* (L.) Mill. being previously described [4,6]. The structures of 5-O-allosylantirrinoside (**1**), which was the predominant IGE component, and 6β-hydroxyantirride **(4)** have been confirmed by means of NMR spectroscopy, as

already reported [4,6], while antirrinoside **(2)** and linarioside **(3)** were identified by comparison of their physico-chemical properties with the literature data [8] (Figure 1).

The winter wheat Odesschi 51 constituted the object of the study. Prior to sowing, seeds of the winter wheat Odesschi 51 were soaked in IGE aqueous solutions having the mass fractions 10^{-5}, 10^{-4}, 10^{-3}, 10^{-2} %. As a control version the water soaked grains served. For comparison, a part of the grains was soaked in the same concentrations aqueous solutions of Moldstim – a certificated product for agricultural usage [12]. After drying the grains were soaked in *F. oxysporum* and *H. avenae* 21 days culture filtrates (CF) for 18 hours, then rinsed with distilled water and placed in a Petri dish, on filter paper moistened with distilled water. The seedlings were cultivated for 6 days at a temperature of 22ºC.

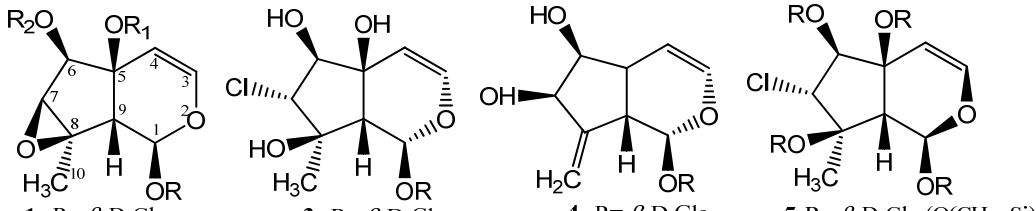

1 R= β-D-Glc
R_1= β-D-All, R_2= H
2 R= β-D-Glc; R_1=R_2= H
C_1Hquasi-ax. [8]
6 R= β-D-Glc$(OAc)_4$;
R_1=R_2= Ac, C_1Hquasi-eq. [8]

3 R= β-D-Glc
C_1Hquasi-eq. [8]

4 R= β-D-Glc
C_1Heq. [4]

5 R= β-D-Glc-$(O(CH_3)_3Si)_4$
C_1Hquasi-ax. [8]

Figure 1. Structures of compounds 1 – 4, the major IGE components, and obtained *via* synthesis compounds 5 and 6 [8].

The plant response was assessed on the basis of its germination capacity and the length of embryonic root. The obtained results show that by infecting the grains with the *F. oxysporum* and *H. avenae* CF, the seed germination is being diminished by 33.4 and 16.7%, respectively, while the embryonic root is being reduced by 35.7 and 30.2%, as compared to the control version (Tables 1 and 2). This proves the toxicity of the fungi that causes root rot. When treating the infected grains with Moldstim, the most efficient concentrations were in the range of 10^{-4}... 10^{-3}%; it caused an increase in the germination process by 3.4 – 11.7% and 9.7 – 18.4%, and the augment of the length of embryonic root by 13.72 – 18.8% and 6.7 – 10.0%, correspondingly, in comparison with the *F. oxysporum* and *H. avenae* CF versions. It was interesting to note the same beneficial effect of IGE from *L. genistifolia* (L.) Mill. on the infected wheat grains and to compare the furnished by both experimental protocols results. For instance, the IGE-treated and infected with *F. oxysporum* plants showed a germination level of 98.3 %, which is by 35% more, and a root longer by cca 27%, when compared to *F. oxysporum* CF. (Table 1). These data speak in favour of higher biological activity of IGE *versus* Moldstim (about three times in the germination process and one and a half- in embryonic root elongation in the best versions, entries 4 and 8-9 in Table 1), the most efficacious IGE concentration being found also in the range of 10^{-4} - 10^{-3}%.

Table 1

The influence of IGE on the winter wheat Odesschi 51 plant response to the *Fusarium oxysporum* culture filtrate.

No.	*Version/concentration, %*	*Germination, %*	*Embryonic root length, mm*	*% compared to CF F. oxysporum*
1	Control version (H_2O)	96.7	80.81±1.80	155.5
2	CF *F. oxysporum*	63.3	51.97±2.57	-
3	CF *F. oxysporum* + Moldstim, 10^{-2}	63.6	57.08±1.65*	109.8
4	CF *F. oxysporum* + Moldstim, 10^{-3}	75.0	61.76±1.93*	118.8
5	CF *F. oxysporum* + Moldstim, 10^{-4}	66.7	59.10±2.22*	113.7
6	CF *F. oxysporum* + Moldstim, 10^{-5}	65.0	46.74±2.77	89.9
7	CF *F. oxysporum* + IGE, 10^{-2}	96.7	59.59±1.82*	114.7
8	CF *F. oxysporum* + IGE, 10^{-3}	98.3	67.75±1.63*	130.4
9	CF *F. oxysporum* + IGE, 10^{-4}	98.3	64.15±1.59*	123.4
10	CF *F. oxysporum* + IGE, 10^{-5}	86.7	55.67±0.94	107.1

** true in relation to F. oxysporum CF at p≤0.05.*

Similar effects can be observed in the presence of IGE in CF of the infected by *H. avenae* fungi grains of the winter wheat: the length of the embryonic root grows by 30.4% and germination by 13.3% (entries 9 and 8 in Table 2, IGE concentration 10^{-4} and 10^{-3}%, respectively), in comparison with the *H. avenae* CF version (entry 2, Table 2). Thus, the IGE biological properties against *H. avenae* infection are rather comparable with the activity, exerted by Moldstim (about two times higher stimulation of root elongation and 1.3 times higher promotion of germination process (entries 5/9 and 4/8 in Table 2).

Table 2

The influence of IGE on the winter wheat Odesschi 51 plant response to the *Helminthosporium avenae* culture filtrate.

No.	*Version/concentration, %*	*Germination, %*	*Embryonic root length, mm*	*% compared to CF H. avenae*
1	Control version (H_2O)	96.7	80.81±1.80	143.3
2	CF *H.avenae*	80.0	56.38±2.59	-
3	CF *H.avenae* + Moldstim, 10^{-2}	86.7	58.54±1.25*	103.8
4	CF *H.avenae* + Moldstim, 10^{-3}	90.0	61.82±0.98*	109.5
5	CF *H.avenae* + Moldstim, 10^{-4}	86.7	66.75±1.14*	118.4
6	CF *H.avenae* + Moldstim, 10^{-5}	85.0	59.92±2.11	106.3
7	CF *H.avenae* + IGE, 10^{-2}	83.3	65.40±1.60*	116.0
8	CF *H.avenae* + IGE, 10^{-3}	93.3	69.32±1.44*	123.0
9	CF *H.avenae* + IGE, 10^{-4}	83.3	73.52±2.40	130.4
10	CF *H.avenae* + IGE, 10^{-5}	90.0	67.9±2.04	120.4

***** *true in relation to H. avenae CF at p≤0.05.*

Thus, the achieved by us results indicate that the obtained from *L. genistifolia* (L.) Mill. iridoid glycosides can be successfully utilized as substances of natural origin that stimulate wheat grains germination and embryonic root growth, considering the infected by fungi grains [13]. Our data are particularly attractive in terms of availability of the iridoid glycosides source: *L. genistifolia* (L.) Mill. grows in spontaneous flora and can be collected in large quantities.

Broadening the range of natural biologically active and environmentally inoffensive fungicidal substances is a very actual issue for agricultural workers and researchers, since biological control of insect pests, plant pathogens and weeds, is the only alternative to the use of pesticides in agriculture and forestry.

It should be mentioned, that during confirmation the stereochemical structure of compounds **1** and **4** our attention was especially drawn to the reported individual NMR spectroscopic data of compounds, which prove the reliability of structure assignments. Thus, N. Handjieva et al. have established the structure and relative stereochemistry of 6β-hydroxyantirride **4** on the basis of spectral studies, corroborating the NMR experimental data by molecular mechanics calculations, by using Haasnoot equation [4,14]. The minimum-energy stereostructure of **4** and its analog with OMe instead of OGlc residue indicated that the conformation of the six-membered ring of aglycon is close to a half-chair with an axially oriented substituent at C-1, which perfectly corresponded to the experimental $J_{1,9}$ value of 2.3-2.5 Hz. The recorded by us in D_2O ^1H and ^{13}NMR spectra of **4** demonstrated identical NMR characteristics of our compound to the published one [4].

The prevailing in IGE component, compound **1** is quite widespread in the plants of the genus *Linaria*, being formerly found in five *Linaria* species [6], including the investigated by us specimen. Likewise, comparison of its ^1H and ^{13}C NMR spectral characteristics, proved its identity to the published 5-O-allosylantirrinoside **1**, when D_2O was employed as NMR solvent, Table 3 [6]. The opportunity of NMR characterization of compound **1** in deuterated pyridine (Py-d_5) as a weakly interacting solvent has been by us considered, by this intending to update the information on solvent effects in its NMR data profile. It should be mentioned, that Py-d_5 presents some important advantages as NMR solvent, particularly, for investigations in the field of glycosides, namely: avoidance of the solvent interactions and signal overlapping, better solubility then in D_2O or MeOD etc. But its use is limited by the high cost, D_2O being much more attractive in terms of price.

The spectral data of compound **1**, obtained after recording it's ^1H and ^{13}C NMR spectra in Py-d_5 were rather different from the obtained in D_2O solution ones (Table 3). This was not so unusual, at first appearance, since it is a matter of common knowledge, that the nature of solvent can influence both ^1H and ^{13}C chemical shifts and spin - spin coupling constants of protons [15-17]. From the other side, the noted differences could be favorable to the structural identity either of an epimeric structure, possessing the opposite stereochemistry at C_1 (*i.e. R*-configuration), or, in accordance to the data of I. Kitagawa et al. [8], to a conformer of **1.** Since the configuration of the glucosyloxy moiety at C_1 in antirrinoside **2** has been previously proved to be *β* [18] (*i.e.*, *S*-configuration), the possibility of examination the C_1

epimer of **1** has been omitted. No evidence was found in the literature, regarding the dihydropyrane ring conformation of 5-O-allosylantirrinoside **1** [6], but the data are available for the conformers of its congeners: antirrinoside **2**, linarioside **3** and some their synthetic derivatives [8]. In this light, clarifying the conformation of natural **1** has been planned, by analysis both the NMR spectroscopy and molecular modelling (MM) with energy minimization data, taking into account the traced by N. Handjieva et al. route [4].

The predominant molecule geometry of compound **2,** four it's Me, Ac, TMS derivatives and hepta-O-trimethylsilyl-linarioside **5** involved quasi-axial orientation of C_1 proton, for them the values of $J_{1,9}$ coupling constant varying from 5.5 to 10.5 Hz, (spectra recorded in D_2O, $CDCl_3$ and CCl_4), as reported [8]. Whilst for linarioside **3**, two it's acetates and hexaacetilated derivative of antirrinoside **2,** compound **6,** the quasi-equatorial position of proton at C-1 has been assigned by the same authors on the basis of PMR evidence and Dreiding model inspection (*e.g.* for compound **3**: 5.70 ppm (br.s.), $W_{1/2}$=2.0 Hz, C_1-H; for compound **6**: 2.77 ppm (br.s.), $W_{1/2}$=4.5 Hz, C_9-H) (spectra recorded in D_2O and $CDCl_3$, respectively, at 60MHz) [8].

On the basis of our experimental data and taking advantage of the formulated by the Japanese chemists observation, on the relation between the splitting pattern of proton at C_9 and dihydropyrane ring conformation in **2** and its derivatives [8], we explain the discussed differences in NMR data of compound **1** in two mentioned NMR solvents by conformational difference of dihydropyrane ring, as well, judging by the values of $J_{1,9}$ vicinal coupling constants: 5.48 ppm, d, $J_{1,9}$ =6.8 Hz, C_1 ax. H, (D_2O) *versus* 5.84 ppm, d, $J_{1,9}$ =3.7 Hz, C_1eq. H, (Py-d_5), Table 3.

Interestingly, as it can be noted from the afore-mentioned, the nature of solvent proved no impact on the conformations of compounds **2**, **3** and their derivatives [8]. However, in the case of the analyzed by us glycoside **1** change of the used NMR solvent causes, according to the established by us values of $J_{1,9}$ coupling constants, switching from one conformation to another.

The minimum-energy stereo-structures for the examined conformers of 5-O-allosylantirrinoside **1** have been obtained, which are depicted in Figure 2: **1a-** in Py-d_5, and **1b-** in D_2O, correspondingly, and the $^1H/^1H$ coupling constants have been calculated, by using molecular modelling with energy minimization software, namely PERCH NMR TOOLS (version 2014.1)). The results indicated on a good agreement between the calculated and experimental vicinal $J_{1,9}$-values in pyrenone ring of conformers **1a** and **1b** of **1**. Thus, for conformer **1a** the calculated value of $J_{1,9}$ is 3.12 Hz (experimental value 3.7 Hz), while for **1b** the calculated $J_{1,9}$ constitutes 10.84 Hz (experimental value 6.8 Hz). The minimum-energy stereo-structures of both conformers **1a** and **1b** indicate that the conformations of the six-membered pyrenone ring is close to a half-chair, with an axially oriented substituent at C_1 in **1a** and an equatorially oriented substituent in **1b.** The recorded in Py-d_5 NOE experiments have demonstrated strong NOE interactions between CH_3-10 and C_1-H, while in D_2O these interactions were less pronounced, also supporting the indicated in Figure 2 structures of the conformers **1a** and **1b**.

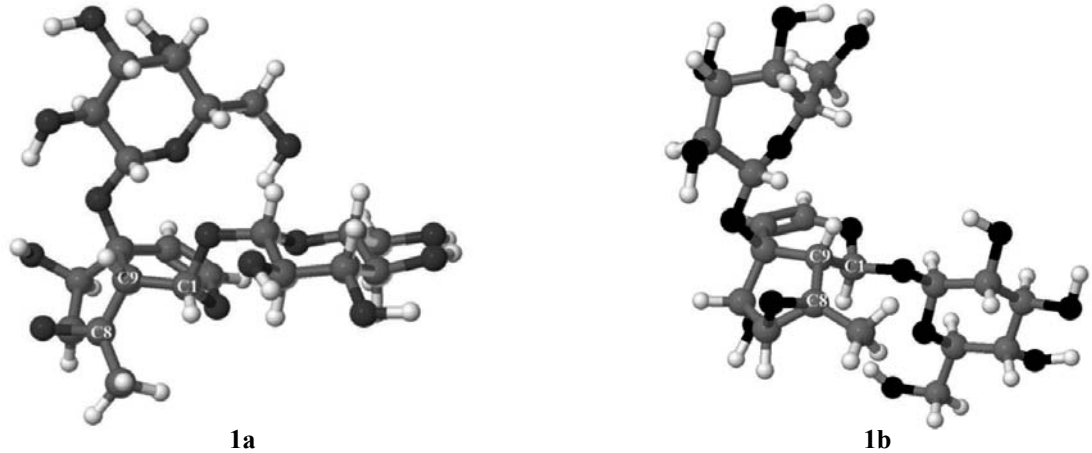

1a **1b**

Figure 2. Minimum-energy conformations 1a and 1b of 5-O-allosylantirrinoside 1.

In the case of the pair of diastereoisomers of **1**, hypothetic conformers of the epimer with the opposite stereochemistry at C_1 (*i.e. R*-configuration), the calculated values of $J_{1,9}$ were very close, constituting 3.15 and 3.18 Hz, thus confirming the only bigger value of $J_{1,9}$ for **1b** and, implicitly, conclusions of Scarpati et al. [18].

Being occurred together in the same plant, question about conformational differences amongst compounds **1-4** in D_2O solutions is of interest also from the biogenetic point of view, since water is the solvent of life. Thus, for the natural epoxide **2** and it's 5-O-allosyl ether **1,** belonging to the antirrinoside iridoid type, the same conformation of dihydropirane ring of aglycon is adopted in D_2O, whereas for the corresponding to epoxide **2** clorohydrine **3-** the opposite one, which is characteristic also for the representative of the rare antirride type- compound **4**, as depicted in Figure 1.

Thus, putting together the results of our joint NMR-MM study, it can be concluded, that the noted differences in ^{1}H and ^{13}C NMR characteristics of compound **1** demonstrate solvent influence on the molecule geometry. Our data seem not to be in the same line with that of I. Kitagawa [8], in fact, completing them. According to the MM data, in D_2O the conformer molecule is spatially more relaxed, being maximally available for hydration, whilst in Py-d_5 it is more compactly packed. Strong hydration of 5-O-allosylantirrinoside molecules, especially it's highly hydrophilic glucose and allose moieties, most likely exerts shielding effect upon ^{1}H and ^{13}C nuclei, causing their upfield shifts in D_2O solution.

Table 3

^{1}H and ^{13}C NMR spectral data for compound 1 (δ ppm, J (Hz)[a].

C/H atom	*Py-d_5*		*D_2O*	
	δ_H [b]	δ_C [c]	δ_H [b,d]	δ_C [c,e]
Aglycon				
1	5.84 d, J=3.7	93.1	5.48 d, J=6.8	95.5
3	6.64 d, J=6.4	143.9	6.61 d, J=6.2	144.8
4	5.34 d, J=6.4	105.2	5.12 d, J=6.2	106.3
5	-	80.5	-	80.4
6	4.23 d, J=2.8	75.9	4.30 d, J=1.9	77.8
7	3.46 d, J=2.8	66.0	3.60 d, J=1.8	66.0
8	-	63.5	-	64.7
9	3.10 d, J=3.7	50.3	3.01 d, J=6.8	50.5
10	1.32 s	17.4	1.51 s	17.4
Glucose				
1'	5.28 d, J=7.9	98.3	4.82 d, J=8.0	98.8
2'	4.05*	75.5	**	73.7
3'	4.23*	77.6	**	76.4
4'	4.17*	72.1	**	70.4
5'	3.98*	79.6	**	77.1
6'	4.40- 4.50*	63.2	3.60- 3.95	61.8
Allose				
1''	5.70 d, J=7.9	97.8	4.89 d, J=8.3	96.5
2''	4.00*	73.3	**	72.0
3''	4.70 t, J=2.7	72.9	4.19 t, J=2.8	71.0
4''	4.28*	68.4	**	67.4
5''	4.40*	76.9	**	74.3
6''	4.36-4.40*	62.6	3.60-3.85	61.8

[a] *Assignments of ^{1}H and ^{13}C signals in spectra are made on the basis of 1D: (^{1}H, ^{13}C, DEPT-135°) and 2D: homo-($^{1}H/^{1}H$ COSY-45°, NOE) and heteronuclear ($^{1}H/^{13}C$ HSQC, HSQC-TOCSY and HMBC) experiments.*

[b] *400 MHz.*

[c] *100 MHz.*

[d] *300 MHz [6].*

[e] *75 MHz [6].*

[b,c] *Bruker Avance 400 spectrometer.*

**Unclear signal pattern due to overlapping.*

***Data are not reported.*

Conclusions

The influence of the iridoid glycosides extract from *Linaria genistifolia* (L.) Mill. has been investigated on the resistance of the winter wheat Odesschi 51 plant to the caused by *F. oxysporum* and *H. avenae* pathogenic fungi root rot. We have established, that the iridoid glycosides extract from this plant, containing four major known compounds: 5-O-allosylantirrinoside, antirrinoside, linarioside and 6-β-hidroxiantirride, can be successfully employed in biological control of the mentioned wheat pathogens: it stimulates wheat grains germination and embryonic root growth in conditions of fungal infection. ^{1}H si ^{13}C NMR characteristics of 5-O-allosylantirrinoside in Py-d_5 are for the first time presented. Structures of two conformers of 5-O-allosylantirrinoside in D_2O and Py-d_5 solutions are proposed, based on the experimental NMR data and molecular modelling studies.

Experimental

Obtaining the IGE

IGE from *L. genistifolia* were extracted from the dried aerial part of the plant (300 g), which was chopped and then subjected to reflux (3x6 hours in a 60% methanol aqueous solution, 3x1.5L). The extracts were combined and concentrated

through vacuum distillation, thereupon, the aqueous residue was decanted with chloroform; the aqueous fraction was passed through Sephadex LH-20. The column was eluted with 10% aqueous methanol and the resulting eluate was evaporated through vacuum distillation to dryness. The dry residue (4.6g) contained a mixture of components, the iridoid glycosides **1 - 4** being detected in it as major products by thin-layer chromatography on silica gel. For investigation of the biological properties, IGE extract has been employed as such; 5-O-allosyilantirrinoside **1** was its predominant component. For the identification of individual mixture components, a portion of it (0.6g) was separated by column chromatographic method, by using silica gel (40 x 100 μm, Merck) with a solvent systems of chloroform/methanol (4:1) and chloroform/methanol/water (95:5:0→10:4:1), and then Sephadex LH-20 with the elution system methanol/water (1:9). After chromatographic isolation compounds **1** - **4** were obtained in the following amounts: **1-** 52.4 mg, **2-** 36.6 mg, **3-** 32.8 mg, **4-** 27.5 mg. By ^{1}H and ^{13}C NMR spectroscopy and *via* comparison with bibliographic data the IGE components **1** - **4** were identified as follows: **1** - 5-O-allosylantirrinoside; **2** - antirrinoside; **3** - linarioside; **4** - 6-β-hidroxiantirride.

Testing the biological activity of IGE

F. oxysporum and *H. avenae* fungi stems were isolated from the stem of the winter wheat stem that manifested disease symptoms (brown spots), on a solid nutrient medium *Potato Dextrose Agar* (PDA) and identified trough macro and microanalysis. *F. oxysporum* and *H. avenae* fungi CF were obtained by inoculating mycelium in a Czapex Dox liquid medium and cultivating it, afterwards, for 21 days at temperatures of 22…24ºC [19].

Prior to sowing, the grains were soaked for 4 hours in aqueous solutions of IGE from *L. genistifolia* (L.) Mill. or Moldstim with the mass fractions of 10^{-5}, 10^{-4}, 10^{-3} and 10^{-2} %. As a control version the water soaked grains were employed. After drying the seeds for 24 hours, part of them was soaked for 18 hours in *F. oxysporum* CF, while another part was soaked in *H. avenae* CF for 21 days then they were rinsed twice with distilled water and placed in a Petri dish on moistened with distilled water filter paper. The seedlings were cultivated for 6 days at a temperature of 22ºC. The plant response was assessed based on its germination capacity and embryonic root length. For determination the germination capacity the wheat grains (100 pieces) were soaked for 24 hours in water then placed in sterile Petri dishes on moistened with distilled water filter paper. Germination was carried out in a climate chamber at a temperature of 20ºC, the number of germinated seeds being determined on the 7th day. The experiments were run 5 times. Data were processed by STATISTICA 7 program.

References

1. Stojanov, N. Our Medicinal Plants. Nauka i Iskustvo: Sofia, 1973, Part II, 99p.
2. Baytop, T. Therapy with Medicinal Plants (Past and Present), 2nd ed. Nobel Tip Kitabevleri Ltd., Istanbul, 1999, 373 p.
3. San Feliciano, A.; Gordaliza, M.; Del Corral, J.M.M.; De La Puente, M.L. Neo-clerodane diterpenoids from roots of *Linaria saxatilis* var. *Glutinosa.* Phytochemistry, 1993, 33, pp. 631-633.
4. Handjieva, N.V.; Ilieva, E.I.; Spassov, S.L.; Popov, S.S. Iridoid glycosides from *Linaria* species. Tetrahedron, 1993, 49, pp. 9261-9266.
5. Ilieva, E.I.; Handjieva, N.V.; Popov, S.S. Iridoid glucosides from *Linaria vulgaris.* Phytochemistry, 1992, 31(3), pp. 1040-1041.
6. Ilieva, E.; Handjieva, N.; Spassov, S.; Popov, S. 5-O-allosylanirrinoside from *Linaria* species. Phytochemistry, 1993, 32(4), pp. 1068-1070.
7. Ercil, D.; Sakar, M. K.; Del Olmo, E.; San Feliciano, A. Chemical constituents of *Linaria aucheri*. Turkish Journal of Chemistry, 2004, 28, pp. 133-139.
8. Kitagawa, I., Tani, T., Akita, K. Yoshika, I. On the constituents of *Linaria laponica* $M_{IQ.}$ I. The structure of linarioside, a new chlorinated glucoside and identification of two related glucosides. Chemical and Pharmaceutical Bulletin, 1973, 21, pp. 1978-1987.
9. Mashcenko, N.; Kintia, P.; Gurev, A.; Marchenko, A.; Bassarello, C.; Piacente, S.; Pizza, C. Glycosides from *Linaria vulgaris* Mill. Chemistry Journal of Moldova, 2008, 3(2), pp. 98-100.
10. Grigoriev, M. F.; Zincenco, V. A.; Grigoriev, A. M. Manifestation of caused by *Fusarium* and helminthes root rot on barley varieties depending on the weather conditions of the year, reproduction and sowing dates. Bulletin of Timireazev Agricultural Academy, 2006, No. 3, pp. 41-45 (in Russian).
11. Jalieva, L.D. Species composition of root and basal rot pathogens of wheat. Micology and Phytopathology, 2001, 35(6), pp. 52-56 (in Russian).
12. Lazări, I. Chemical and biological preparations for protection and stimulation of plant growth. Stiinta: Chisinau, 1997, 230 p. (in Romanian).
13. Mascenco, N.; Lupascu, G.; Guriev, A.; Barba, A.; Gorincioi, E.; Gavzer, S. Procedure of treatment the winter wheat against *Fusarium oxysporum*. Decision to grant a patent Nr.7887 from 2014.08.25. (in Romanian).
14. Haasnoot, C.A.G.; De Leeuw, F.A.M.; Altona, C. The relationship between proton-proton NMR coupling constants

and substituent electronegativities-I: An empirical generalization of the Karplus equation. Tetrahedron, 1980, 36(19), pp. 2783-2792.
15. Reich, H. J. Structure determination using NMR, 2014. http://www.chem.wisc.edu/areas/reich/chem605/
16. Silverstein, R. M.; Webster, F. X.; Kiemle, D. J. Spectrometric identification of organic compounds. John Wiley & Sons, Inc.: U.S.A., Seventh edition, 2005, 512 p.
17. Rahman, A.; Chouldhary, M.I. Solving problems with NMR spectroscopy. Academic Press, Inc.: San Diego, 1996, 430p.
18. Scarpati, M. L.; Guiso, M.; Esposito, P. Iridoids (V). Structure and configuration of Antirrinoside. Gazzetta Chimica Italiana, 1968, 98, pp. 177-190 (in Italian).
19. Methods of experimental mycology. Naukova dumka: Kiev, 1982, 550 p. (in Russian).

THE SYNTHESIS OF NEW SPIROLACTONES FROM SUBSTITUTED ISATINS

Natalia Sucman[a], Vsevolod Pogrebnoi[a], Mykola Obushak[b],
Elena Melnic[c], Victor Kravtsov[c], Fliur Macaev[a*]

[a]*Institute of Chemistry of Academy of Sciences of Moldova, 3, Academy str., Chisinau MD-2028, Republic of Moldova*
[b]*Ivan Franko National University of Lviv, 6, Kyryla i Mefodiya str., Lviv 79005, Ukraine*
[c]*Institute of Applied Physics of Academy of Sciences of Moldova, 5, Academy str., Chisinau MD-2028, Republic of Moldova*
[*]*e-mail: flmacaev@cc.acad.md*; *phone (+373 22) 73 97 54; fax (+373 22) 73 99 54*

Abstract. Interaction of *N*-ethyl isatin **3** with dimethyl acetylenedicarboxylate in the presence triphenylphosphine has led to good selectivity of methyl 1'-ethyl-4-methoxy-2',5-dioxo-5*H*-spiro[furan-2,3'-indoline]-3-carboxylate **4** formation. Similar yields of *spiro*lactones **6,8** were obtained by addition of dimethyl acetylenedicarboxylate to 5-bromo functionalized isatins **5**,**7**. However, reaction of *N*-butyl isatin **9** resulted in formation of an inseparable mixture of compounds. Treatment of *N*-benzyl isatin **10** and dimethyl acetylenedicarboxylate with triphenylphosphine proceeded with reduced selectivity of the spirooxindole **11** formation**.**

Keywords: spirolactones, isatins, triphenylphosphine, dimethyl acetylenedicarboxylate.

Received: March 2015/ Revised final: April 2015/ Accepted: April 2015

Introduction

The widespread distribution of butenolides in naturally occurring [1-3] and synthetic bioactive substances strongly motivate an interest for improving the methodology of the selective synthesis of butenolide functionalized spirooxindoles in high yield [4,5]. Such developments are of interest not only for the possible total synthesis of therapeutically useful spirooxindoles [6-15], but also for the preparation of synthetic analogs [16-30] in order to improve our knowledge in structure-activity relationships [12-14, 31, 32]. So-called butenolide functionalized spirooxindoles **1** provide the most interesting subject for synthetic investigations in view of the large and ever increasing number of the members of this family which have furan-2(5*H*)-one **2** as a building block (Scheme 1).

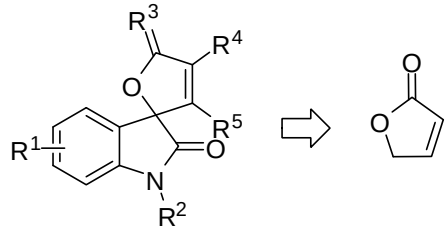

1 **2**

Scheme 1. Retro-synthesis of butenolide functionalized spirooxindoles.

Herein, we focused on developing of a cycloaddition method of dimethyl acetylenedicarboxylate to 5-bromo functionalized isatins for a selective construction of spiro-butenolide oxindoles **1** featuring several functionalized centres.

Results and discussion

It has been reported [4] that mixture of equal amount of *N*-ethyl isatin **3,** dimethyl acetylenedicarboxylate and triphenylphosphine is a satisfactory system for the high yield (up to 90%) construction of spirane **4** (Scheme 2). For this reason, our research was initiated toward the investigation of structure-reactivity relationships of *N*-alkyl isatins, acetylenedicarboxylate and triphenylphosphine to cope with such classical problem of heterocyclic chemistry. However, this approach for the synthesis of substance **4** provided a complex of products and main of them was isolated only with yield 60% by preparative TLC on silica gel.

The ^{1}H NMR spectrum of the white solid compound with m.p. 122-124^{0}C, has two doublets and two triplets at δ_H 6.79-7.40 ppm. Moreover, product has signal of two methylene protons (δ_H 3.67-3.90 ppm) and one secondary methyl group at δ_H 1.26-1.30 ppm and singlet attributable to MeO group at δ_H 3.55 ppm, the chemical shift of the last reflecting its attachment to a carbonyl atom. It was observed a chemical shift difference for protons position of =C-O-Me between reported [4] and our spectrum data at δ_H 3.38 ppm and δ_H 4.34 ppm, respectively. Moreover, m.p. of our sample also is different with published in [4].

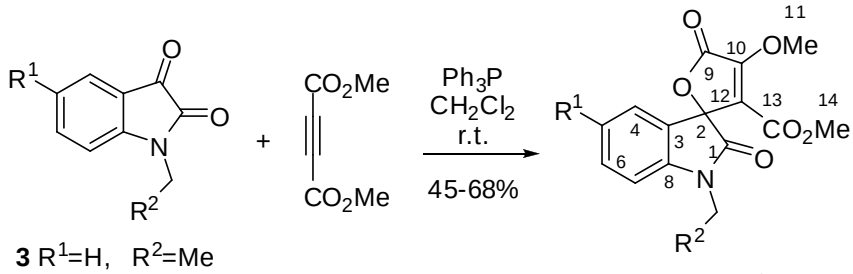

3 R^1=H, R^2=Me
5 R^1=Br, R^2=Me
7 R^1=Br, R^2=Et
9 R^1=Br, R^2=n-Pr
10 R^1=Br,R^2=Ph

4 R^1=H, R^2=Me
6 R^1=Br, R^2=Me
8 R^1=Br, R^2=Et
11 R^1=Br,R^2=Ph

Scheme 2. Synthesis of butenolide functionalized spirooxindoles.

We confirmed the structure of **4** by single-crystal X-ray analysis (see Figure 1). Monocrystals of composition $C_{16}H_{15}NO_6$ belong to centrosymmetric space group $P2_1/n$, thus represent racemate. The indole moiety is orthogonal to the furan ring as indicated by the dihedral angle of 88.85(5)° between them. The methyl ester group is about coplanar with furan ring and the dihedral angle between these fragments equals 10.6(1)°. The methoxy fragment of ester and attached to C10 methoxy group are in a proximate positions. Torsion angle O6-C13-C12-C10 equals -12.8(3)°.The C10-C12 bond distance equals 1.343(2)Å and unambiguously indicates the double character of this bond. The O2–C9 =1.353(2)Å and O2-C2=1.453(2) Å distances differ due to different hybridization of bonded carbon atoms. The compound exhibits structural similarities with an already reported related structure [33-36].

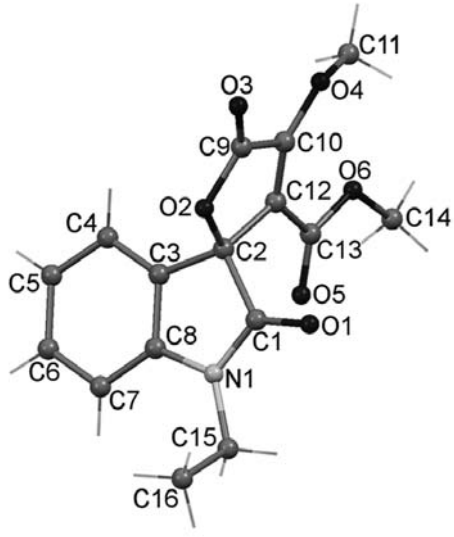

Figure 1. Single-crystal X-ray structure of 4.

Thus the major component in reaction of *N*-ethyl isatin **3,** dimethyl acetylenedicarboxylate and triphenylphosphine could be formulated as **4**.

5-Bromoisatines has been reported to be a suitable derivatives of indolinedione-2,3 in synthesis of a variety of its N-substituted oxindoles [7, 8, 13, 16, 31, 32].

In our case, *N*-ethyl 5-bromoisatin **5** reacted with an equivalent of dimethyl acetylenedicarboxylate and triphenylphosphine, the crude products were obtained in 86% yield (calculated as pure **6**) and 11% of initial **5** was reclaimed. The crude material was separated into fractions by column chromatography. The main product formed was characterized as methyl 5'-bromo-1'-ethyl-4-methoxy-2',5-dioxo-5*H*-spiro[furan-2,3'-indoline]-3-carboxylate **6**. The overall yield of the crystalline material **6** with m.p. 176-179^{0}C was 56%. It is note that numeration of atoms in Scheme 2 is given direct in structure, that is why spectra of compounds synthesized and doesn't obey the IUPAC rules. It should be noted, also the present of two doublets attributable to δ_H 6.79-6.81 ppm (7CH), δ_H 7.24-7.25 ppm (6CH), two multiplet at δ_H 3.66-3.71, δ_H 3.84-3.89 ppm (CH_2), triplet at δ_H 1.26-1.30 ppm ($CH_2\underline{Me}$) and two singlets at δ_H 3.61 ppm (CO_2Me) and δ_H 4.37 ppm (OMe).

Condensation of 5-bromoisatine **7** with dimethyl acetylenedicarboxylate in presence of the equal amount of triphenylphosphine in dichloromethane at room temperature for 5 hours afforded the complex of products (TLC data) and methyl 5'-bromo-4-methoxy-2',5-dioxo-1'-propyl-5H-spiro[furan-2,3'-indoline]-3-carboxylate **8** was isolated in 50% yield (from compound **7**) by column chromatography on silica gel. This compound gave a ^{1}H NMR spectrum δ_H 0.97-1.00 ppm ($CH_2\underline{Me}$), δ_H 1.68-1.74 ($\underline{CH_2}Me$), δ_H 3.63-3.68, 3.72-3.75 (N-CH_2), δ_H 3.62 ppm (CO_2Me), δ_H 4.36 ppm (COMe), δ_H 6.78-6.80 ppm (7CH), δ_H 7.23-7.24 ppm (6CH), δ_H 7.48-7.51 ppm (4-CH), which was in agreement with the structure **8**.

There has been no study of the stereochemistry of the atom C(2) of the spiro compound **8** by X-ray crystallography. The structure of **8** was also unambiguously confirmed by single crystal X-ray analysis. Monoclinic crystals of **8** have composition $C_{17}H_{16}BrNO_6$ and crystallize in centrosymmetric space group $P2_1/n$. View of molecule is shown on Figure 2. The five-membered furan ring forms dihedral angle of 86.6(1)° with planar indole moiety and coplanar with methyl ester making a dihedral angle of 2.8(3)°. In contrast to structure of **4** the methoxy fragment of ester and attached to C10 methoxy group are in distant positions. Torsion angle O6-C13-C12-C10 equals -175.5(3)°. The O2–C9 =1.362(4)Å, O2-C2=1.449(4)Å, and C10-C12=1.335(5) Å bond distances are well agree with those found in the structure of **4.** The other geometrical parameters of **8** and **4** are in well agreement too.

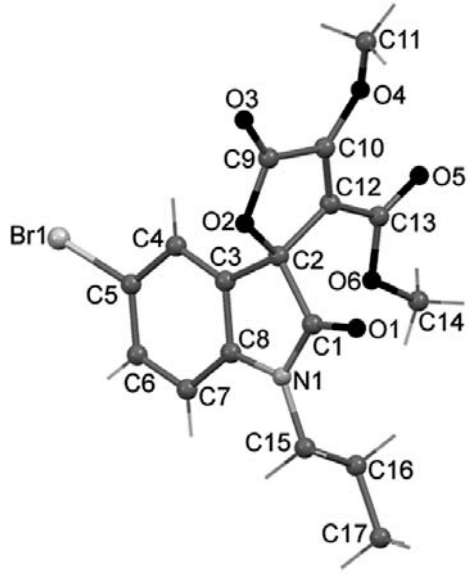

Figure 2. Single-crystal X-ray structure of 8.

Taking into account the previous experimental data (formation of the compounds **4**,**6**,**8**) we introduced one more CH_2 group in substrate (compound **9**) for obtaining the similar spirocyclic oxindole-butenolide derivative. But the reaction in the same conditions gave a complex of products without target butenolide, even standing at room temperature for a week.

Based on these results it is concluded that reaction of isatin **9** with reagents occurs slowly and is not selective. The opposite situation is observed in the case of spirolactone formation **11** from isatin **10** during one hour, which was indeed a major product (67% yield).

If the structure of product is **11**, CH_2 group of the derived oxindole-butenolide with m.p. 188-190^{0}C should give rise to an two doublets in the ^{1}H NMR spectrum while in low field shown two protons. In fact the product shows a clear doublet (δ_H 3.75 ppm) with a spin-spin coupling (J_{AB} = 16 Hz) of the magnitude predicted for a methylene group between the phenyl and amide fragments.

Second, the values of the chemical shifts of the phenylic (δ_H 7.28-7.32, 7.35-7.36 ppm) and aromatic (δ_H 7.00-7.01, 7.56-7.59, 7.89-7.90 ppm) protons are closely with those expected for spirane **11**. Third, the evidence of such structural features like C-Br bonding (ν_{max} 600 cm^{-1}), conjugated cyclic keto-ester (ν_{max} 1732.4 cm^{-1}), amide (ν_{max} 1652 cm^{-1}), conjugated ether (ν_{max} 1229.5 cm^{-1}), methylene group (ν_{max} 1484.4 cm^{-1}) in the IR spectrum led us to consider structure **11**.

The synthesis of the polyfunctionalized spirolactones from the C4, C6, C7 as well as N-substituted isatines is in progress and the results will be presented later along with a detailed discussion of the pathways to the various products. However, a provisional scheme which satisfactorily explains the production of discussed spirocyclic oxindole-butenolides is outlined (Scheme 3).

The construction of spirocyclic oxindole-butenolides involves a formation vinyltriphenylphosphonium salt [4, 38, 39] and concomitant addition to activated carbonyl atom of starting isatins.

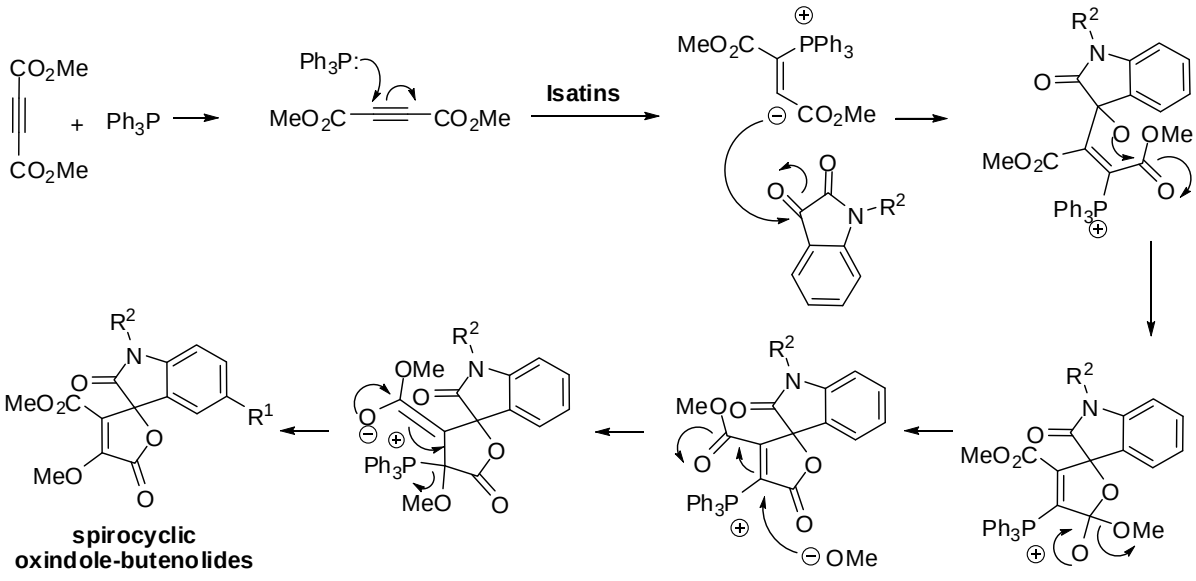

Scheme 3. The formation of spirocyclic oxindole-butenolides.

Conclusions

In conclusion, we contend that the above-described synthesis of 5-bromo substituted oxindoles linkages in spirocyclic butenolides exhibit relatively dependence of the structure-reactivity relationships of *N*-substituted isatines**,** dimethyl acetylenedicarboxylate. In the future it is planned to use chiral phosphine to provide the corresponding optically active spirolactones.

Experimental methods

All used solvents were of reagent quality, and all commercial reagents were used without additional purification. Removal of all solvents was carried out under reduced pressure. Analytical TLC plates were Silufol® UV-254 (Silpearl on aluminium foil, Czecho-Slovakia). IR spectra were recorded on a Spectrum 100 FT-IR spectrophotometer (Perkin –Elmer) using the universal ATR sampling accessory. ^{1}H and ^{13}C NMR spectra have been recorded for $CDCl_3$ 2-% solution on a "Bruker -Avance III" (400.13 and 100.61 MHz).

Isatines **3, 5, 7, 9, 10** were prepared using the methods [13, 40].

General procedure for the synthesis of methyl 2',5-dioxo-5*H*-spiro[furan-2,3'-indoline]-3-carboxylate 4, 6, 8, 11. To a solution of triphenylphosphine (0.262 g, 0.001 mol) in 5 mL CH_2Cl_2 was added N-substituted isatin (0.001 mol). The mixture was cooled to 10^{0}C, and then dimethyl acetylenedicarboxylate (0.142 g, 0.001 mol) was added. The reaction mixture was stirred for about 1-5 hours while maintaining the temperature to 25^{0}C. The solvent was removed in vacuum, oil like mass obtained was separated into fractions by preparative TLC on silica gel.

Methyl 1'-ethyl-4-methoxy-2',5-dioxo-5H-spiro[furan-2,3'-indoline]-3-carboxylate 4.

Yield 60%, red-brown solid, m.p. 122-124^{0}C. IR ν, cm^{-1}: 1213.1 (=C-O-), 1435.1 (CO_2Me), 1467.1 (CH_2), 1697.3 (N-C=O), 1726.6 (conjugated cyclic keto-carboxylic ester), 2878.4 (Me-CH_2). ^{1}H NMR δ, ppm, *J*/Hz: 1.26-1.30 t (Me-CH_2, 3H, *J*=16 Hz), 3.67-3.76 m (1H, CH_2), 3.82-3.90 m (1H, CH_2), 3.55 s (3H, CO_2Me), 4.34 s (3H, =C-OMe), 6.79-6.81 d (1H, 7CH, *J*=8 Hz), 6.89-6.91 d (1H, 4CH, *J*=8 Hz), 7.01-7.05 t (1H, 5CH, *J*=16 Hz), 7.36-7.40 t (1H, 6CH, *J*=16 Hz). ^{13}C NMR, δ, ppm: 12.32 (Me-CH_2), 35.46 (CH_2), 55.25 (C14), 60.44 (C11), 81.73 (C2), 109.17 (C7), 119.19 (C12), 123.20 (C6), 124.47 (C5), 128.20 (C3), 131.70 (C4), 143.97 (C8), 149.49 (C13), 160.55 (C10), 165.67 (C9), 169.56 (C1). Found, %: C 60.55; H 4.59; N 4.32. $C_{16}H_{15}NO_6$. Calculated, %: C 60.57; H 4.77; N 4.41.

Methyl 5'-bromo-1'-ethyl-4-methoxy-2',5-dioxo-5H-spiro[furan-2,3'-indoline]-3-carboxylate 6.

Yield 56%, yellow-brown solid, m.p. 176-179^{0}C. IR ν, cm^{-1}: 600 (CBr), 1228.4 (=C-O-), 1435.9 (CO_2Me), 1484.5 (CH_2), 1663.1 (N-C=O), 1720.8 (conjugated cyclic keto-carboxylic ester), 2873.0 (Me-CH_2). ^{1}H NMR δ, ppm, *J*/Hz: 1.26-1.30 t (Me-CH_2, 3H, *J*=16 Hz), 3.66-3.71 m (1H, CH_2), 3.84-3.89 m (1H, CH_2), 3.61 s (3H, CO_2Me), 4.37 s (3H, =C-OMe), 6.79-6.81 d (1H, 7CH, *J*=8 Hz), 7.24-7.25 d (1H, 6CH, *J*=4 Hz), 7.49-7.52 dd (1H, 4CH, *J*=4 Hz, *J*=4 Hz). ^{13}C NMR, δ, ppm: 12.13 (Me-CH_2), 35.63 (CH_2), 52.40 (C14), 60.49 (C11), 81.08 (C2), 110.60 (C7), 115.62 (C12), 118.69 (C5), 125.33 (C3), 127.67 (C6), 134.49 (C4), 143.12 (C8), 149.59 (C13), 160.36 (C10), 165.21 (C9), 169.16 (C1). Found, %: C 48.52; H 3.77; N 3.61. $C_{16}H_{14}BrNO_6$. Calculated, %: C 48.50; H 3.56; N 3.54.

Methyl 5'-bromo-4-methoxy-2',5-dioxo-1'-propyl-5H-spiro[furan-2,3'-indoline]-3-carboxylate 8.

Yield 50%, red solid, m.p. 90-100^{0}C. IR ν, cm^{-1}: 595 (CBr), 1231.9 (=C-O-), 1435.4 (CO_2Me), 1485.2 (CH_2), 1659.5 (N-C=O), 1719.8 (conjugated cyclic keto-carboxylic ester), 2878.0 (Me-CH_2). ^{1}H NMR δ, ppm, *J*/Hz: 0.97-1.00 t (Me-CH_2, 3H, *J*=12 Hz),1.68-1.74 m (2H, Me-CH_2), 3.63-3.68 m (1H, N-CH_2), 3.72-3.75 m (1H, N-CH_2), 3.62 s (3H,

CO_2Me), 4.36 s (3H, =C-OMe), 6.78-6.80 d (1H, 7CH, *J*=8 Hz), 7.23-7.24 d (1H, 6CH, *J*=4 Hz), 7.48-7.51 dd (1H, 4CH, *J*=1.9 Hz, *J*=4 Hz). ^{13}C NMR, δ, ppm: 11.18 (Me-CH_2), 20.54 (Me-CH_2), 42.62 (N-CH_2), 52.32 (C14), 60.40 (C11), 81.07 (C2), 110.88 (C7), 111.95 (C12), 115.52 (C5), 125.25 (C3), 127.52 (C6), 134.41 (C4), 143.57 (C8), 149.50 (C13), 160.46 (C10), 165.13 (C9), 169.16 (C1). Found, %: C 49.58; H 4.11; N 3.61. $C_{17}H_{16}BrNO_6$. Calculated, %: C 49.77; H 3.93; N 3.41.

Methyl 1'-benzyl-5'-bromo-4-methoxy-2',5-dioxo-5H-spiro[furan-2,3'-indoline]-3-carboxylate 11.

Yield 67%, yellow solid, m.p. 188-190^{0}C. IR ν, cm^{-1}: 585 (CBr), 1229.5 (=C-O-), 1430.2 (CO_2Me), 1484.4 (CH_2), 1652.3 (N-C=O), 1732.4 (conjugated cyclic keto-carboxylic ester), 2902.1 (Me-CH_2). ^{1}H NMR δ, ppm, *J*/Hz: 3.49 s (3H, CO_2Me), 4.30 s (3H, =C-OMe), 4.87-4.91 d (1H, CH_2, *J*=16 Hz), 5.01-5.05 d (1H, CH_2, *J*=16 Hz), 7.00-7.01 d (1H, 7CH, *J*=4 Hz), 7.56-7.59 dd (1H, 6CH, *J*=4 Hz, *J*=4 Hz), 7.89-7.90 d (1H, 4CH, *J*=4 Hz, *J*=4 Hz). ^{13}C NMR, δ, ppm: 44.09 (CH_2), 52.86 (C14), 60.97 (C11), 81.09 (C2), 115.65 (C7), 112.73 (C12), 117.47 (C5), 129.25 (C3), 127.76, 128.27, 128.70 (benzylic), 135.60 (C6), 134.84 (C4), 143.49 (C8), 150.43 (C13), 160.74 (C10), 165.61 (C9), 170.16 (C1). Found, %: C 55.21; H 3.71; N 2.87. $C_{21}H_{16}BrNO_6$. Calculated, %: C 55.04; H 3.52; N 3.06.

Crystal structure determination

The X-ray data for **4** and **8** were collected at room temperature on an Oxford Diffraction *Xcalibur-E* diffractometer equipped with CCD area detector and a graphite monochromator utilizing MoKα radiation. The final unit cell dimensions were obtained and refined on an entire data set. The structures were solved by direct methods using SHELX-97 program package [41] and refined with full-matrix least squares method with anisotropic thermal parameters for the non-hydrogen atoms.

In both structures the C(sp^2)-bound H atoms and methylene groups H atoms were placed in calculated positions and were treated using AFIX 43 and AFIX 23 instructions, respectively, and a model approximation with Uiso(H) = 1.2Ueq(C), the H atoms of methyl groups were found and refined using AFIX 137 instruction and Uiso(H) = 1.5Ueq(C). The figures were produced using MERCURY [38].

The X-ray data and the details of the refinement for **4** and **8** are summarized in Table 1.

Crystallographic data for new structures reported herein were deposited with the Cambridge Crystallographic Data Centre and allocated the deposition numbers CCDC 1053146 and CCDC 1053147. These data can be obtained free of charge from the Cambridge Crystallographic Data Centre via www.ccdc.cam.ac.uk/data_request/cif.

Table 1

Crystal and structure refinement data for structure of 4 and 8.

	4	**8**
Empirical formula	$C_{16}H_{15}NO_6$	$C_{17}H_{16}NO_6Br$
Formula weight	317.29	410.22
Temperature (K)	293(2)	293(2) K
Crystal system	*Monoclinic*	*Monoclinic*
Space group	$P2_1/n$	$P2_1/n$
Z	4	4
Unit cell dimensions		
a (Å)	11.4801(4)	9.5655(7)
b (Å)	8.4072(3)	18.1782(7)
c (Å)	15.5386(6)	11.0198(6)
α (deg)	90	90
β (deg)	96.723(3)	114.592(8)
γ (deg)	90	90
V (Å^3)	1489.41(9)	1742.4(2)
D_c(g/cm^{-3})	1.415	1.564
μ(mm^{-1})	0.110	2.392
F(000)	664	832
Reflections collected	4988/2607	6088/ 3067
Independent reflections	1852	2207
Data/restraints/parameters	2607 / 0 / 211	3067 / 0 / 229
Goodness-of-fit on F^2	1.000	1.000
R_1, $wR_2[I>2\sigma(I)]$	0.0347, 0.0826	0.0462, 0.1133
R_1, wR_2(all data)	0.0535, 0.0865	0.0727, 0.1252
Largest difference in peak and hole (e Å^{-3})	0.141 and -0.153	0.870 and -0.515

Acknowledgments

We thank the bilateral Moldova-Ukraine projects (Ref. No. 14.820.18.02.06/U and Ref. No. M/129-2014) for financial support.

References

1. Wright, A.D.; Nys, R.; Angerhofer, C. K.; Pezzuto, J.M.; Gurrath, M. Biological activities and 3D QSAR studies of a series of *Delisea pulchra* (cf. *fimbriata*) derived natural products. Journal of Natural Products, 2006, 69, pp. 1180-1187.
2. Mansoor, T.A.; Hong, J.; Lee, C.O.; Sim, C. J.; Im, K.S.; Lee, D.S.; Jung, J. H. New Cytotoxic Metabolites from a Marine Sponge *Homaxinella* sp. Journal of Natural Products, 2004, 67, pp. 721-724.
3. Grossmann, G.; Poncioni, M.; Bornand, M.; Jolivet, B.; Neuburger, M.; Sequin U. Bioactive butenolides from *Streptomyces antibioticus* TU¨ 99: absolute configurations and synthesis of analogs. Tetrahedron, 2003, 59, pp. 3237-3251.
4. Esmaili, A.A.; Bodaghi, A. New and efficient one-pot synthesis of functionalized γ-spirolactones mediated by vinyltriphenylphosphonium salts. Tetrahedron, 2003, 59, pp. 1169-1171.
5. Yavari, I.; Hossaini, Z.; Sabbaghan, M.; Ghazanfarpour-Darjani, M. Efficient synthesis of functionalized spiro-2,5-dihydro-1,2-γ-oxaphospholes. Tetrahedron, 2007, 63, 9423-9428.
6. Santos, M.M.M. Recent advances in the synthesis of biologically active spirooxindoles. Tetrahedron, 2014, 70, pp. 9735-9757.
7. Macaev, F.; Geronikaki, A.; Sucman, N. Recent application of isatins in synthesis of functionalized spirocyclic oxindoles. *In* Targets in heterocyclic systems. Chemistry and Properties. O. A. Attanasi D. Spinelli. Eds. Società Chimica Italiana: Pesaro-Urbino, 2011, Vol. 15, pp. 294-326.
8. Macaev F. Synthesis of spiroindolin-2-ones from 1*H*-indole-2,3-dione. Selected methods for synthesis and modification of heterocycles. The chemistry of synthetic indole systems. InterBioScreen press: Moscow, 2004, Vol. 3, pp. 75-102.
9. Millemaggi, A.; Taylor, R.J.K. 3-Alkenyl-oxindoles: Natural products, pharmaceuticals, and recent synthetic advances in tandem/telescoped approaches. European Journal of Organic Chemistry, 2010, 24, pp. 4527-4547.
10. Kumar, A., Chimni, S.S. Catalytic asymmetric synthesis of 3-hydroxyoxindole: a potentially bioactive molecule. RSC Advances, 2012, 2, pp. 9748-9762.
11. Aleman, J.; Cabrera, S. Application of asymmetric organocatalysis in medicinal chemistry. Chemical Society Reviews, 2013, 42, pp. 774-793.
12. Sucman, N.; Macaev, F. Process for obtaining of derivatives of carbonitril spirocyclopropanoxindoles. MD Patent, 2012, No. 4201 (in Romanian).
13. Sucman, N. Synthesis and properties of new spirocompounds. Ph.D. Thesis, Institute of Chemistry of ASM, Chisinau, Moldova, 2013 (in Russian).
14. Sucman, N.; Macaev, F. Process for obtaining of derivatives of carbomethoxy spirocyclopropanoxindoles. MD Patent, 2012, No. 4202 (in Romanian).
15. Marti, C.; Carreira, E.M. Construction of spiro[pyrrolidine-3,3-oxindoles]: recent applications to the synthesis of oxindole alkaloids. European Journal of Organic Chemistry, 2003, 12, pp. 2209-2219.
16. Singh, G.S.; Desta, Z.Y. Isatines as privileged molecules in design and synthesis of spiro-fused cyclic frameworks. Chemical Reviews, 2012, 112, pp. 6104-6155.
17. Chauhan, P.; Chimni, S.S. Organocatalytic asymmetric synthesis of 3-amino-2-oxindole derivatives bearing a tetra-substituted stereocenter. Tetrahedron: Asymmetry, 2013, 24, pp. 343-356.
18. Ball-Jones, N.R.; Badillo, J.J.; Franz, A.K. Strategies for the enantioselective synthesis of spirooxindoles. Organic and Biomolecular Chemistry, 2012, 10, pp. 5165-5181.
19. Hong L.; Wang, R. Recent advaces in asymmetric organocatalytic construction of 3,3'-spirocyclic oxindoles. Advanced Synthesis and Catalysis, 2013, 355, pp. 1023-1052.
20. Pellissier, H. Recent developments in asymmetric organocatalytic domino reactions. Advanced Synthesis and Catalysis, 2012, 354, pp. 237-294.
21. Liu, X.; Lin, L.; Feng, X. Amide-based bifunctional organocatalysts in asymmetric reactions. Chemical Communications, 2009, 41, pp. 6145-6158.
22. Duan, J.; Li, P. Asymmetric organocatalysis mediated by primary amines derived from cinchona alkaloids: recent advances. Catalysis Science and Technology, 2014, 4, pp. 311-320.
23. Phillips, A.M.F. Applications of carbohydrate-based organocatalysts in enantioselective synthesis. European Journal of Organic Chemistry, 2015, 33, pp. 7291-7303.
24. Shen, K.; Liu, X.; Lin, L.; Feng, X. Recent progress in enantioselective synthesis of C3-functionalized oxindoles: rare earth metals take action. Chemical Science, 2012, 3, pp. 327-334.
25. Cao, Z.Y.; Wang, Y.H.; Zeng, X.P.; Zhou, J. Catalytic asymmetric synthesis of 3,3-disubstituted oxindoles: diazooxindole joins the field. Tetrahedron Letters, 2014, 55, pp. 2571-2584.
26. Nakamura, S. Catalytic enantioselective decarboxylative reactions using organocatalysts. Organic and Biomolecular Chemistry, 2014, 12, pp. 394-405.

27. Mrowczynski, R.; Nan, A.; Liebscher, J. Magnetic nanoparticle-supported organocatalysts – an efficient way of recycling and reuse. RSC Advances, 2014, 4, pp. 5927-5952.
28. Dalpozzo, R.; Bartoli, G.; Bencivenni, G. Recent advances in organocatalytic methods for the synthesis of disubstituted 2- and 3-indolinones. Chemical Society Reviews, 2012, 41, pp. 7247-7290.
29. Dai, C.; Liang, B.; Stephenson, C.R.J. Expanding the chemical diversity of spirooxindoles via alkylative pyridine dearomatization. Beilstein Journal of Organic Chemistry, 2012, 8, pp. 986-993.
30. Gu, Y. Multicomponent reactions in unconventional solvents: state of the art. Green Chemistry, 2012, 14, pp. 2091-2128.
31. Radul, O.; Sucman, N.; Pogrebnoi, S.; Barba, A.; Geronikaki, A.; Macaev, F. Synthesis and antiviral activity of new thiazole, 1,2,4-triazol and oxindole derivatives. Chemistry Journal of Moldova, 2011, 6(1), pp. 101-109.
32. Noole, A.; Sucman, N. S.; Kabeshov, M.A.; Kanger, T.; Macaev, F.Z.; Malkov A.V. Highly enantio- and diastereoselective generation of two quaternary centers in spirocyclopropanation of oxindole derivatives. Chemistry: A European Journal. 2012, 18, pp. 14929-14933.
33. Gangadharan, R.; Sethusankar, K.; Kiruthika, S.E.; Perumal, P.T. Methyl 4-anilino-2′,5-dioxo-1′,2′-dihydro-5*H*-spiro[furan-2,3′-indole]-3-carboxylate. Acta Crystallographica Section E: Structure Reports Online, 2013, 69, o1055, doi:10.1107/S1600536813014967.
34. Gangadharan, R.; Kiruthika, S.E.; Sethusankar, K.; Perumal, P.T. Methyl 4-(4-bromoanilino)-2′,5-dioxo-5*H*-spiro[furan-2,3′-indoline]-3-carboxylate. Acta Crystallographica Section E: Structure Reports Online, 2014, 70, pp. o210-o211.
35. Zhang, Y.; Lu, Y.; Tang, W.; Lu, T.; Du, D. Cooperative *N*-heterocyclic carbene (NHC)/Lewis acid-mediated regioselective umpolung formal [3+2] annulations of alkynyl aldehydes with isatins. Organic and Biomolecular Chemistry, 2014, 12, pp. 3009-3015.
36. Li, J.; Liu, Y.; Li, C.; Jie, H.; Jia, X. Atom-economical synthesis of the functionalized spirocyclic oxindole-butenolide via three-component [2+2+1] cycloaddition strategy. Green Chemistry, 2012, 14, pp. 1314-1321.
37. Macrae, C. F.; Edgington, P. R.; McCabe, P.; Pidcock, E.; Shields, G. P.; Taylor, R.; Towler, M.; van de Streek, J. Mercury:Visualization and Analysis of Crystal Structures. Journal of Applied Crystallography, 2006, 39, pp. 453-457.
38. Xu, S.; He, Z. Recent advances in stoichiometric phosphine-mediated organic synthetic reactions. RSC Advances, 2013, 3, pp. 16885-16904.
39. Macaev, F.Z; Sucman, N.S.; Boldescu, V.V. Selective transformation of isatinsintosubstituted 2-oxindoles. Russian Chemical Bulletin, International Edition, 2014, 63, pp. 15-25.
40. Macaev, F.Z.; Radul, O.M.; Shterbet, I.N.; Pogrebnoi, S.I.; Sucman, N.S.; Malinovskii, S.T.; Barba, A.N., Gdaniec, M. Synthesis and structure of new oxoindoles. Chemistry of Heterocyclic Compounds, 2007, 43, pp. 298-305.
41. Sheldrick, G. M. A short history of SHELX**.** Acta Crystallographica, 2008, A64, pp. 112-122.

AN INVESTIGATION OF THE PROTONATION STATES OF HUMAN LACTOFERRIN IRON-BINDING PROTEIN

Lilia Anghel

Institute of Chemistry of Academy of Sciences of Moldova, 3, Academiei str., Chisinau MD-2028, Republic of Moldova
e-mail: anghel.lilia@gmail.com

Abstract. In this study, the protonation states of ionizable groups of human lactoferrin in various conformations were investigated theoretically, at physiological pH (7.365). These calculations show that the transition of the protein from a conformation to another one is accompanied by changes in the protonation state of specific amino acid residues. Analysis of the pK_a calculatons underlined the importance of participation of two arginines and one lysine in the opening / closing of the protein. In addition, it was found that the mechanism of iron release depends on the protonation state of TYR-192. Protonated state of this residue in the closed form of lactoferrin will trigger the opening of protein and release of iron ions.

Keywords: lactoferrin, ionizable residues, protonation, continuum electrostatics.

Received: May 2014/ Revised final: March 2015/ Accepted: April 2015

Introduction

Human lactoferrin is an iron-binding glycoprotein member of the transferrin family. This protein was firstly isolated from milk, where it was found in elevated concentrations. Later, according to Steijns and Hooijdonk [1], this protein was identified in various products of exocrine glands located in the gateways of respiratory, digestive and reproductive systems suggesting a role in the defense against invading pathogens.

The high affinity of lactoferrin for iron determines a great part of its biochemical properties. Iron is an essential element for life and is used by microorganism to survive and replicate [2]. It is also a key element for many pathogenic microorganisms. The iron uptake by lactoferrin will make this element inaccessible for pathogenic microorganisms, preventing them from further development. In unbounded state, iron catalyses the reaction of formation of free radicals [3]. In a living organism, free radicals will generate many other harmful biochemical processes [4]. Thus, iron acquisition by lactoferrin has an indirect role in the protection of living organism from oxidative stress.

Lactoferrin molecules reversibly bind ferric ions and therefore they can be found in the iron-free form (apolactoferrin) and associated with iron ions (hololactoferrin). Apolactoferrin has an open conformation whilst hololactoferrin has a closed conformation (see Figure 1).

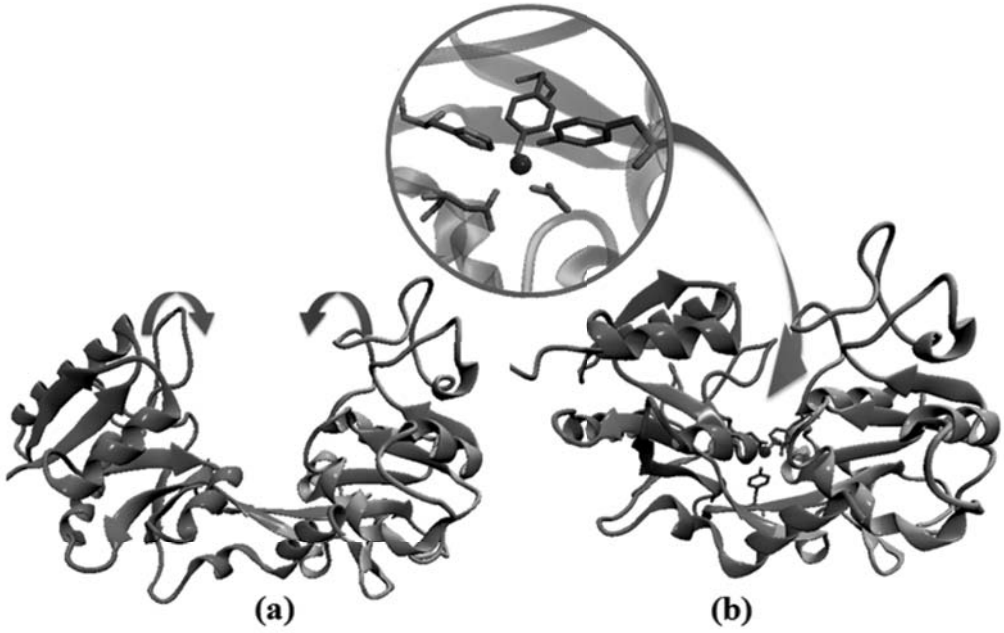

Figure 1. Graphical representation of the N-lobe of human lactoferrin open form (a) and closed holo-form (b). The position of carbonate and iron ions in the closed form are indicated. N-lobe structure is presented in ribbon, ferric ion is presented as van der Waals sphere and carbonate ion as sticks.

The X-ray crystallographic structure of this glycoprotein, 1B0L Protein Data Bank (PDB) code [5], consists of a polypeptide chain of 691 amino acid residues. Its structure is folded in two globular lobes referred as N-(residues 1-333) and C-(residues 345-691) lobes connected with a short helical peptide chain (residue 334-344). Each lobe is further divided into domains (NI and NII and CI and CII). Both lobes are able to bind one ferric ion. The iron binding sites are similar in both lobes and among members of transferrin family. The coordination of a ferric ion is produced via one carboxylate oxygen, two phenolate oxygens and one imidazole nitrogen from one aspartate, two tyrosines and one histidine, respectively. Ferric ion is stabilized in the protein binding site through two oxygens from carbonate ion. X-ray high-resolution structures of lactoferrins [5-9] isolated from various species show a high degree of similarity, approximately 70% identity between their structures. And each of the family members has a high degree of internal similarity ~ 40% of sequence identity between N-lobe and C-lobe [10, 11].

Experimental evidence [12] has shown that lactoferrin molecule binds tightly ferric ions and retains them until ~pH 3.0 this suggests that conformational changes induced by iron binding and release are pH sensitive processes. Thus, investigation of the titratable residues from the lactoferrin structure is an important step in the studies of the mechanistic aspects of iron binding and release by lactoferrin protein molecules. The goal of this study is to compare the protonation states of ionizable groups of human lactoferrin in various conformations at the same pH value. This should allow the identification of the key residues from the protein structure involved in the process of iron-binding.

Methods and computational details

Structure and biochemical properties of proteins depend critically on the protonation state of ionizable groups of protein residues. Thus, various theoretical methods to determine ionization constants of residues in proteins through pK_a calculations have been developed. In the present study, the pK_a calculations were performed using H++ web server [13-15]. Bashford and Karplus [16] described the basic methodology that H++ relies upon. The method consists in pK_a calculations for relevant ionizable groups in the system based on continuum electrostatic model within the framework of the Poisson Boltzmann model [17, 18]. According to the continuum electrostatic model, the protein is assumed to have a structure and is modeled as low dielectric region, which is embedded in a high dielectric region that represents the solvent. Atoms from the protein structure are considered as fixed-point charges, which are used to represent the charge of amino acids. The mathematical model of this concept is presented elsewhere [19].

The X-ray high-resolution crystallographic structures of open apolactoferrin and closed hololactoferrin were used as starting structures for the pK_a calculations. These structures had the Protein Data Bank codes of 1LFH [20] determined at 2.80 Å resolution and 1B0L [5] determined at 2.20 Å resolution, respectively. All water molecules present in both PDB structure files were removed, according to the protocol for conducting computational experiments using H++ server [13].

pK_a calculations were conducted for typical physiological conditions, pH 7.365 and an ionic strength of 150 mM. Dielectric constants of 4.0 and 80.0 were used for protein and solvent (water), respectively. The PDB structures were initially protonated using AMBER force field [21] assuming pH of 7.365. Protonation state of histidine was automatically deduced from the van der Waals and hydrogen bond pattern in crystal structure of lactoferrin.

Visual Molecular Dynamics Software (VMD) is a molecular visualization program for displaying, animating, and analyzing large biomolecular systems using 3-D graphics and built-in scripting [22]. The graphical representation depicted in Figure 1 was generated using VMD.

Results and discussion

Metal binding capacity of proteins is influenced by intramolecular electrostatic interactions. The electrostatic interactions within a protein molecule are induced by ionization (protonation) states of titratable groups of the amino acids present in the protein structure. The latter will depend on the group type, location within the protein molecule, ionization state of other titratable sites in the proximity and the pH and ionic strength of the surrounding solvent [13]. Investigation of the ionizable residues of human lactoferrin and determination of key residues that trigger the conformation changes during the iron binding and release were performed using pK_a calculations.

Table 1 summarizes the measured pK_a values for the ionizable groups of human lactoferrin in four conformations at physiological pH. Only those residues for which there is a difference greater than one pK unit between any two of the models are listed in Table 1.

The protonation probability $\langle x \rangle$ (see Eq.(1)) of an isolated amino acid site is algebraically equivalent to the Henderson-Hasselbalch (HH) equation [23, 24] which describes the sigmoidal standard titration curve:

$$\langle x \rangle = \frac{10^{pKa - pH}}{1 + 10^{pKa - pH}} \quad (1)$$

In this case, pK_a value is equal to the pH at which the protonation probability of the amino acid site is ½. Therefore, the so-called $pK_{1/2}$ values are often used to describe the titration behavior. The $pK_{1/2}$ values are not directly related to the free energy of the proton uptake and therefore in the case when titration curves are not monotonic these values can be ill-defined [23]. Lactoferrin polypeptide contains 691 amino acid residues and therefore most of the titration curves of its amino acid sites will have nonsigmoidal shapes because of the multitude of intramolecular interactions. For a better assessment of the protonation state of lactoferrin molecule in various conformations, the intrinsic pK_a value was taken into account; this is the pK_a value that a specific amino acid site would have if all other titratable sites were in the reference state.

Data have been collected for the open apo-form of human lactoferrin. For the comparison, the pK_a values for the same groups measured in the closed apo-form (the holo-form with iron and carbonate ions removed), closed apo-form with iron ions only and holo-form (with both carbonate and iron ions). In the X-ray high-resolution crystallographic structure of open lactoferrin (1LFH PDB entry), only N-lobe is open whilst C-lobe is closed, therefore further only residues from the N-lobe will be discussed as they could provide the necessary information about the protein conformation changes.

ASP-60 has a lower pK_a value in all closed conformations. According to the structural information from the PDB file, ASP-60 has a hydrogen bond with LYS-301 in the open conform, in the closed conformation this bond is missing, this might explain these pK_a shifts (ΔpK_a).

At physiological pH tyrosines are deprotonated in the closed conformations except TYR-92, which has a relative stable protonation state in all conformations, and TYR-192 which is protonated in the closed conformations. TYR-192 has a lower pK_a value in the open form and elevated pK_a values in all closed conformations. This indicates that deprotonated TYR-192 will favor the iron binding whilst protonated TYR-192 state will trigger the iron release. Protonated state of TYR-192 in the closed models is mostly caused by interactions with the residue ASP-60.

Table 1

pK_a values calculated for various conformations of human lactoferrin.

	pK_a			
Residue	*a*	*b*	*c*	*d*
GLU-51	6.973	5.318	5.296	5.293
*ASP-60	3.154	-0.405	-0.055	0.020
TYR-65	14.139	12.972	12.986	12.977
TYR-72	12.500	11.444	11.436	11.434
GLU-80	3.016	4.147	3.967	3.980
ARG-89	11.040	9.989	9.696	9.722
HIS-91	4.670	4.387	3.462	3.476
*TYR-92	12.218	12.034	12.615	12.857
ARG-121	8.169	3.781	3.781	3.667
ARG-133	16.499	11.879	11.946	11.936
LYS-163	9.867	7.833	7.826	7.815
ARG-171	14.304	11.913	11.908	11.908
*TYR-192	9.463	12.315	13.265	13.687
ARG-210	9.781	5.317	5.945	6.065
GLU-211	5.808	4.472	4.741	4.806
ARG-224	11.022	12.412	12.408	12.349
TYR-227	16.134	14.127	14.145	14.152
LYS-237	8.276	9.728	9.727	9.708
LYS-243	10.328	9.117	7.868	7.868
*HIS-253	2.371	-2.260	-1.762	-1.662
ARG-258	14.548	10.862	10.821	10.824
ASP-297	2.468	3.987	3.625	3.616
LYS-301	7.727	4.980	4.634	4.676
ASP-315	2.828	4.931	4.927	4.929

a – pK_a values computed for open apo-form of human lactoferrin;

b - pK_a values computed for closed apo-form (the holo-form with iron and carbonate ions removed);

c - pK_a values computed for closed apo-form with iron ions only;

d - pK_a values computed for holo-form (with both carbonate and iron ions).

** amino acids involved in iron coordination.*

At physiological pH, amino acid HIS-253 was found to have low pK_a values in all protein conformations. In all closed forms pK_a value shifts downwards with 4 *pK* units. According to PDB structure files, protein closure creates an environment that induces a deprotonation of histidine through electrostatic interactions with the amino acids from its proximity.

LYS-301 also undergoes a pK_a shift in the transition from the open to the closed form of lactoferrin, indicating that the side chains of this amino acid undergo electrostatic interactions with other amino acids in the proximity.

All arginine residues, ARG-121, ARG-133, ARG-171, ARG-258 have elevated pK_a in the open form, and lower pK_a in all closed conformations. In comparison to other arginines, ARG-121 and ARG-210 suffer great *pK* shifts ($\Delta pK_a \approx 4$) in the transition from the open conformation to the closed at physiological pH, indicating on their importance in the process of iron binding.

Figure 2 presents the plot of the total charge of the open and closed conformations of lactoferrin molecules as a function of pH. The curves present typical shapes characteristic to the proteins of the transferrin family. As it is depicted in Figure 2, lactoferrin is a basic, positively charged protein with an isoelectric point of 9.48 (open apo-form) and 9.78 (closed holo-form). Experimentally determined isoelectric point for human lactoferrin varies between 8.40 and 9.00 [25, 26], this is in reasonable agreement with the computed values, confirming the correctitude of the pK_a calculations.

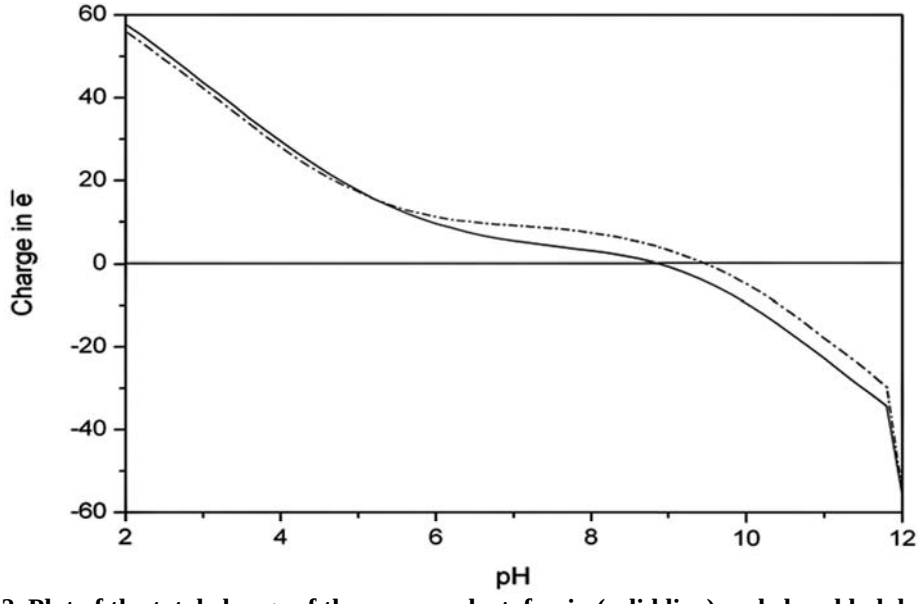

Figure 2. Plot of the total charge of the open apolactoferrin (solid line) and closed hololactoferrin (dashed line) as a function of pH.

Conclusions

Human lactoferrin reversibly binds ferric ions, involving conformation changes of the protein state. Due to large intramolecular interactions, transition of the protein from the open to the closed form is accompanied by changes in the protonation states of protein residues. A continuum electrostatic model within the framework of the Poisson Boltzmann model was applied to investigate the protonation state of the protein residues at physiological pH in various protein conformations. These calculations confirm that the transition of the protein from a conformation to another is accompanied by changes in the protonation state of specific amino acid residues. In this sense, it was underlined the importance of participation of amino acids ARG-121, ARG-210, LYS-301 in the opening / closing of the protein. They also provided details about the mechanism of iron release, pointing on the importance of the protonation state of TYR-192. Protonated state of this residue in the closed form of lactoferrin will trigger the opening of protein and release of iron ions.

Acknowledgements

I would like to acknowledge gratefully the supervision of Acad. Gheorghe Duca through each stage of my research.

I gratefully acknowledge the Program of the Romanian Plenipotentiary at JINR-Dubna (projects No.81/18.02.2013-37 and No.95/17.02.2014-26 within the JINR Theme No.04-4-1069-2009/2014) and the Moldovan State Programs (project No. 14.518.02.05A) for support.

References

1. Steijns, J.M.; van Hooijdonk, A.C.M. Occurrence, structure, biochemical properties and technological characteristics of lactoferrin. British Journal of Nutrition, 2000, 84(1), pp. S11-S17.
2. Duca, Gh. Homogeneous Catalysis with Metal Complexes: Fundamentals and Applications. Springer Series in Chemical Physics: Berlin Heidelberg, 2012, XII, 478 p.
3. Duca, Gh.; Scurlatov, Yu.; Sychev, A. Redox Catalysis and Ecological Chemistry, Publishing Centre M.S.U.: Chisinau, 2002, 316 p.
4. Duca, Gh.; Secara, N. The free radicals in biological systems: formation and protection mechanisms. AKADEMOS: Journal of Science, Innovation, Culture and Art, 2010, 4(19), pp. 115-118.
5. Sun, X.L.; Baker, H.M.; Shewry, S.C.; Jameson, G.B.; Baker, E.N. Structure of recombinant human lactoferrin expressed in *Aspergillus awamori*. Acta Crystallographica, Section D, 1999, 55, pp. 403-407.
6. Karthikeyan, S.; Yadav, S.; Paramasivam, M.; Srinivasan, A.; Singh, T.P. Structure of buffalo lactoferrin at 3.3 A resolution at 277 K. Acta Crystallographica, Section D, 2000, 56, pp. 684-689.
7. Moore, S.A.; Anderson, B.F.; Groom, C.R.; Haridas, M.; Baker, E.N. Three-dimensional structure of diferric bovine lactoferrin at 2.8 Å resolution. Journal of Molecular Biology, 1997, 274, pp. 222-236.
8. Kumar, P.; Khan, J.A.; Yadav, S.; Singh, T.P. Crystal structure of equine apolactoferrin at 303 K providing further evidence of closed conformations of N and C lobes. Acta Crystallographica, Section D 2002, 58, pp. 225-232.
9. Khan, J.A.; Kumar, P.; Srinivasan, A.; Singh, T.P. Protein intermediate trapped by the simultaneous crystallization process. Crystal structure of an iron-saturated intermediate in the Fe^{3+} binding pathway of camel lactoferrin at 2.7 Å resolution. The Journal of Biological Chemistry, 2001, 276, pp. 36817-36823.
10. Baker, E.N.; Baker, H.M. Molecular structure, binding properties and dynamics of lactoferrin. Cellular and Molecular Life Sciences, 2005, 62, pp. 2531-2539.
11. Anghel, L. Lactoferrin: analysis of the structure profile. Chemistry Journal of Moldova, 2014, 9(2), pp. 99-106.
12. Baker, E.N.; Baker, H.M. Lactoferrin and iron: structural and dynamic aspects of binding and release. BioMetals, 2004, 17, pp. 209-216.
13. Gordon, J.C.; Myers, J.B.; Folta, T.; Shoja, V.; Heath, L.S.; Onufriev, A. H++: a server for estimating pK_as and adding missing hydrogens to macromolecules, Nucleic Acids Research, 2005 1(33), pp. W368-W371.
14. Myers, J.; Grothaus, G.; Narayanan, S.; Onufriev, A. A simple clustering algorithm can be accurate enough for use in calculations of pKs in macromolecules, Proteins, 2006, 63, pp. 928-938.
15. Anandakrishnan, R.; Aguilar, B.; Onufriev, A.V. H++ 3.0: automating pK prediction and the preparation of biomolecular structures for atomistic molecular modeling and simulation, Nucleic Acids Research, 2012, 40(W1), pp. W537-W541.
16. Bashford, D.; Karplus, M. pKa of Ionizable Groups in Proteins: Atomic Detail from a Continuum Electrostatic Model. Biochemistry, 1990, 29, pp. 10219-10225.
17. Georgescu, R.; Alexov, E.; Gunner, M. Combining Conformational Flexibility and Continuum Electrostatics for Calculating pK_as in Proteins. Biophysical Journal, 2002, 83, pp. 1731-1748.
18. Leimkuhler, B.; Chipot, C.; Elber, R.; Laaksonen, A.; Mark, A.; Schlick, T.; Schutte, C.; Skeel, R, Eds. New Algorithms for Macromolecular Simulation. Springer: Berlin Heidelberg, 2006, pp. 263-295.
19. Ullmann, G.M.; Kloppmann E.; Essigke, T.; Krammer, E.-M. Klingen, A.S.; Becker, T.; Bombarda, E. Investigating the mechanism of photosynthetic proteins using continuum electrostatics. Photosynthetic resources, 2008, 97, pp. 33-53.
20. Norris, G.E.; Anderson, B.F.; Baker, E.N. Molecular replacement solution of the structure of apolactoferrin, a protein displaying large-scale conformational change. Acta Crystallographica, Section B, 47, pp. 998-1004.
21. Ponder, J.W.; Case, D.A. Force fields for protein simulations. Advances in Protein Chemistry, 2003, 66, pp. 27-85.
22. Humphrey, W.; Dalke, A.; Schülten, K. VMD - Visual Molecular Dynamics. Journal of Molecular Graphics, 1996, 14, pp. 33-38.
23. Onufriev, A.; Case, D.A.; Ullmann, G.M. A Novel View of pH Titration in Biomolecule, Biochemistry, 2001, 40(12), pp. 3413-3419.
24. Cantor, C.R.; Schimmel, P.R. Biophysical Chemistry. Part III. The Behavior of Biological Macromolecules, W. H. Freeman and Co., New York, 1980, 597 p.
25. Farnaud, S.; Evans, R.W. Lactoferrin-a multifunctional protein with antimicrobial properties. Molecular Immunology, 2003, 40, pp. 395-405.
26. Moguilevsky, N.; Retegui, L.A.; Masson, P.L. Comparison of human lactoferrins from milk and neutrophilic leucocytes. Biochemical Journal, 1985, 229, pp. 353-359.

OXIDATION AND CHARACTERIZATION OF ACTIVE CARBON AG-5

Tatiana Goreacioc

Institute of Chemistry of Academy of Sciences of Moldova, 3, Academiei str., Chisinau MD-2028, Republic of Moldova
Institute of Ecology and Geography of Academy of Sciences of Moldova, 1, Academiei str., Chisinau MD-2028, Republic of Moldova,
e-mail: araputatiana@yahoo.com

Abstract. The surface chemistry of the commercial active carbon AG-5 has been modified by oxidation with concentrated nitric acid. The structural changes caused by oxidative treatment were estimated on the basis of nitrogen adsorption-desorption isotherms and thermal analysis. Boehm titration method and infrared spectral analysis have been used in order to evaluate surface chemistry characteristics of active carbon samples. After oxidation process the amount of total acidic groups on oxidized active carbon surface (AG-5ox) increases by about 6 times in comparison with unmodified sample (AG-5). The concentration of the acidic groups on the oxidized active carbon surface (AG-5ox) was in the following order: strong acidic >>> weak acidic > phenolic.

Keywords: active carbon, oxidation, surface properties, thermal analysis, infrared spectroscopy.

Received: August 2014/ Revised final: October 2014/ Accepted: October 2014

Introduction

For the treatments of drinking and waste waters, packed beds of granular activated carbon are frequently used. The type of contaminant which will be adsorbed and the adsorption/removal efficiency of the active carbons are strongly dependent on their both porous structure and surface chemistry [1-4]. Therefore, the surface chemical modification of active carbons is of great interest in order to produce materials for specific applications. This modification has been mainly carried out by oxidative methods, producing a more hydrophilic structure with a large number of oxygen-containing groups [5]. Various reagents have been used as oxidants: nitric acid, hydrogen peroxide, sodium hypochlorite, permanganate, transition metals etc. [5-10]. A review of the literature concerning oxidation of the active carbons shows, that using nitric acid as oxidizing agent provides strong acidic functional groups on the carbon surface [6, 11-13].

In order to minimize operational problems during the water treatment processes, attention must be given to the size of the granular active carbon particles. The large particles have a small external surface area and long internal diffusion path lengths [14]. This reduces the mass transfer velocity, resulting in long adsorption/removal processes of pollutants from waters.

The aim of this work was to modify the surface chemistry of the commercial granular active carbon AG-5, using the concentrated nitric acid as oxidizing agent. In order to characterize unmodified and oxidized active carbon samples, the standard test methods for evaluation of physical properties (particle size distribution and bulk density), physical-chemical characteristics (elemental analysis, thermal analysis, nitrogen adsorption measurements) and surface chemistry characteristics (pH of surface, Boehm titration method and IR spectral analysis) have been used.

Experimental

Materials

In this study commercially available granular activated carbon AG-5 (GOST 20777-75) has been used. Activated carbon AG-5 is obtained from pit coal by steam activation representing granules of cylindrical shape [15]. All the chemical reagents used in this study were of analytical grade.

Sample oxidation method

The oxidation was carried out as follows: the solution of concentrated nitric acid (63%) was added to 400g of granular active carbon AG-5 (at a ratio of solid:liquid of 1:3), which was placed in the glass flask on the water bath. The flask was connected with reflux condenser ended with absorption bulb filled with the NaOH solution. The carbon-nitric acid mixture was kept at the temperature of 95 ºC for 8 h. The released nitrogen oxides were absorbed in the absorption bulb. After finishing the oxidation process the mixture was cooled and decanted. The humic acids formed during oxidation processes have been removed with 1.0 N solution of KOH. After removal of humic acids the oxidized active carbon sample has been treated with 1.0 N solution of HCl in order to neutralize residual KOH and to obtain the H^+ form of oxidized active carbon.

Afterwards, the oxidized sample was extensively washed with distilled water until chlorine ions have not been detected in the washing water, dried at 110±5ºC and labelled as AG-5ox.

Characterization methods

Prior characterization measurements the active carbon samples were dried at 110±5ºC for 3 h.

Physical characteristics

Particle size is an important property influencing the flow characteristics, adsorption kinetics and catalytic behaviour of granular activated carbon layers. The granular active carbon samples were separated according to particle size using a set of standard sieves with decreasing size opening (in mm). The results are given in weight percent for those particles between different sieves expressed as particle size [16].

The *bulk density* is defined as the mass of a unit volume of the sample in air, including both the pore system and the voids between the particles. The bulk density (D_b) is given in g/cm^3 and determined by Eq.(1) [16]:

$$D_b = \frac{m}{V} \quad (1)$$

where, *m*- mass of the dry sample in g;

V- volume of the sample, measured under test condition in cm^3.

Physical-chemical characteristics

Elemental analysis (C, H, N) was carried out by the Elemental Analysis group of the Institute of Chemistry of the Academy of Sciences of Moldova.

The *content of metals* was determined by atomic absorption spectroscopy (AAS-1N).

The *surface area, pore volumes and pore size distributions* of the carbons were performed on a surface area analyzer (Autosorb 1-MP) through N_2 adsorption-desorption at 77 K after outgassing the samples at 250 ºC to a residual vacuum 10^{-5} Pa [17]. Surface area (S_{BET}) was measured by the BET (Brunauer-Emmet-Teller equation) method. Pore size distribution was determined by the Non-Local Density Functional Theory (NLDFT) method assuming slit pore geometry. The total pore volume (V_{total}) was deduced from the manufacturer's software [18]. Micropore volume (V_{micro}) was calculated using Dubinin Radushkevich (DR) method. Mesopore volume (V_{meso}) was determined by the subtraction of the V_{micro} from the V_{total}.

Thermal analysis measurements were performed using a Derivatograph Q-1000 analyzer. The samples were heated from room temperature up to 1000 °C in air at a heating rate of 10 °C/min.

Surface chemistry characteristics

The *pH of the active carbon surface* has been evaluated by determination of pH value of active carbon suspension (0.4 g of dried sample/20 mL of distilled water) equilibrated for 24 h [19].

The *quantification of the surface functional groups* have been done by selective neutralization technique of Boehm [20]. According to this method, carbon sample (0.5g) was equilibrated with 50 mL of each of three bases 0.05N $NaHCO_3$, Na_2CO_3, NaOH, sealed and shaken for 72 h, and then 10 mL of each filtrate was back-titrated with 0.05N HCl. The surface concentrations of each acidic groups: strong-carboxyl, weak-carboxyl and phenolic; have been determined by differences between the amounts reduced by each of the bases [11]. The total basic surface oxides have been determined with a similar titration technique using 0.05 N HCl and back-titrating with 0.05 N NaOH. Titrations have been done using automated titrator TitroLine®6000 (SI Analytics, Germany).

The concentrations of surface acidic groups (N^A, meq/g) have been calculated by Eq.(2):

$$N^A = \frac{(C_0 - C_e)V}{m} \quad (2)$$

where, C_0 and C_e are initial and equilibrium concentrations of bases $NaHCO_3$, Na_2CO_3, NaOH;

V – volume of bases added to active carbon sample, in mL;

m- mass of active carbon sample, in g.

The quantity of the basic functional groups (N^B, meq/g) has been calculated by Eq.(3):

$$N^B = \frac{(C_0 - C_e)V}{m} \quad (3)$$

where, C_0 and C_e are initial and equilibrium concentrations of HCl;

V – volume of HCl added to active carbon sample, in mL;

m- mass of active carbon sample, in g.

The *Fourier Transform Infrared spectra* (*FTIR)* of the active carbons were recorded in the range 400 – 4000 cm^{-1} using a Fourier Transform Infrared Spectrometer (PerkinElmer, Spectrum 100, USA). Prior to spectral analysis the samples were dried and the dilutions in KBr have been used (0.15wt%).

Results and discussion

Physical characteristics

The particle size distribution evaluated by sieve analysis is presented in Figure 1. For both samples, initial granular active carbon AG-5 and modified by oxidation AG-5ox, the size fraction between 1.3 and 2.0 represents about 65% of total weight. For further experiments the size fraction between 0.8 and 2.0 mm was chosen.

The bilk density has been determined only for the size fraction 0.8÷2.0mm, which was selected for further experiments. After oxidation process the bulk density of active carbon AG-5ox decreases with about 4%, it can be explained by removal of soluble inorganic (ash) with nitric acid (Table 1).

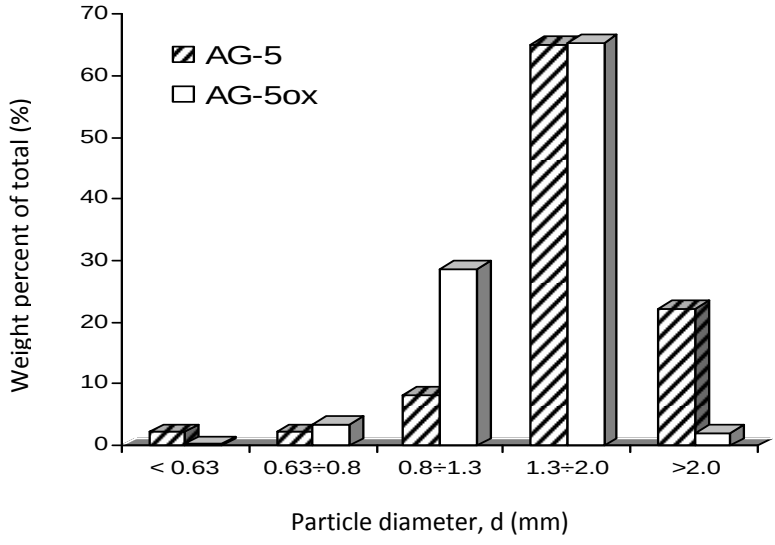

Figure 1. Weight percent of different size fractions of the initial granular active carbon AG-5 and modified by oxidation AG-5ox.

Table 1

The bulk density of size fraction 0.8÷2.0mm for initial and oxidized active carbon samples.

Sample	*Characterization*	*Bulk density D_b, g/cm³*
AG-5	initial	<0.578> ±0.005
AG-5ox	oxidized with nitric acid	<0.553> ±0.004

Physical-chemical characteristics

The elemental analysis, the metals and ash content for studied active carbon samples, are presented in Tables 2 and 3. The initial active carbon AG-5 contains about 16.6% ash, while after oxidation with nitric acid this value decreased to ca. 6% (Table 2). Similar results have been obtained by Jaroniec et al. during oxidation of AG-5 active carbon with concentrated nitric acid [21]. After oxidation process most of the metals are removed from the active carbon sample (Table 3).

Table 2

Proximate and ultimate analyses of active carbon samples.

Sample	*Ash (wt%)**	*Ultimate analysis (wt%, daf**)*				
		C	*H*	*S*	*N*	*O****
AG-5	16.60	80.24	2.73	1.37	-	15.66
AG-5ox	5.93	77.73	2.92	-	0.32	19.03

**Ash content has been determined from thermo-gravimetric analysis (TGA) curve at 1000ºC*

***Determined on dry and ash free basis*

****By difference*

Table 3

Analyses of mineral matters in active carbon samples.

Sample	*Ash (wt%)*	*Constituents in mineral matter (wt%)*								
		Na_2O	*K_2O*	*CaO*	*MgO*	*Fe_2O_3*	*MnO_2*	*CuO*	*Cr_2O_3*	*NiO*
AG-5	16.60	0.40	1.49	1.11	0.41	5.63	0.04	0.03	-	0.01
AG-5ox	5.93	0.03	1.08	-	0.01	0.18	-	-	-	-

Nitrogen adsorption isotherms and pore size distribution curves for studied samples are shown in Figures 2 and 3. Both samples exhibit microporous structure. The porous structure parameters calculated from nitrogen adsorption isotherms are presented in Table 4. As can be seen, the values of the BET surface area (S_{BET}), total pore volume (V_{total}) and micropore volume (V_{micro}) slightly increase after oxidation treatment with about 14-16% (Table 4).

The impact of nitric acid on porous structure of the active carbon AG-5 is quite different described in the literature. Some authors have been reported an increase of total pore volume after oxidation of AG-5 with nitric acid, while other authors have been presented opposite results, degradation of porous structure and decrease of structural parameters values over 50% [6, 12, 13, 21]. In our case, we suggest, the slight increase of structural parameters values after oxidation process is due to dissolution of inorganic species that may block the entrance of micropores.

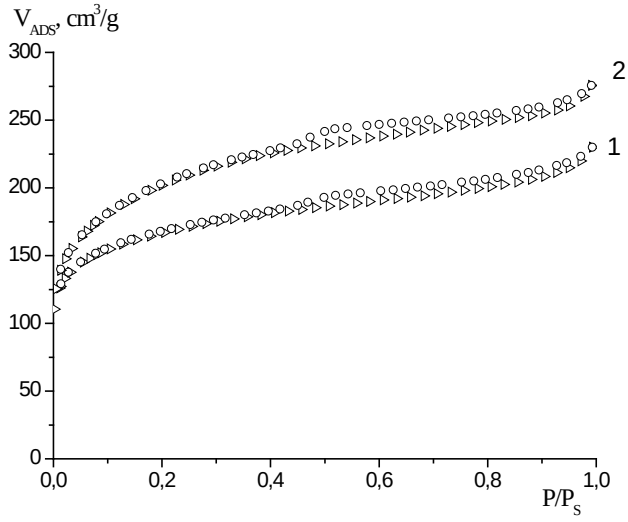

Figure 2. Adsorption and desorption isotherm of nitrogen at 77K for initial active carbon AG-5 (1) and oxidized sample AG-5ox (2).

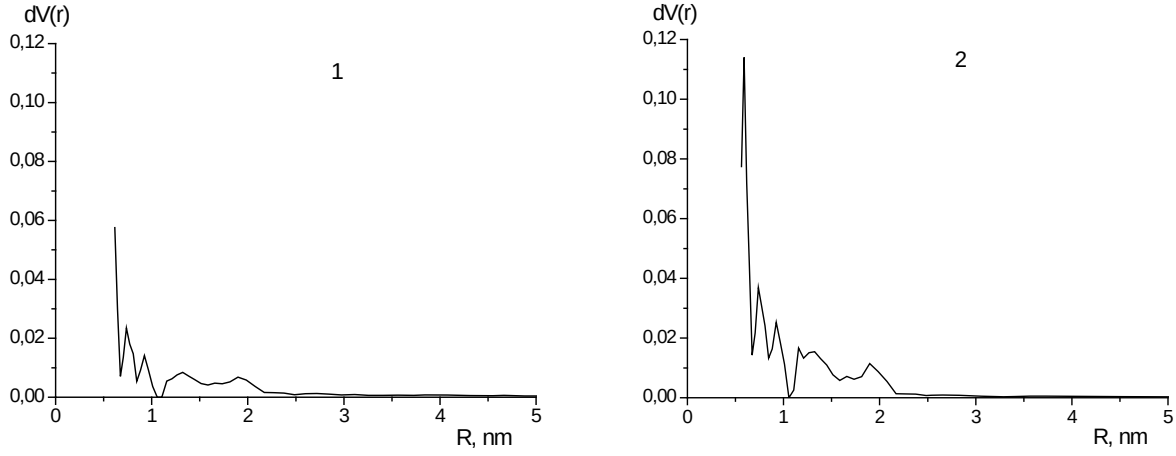

Figure 3. Pore size distribution using NLDFT method for active carbon samples: (1)- AG-5; (2)- AG-5ox.

Table 4

Parameters of porous structure determined from nitrogen adsorption isotherms.

Sample	S_{BET}, m^2/g	V_{total}, cm^3/g	V_{meso}, cm^3/g	V_{micro}, cm^3/g	R_{micro}, *nm*	E_{micro}, *kJ/mol*
AG-5	611	0.36	0.09	0.27	1.08	12.07
AG-5ox	717	0.43	0.11	0.32	1.11	11.72

S_{BET} – surface area determined by Brunauer-Emmet-Teller equation;
V_{total} – total pore volume;
V_{meso} - mesopore volume;
V_{micro} – micropore volume;
R_{micro} – average micropore radius;
E_{micro} – adsorption energy in micropores.

Thermo-gravimetric analysis (*TGA*) and derivative thermo-gravimetric (*DTG*) curves of active carbon samples are presented in Figures 4 and 5. *TGA* curve of the oxidized sample AG-5ox differs from that of unmodified sample AG-5, which indicates that the oxidation with concentrated nitric acid has changed not only the surface properties, but also destroyed the active carbon structure making its decomposition much easier. *TGA* and *DTG* curves of the two samples show an initial weight loss around 100 ºC, which is related to thermodesorption of physically adsorbed water [13, 21, 22]. The weight loss at 250 ºC is presented only on the *DTG* profile of the oxidized sample (AG-5ox) being attributed by many researchers to the decomposition of carboxylic surface groups [23-25]. Till around 400 ºC the decomposition of lactonic and phenolic groups takes place [23-25] and then the active carbon sample buns out (Figure 5). The unmodified sample, AG-5, is much more thermally stable in comparison with oxidized sample (Figure 4). The *DTG* profile of this sample does not present any significant weight loss until 450 ºC. Both samples present ash content at 1000 ºC much high for AG-5, about 16% (Figure 4).

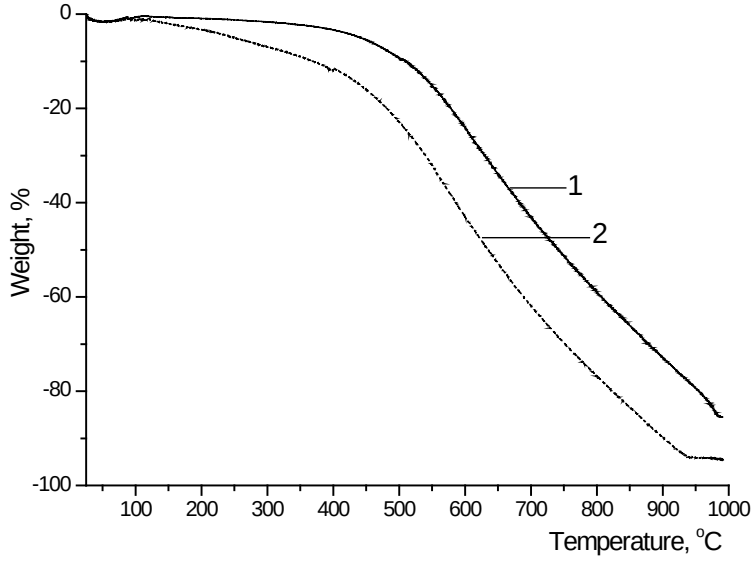

Figure 4. TGA curves measured in air for unmodified AG-5 (1) and oxidized AG-5ox (2) samples.

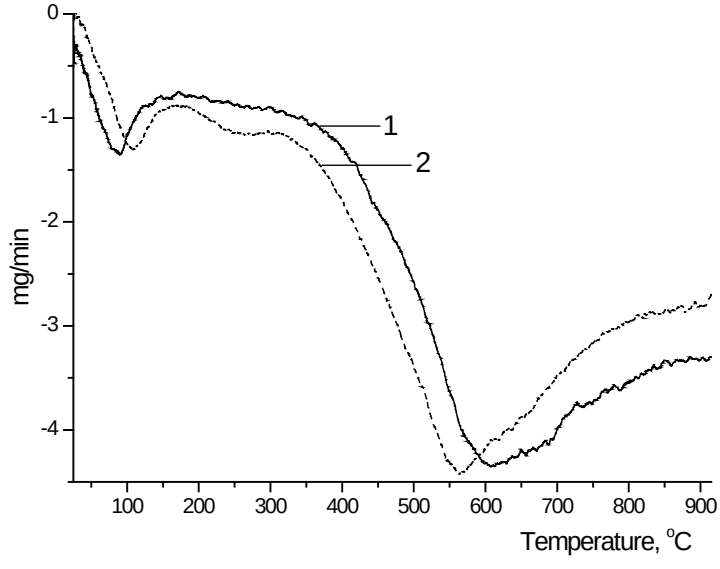

Figure 5. DTG curves for unmodified AG-5 (1) and oxidized AG-5ox (2) samples.

Surface chemistry characteristics

The surface properties of the active carbons were evaluated by pH of the carbon surface, Boehm titration method and spectral analysis under IR range.

The results of Boehm's titration method and pH value of the carbon surface are given in Table 5. Significant differences have existed on the amount of acidic and basic functional groups of the active carbons. After oxidation process with nitric acid the surface of AG-5ox sample becomes acidic and pH of active carbon suspension decrease till 3.30.

The amount of total acidic groups (titrated with NaOH) on active carbon surface AG-5ox increases by about 6 times and strong acidic groups - by about 9 times in comparison with initial sample AG-5. At the same time the amount of basic groups decreases by about 4 times (Table 5). The concentration of the acidic groups on the active carbon surface (AG-5ox) was in the following order: strong acidic >>> weak acidic > phenolic.

Table 5

Surface chemistry of active carbons samples evaluated by Boehm method and pH of suspension.

Sample	*pH of suspension*	*Quantity of the functional groups. Amount, meq/g*				*Character of the functional groups. Amount, meq/g*			
		Titrant				*Carboxylic*		*Phenolic*	*Basic*
		0.05 N $NaHCO_3$	*0.05 N Na_2CO_3*	*0.05 N NaOH*	*0.05N HCl*	*Strong acidic*	*Weak acidic*		
AG-5	6.65	0.16 ±0.02	0.22 ±0.02	0.38 ±0.01	0.48 ±0.03	0.16	0.06	0.16	0.48
AG-5ox	3.30	1.48 ±0.02	1.99 ±0.02	2.33 ±0.01	0.13 ±0.02	1.48	0.51	0.34	0.13

The FTIR spectral analysis is an important tool to identify some characteristic functional groups on the active carbons surface. In Figure 6 the IR spectra for active carbons AG-5 and AG-5ox are compared. For both of the activated carbons, before and after oxidation, there are a number of common bands. The absorptions around 800 cm^{-1} are assigned to the out of plane bending of the ring C-H bonds [25-27].

Bands in the 1000-1200 cm^{-1} region are difficult to assign because there is a superposition of a number of broad overlapping bands. It could be assign to C-O as in phenols/ethers/esters (1200 cm) [9, 27]. The shoulder at 1164 cm^{-1}, together with two absorptions of low intensity (1385 and 1399 cm^{-1}), confirm the presence of phenolic groups on the oxidized active carbon surface (AG-5ox, Figure 5 (2)).

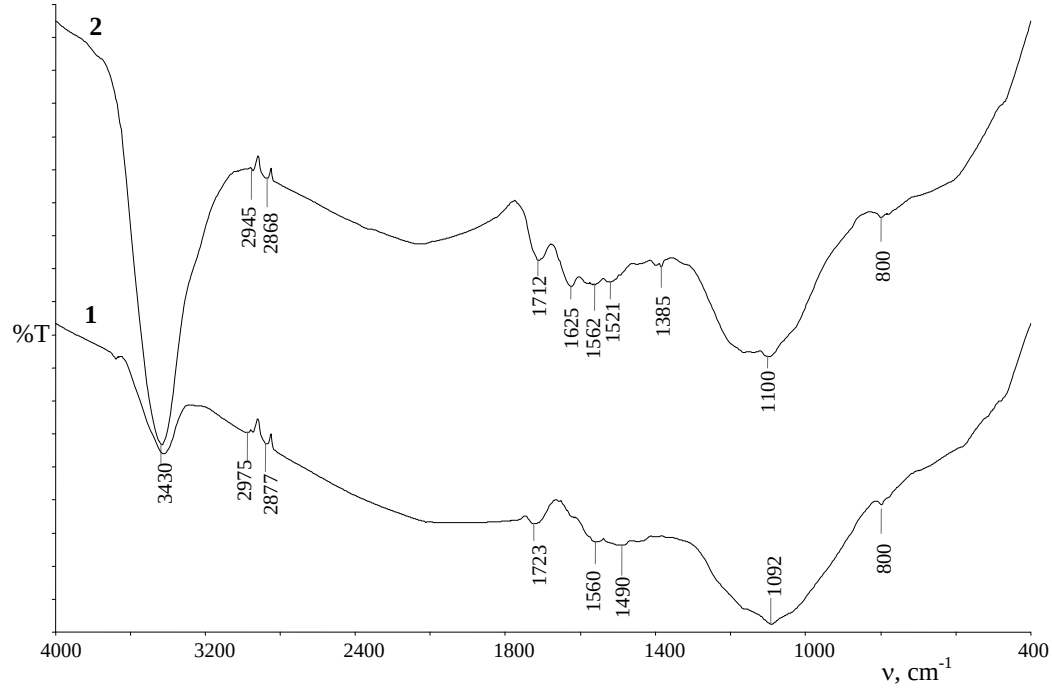

Figure 6. FTIR spectra of the initial activated carbon AG-5 (1) and oxidized with nitric acid AG-5ox (2).

The bands in the region of 1500-1600 cm^{-1} have been observed by many authors and have not been interpreted unequivocally. These bands, presented in the spectrum of AG-5ox at 1521, 1562 and 1625 cm^{-1}, and in the spectrum of AG-5 at 1490 and 1560 cm^{-1}, can be assigned to aromatic ring stretching (C=C) coupled to highly conjugated carbonyl groups (C=O) [24, 26].

The band between 1700 and 1730 cm^{-1}, that can be assigned to the stretching vibration of C=O bonds, characteristic of carboxylic, ketone and aldehide groups [11, 24] is much higher in AG-5ox than in AG-5 spectrum.

In the region 2860-2980 cm^{-1}, two bands of low intensity are presented, frequently attributed to aliphatic CH bond in the CH, CH_2 and CH_3 groups [26].

Broadband in the region 3300-3600 cm^{-1} is assigned to (OH stretching) vibrations of OH groups of related alcohols, phenols and carboxylic acids [11, 26, 27].

Generally, used methods to quantify the surface characteristic groups on active carbon samples show an increase of acidic surface groups on oxidized sample, presented as strong acidic – carboxylic groups, weak acidic – ketones and aldehide groups, and phenolic groups.

Conclusions

Evaluation of physical-chemical and surface chemistry characteristics of unmodified and oxidized active carbon samples indicates that oxidation with concentrated nitric acid changed not only the surface properties but also destroyed the active carbon structure making its decomposition much easier. The unmodified sample, AG-5, is much more thermally stable in comparison with oxidized sample (AG-5ox).

The slight increase of structural parameters (S_{BET}, V_{total}, V_{micro}) after oxidation treatment with about 14-16% is due to dissolution of inorganic species that may block the entrance of micropores.

After oxidation process with nitric acid, the surface of AG-5ox sample becomes acidic and pH of active carbon suspension decreases till 3.30. The amount of total acidic groups on active carbon surface AG-5ox increases by about 6 times in comparison with initial sample AG-5. The obtained results show an increase of acidic surface groups on oxidized sample, presented as strong acidic – carboxylic groups, weak acidic – ketones and aldehide groups, and phenolic groups.

Acknowledgements

I wish to express the deep appreciation to my supervisor Corresponding member, Professor Tudor Lupascu for his guidance and encouragement during the performed researches.

References

1. Kawamura, S. Integrated design of water treatment facilities. John Wiley & Sons: New York, 1991, 658 p.
2. Lupascu, T. Active carbons from vegetable raw materials. Stiinta: Chisinau, 2004. 224 p. (in Romanian).
3. Timbaliuc, N.; Lupascu, T. The influence of the porous structure of local activated carbons on the immobilization of the congo red dye and vitamin B12. Chemistry Journal of Moldova, 2013, 8(1), pp. 90-94.
4. Lupascu, T.; Ciobanu, M.; Botan, V.; Gromovoy, T.; Cibotaru, S.; Petuhov, O.; Mitina T. Study of hydrogen sulfide removal from grundwater. Chemistry Journal of Moldova, 2013, 8(1), pp. 37-42.
5. Tarkovskaja, I.A. Oxidized carbon. Naukova dumka:Kiev, 1981, 200 p. (in Russian).
6. Farberova, E.A.; Vinogradova, A.V.; Shergina, E.S. Development of modified carbonaceous adsorbent for water treatment. Vestnik Permskogo Nacional''nogo Issledovatel''skogo Politehnicheskogo Universiteta. Himicheskaja Tehnologija i Biotehnologija, 2010, 11, pp. 22-30 (in Russian).
7. Moreno-Castilla, C.; Ferro-Garcia, M.A.; Joly, J.P.; Bautista-Toledo, I.; Carrasco-Marin, F.; Rivera-Utrilla, J. Activated carbon surface modifications by nitric acid, hydrogen peroxide, and ammonium peroxydisulfate treatments. Langmuir, 1996, 11, pp. 4386-4392.
8. Vivo-Vilches, J.F.; Bailon-Garcia, E.; Perez-Cadenas, A.F.; Carrasco-Marin, F.; Maldonado-Hodar, F.J. Tailoring the surface chemistry and porosity of activated carbons: Evidence of reorganization and mobility of oxygenated surface groups. Carbon, 2014, 68, pp. 520-530.
9. Moreno-Castilla, C.; Lopez-Ramon, M.V.; Carrasco-Marin, F. Changes in surface chemistry of activated carbons by wet oxidation. Carbon, 2000, 38, pp. 1995-2001.
10. Al-Qodah, Z.; Shawabkah, R. Production and characterization of granular activated carbon from activated sludge. Brazilian Journal of Chemical Engineering, 2009, 26(1), pp. 127-136.
11. Nastas, R.; Rusu, V.; Giurginca, M.; Meghea, A.; Lupascu, T. Alteration of chemical structure of the active vegetal coals. Revista de Chimie (Bucharest), 2008, 59(2), pp. 159-164 (in Romanian).
12. Kuzin, I.A.; Strashko, B.K.; Mironenko, V.M.; Zarubin, O.V. Oxidation of active carbons with nitric acid. Ionnyj obmen i ionity. Nauka: Leningrad, 1970, pp. 178-181 (in Russian).
13. Choma, J.; Jaroniec, M.; Burakiewicz-Mortka, W.; Klinik, J.; Olejniczak, K. Structural and surface properties of active carbons oxidized with nitric acid at high temperature. Polish Journal of Chemistry, 1998, 72(5), pp. 860-868.

14. Sontheimer, H.; Crittenden, J.C.; Summers, R.S. Activated Carbons for Water Treatment. DVGW-Rorschungsstelle: Karlsruhe, 1988, 722 p.
15. Characteristics of the activated carbon AG-5. http://mtksorbent.ru/ugol-aktivnyj-aktivirovannyj/ugli-aktivnye-na-kamennougolnoj-osnove/ugol-aktivnyj-ag-5-detail.
16. STAS 5388-80. Vegetable active carbon. Tests methods. Editura Tehnica: Bucuresti, 1980, 18 p. (in Romanian).
17. Cibotaru, S. Study of processes of activated carbon obtaining from wood charcoal. Chemistry Journal of Moldova, 2012, 7(2), pp. 93-97.
18. Autosorb AS-1. AS1Win. Gas Sorption System. Operation Manual. Firmware: version 2.55. AS1Win Software: version 2.0 and newer. Quantachrome Instruments, 2008.
19. Tcaci, M.; Himcinschi, C.; Nastas, R.; Petuhov, O.; Lupascu, T.; Zahn, D.R.T. Non-destructive characterization of modified activated carbon. Revista de Chimie (Bucharest), 2011, 62(7), pp. 727-731.
20. Boehm, H.P. Chemical identification of surface groups. In Advances in Catalysis. Academic Press: New York, 1966, 16, pp. 179-274.
21. Li, Z.; Jaroniec, M.; Choma, J. Thermogravimetric and adsorption studies of oxidized active carbons by using different probe molecules. Thermochimica Acta, 2000, 345, pp. 165-72.
22. Maroto-Valer, M.M.; Dranca, I.; Clifford, D.; Lupascu, T.; Nastas, R.; Leon y Leon, C.A. Thermal regeneration of activated carbons saturated with ortho- and meta-chlorophenols. Thermochimica Acta, 2006, 444 pp. 32-40.
23. Figueiredo, J.L.; Pereira, M.F.R.; Freitas, M.M.A.; Órfão, J.J.M. Modification of the surface chemistry of activated carbons. Carbon, 1999, 37(9), pp. 1379-1389.
24. Radovic, L.R. Ed. Chemistry & Physics of Carbon. CRC Press, 2008, 30, 264 p.
25. Bingzheng, L. Characterization of pore structure and surface chemistry of activated carbons – A Review. In Salih, S. Ed. Fourier Transform - Materials Analysis. InTech, 2012, pp. 165-190. Available from: http://www.intechopen.com/books/fourier-transform-materials-analysis/charaterization-of-porestructure-and-surface-chemistry-of-activated-carbons-a-review.
26. Zawadzki, J. Infrared spectroscopy in surface chemistry of carbons. In Thrower, P.A. Ed. Chemistry and Physics of Carbon. Marcel Dekker: New York, 1989, 21, pp. 147-380.
27. Akolekar, D.B., Bhargava, S.K. Influence of thermal, hydrothermal, and acid-base treatments on structural stability and surface properties of macro- meso-, and microporous carbons. Journal of Colloid and Interface Science, 1999, 216(2), pp. 309-319.

TEMPERATURE DEPENDENCE OF ^{57}Fe-MÖSSBAUER SPECTRA FOR A $Fe^{II}_{Fc} - Fe^{II}_{tpy} - Fe^{II}_{Fc}$ TRINUCLEAR SYSTEM

Dumitru Sirbu

Institute of Chemistry of Academy of Sciences of Moldova, 3, Academiei str., Chisinau MD-2028, Republic of Moldova
e-mail: sirbudyma@gmail.com, tel. (+373 22) 73 97 22, fax (+373 22) 73 99 54

Abstract. ^{57}Fe Mössbauer spectra were recorded for 1'-terpyridine ferrocenecarboxylic acid and [bis(1'-terpyridine ferrocenecarboxylic acid) Fe(II)]$^{2+}$ in the temperature range 7 – 293 K. The temperature dependence of the Quadrupole Splitting, Isomer Shift and Debye-Waller factor are discussed. The Debye temperature for the iron nuclei in the investigated compounds was determined.

Keywords: ferrocene, terpyridine, Mössbauer, Debye temperature.

Received: August 2014/ Revised final: September 2014/ Accepted: September 2014

Introduction

Mössbauer spectroscopy is a powerful tool for the study of various elements, especially for ^{57}Fe [1]. Its main hyperfine interaction parameters are the Isomer Shift (IS), Quadrupole Splitting (QS) and magnetic hyperfine interaction. While the first one depends on the total electron density on the examined nucleus (mainly s orbitals), the second is a measure of the electric field gradient. Using these parameters a comprehensive description of the studied atom can be made (e.g. the oxidation state, spin state, changes in symmetry). The temperature dependence of the Debye-Waller factor of the Mössbauer Spectra (MS) gives information on the vibration of atom in the molecule and of molecule in the crystal. The Debye temperature, , can be determined and used for comparison of forces that bind an atom in the molecule [2].

We have previously described [3] the synthesis of 1'-terpyridine ferrocenecarboxylic acid **FcT** (Figure 1) from the asymmetrical 1'-formyl-ferrocenecarboxylic, as a ligand with an anchoring group to semiconductor surfaces (e.g. NiO). Surprisingly it underwent a light induced decomposition as result of ferrocene "sandwich" destruction and formation of the iron (II) bis-terpyridine $[Fe(tpy)_2]^{2+}$ complex. The [bis(1'-terpyridine ferrocenecarboxylic acid) Fe(II)]$^{2+}$ complex **FeFcT** (Figure 1) was isolated and its crystalline structure described [3]. Herein we describe the ^{57}Fe Mössbauer study of this $Fe^{II}_{Fc} - Fe^{II}_{tpy} - Fe^{II}_{Fc}$ trinuclear system.

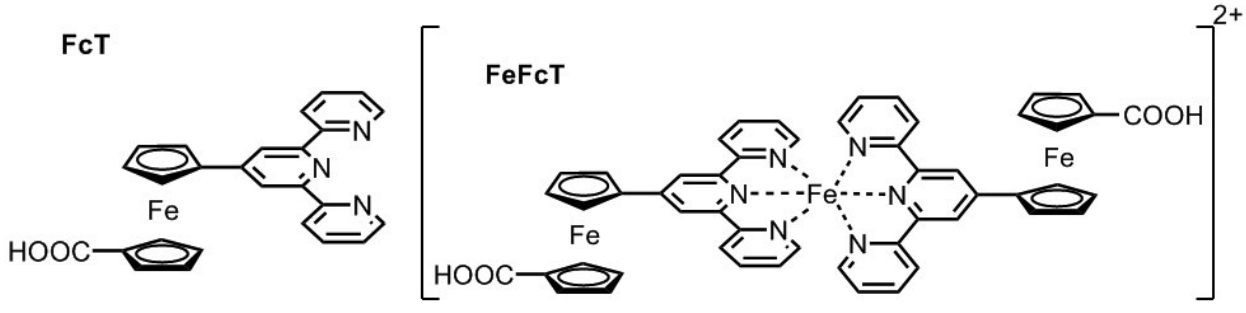

Figure 1. The molecular structures of FcT and FeFcT.

Experimental

The ^{57}Fe-Mössbauer spectra were acquired with a conventional spectrometer in the constant-acceleration mode (MS4, Edina, USA) equipped with a ^{57}Co source in a rhodium matrix. Variable temperature Mössbauer experiments were done using closed cycle He gas refrigerator cryostat and a dual channel temperature controller SeeCo Model 106. Isomer shifts are given relative to α-Fe at RT. The spectrum was fitted using the Mössbauer Spectral Analysis Software WMOSS4 Version F. The error limits for the each experimental point in the MS is ±0.02 mm/s on X-axis and less than 0.5 % on Y-axis. All spectra were fitted for a lowest value, < 0.60 for **FcT** and < 0.75 for **FeFcT**. The linearity of plots was checked by use of R^2 factor and respective error limits were determined.

Synthesis

Ferrocene was purchased from Sigma-Aldrich and used as received. Compounds **FcT** and **FeFcT** were prepared as we described previously [3].

Results and discussion

The MS for **FcT** and **FeFcT** are shown in Figure 2 with relevant parameters presented in Table 1. The room temperature MS for **FcT** is typical for a ferrocene derivative and consists of a large and clear doublet. The IS value of

0.43 mm/s is similar (within the error limits) to the parent ferrocene, while the QS decreased by 0.22 mm/s. This is a result of the electron withdrawing effect of the carboxylic substituent which increase the symmetry of the electron environment on the iron nucleus, by removing electron density from the cyclopentadienide ring and consequently from Fe $d_{z2,}$ d_{xz}, d_{yz} orbitals. The QS is even lower than for ferrocene-carboxylic acid [4], which suggest an additional effect of the terpyridine group. A similar effect was reported for the ferrocene diketones [5] and confirmed by Density Functional Theory, DFT, calculations [2]. The spectrum of **FeFcT** comprises two partially overlapped doublets attributed to the two carboxy-ferrocenes and $[Fe(tpy)_2]^{2+}$ components, with parameters consistent with the literature data [6,7]. All Fe nuclei are low-spin (S=0) iron (d^6), but a more symmetrical pseudo-octahedral N_6 coordination results in a lower QS for $[Fe(tpy)_2]^{2+}$ compared to ferrocene. Decrease of the QS could be expected for ferrocene in **FeFcT** compared to **FcT** as result of terpyridine-to-Fe^{II} electron pair donation but experimentally a slightly higher (+0.04 mm/s) QS is observed. An explanation for this is the well-known for $[Fe(tpy)_2]^{2+}$ metal-to-ligand back donation [8], which is partially compensating the electron density on terpyridines and consequently on cyclopentadienide rings. However, the "bowing" of the terpyridine ring upon complexation should be taken into account too.

The temperature dependence of Mössbauer spectra parameters is resulting in a number of observed changes. With decreasing the temperature a strong increase of the absorption for the Fc was observed, less pronounced for the $[Fe(tpy)_2]^{2+}$ nucleus.

Table 1

Experimental Mössbauer parameters for FcT, FeFcT and reference compounds.

Compound	*Temperature, K*	*Isomer Shift*, δ, mm/s*	*Quadrupole Splitting*, ΔE_Q, mm/s*	*Relative Absorption f'_T/f'_{7K}*
FcT	7	0.53	2.18	1.00
	40	0.53	2.18	0.97
	80	0.53	2.17	0.90
	120	0.52	2.18	0.83
	150	0.50	2.18	0.76
	180	0.50	2.17	0.63
	200	0.49	2.18	0.59
	250	0.46	2.17	0.46
	297	0.43	2.17	0.30
Fc in FeFcT	7	0.55	2.22	1.00
	40	0.54	2.22	0.94
	80	0.53	2.23	0.82
	120	0.52	2.22	0.73
	150	0.51	2.22	0.64
	180	0.50	2.23	0.58
	200	0.49	2.22	0.50
	250	0.46	2.22	0.36
	293	0.44	2.21	0.20
$[Fe(tpy)_2]^{2+}$ in FeFcT	7	0.27	1.10	1.00
	40	0.27	1.08	0.99
	80	0.27	1.07	0.97
	120	0.27	1.06	0.98
	150	0.27	1.05	0.91
	180	0.26	1.05	0.85
	200	0.25	1.06	0.76
	250	0.23	1.05	0.66
	293	0.21	1.05	0.38
Fc	7	0.54	2.40	1.00
	80	0.53	2.39	0.93
	120	0.52	2.40	0.79
	160	0.51	2.41	0.66
	200	0.50	2.40	0.54
	293	0.45	2.39	0.31
$[Fe(tpy)_2]^{2+}$ **	80	0.28	1.05	n/a
Fc-COOH*	293	0.53	2.21	n/a

* *the error for values of IS and QS is ±0.02 mm/s.*

, * *Data taken from references [6] and [4], respectively.*

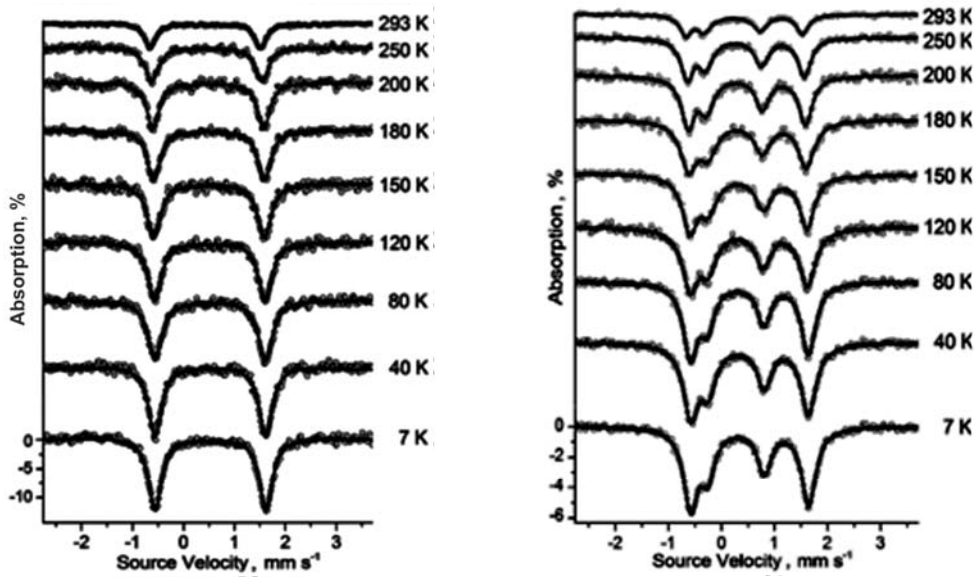

Figure 2. The Mössbauer spectra for FcT (left) and FeFcT (right) over 7 – 293 K temperature range.

The effect of the increase of recoil free fraction with decreasing the temperature was previously explained as the result of vibration diminution for the examined atom in the crystal lattice. The logarithmic form of the relation between recoil free absorption *f'* of the γ rays and temperature *T* for a "thin" absorber is given by Eq.(1) [9].

$$lnf' = -\frac{6E_r}{k\theta_D^2}\text{, where } T > \frac{\theta_D}{2} \quad (1)$$

were E_r is the recoil energy, *k* is Boltzmann's constant. Plots of lnf' versus *T* allow us to calculate the Debye temperature from the slope of the line $\Delta(lnf')/\Delta T$. The $f_T'/f_{7K}' = k_{eff} \times A_T / k_{eff} \times A_{7K} = A_T/A_{7K}$ can be used instead of f', where A is the experimentally determined area of peak and k_{eff} is an effective constant which take into consideration the experimental conditions (sample and equipment). The plot of $ln\, f_T'/f_{7K}'$ versus *T* (Figure 3) for **FcT** is linear over the temperature range 80 K to 200 K and has a slope $\frac{6E_r}{k\theta_D^2}$= (4.0±0.3) x 10^{-3} which corresponds to θ_D=(184±14) K. This value is somehow higher compared to that of parent ferrocene θ_D= (173±10) K. For the **FeFcT** two linear regressions with the slopes of (4.2±0.4) x 10^{-3} and (2.9±0.2) x 10^{-3} were obtained for Fc and $[Fe(tpy)_2]^{2+}$ nuclei, which give θ_D= (180±17) K and θ_D= (218±15) K. The higher Debye temperature for the latter is suggesting a more rigid N_6 bonding of Fe atom by two terpyridine molecules compared to the ferrocene "sandwich". This is a reasonable result taking in account the well-known stability of the $[Fe(tpy)_2]^{2+}$ complexes [10] and is in perfect accordance with the instability of ferrocene derivatives in the presence of terpyridine ligand [3].

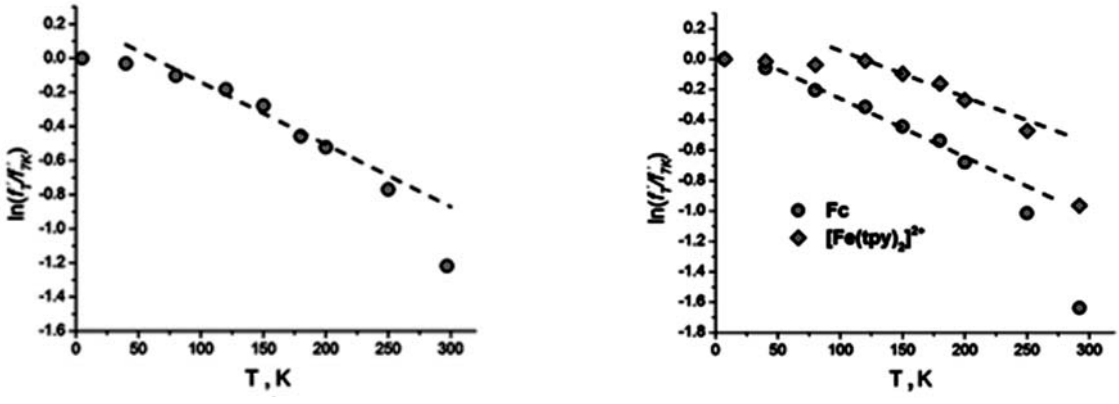

Figure 3. Plots of versus T for FcT (left) and FeFcT (right). Points between 80-200 K for Fc in FcT and FeFcT, but 120-200 K for $[Fe(tpy)_2]^{2+}$ component were least-squares linearly fitted (R^2> 0.99).

The difference in Debye temperature for the two types of Fe nuclei in **FeFcT** results in a different ratio of Fc/$[Fe(tpy)_2]^{2+}$ peaks area at temperature variation (Figure 4**).** The plot of area ratio versus temperature can be seen in Figure 5, showing a smooth transition from Fc/$[Fe(tpy)_2]^{2+}$ = 1 at RT to the stoichiometrically expected Fc/$[Fe(tpy)_2]^{2+}$ =2 at 7 K.

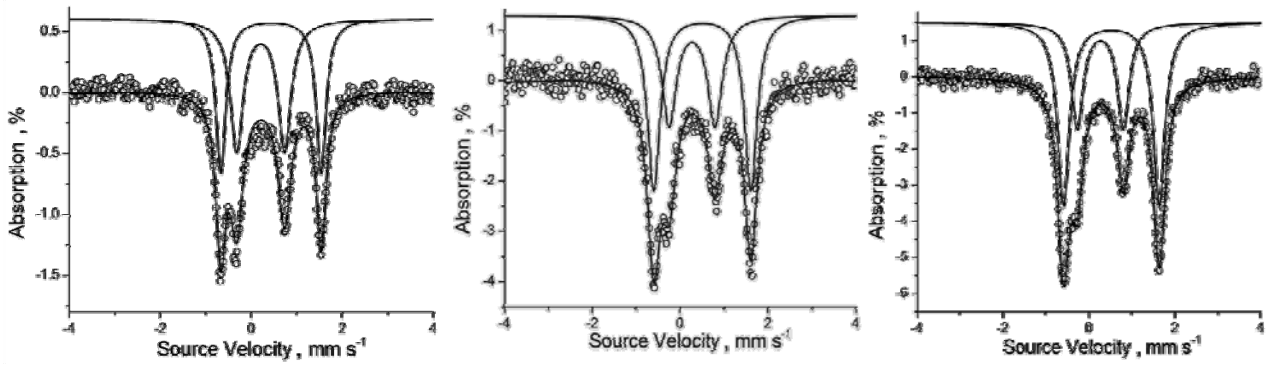

Figure 4. The experimental and fitted Mossbauer spectra for FeFcT at 293 K (left), 150 K (centre) and 7K (right).

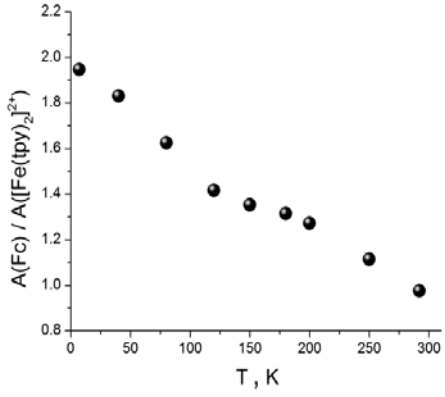

Figure 5. Plot of A(Fc) / A($[Fe(tpy)_2]^{2+}$) ratio versus T for FeFcT.

Another observed change in the spectra with the decrease of temperature is the increment of the IS (Figure 6). This is a result of the temperature dependent second-order Doppler shift contribution to the IS [11]. This effect was observed for all studied nuclei but while for the Fc the IS was increasing over the whole range of temperature, the $[Fe(tpy)_2]^{2+}$ IS almost stopped to increase at 150 K. The IS increased with 0.1 mm/s for Fc from both **FcT** and **FeFcT**, but with only 0.07 mm/s for the $[Fe(tpy)_2]^{2+}$ component.

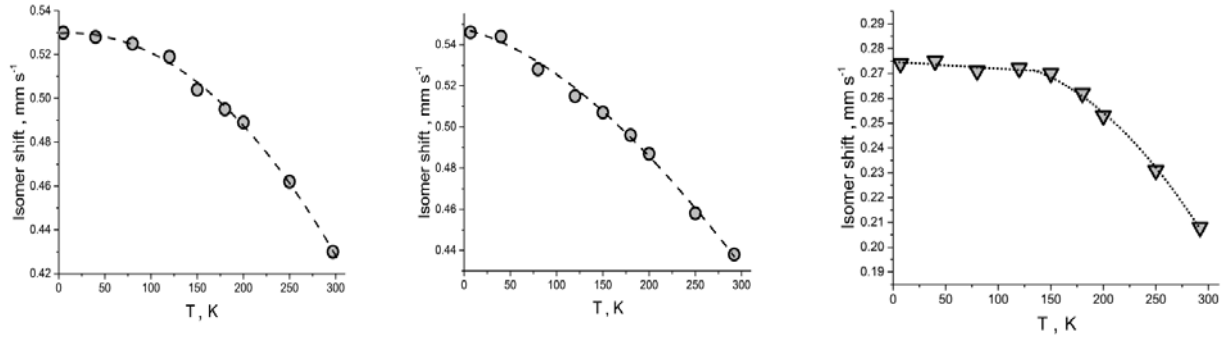

Figure 6. Plot of IS vs T for Fc from FcT (left), FeFcT (centre) and for $[Fe(tpy)_2]^{2+}$ from FeFcT (right).

The QS is more "inert" to the temperature variation (Figure 7) so that only a minor increment of 0.01 mm/s was observed for Fc but a more pronounced effect of 0.04 mm/s was noticed for $[Fe(tpy)_2]^{2+}$. As result of these changes the two doublets are less overlapped at higher temperatures.

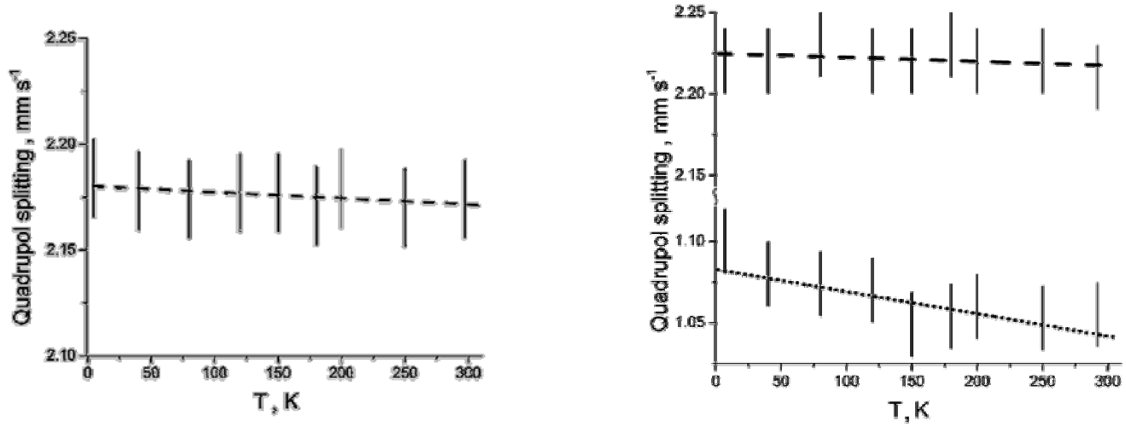

Figure 7. Plot of QS vs T for FcT (left) and FeFcT (right). Dashed lines (- - -) show the trend for Fc components, while dotted line (···) - for $[Fe(tpy)_2]^{2+}$ from FeFcT.

Conclusions

The temperature dependence of the ^{57}Fe Mössbauer spectra for 1'-terpyridine ferrocenecarboxylic acid and [bis(1'-terpyridine ferrocenecarboxylic acid) Fe(II)]$^{2+}$ was fully described. The Debye temperature was found to be (184±14) and (180±17) K for ferrocene components of **FcT** and **FeFcT** and = (218±15) K for $[(Fe(tpy)_2)]^{2+}$ unit, which supports the stronger metal-ligand binding and higher stability of the latter. Altogether, this example shows how the difference of Debye temperatures in polynuclear systems strongly affects the Mössbauer spectrum and should be taken in account when interpreting the experimental results.

Acknowledgments

I thank the national grant No. 11.817.08.22F for financial support and FP7-PEOPLE-2009-IRSES grant (246902) for funding to cover the exchange of researchers. I would like to thank as well my supervisors Prof. Constantin Turta from the Institute of Chemistry of ASM and Prof. Andrew Benniston from Newcastle University for the help in writing this paper.

References

1. Gütlich, P.; Bill, E.; Trautwein, A.X. Mössbauer Spectroscopy and Transition Metal Chemistry. Springer - Verlag: Berlin Heidelberg, 2011, XV, 569 p.
2. Pingheng, Z.; Desheng, X.; Haiqing, L.; Huigang, S. Temperature Dependence of the Mössbauer Effect on Prussian Blue Nanowires. Hyperfine Interactions, 2002, 142, pp. 601–606.
3. Benniston, A.C.; Sirbu, D.; Turta, C.; Probert, M.R.; Clegg, W. A simple method for desymmetrizing 1,1′-ferrocenedicarboxaldehyde. Tetrahedron Letters, 2014, 55 (28), pp. 3777-3780.
4. Korecz, L.; Abou, H.; Ortaggi, G.; Graziani, M.; Belluco, U.; Burger, K. The Mössbauer investigation of some derivatives of ferrocenes. Inorganica Chimica Acta, 1974, 9, pp. 209-212.
5. Clemance, M.C.; Roberts, R.M.G.; Silver, J. Mössbauer studies on ferrocene complexes VIII. Diacetyl ferrocene-metal halide complexes. Journal of Organometallic Chemistry, 1983, 247, pp. 219-222.
6. England, J.; Scarborough, C.C.; Weyhermüller, T.; Sproules, S.; Wieghardt, K. Electronic Structures of the Electron Transfer Series $[M(bpy)_3]^n$, $[M(tpy)_2]^n$, and $[Fe(^tbpy)_3]^n$ (M = Fe, Ru; n = 3+, 2+, 1+, 0, 1–): A Mössbauer Spectroscopic and DFT Study. European Journal of Inorganic Chemistry, 2012, pp. 4605–4621.
7. Oshio, H.; Spiering, H.; Ksenofontov, V.; Renz, F.; Gutlich, P. Electronic Relaxation Phenomena Following ^{57}Co(EC) ^{57}Fe Nuclear Decay in $[Mn(II)(terpy)_2](ClO_4)_2 \cdot 1/2H_2O$ and in the Spin Crossover Complexes $[Co(II)(terpy)_2]X_2 \cdot nH_2O$ (X = Cl and ClO_4) - A Mössbauer Emission Spectroscopic Study. Inorganic Chemistry, 2001, 40, pp. 1143-1150.
8. Hofmeier, H.; Schubert, U.S. Recent developments in the supramolecular chemistry of terpyridine–metal complexes. Chemical Society Reviews, 2004, 33, pp. 373-399.
9. Herber, R.H. Chemical Mössbauer Spectroscopy, Plenum Press: New York, 1984, pp. 199-216.
10. Ulrich, S.; Schubert, H.H.; Newkome G.R. Modern Terpyridine Chemistry. Wiley-VCH: Weinheim, 2006, pp. 37-68.
11. Pound R.V., Rebka G.A. Variation with Temperature of the Energy of Recoil-Free Gamma Rays from Solids. Physical Review Letters, 1960, 4 (6), pp. 274-275.

ANTIOXIDANT PROPERTIES OF DIHYDROXYFUMARIC ACID AND ITS DIMETHYL ETHER: A COMPARATIVE DFT STUDY OF THEIR REACTIONS WITH THE STABLE RADICAL DPPH*

Mikhail Gorbachev, Natalia Gorinchoy*, Ion Arsene

Institute of Chemistry of Academy of Sciences of Moldova, 3, Academiei str., Chisinau MD-2028, Republic of Moldova
**e-mail: ngorinchoy@yahoo.com*

Abstract. The preferred mechanism of the reaction of dihydroxyfumaric acid and its dimethyl ether with the free stable radical 1,1-diphenyl-2-picrylhydrazyl (DPPH*) was revealed by means of Density Functional Theory (DFT) calculations. The proposed mechanism has an ionic character and includes the formation of charge-transfer complexes as the main stage. It is also shown that the lower antioxidant activity of dimethyl ether of dihydroxyfumaric acid is caused by both its lower acidity (as compared with its precursor acid) and formation of more stable intermediates during its reaction with DPPH*. Our results allow one to rationalize the available experimental data.

Keywords: antioxidant activity, DPPH*, dihydroxyfumaric acid, dimethyl ether of dihydroxyfumaric acid, DFT calculations.

Received: September 2014/ Revised final: November 2014/ Accepted: November 2014

Introduction

Many organic compounds with enol or phenol groups are effective antioxidants which transform various free radicals into their diamagnetic derivatives [1]. Usually their relative antioxidant activity is evaluated by the reaction rate with the free stable radical – DPPH* (1,1-diphenyl-2-picrylhydrazyl) in the methanol-water medium. It was shown [2] that DPPH* reacts with compounds containing active hydrogen atoms (phenols, mineral and organic acids, etc.) forming 1,1-diphenyl-2-picrylhydrazine. According to [2], DPPH* solutions immediately change their color by adding of diluted aqueous mineral acids therein, in methanol or ethanol (whose acidity is lower) they demonstrate change of the color within several days, while solutions of DPPH* in liquid media without active hydrogen atoms (for instance, in benzene, chloroform, acetone, etc.) remain unchanged within a period of 50 days. Thus, the higher acidity of liquid media leads to the faster decomposition of DPPH*.

In its turn, the rate of the reaction of DPPH* with some phenols depends on the stability of the free radicals formed from the above phenol diamagnetic molecules when their hydrogen atoms migrate to DPPH* ones. So, for example, isoeugenol reacts very quickly (immediately) with DPPH*, while the reaction between DPPH* and eugenol (whose double bond is not conjugated with its benzene cycle) requires several hours (see [1]). It has been also shown [1] that the compounds containing enol groups (ascorbic acid and isoascorbic one) possess the maximum antioxidant activity, i. e. they are the best scavengers of the free radical DPPH*.

The other effective antioxidant compounds containing in their structures enol groups are the dihydroxyfumaric acid – DHFA and its derivatives (for instance, its dialkylethers). In the work [3] it was shown by means of the method of stopped-flow that in the methanol-water medium the reaction between DHFA and DPPH* includes two stages. During the first stage which requires only 7-10 s at T = 293.15K one half of DPPH* reacts with DHFA. The second reaction step is slower and requires around 1-2 hours [3]. Basing on these facts, some theoretical suppositions were done [3] in order to describe the reaction mechanism between DPPH* and DHFA. So, it was assumed that the first stage describes the transfer of one of the two hydroxyl hydrogen atoms of a DHFA molecule to that of DPPH* with formation of 1,1-diphenyl-2-picrylhydrazine. The transfer of the second hydroxyl hydrogen atom of DHFA molecules to the second half of DPPH* ones has been suggested (see [3]) many times slower.

However, the above-mentioned molecular mechanism is in contradiction with the author's own experimental data [3]. So, the experiment shows that the rate of the fast stage of this reaction is proportional to the square root of the molar concentration of DHFA, whereas in accordance with the assumed mechanism it would have to be proportional to this concentration in the first degree. The given contradiction indicates that the considered mechanism can have an ionic character.

Moreover, in the work [4] the relative antioxidant activity against DPPH* was studied for a number of derivatives of DHFA. It was shown that for each of them the time required for the above two reaction stages is several times longer than that for DHFA. However, these data did not find any theoretical interpretation. As far as we know, there are none quantum-chemical studies clarifying the mechanisms of the reactions of DHFA and its derivatives with DPPH*. Only a number of quantum chemical calculations were mainly devoted to determination of the structure- antioxidant activity relationships for various free radical scavengers [5, 6].

In this context the aim of the present work is twofold: to reveal (using DFT calculations) the preferred mechanism of reaction between DHFA and DPPH*; to explain the decrease in the antioxidant activity by passing from DHFA to one of its derivatives, namely, to its dimethyldihydroxyfumarate ether – DMDHFE.

Computational details

The electronic and geometrical structures of all the considered compounds have been investigated by means of the DFT method, including Becke's three-parameter nonlocal-exchange functional [7] with the correlation functional of Lee, Yang and Parr (B3LYP) [8]. For each of the compounds considered, a full geometry optimization was carried out using the 6-31G* basis sets including polarization functions for all the atoms in the systems [9]. The calculations were performed with the GAUSSIAN 09 program package [10].

Results and discussion

At the first stage of our quantum-chemical calculations we have tried to find the molecular transition state responsible for transfer of the first hydrogen atom from a DHFA molecule to the corresponding first molecule of DPPH*. However, all these attempts have not been successful, that is clear from the chemical point of view. Really, the direct transition of the hydrogen atom from the oxygen atom of DHFA (belonging to one of its hydroxyl groups) to the corresponding nitrogen atom of DPPH* cannot occur due to the higher electronegativity of the oxygen atom. At the same time the reaction between DPPH* and DHFA is exothermic with the energy gain 0.0075 a.u. or 19.7 kJ/mol (see the reaction below, where DHFA is denoted as AH_2 in order to show its active hydrogen atoms, and AH* is the radical-acid formed from AH_2):

DPPH*	+	AH_2	→	DPPH-H	+	AH*
-1417.8717 a.u.		-606.1632 a.u.		-1418.5014 a.u.		-605.5411 a.u.
-2024.0349 a.u.				-2024.0424 a.u.		

It means that the above reaction is energetically allowed. This discrepancy shows that the mechanism of the hydrogen transfer from DHFA to DPPH*is essentially more complex. In order to explain it, we have taken into account the above fact that the solutions of DPPH* change their color by adding of mineral acids therein [2]. Based on this circumstance one can assume that the given rapid loss of the characteristic DPPH*solutions can be caused by the fast protonation of this radical.

Basing on this interpretation we have supposed that the reaction between DPPH* and DHFA begins from the protonation of one of the heteroatoms of DPPH* by means of one of the free protons existing in the water-methanol solution of DHFA due to the electrolytic dissociation of one of its carboxyl groups. In Figure 1 some calculated heteroatoms' charges of DPPH* are presented. The comparison of these charges indicates that the protonation of the DPPH* molecule will most likely be realized through its oxygen atom O4 (but not by means of the nitrogen atom N2). The such protonation way is more preferable also from the stereochemical point of view. Really, all the oxygen atoms O3, O4, O5, and O6 are out of the plane of the picryl cycle of DPPH* and, therefore, they shield the nitrogen atom N2. Besides, the atom N2 is spatially shielded by the bulk phenyl groups connected with N1.

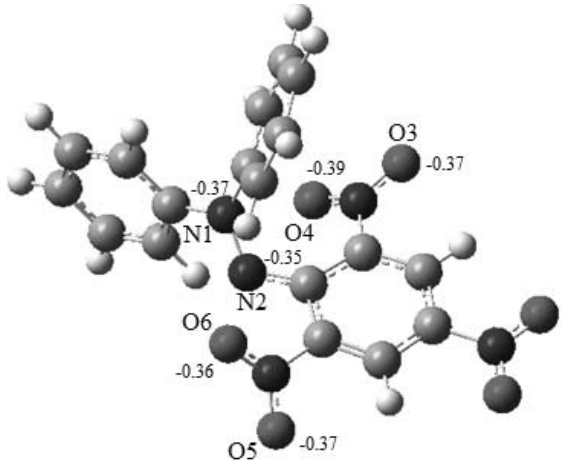

Figure 1. The calculated charges on some heteroatoms in the DPPH* molecule.

Preference for the protonation way via O4 (as compared with that via N2) follows also from the comparison of the calculated total energies of the two arising cation-radical systems: -1418.2152 a.u. and -1418.0283 a.u., respectively.

Note also that calculations of the cation $[DPPH\text{-}H]^{*+}$ allow one to understand the above mentioned color changes of DPPH* solutions. Indeed, in the DPPH* molecule the spin density of its unshared electron is mainly localized on the atom N2, while in the above $[DPPH\text{-}H]^{*+}$ system it is mainly shared between the atom O3 and the nitrogen atom connected with O3 (see Figure 1). It is clear that this shift of the spin density must change the absorption spectrum in the visible region.

One can expect that the ionic interaction between the cation-radical $[DPPH-H]^{*+}$ and the anion of DHFA (hereafter $[AH]^-$) formed due to electrolytic dissociation of the latter will occur without any energy barrier at the room temperature. Our present and the previous [11] quantum-chemical calculations of the whole system ($[DPPH-H]^{*+}$ ••••$[AH]^-$) indicate the formation of the charge-transfer complex (CTC) presented in Figure 2.

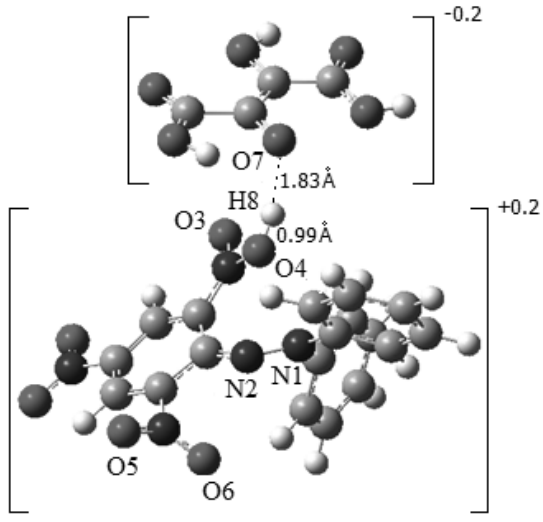

Figure 2. The mutual geometry orientation and the summarized charges in the CTC formed by $[AH]^-$ and $[DPPH-H]^{*+}$.

The calculated energy value of the CTC is -2024.0006 a.u. At the same time, the summarized energy of free ions $[DPPH-H]^{*+}$ and $[AH]^-$ is -2023.8360 a.u. (the energy of $[DPPH-H]^{*+}$ is -1418.2152 a.u.; and that of $[AH]^-$ is -605.6208 a.u.). Thus, the formation of the CTC from the given ions leads to the energy release of 0.1645 a.u. (i.e. 432.2 kJ/mol). Here it is to be noted (see Figure 2) that the formation of this CTC is accompanied by the transfer of the negative charge 0.8e from $[AH]^-$ to $[DPPH-H]^{*+}$. The unshared spin density of the CTC is mainly localized on the carbon atoms belonging to the double C=C bond of $[AH]^-$. In its turn, due to the subsequent tautomeric transition of one hydrogen atom from O4 to N2 the considered CTC decays into one molecule of 1,1-diphenyl-2-picrylhydrazine and one molecule of the radical-acid AH*. The given decay leads to the energy release which is equal to 97.6 kJ/mol. Further, two molecules of the radical-acid AH* easily form their dimmer $(AH)_2$ which has four carboxyl groups. The electrolytic dissociation of any of these groups in water-methanol medium gives the anion $[A_2H]^-$. However, our DFT calculations show that $[A_2H]^-$ is an unstable particle. It decays into one new anion $[AH]^-$ of DHFA and one molecule of dioxosuccinic acid [11].

Thus, basing on our DFT calculations, the following mechanism (Scheme 1) can be proposed for the reaction between the acid DHFA (AH_2) and the free radical DPPH*:

Scheme 1

$$AH_2 \leftrightarrow [AH]^- + H^+ \quad (1)$$

$$DPPH^* + H^+ \rightarrow [DPPH-H]^{*+} \quad (2)$$

$$[DPPH-H]^{*+} + [AH]^- \rightarrow CTC \quad (3)$$

$$CTC \rightarrow AH^* + \text{1,1-diphenyl-2-picrylhydrazine} \quad (4)$$

$$2AH^* \rightarrow (AH)_2 \quad (5)$$

$$(AH)_2 \leftrightarrow [A_2H]^- + H^+ \quad (6)$$

$$[A_2H]^- \rightarrow [AH]^- + \text{dioxosuccinic acid} \quad (7)$$

First of all, it is to be noted here that the mechanism described by Scheme 1 has an ionic character. All its elementary stages (reactions) are accompanied by the corresponding energy release (see the data above). Both these facts allow one to understand the high reaction rate which describes the interaction of DHFA (AH_2) with the first molecule of DPPH* (the reaction time is 7-10 s [3]). Moreover, as the volume concentration of H^+ formed by the reaction (1) is proportional to the square root $[AH_2]^{1/2}$ (due to the law of mass action), so the rate of the reaction (2) which defines the total rate of the interaction between AH_2 and the first molecule of DPPH* will be proportional to the product of the concentrations $[DPPH^*][H^+]$, i.e. $[DPPH^*][AH_2]^{1/2}$. Indeed, this theoretical conclusion is completely confirmed by the experimental data [3].

In their turn, the new ions $[AH]^-$ and H^+ are formed by the reactions (4)-(7). These new ions will interact with the second molecule of DPPH* (see the stages (2) and (3)). However, their formation is caused by the reaction of the electrolytic dissociation of $(AH)_2$ (the dimmer of the radical-acid AH*) and by the further decay of the anion $[A_2H]^-$ (see Scheme 1). The realization of these reactions (6) and (7) leads to the corresponding elongation of the time required for the reaction of AH_2 with the second molecule of DPPH* (up to 90 minutes [3]). Thus, the mechanism of the reaction between DPPH* and DHFA found theoretically in the present work allows one to understand these experimental data.

In order to explain the lower antioxidant activity of the derivatives of DHFA (compared to the free acid), we have considered the interaction of dimethyldihydroxyfumarate ether (DMDHFE) with DPPH*. It has been noted in the Introduction that the average reaction time of this process is several times greater than that for the case of DHFA. As above, the DFT calculations do not demonstrate any molecular transition state for the reaction between DPPH* and DMDHFE. In its turn, the described ionic mechanism requires the presence of free protons in reaction medium. In this case the given protons can appear only due to dissociation of one of two hydroxyl groups of DMDHFE. However, these hydroxyl groups dissociate harder than carboxyl ones do [12]. Due to this fact the time required for the elementary reaction (1) in Scheme 1 for DMDHFE will be longer than that for DHFA.

For DMDHFE the elementary reactions (2)-(5) are just the same as in the case of DHFA. So, for example, the optimized geometry of the CTC formed by $[DPPH\text{-}H]^{*+}$ and $[DMDHFE]^-$ (where $[DMDHFE]^-$ is the anion of DMDHFE) has the same interatomic distances O7-H8 as in the CTC of DHFA (Figure 3).

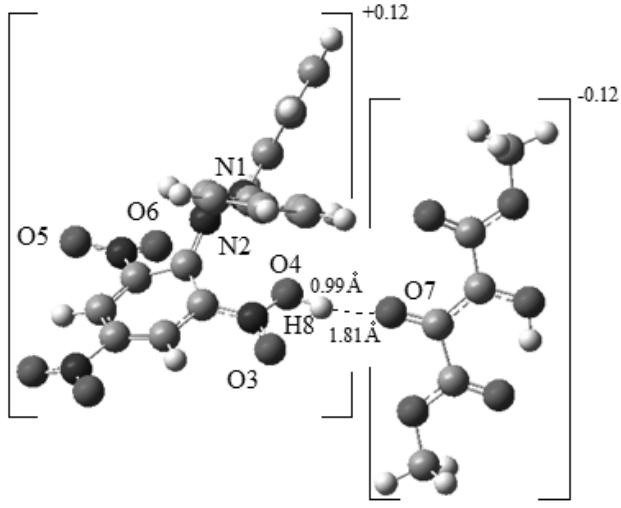

Figure 3. The mutual geometry orientation and the summarized charges in the CTC formed by $[DMDHFE]^-$ and $[DPPH\text{-}H]^{*+}$.

Here it is to be noted the following circumstance. The summarized reaction of the hydrogen transfer between DPPH* and DHFA (AH_2) is exothermic with the energy effect of 19.7 kJ/mol (see above). However, the similar summarized reaction for DMDHFE:

$$[DPPH]^* + DMDHFE \rightarrow [DPPH\text{-}H] + [DMDHFE]^*$$

is endothermic. Our DFT calculations show that it requires 20.5 kJ/mol. At the same time, the reaction of the dimerization of the radicals [DMDHFE]*:

$$2[DMDHFE]^* \rightarrow [DMDHFE]_2$$

is an exothermic process. It is accompanied with the energy release of 96.0 kJ/mol. This energy is sufficient for realization of the above reaction between DPPH* and DMDHFE (when the considered molecule of DMDHFE interacts with its first molecule of DPPH*). Thus, the summarized process:

$$2[DPPH]^* + 2\ DMDHFE \rightarrow 2\ [DPPH\text{-}H] + [DMDHFE]_2$$

will be also exothermic as in the case of DHFA.

It is to be noted that the dimmer $[DMDHFE]_2$ is formed (similar to the reaction (5) in Scheme 1) by two radicals [DMDHFE]* received in its turn after the decay of the CTC between $[DPPH\text{-}H]^{*+}$ and $[DMDHFE]^-$. However, our calculations show that $[DMDHFE]_2$ is not the end product of the reaction between DPPH* and DMDHFE. The optimized structure of the dimmer $[DMDHFE]_2$ is shown in Figure 4.

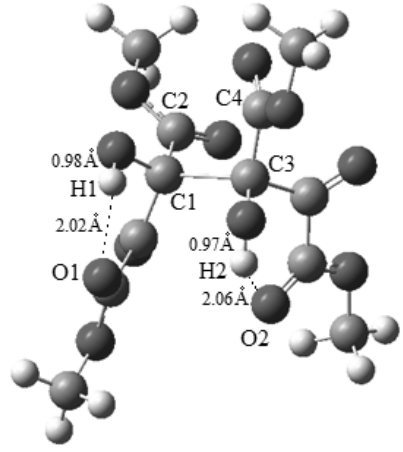

Figure 4. The optimized structure of $[DMDHFE]_2$ with the intramolecular hydrogen bonds.

It contains the intramolecular hydrogen bonds (marked by the dotted lines) which prevent the possible dissociation of any of the hydroxyl groups of $[DMDHFE]_2$. In this case the ionization of one of its hydroxyl groups (due to elimination of the corresponding proton) does not lead to the further decay of the anion $[[DMDHFE]_2]^-$ as it takes place in the considered case of DHFA (See the reactions (6) and (7) in Scheme 1, and the work [12]). Further, our calculations indicate that the new radical $[[DMDHFE]_2]^*$ formed by the reaction between $[[DMDHFE]_2]^-$ and the cation-radical $[DPPH\text{-}H]^{*+}$ is also a relatively stable particle. Its molecular structure demonstrates only one elongated (up to 1.63 Å) bond C1–C2 which is shown by the dotted line in Figure 5.

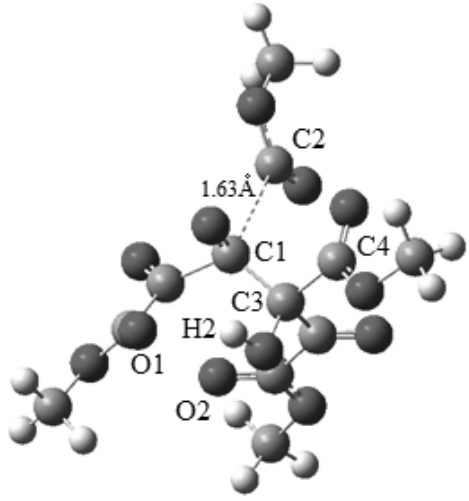

Figure 5. The optimized structure of the radical $[[DMDHFE]_2]^*$.

In its turn, the derivative DV of $[[DMDHFE]_2]^*$ received by the elimination of the last hydrogen atom from the latter (H2 in Figure 5) due to its reaction with the new molecule of DPPH* (via the above-considered formation of $[DPPH\text{-}H]^{*+}$) is the essentially more active particle than $[[DMDHFE]_2]^*$. This derivative spontaneously decays into two molecules of dimethyl ether of dioxosuccinic acid. Our calculations show that the following final reactions take place:

$$[[DMDHFE]_2]^* + DPPH^* \rightarrow DPPH\text{-}H + DV$$
$$-1367.6810 \text{ a.u.} \quad -1417.8717 \text{ a.u.} \quad -1418.5014 \text{ a.u.} \quad -1366.9674 \text{ a.u.}$$
$$-2785.5527 \text{ a.u.} \qquad -2785.4688 \text{ a.u.}$$

$$DV \rightarrow 2\ CH_3O\text{-}(C{=}O)_4\text{-}OCH_3$$
$$-1366.9674 \text{ a.u.} \qquad 2 \times (-683.5629 \text{ a.u.}) = -1367.1258 \text{ a.u.}$$

The summarized energy release of the above reactions equals to 0.0745 a.u. (195.7 kJ/mol). It means that the transformation of $[[DMDHFE]_2]^*$ into dimethyl ether of dioxosuccinic acid is an exothermic process.

Interaction of the antioxidants DHFA and DMDHFE with DPPH* requires the electrolytic dissociation of their neutral molecules (see the first stage in Scheme 1). It means that the compound with the higher acidity will have the higher antioxidant activity.

In the case of DHFA one molecule possesses four active hydrogen atoms (two of them belong to its easily dissociated carboxyl groups and two belong to its hydroxyl ones). On the other hand, DMDHFE, whose antioxidant activity is essential lower, has only two hydrogen atoms belonging to two hardly dissociating hydroxyl groups per one molecule. Thus, we can conclude that any increase in molecular acidity of an antioxidant will lead to the corresponding increase in its antioxidant activity (against DPPH*). The same conclusion holds not only for DHFA and DMDHFE [3, 4], but also for other antioxidants. For example, the antioxidant activity of various derivatives of gossypol against DPPH* increases, firstly, with the increase in the number of hydroxyl phenol groups per one molecule (i.e. with the increase in the number of active acid hydrogen atoms) and, secondly, by passing from neutral compounds to their derivatives containing positively charged organic cations whose phenol hydroxyl groups possess the increased acidity [13].

It is clear that the consecutive formation of $[DMDHFE]_2$, $[[DMDHFE]_2]^-$, and $[[DMDHFE]_2]^*$ together with the just considered decay of $[[DMDHFE]_2]^*$ (via DV) require an essential additional time for their realization. The given circumstances, along with the above-mentioned low acidity of hydroxyl groups of DMDHFE, allow one to understand the sufficient decrease in the rate of the reaction between DPPH* and DMDHFE [4].

Conclusions

The following conclusions can be drawn. The preferred mechanisms describing the antioxidant activities of dihydroxyfumaric acid and its dimethyl ether were proposed on the basis of the DFT calculations of their reactions with the stable radical DPPH*. It is shown that the main stage of both these reactions is the formation of the charge-transfer complexes. They are formed from the protonated DPPH* molecules and the anions of the above antioxidants arising due to their electrolytic dissociation in the water-methanol medium. The comparison of these two cases indicates that the studied antioxidant activity increases together with the acidity of the investigated compounds, i.e. by passing from the dimethyl ether to its precursor acid. The lower antioxidant activity of the ether is also caused by formation of additional number of intermediates during its reaction with DPPH*. The found results are in a good agreement with the available experimental data. In particular, they allow one to explain the kinetic data describing the experimental concentration dependences for the rates of the investigated reactions and to understand the high stability of DPPH* solutions in various solvents without active hydrogen atoms.

References

1. Brand-Williams, W.; Cuvelier, M.E.; Berset, C. Use of a Free Radical Method to Evaluate Antioxidant Activity. LWT – Food Science and Technology, 1995, 28, pp. 25-30.
2. Yordanov, N.D. Is Our Knowledge about the Chemical and Physical Properties of DPPH Enough to Consider It as a Primary Standard for Quantitative EPR Spectrometry. Applied Magnetic Resonance, 1996, 10, pp. 339-350.
3. Secara, N. Stopped-Flow Spectrophotometric Studies of the Kinetics of Interaction of Dihydroxyfumaric Acid with the DPPH Free Radical. Chemistry Journal of Moldova, 2010, 5(2), pp. 83-87.
4. Secara, N.; Duca, Gh.; Vlad, L.; Macaev, F. Observation on the Antioxidant Activity of Novel Dixydroxyfumaric Acis Derivatives. Chemistry Journal of Moldova, 2010, 5(2), pp. 59-67.
5. Borges, R.S.; Queiroz, A.N.; Mendes, A.P.S.; Araújo, S.C.; França, L.C.S.; Franco, E.C.S.; Leal, W.G.; da Silva, A.B.F. Density Functional Theory (DFT) Study of Edaravone Derivatives as Antioxidants. International Journal of Molecular Sciences, 2012, 13, pp. 7594-7606.
6. Velkov, Z.A.; Kolev, M.K.; Tadjer, A.V. Modeling and statistical analysis of DPPH scavenging activity of phenolics. Collection of Czechoslovak Chemical Communications, 2007, 72, pp.461–1471.
7. Kohn, W.; Becke, A.D.; Parr, R.G. Density functional theory of electronic structure. Journal of Physical Chemistry, 1996, 100, pp. 12974–12980.
8. Lee, C.; Yang, W.; Parr, R.G. Development of the Colle-Salvetti correlation-energy formula into a functional of the electron density. Physical Review B, 1988, 37, pp. 785-789.
9. Hehre, W.J.; Radom, L.; Schleyer, P.V.R.; Pople, J.A. Ab Initio Molecular Orbital Theory; Wiley: New York, 1986, 548 p.
10. Frisch, M. J.; Trucks, G.W.; Schlegel, H.B. et al. Gaussian 09, Revision B.01; Gaussian, Inc.: Wallingford, CT, 2009.
11. Gorbachev, M.Yu.; Gorinchoy, N.N. DFT Evidence of Ionic Character of Interaction of Dihydroxyfumaric Acid with the Free Radical DPPH. In Conference book of 24th Austin Symposium on Molecular Structure and Dynamics, Dallas, USA, March 3-6, 2012, p. 159.
12. Gorbachev, M.Yu.; Gorinchoy, N.N.; Arsene, I. Comparative DFT Study of Interaction between Dimethyldihydroxyfumarate and its Precursor Acid with the Stable Radical DPPH*. In Book of Abstracts of the XVIIth International Conference "Physical Methods in Coordination and Supramolecular Chemistry", Chisinau, Republic of Moldova, October 24-26, 2012, p. 34.
13. Ilkevich, N.S.; Rybachenko, V.I.; Shroeder, G.; Dmitruk, A.F.; Chotyi, K.Yu. Antioxidative properties of gossypol and some its imino-derivatives. Proceedings of Donetsk National Technical University, Series: Chemistry and Chemical Engineering, 2009, Section 2, pp. 110-117 (in Russian).

APPLICATION OF TAGUCHI OPTIMIZATION METHOD IN THE PREPARATION OF ACTIVATED CARBON BY MICROWAVE TREATMENT

Oleg Petuhov

Institute of Chemistry of Academy of Science of Moldova, 3, Academiei str., Chisinau MD-2028, Republic of Moldova, e-mail: petuhov.chem@gmail.com; phone: (+373 22) 72 54 90; fax: (+373 22) 73 99 54

Abstract. This paper reports on the preparation of activated carbon from walnut shell. Orthogonal array experimental design method was used to optimize the preparation of activated carbon with phosphoric acid by using microwave treatment. The optimization parameters were: microwave power, activation time, phosphoric acid concentration and particle sizes of nut shells. Thermal analysis of the intact and impregnated with phosphoric acid walnut shells was used for the simulation of activation process. Activated carbon with the optimal parameters was obtained, being characterized by gas adsorption method and scanning electron microscopy.

Keywords: activated carbon, walnut shells, microwave radiation, experimental design, analysis of variance.

Received: March 2015/ Revised final: April 2015/ Accepted: April 2015

Introduction

Widespread use of activated carbon (AC) in different areas continues to maintain interest in the increase of its production. Along with this, requirements are growing to the quality of AC. The high number both of methods of activation and AC precursors makes possible diversification and optimization of the processes of their obtaining. Currently tendencies are known for obtaining AC from cheap and renewable raw materials [1] and by methods with low energy consumption, as well [2]. Literature data indicate that nowadays AC is obtained from a variety of precursors, such as waste, both of natural [1] and synthetic origin [3], in addition to the traditional ones (wood, coal, nut shells). The process of obtaining AC involves an increased consumption of energy; therefore development of methods aimed at reducing energy consumption represents an important direction of investigations. A perspective research line in this context is the use of microwaves in the process of AC preparation [2, 4].

The employment of microwaves finds a widening application in various fields [5, 6]. This is explained by many advantages of microwave heating, in comparison with traditional methods. Rapid heating, lack of inertia in heat transfer and reduced activation time [4], which in turn leads to diminished consumption of energy and activation agents, are amongst the main advantages of its usage. Apart from obvious advantages, the following drawbacks of this method can be revealed: non-carbonized raw material weakly absorbs microwaves [7, 8]; materials that are used for production of the activation reactors in laboratory are not appropriate for their application at industrial level and existence of a maximum threshold, up to which substance can be heated. Nevertheless, some successful attempts of obtaining AC by microwave treatment on semi-industrial scale have been registered [9]. The listed problems were solved *via* carbonization the raw material by traditional heating; use of ceramic activation reactor and optimization the activation requirements.

In order to get optimized conditions for AC preparation, a large number of experiments must be carried out, since there are many variables determining the final AC parameters. Experimental design technique is an effective statistical method, which allows setting the optimal parameters in a technologic process, as well as establishing the interactions between variables. Taguchi experimental design method is a mathematical and statistical tool for organizing and systematization the experiment, aimed at obtaining the optimum parameters in terms of performance/cost. This method allows the analysis of a large number of variables in a reduced series of the experiments, by using the orthogonal matrix.

The purpose of this study is to obtain AC from the walnut shells by chemical activation and microwave treatment. Taguchi optimization method was employed to determine the optimum parameters for obtaining the AC. The structural and adsorption parameters of obtained AC were also determined.

Experimental

Materials

Walnut shells of local origin were used as raw material for obtaining the AC. Phosphoric acid (85 wt.%) of analytical grade was used as activating agent. Nitrogen (4.0 purity grade) was used to maintain the inert atmosphere during the activation process and recording the thermograms.

Preparation of AC

The walnut shells were crushed and separated into three fractions: 0.8-2.0 mm; 2.0-3.15 mm; 3.15-5.0 mm; the non-crushed walnut shells were also used. Shells (5.0 g) were mixed with 10 mL of phosphoric acid (40-85 wt.%) and allowed to contact at room temperature for 24 hours. Thereafter, the mixture of acid and shells was transferred to the quartz reactor and subjected to the activation process. During the activation process and before cooling the carbons

nitrogen with flow rate 100 cm^3/min has been passed through the reactor. After cooling the AC was washed with a solution of KOH (0.05 M), hot and cold distilled water until the pH value of washing solution (6-7). Then AC samples were dried at 110 °C to the constant mass.

Optimization the conditions for AC preparation

In order to optimize conditions for obtaining the AC, Taguchi experimental design method was used. Application of Taguchi method involves the following steps:

1. Selection of the final product control parameters;
2. Selection of independent variables and their limits of variation;
3. Choosing the appropriate model of the orthogonal matrix, based on the number of variables;
4. Performing the experiment on the base of orthogonal matrix;
5. Analysis of the obtained results;
6. Conducting the control experiment.

An L_{16} orthogonal array with four operational parameters each in four levels was used to evaluate the corresponding optimal values. The used variables and their levels are shown in Table 1. The complete design matrix of the experiments and the obtained results are shown in Table 2. An L_{16} orthogonal array was chosen with four operational parameters known as control factors, namely the microwave power (*A*), the activation time (*B*), the concentration of phosphoric acid (*C*) and the fraction of the walnut shells (*D*). The studied parameters and their limits of variation were chosen based on preliminary experiments and analysis of the literature data. As control parameters specific surface area (S_{BET}) and yield of obtained AC were chosen. As a result of data processing, the optimal parameters were obtained and the control activated carbon was synthesized (run 17, Table 2). Data processing of the optimization experiment was carried out in the program Design-Expert Software version 7.0.

Table 1

Levels of the used as preparation parameters control factors.

Independent value	*Symbol*	*Range and levels*			
		1	*2*	*3*	*4*
Microwave power, W	*A*	450	600	700	850
Activation time, minutes	*B*	5	10	15	20
H_3PO_4 concentration, wt.%	*C*	40	55	70	85
Fraction, mm	*D*	whole shells	3.15-5.0	2.0-3.15	0.80-2.0

Table 2

L_{16} orthogonal array of Taguchi method used in the preparation of AC.

Run	*Variables*				*Responses*	
	A	*B*	*C*	*D*	S_{BET}, m^2/g	*Yield of the AC, %*
1	1	1	1	1	406.1	33.4
2	1	2	2	2	600.8	39.1
3	1	3	3	3	623.2	40.4
4	1	4	4	4	793.3	47.8
5	2	1	2	3	588.2	39.1
6	2	2	1	4	647.5	35.5
7	2	3	4	1	441.9	42.1
8	2	4	3	2	636.9	39.1
9	3	1	3	4	851.6	44.8
10	3	2	4	3	367.1	46.1
11	3	3	1	2	467.5	35.7
12	3	4	2	1	598.6	26.3
13	4	1	4	2	349.9	51.9
15	4	3	2	4	709.2	42.6
16	4	4	1	3	619.3	31.4
17	**1**	**4**	**3**	**4**	**917.7**	**39.5**

Analysis of variance

Identification of the most effective parameters for AC preparation was performed by using analysis of variance (ANOVA) technique [10]. This statistical method does not directly analyze the obtained data, but determine their dispersion. In the analysis of variance, many parameters, such as degrees of freedom, sums of squares, mean square [10],

and so on, are computed and organized in a standard tabular format. These parameters and their mathematical relations are presented in Table 3.

Table 3

ANOVA terms and notations [10].

ANOVA terms	*Description of parameter*	*Mathematical relation*
n	number of trials, the total number of trials is the sum of the number of trials at each level	$n= n_1 + n_2 +\ldots+ n_L$
r	number of repetitions	-
Y Y_m	response Y_m is the average value of Y	-
T	total of all results	$T=Y_1+Y_2+\ldots+Y_n$
C.F.	correction factor	$C.F.= T^2/n$
Degrees of freedom (DOF)	it is a measure of the amount of information that can be uniquely determined from a given set of data	$f_t= n * r - 1$
Sum of squares, S	it is a measure of the deviation of the experimental data from the mean value of the data	$S= \sum_{i=1}^{n} (Y_i - Y_m)^2$ $\sum_{i=1}^{n} (Y_i - Y_m)^2$
Total sum of squares, S_T	gives an estimate of the sum of the variations of the individual observations about the mean, Y , of the experimental data	$S_T = \sum_{i=1}^{n} Y_i^2 \sum_{i=1}^{n} Y_i^2$ - $C.F.$
Mean square (variance), *V* V_T V_m V_e	Variance measures the distribution of the data about the mean of the data. total variance mean variance error variance	$V = S/f$ $V_T = S_T/f_T$ $V_m = S_m/f_m$ $V_e = (S_T-S_m)/f_e$
Variance ratio, F	commonly called the *F* statistic, is the ratio of variance due to the effect of a factor and variance due to the error term	$F=V_m/V_e$
Prob >F	Probability of the observed F value. Small probabilities (less than 0.05) indicate that there is a model effect; large values (greater than 0.10) suggest no significant effect.	
Percentage contribution, P	The percent contribution for any factor	$P= S/S_T *100$

Thermal analysis

Thermal analysis was performed on Derivatograph Q-1000 system. The samples were placed in a platinum crucible. Each sample (about 50 mg) was heated under nitrogen flow rate of 100 mL/min and a heating rate of 10°C/min from 20 to 1000°C. Thermogravimetric (*TG*), derivative weight loss (*DTG*) and differential thermal (*DTA*) curves were simultaneously registered.

Gas adsorption characterization

Structure and adsorption parameters of AC were obtained from nitrogen adsorption isotherms at 77 K. The adsorption isotherms were measured using Autosorb-1-MP (Quantachrome), with prior degassing at 200°C for 12 hours. The specific surface area (S_{BET}) was calculated using the Brunauer–Emmett–Teller (*BET*) equation. The total pore volume (V_t) was calculated by converting the amount of N_2 gas adsorbed at a relative pressure of 0.99 to equivalent liquid volume of the adsorbate (N_2). The volume of micropores (V_{mi}) was determined using the *t*-method, the volume of mesopores (V_{me}) was determined from the difference of total volume and the volume of micropores. The Dubinin–Radushkevich (*DR*) method was used to calculate the adsorption energy (E_a). The Density Function Theory (*DFT*) was used to calculate the pore volume distribution as a function of radius and effective radius (r_{ef}).

Surface morphology

The surface physical morphology of AC was identified by using scanning electron microscopy (*SEM*) technique. A TESCAN Vega TS 5130MM with a 30 kV accelerating voltage was used. Prior to SEM analysis AC sample was dried at 110°C under vacuum.

Results and discussion

Thermal analysis

With the purpose of determination the changes occurring in the walnut shells activation process, the thermal analysis of the intact and impregnated with phosphoric acid shells was performed (Figure 1a, b). The main components of the walnut shells are lignin, cellulose and hemicelluloses. Mass fraction of the components, based on the literature data [11, 12], is presented in Table 4. As it can be noted, about 50% by weight of walnut shells consists of lignin. Being

a three-dimensional polymer, lignin is also the most thermally stable component of the wood [13]. This leads to the increased efficiency of the process of obtaining the activated carbons [14] and gives them a high mechanical stiffness.

Thermal decomposition of the walnut shells in a nitrogen atmosphere occurs in several steps, Figure 1a. The first step, in the temperature range of 28-150 °C, leads to a decrease in mass of 7.1% that occurs due to the loss of water and volatile substances. From 200 °C is observed the next stage on the TG curve, which is explained by the beginning the decomposition of the less thermally stable component, hemicellulose. Thermal degradation continues until 323 °C, with a maximum at 286 °C, this leads to a mass loss of 24.4% and is accompanied by an exothermic heat effect. The decomposition process of cellulose, which starts at 323 °C and ends at 390 °C, with a peak at 356 °C, is also accompanied by an exothermic effect. This leads to a loss of 24.11% in mass. Further heating occurs with a slow loss of weight, which is caused by the thermal degradation of lignin. It should be noted, that lignin decomposes into a wide temperature range between 200-900 °C [15] and thermal degradation continuous in parallel with hemicelluloses and cellulose. At 1000 °C, the total loss in mass constitutes 70.9%.

However the impregnated with phosphoric acid walnut shells demonstrate different thermal decomposition, Figure 1b. The presence of phosphoric acid moves the start of process to the lower temperatures. This can be explained by the fact that phosphoric acid promotes the dehydration of wood mass and simultaneously decrease mass fraction of volatile organic substances [16], by this leading to the increase of the yield of final product.

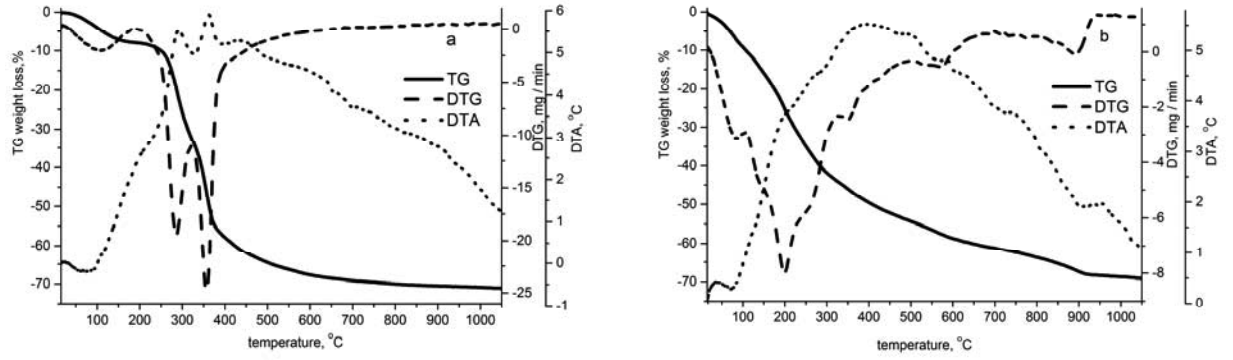

Figure 1. TG-DTG-DTA analysis curves of walnut shells (a) and H_3PO_4-impregnated walnut shells (b).

Table 4

Lignocellulose content of walnut shells.

Hemicelluloses, %	*Cellulose, %*	*Lignin, %*	*Ash, %*	*Reference*
22.1	25.6	52.3	2.8	[11]
22.45	26.87	47.68	0.94	[12]

Optimization of the activation process

Preliminary analysis of parameters for obtaining the AC

There are quite a lot of factors that influence the AC parameters, to be analyzed in one series of experiments. Amongst possible factors the following can be listed: activating agent, raw material, time and contact temperature of the raw material with the activating agent, concentration of the activating agent, weight ratio: raw material/activating agent, mass of raw material, size of the particles of raw material, microwave power, activation time, flow rate of nitrogen in the process of activation etc. Along with the above-listed factors, which can easily controlled, there are more difficult to optimize factors, such as the geometry and material from which the reactor is made, position of the reactor in the microwave oven and others.

Since Taguchi method requires only the use of independent variables, at the initial stage it is necessary to choose the optimal value of the dependent variables. Examples of dependent variables can be the mass of raw material and of activating agent, with respect to the microwave power. Concentration of the activating agent is also a dependent variable, because changing the concentration implies the change of dielectric constant of mixture and therefore, its ability to absorb microwaves. However, in the present study no account was taken on this. Another reason why some preliminary experimental data are required is to establish the main and secondary factors.

In order to determine the optimal ratio of walnut shells/activating agent, a series of activated carbons were prepared. The parameters of produced AC are listed in Table 5.

As evidenced by Table 5, increasing the mass of walnut shells, specific surface area of the produced AC tends to decrease at the same ratio of raw material/activating agent. Thus, the best parameters were obtained for the ratio 1:2

of raw material/activating agent and walnut shells mass of 5 g. Taking into account these data, for optimizing the process of obtaining the AC, 5 g of walnut shells and 10 mL of phosphoric acid of different concentrations were employed.

Table 5

Activation conditions and parameters of AC obtained preliminary.

Ratio m(AC)/ V(H_3PO_4)	*Run*	*Mass AC, g*	*Volume H_3PO_4, mL*	*C H_3PO_4, wt.%*	*Fraction mm*	*Contact time, h*	*Power of microwave, W*	*Time of activation, min*	*Yield, %*	*Surface, m^2/g*
1:1	1	5.01	5.00	85	2.0-3.15	24	600	15	37.5	606
	2	10.01	10.00	85	2.0-3.15	24	600	15	42.1	617
1:2	3	5.02	10.00	85	2.0-3.15	24	600	15	38.6	686
	4	10.01	20.00	85	2.0-3.15	24	600	15	42.2	535
	5	15.00	30.00	85	2.0-3.15	24	600	15	45.9	522
	6	20.01	40.00	85	2.0-3.15	24	600	15	42.3	475
1:4	7	5.00	20.00	85	2.0-3.15	24	600	15	40.4	568
	8	10.01	40.00	85	2.0-3.15	24	600	15	39.4	516

The results obtained by statistical processing of the experimental data are presented in Table 6. ANOVA for specific surface has shown results with a lower error in the case when the power of microwave was not taken into consideration. The method allows omission of some parameters in favour of obtaining the greater signal-to- noise ratio.

ANOVA results indicate that fraction of raw material has the greatest influence (51.8%) on the specific surface area of AC, the second parameter in terms of significance (36.9%) being concentration of phosphoric acid. The yield of the AC is directly influenced by the concentration of acid (51.8 %) and the fraction of carbon (34%).

Table 6

Analysis of the variance of main factors for AC production.

	Parameter	*S^a*	*DOF^b*	*V^c*	*F^d*	*Prob > F^e*	*P^f, %*
ANOVA of the surface area	Time of activation	31837.74	3	10612.58	1.83	0.24	11.3
	Concentration H_3PO_4	104400	3	34812.97	5.99	0.030	36.9
	Fraction	146300	3	48751.14	8.39	0.014	51.8
ANOVA of the activated carbon yield	Power of microwave	8.82	3	2.94	0.59	0.66	1.2
	Time of activation	94.40	3	31.47	6.34	0.081	13.0
	Concentration H_3PO_4	377.25	3	125.75	25.32	0.012	51.8
	Fraction	247.27	3	82.42	16.60	0.022	34.0

[a]- *sum of squares,*
[b]- *degrees of freedom,*
[c]- *variance,*
[d]- *variance ratio,*
[e]- *probability of the observed F value,*
[f]- *percentage contribution.*

These data can be explained by the following: the smaller are the particles of raw material, the deeper phosphoric acid penetrates into the volume of walnut shells, which results in a more homogeneous activation, thereby resulting in a larger surface area. At the same time, increasing the concentration of phosphoric acid prevents the formation of volatile compounds, which is consistent with an increase in the yield of the AC. Obtained data are well-correlated with those taken from the thermal analysis.

At the same time, ANOVA indicates that not all variables have a significant contribution to the activation process of carbons. The microwave power and activation time demonstrate low influence on the AC final parameters. A plausible explanation of this is supported by the limits of variation of these parameters, which have been taken in excess, namely for a mass of 5 grams of the raw material the process of activation with microwave takes a small time interval and do not need a high power microwave. Indeed, during the activation of carbons it was noted that after 5 minutes of microwave treatment the amount of emitted smoke is negligible; at the same time this period is sufficient to reach the maximum temperature, regardless of microwave power. Literature data also indicate that augmentation the microwave power and time of activation lead either to decrease or to insignificant changes of AC parameters [17,18].

Graphical representation of the influence of variables on the yield and specific surface area is shown in Figure 2. Microwave power has the same effect on both parameters: increase of the microwave power leads to the decrease of surface and to the AC yield. The observed effect takes place due to rapid dynamics of heating the raw material under microwave treatment at higher power levels. It favours the appearance of a greater temperature gradient within the material particles and evaporation of phosphoric acid before it starts to react; volatiles quickly evaporate and do not take part in formation of the AC structure. All these phenomena lead to a diminution of yield and surface of the AC.

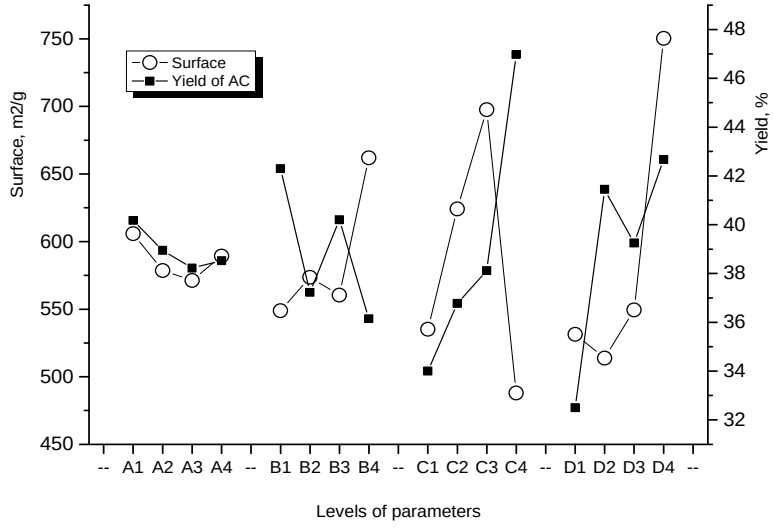

Figure 2. The effect of operational parameters on responses of the prepared AC samples.

Experimental verification of the obtained optimal values

The provided in Figure 2 data allowed us to establish the optimum parameters for obtaining AC. As it can be seen, there is not a unique solution for obtaining maximum values for both parameters: for specific surface area and yield the optimal conditions are different. Since the initial purpose was to obtain the AC with enhanced values of adsorption parameters, optimization of the process was performed for specific surface area. Based on Figure 2, these parameters are: microwave power - 450W (A1), activation time - 20 minutes (B4), phosphoric acid concentration – 70 wt.% (C3) and particle size of walnut shells in the range of 0.8-2.0 mm (D4).

Table 7 offers the modelled values of the analyzed system, as well as experimentally obtained ones. C.V. is the coefficient of variation for this model. It is the error expressed as a percentage of the mean. Adequate precision is a measure of the range in predicted response relative to its associated error, in other words a signal to noise ratio. Its desired value is 4 or more. For both parameters this value is more than 4, indicating on a satisfactory signal. The concordance of the model (C.M.) represents the deviation of the experimental values from the predicted ones and, as one can notice, these values do not exceed the range in predicted response (C.V.).

Table 7

Predicted values of AC for optimal conditions.

Parameter	*Prediction*	*C.V., %*	*Adequate precision*	*Experiment*	*C.M., %*
Specific surface	937.6 m^2/g	13.00	7.40	917.7	2.12
Yield	40.2 %	5.72	12.74	39.5	1.74

Characterization of the prepared at optimized conditions AC

The obtained under the optimum conditions AC was studied in detail by using the method of gas adsorption and electron microscopy with streak.

Gas adsorption

The adsorption - desorption isotherm of nitrogen on the obtained at optimized values activated carbon (OAC) is presented in Figure 3. The absorption and structure parameters are given in Table 8.

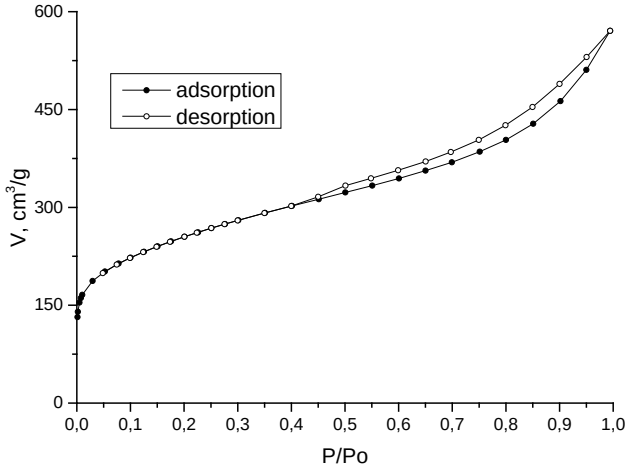

Figure 3. Nitrogen adsorption-desorption isotherm for the prepared at optimum conditions activated carbon.

Table 8

Structure parameters of the OAC.

Active carbon	S_{BET}, m^2/g	V_t, cm^3/g	V_{me}, cm^3/g	V_{mi}, cm^3/g	E_a, *kJ/mol*	r_{ef}, *Å*
OAC	917.7	0.883	0.701	0.182	16.8	5.6

OAC is a predominantly mesoporous activated carbon with a high specific surface area and a pore size distribution in a wide range (5-60 Å), Figure 4. This makes possible its use in water purification processes, when the size of pollutant molecules have a distribution in a large domain too.

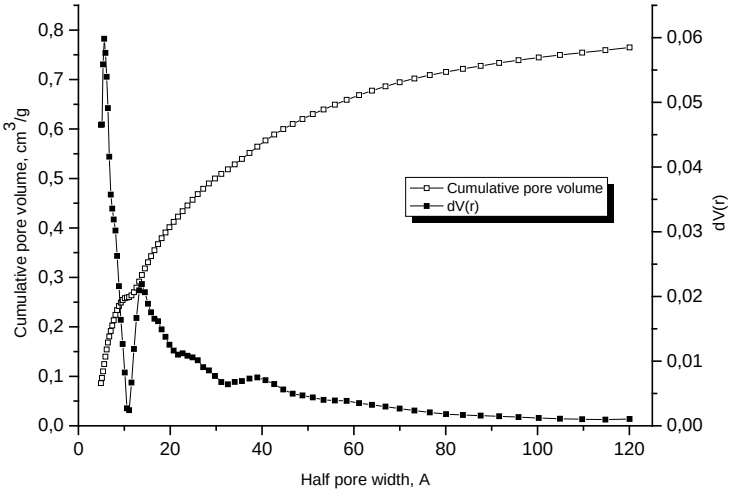

Figure 4. Pore size distributions of OAC by DFT method.

Scanning electron microscopy (SEM)

Electron microscopy images of the OAC sample are shown in Figure 5. According to them, the OAC surfaces were full of cavities and quite irregular as a result of activation. The external surface of the particles demonstrates an advanced roughness, by this increasing the specific surface area of AC.

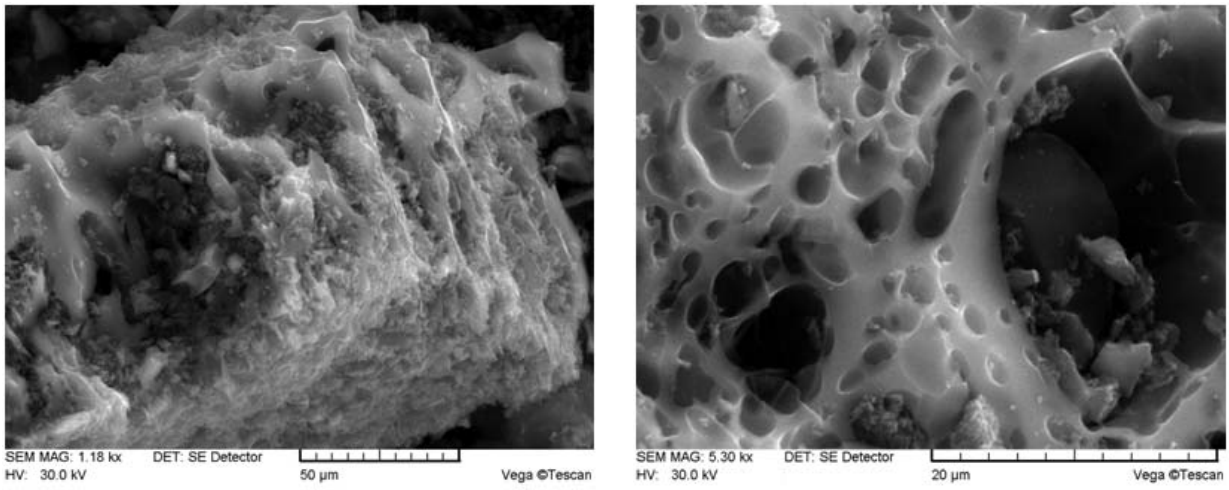

(a) **(b)**

Figure 5. (a,b) SEM micrographs section of the OAC.

Conclusions

Taguchi optimization method was employed to establish the optimal conditions for obtaining the activated carbons from walnut shell under microwave treatment. The walnut shells were impregnated at room temperature with phosphoric acid of different concentrations and subjected to microwave irradiation. Particle size of the raw material and concentration of phosphoric acid were found as the factors which influenced most largely the final parameters of activated carbons.

Based on ANOVA results, the optimal parameters for obtaining the activated carbons are: microwave power - 450W, activation time - 20 minutes, concentration of phosphoric acid – 70 wt.% and shells particle size in the range of 0.8-2.0 mm. The obtained active carbon has mesoporous structure with a large repartition of pores, thereby being possible to use it in the processes of water potabilization. Specific surface area of the obtained under optimum conditions activated carbon constitutes 918 m^2/g and the yield is 39.5%. Control parameters of the activated carbon correlate very well with those predicted by ANOVA. Taguchi optimization method was proved to be very effective and useful for preparation of the activated carbons.

Acknowledgments

The research leading to these results has received funding from the People Programme (Marie Curie Actions) of the European Union's Seventh Framework Programme FP7/2007-2013/ under REA grant agreement no. PIRSES-GA-2013-612484.

References

1. Ioannidou, O.; Zabaniotou, A. Agricultural residues as precursors for activated carbon production—A review. Renewable and Sustainable Energy Reviews, 2007, 11(9), pp. 1966–2005.
2. Yagmur, E. Preparation of low cost activated carbons from various biomasses with microwave energy. Journal of Porous Materials, 2012, 19(6), pp. 995–1002.
3. Mui, E. L.; Ko, D. C.; McKay, G. Production of active carbons from waste tyres-a review. Carbon, 2004, 42(14), pp. 2789–2805.
4. Menéndez, J.; Arenillas, A.; Fidalgo, B.; Fernández, Y.; Zubizarreta, L.; Calvo, E.; Bermúdez, J. Microwave heating processes involving carbon materials. Fuel Processing Technology, 2010, 91(1), pp. 1–8.
5. Lam, S. S.; Chase, H. A. A Review on Waste to Energy Processes Using Microwave Pyrolysis. Energies, 2012, 5(12), pp. 4209–4232.
6. Jones, D.; Lelyveld, T.; Mavrofidis, S.; Kingman, S.; Miles, N. Microwave heating applications in environmental engineering - a review. Resources, Conservation and Recycling, 2002, 34(2), pp. 75–90.
7. Omar, R.; Idris, A.; Yunus, R.; Khalid, K.; Aida Isma, M. Characterization of empty fruit bunch for microwave-assisted pyrolysis. Fuel, 2011, 90(4), pp. 1536–1544.
8. Yang, K. S.; Yoon, Y. J.; Lee, M. S.; Lee, W. J.; Kim, J. H. Further carbonization of anisotropic and isotropic pitch-based carbons by microwave irradiation. Carbon, 2002, 40(6), pp. 897–903.

9. Li, W.; Peng, J.; Zhang, L.; Yang, K.; Xia, H.; Zhang, S.; Guo, S.-H. Preparation of activated carbon from coconut shell chars in pilot-scale microwave heating equipment at 60kW. Waste Management, 2009, 29(2), pp. 756–760.
10. Ranjit K. Roy. A primer on the Taguchi method, 2nd ed.; Society of Manufacturing Engineers, 2010, 329 p.
11. Demirbaş, A. Fuel Characteristics of Olive Husk and Walnut, Hazelnut, Sunflower, and Almond Shells. Energy Sources, 2010, 24(3), pp. 215–221.
12. Kar, Y. Co-pyrolysis of walnut shell and tar sand in a fixed-bed reactor. Bioresource Technology, 2011, 102(20), pp. 9800–9805.
13. Callum A. S. Hill. Wood Modification: Chemical, Thermal and Other Processes; JohnWiley & Sons, 2006, 248p.
14. Cagnon, B.; Py, X.; Guillot, A.; Stoeckli, F.; Chambat, G. Contributions of hemicellulose, cellulose and lignin to the mass and the porous properties of chars and steam activated carbons from various lignocellulosic precursors. Bioresource Technology, 2009, 100(1), pp. 292–298.
15. Hu, J.; Shen, D.; Wu, S.; Zhang, H.; Xiao, R. Effect of temperature on structure evolution in char from hydrothermal degradation of lignin. Journal of Analytical and Applied Pyrolysis, 2014, 106, pp. 118–124.
16. Benadjemia, M.; Millière, L.; Reinert, L.; Benderdouche, N.; Duclaux, L. Preparation, characterization and Methylene Blue adsorption of phosphoric acid activated carbons from globe artichoke leaves. Fuel Processing Technology, 2011, 92(6), pp. 1203–1212.
17. Deng, H.; Zhang, G.; Xu, X.; Tao, G.; Dai, J. Optimization of preparation of activated carbon from cotton stalk by microwave assisted phosphoric acid-chemical activation. Journal of Hazardous Materials, 2010, 182(1-3), pp. 217–224.
18. Hejazifar, M.; Azizian, S.; Sarikhani, H.; Li, Q.; Zhao, D. Microwave assisted preparation of efficient activated carbon from grapevine rhytidome for the removal of methyl violet from aqueous solution. Journal of Analytical and Applied Pyrolysis, 2011, 92(1), pp. 258–266.

TOWARDS SCREENING THE ENHANCE OF LUMINESCENCE PROPERTIES OF OXIDIZED TANNINS BY A FENTON-LIKE REACTION

Alexandru Gonta

Institute of Chemistry of Academy of Sciences of Moldova, 3, Academiei str., Chisinau MD-2028, Republic of Moldova
e-mail: alexandru.gonta@chem.asm.md

Abstract. After modification of enotannins, flavonols monomer units could be obtained with polyfunctional properties. Moreover, polyphenols are known to generate H_2O_2 and other free radicals under alkaline conditions. Reactive oxygen species generation and catalytic influence of ferrous ions enhance the chemiluminescence light. Therefore, Oxidized Tannin/Tris-EDTA/Fe^{2+} ions system have been used for screening luminescent properties of oxidized tannins.

Keywords: oxidation, tannins, free radical, chemiluminescence.

Received: April 2015/ Revised final: May 2015/ Accepted: May 2015

Introduction

One of the most abundant classes of natural compounds found in plants, with advanced therapeutic properties and polyfunctional morphological structure, is considered flavanoid group. These polyphenols contain compounds with monomeric unit, such as quercetin, catechin, rutin, luteolin, kaempherol, or oligo-polymeric chain, such as condensed and hydrolyzable tannins. Significant sources of tannin content with remarkable antibacterial properties, can be found in grape seeds from local Moldavian wine industries [1,2]. Moreover polyphenols are known for their potent antioxidant activity, that have been widely discussed in the literature as efficient free radical scavengers [3]. Polyphenols are exhibiting their antioxidant potential through a complex red-ox mechanism, which mainly is considered to be triggered after hydrogen abstraction followed by electron-donor transfer to molecules with unpaired electrons in their ground state. These unpaired electrons define molecules as highly chemically active, that could act as oxidant species [4,5].

ROS species

Among dangerous oxidant species are considered reactive oxygen species (**ROS**) such as superoxide anion radical ($\mathbf{O_2^{\bullet-}}$), singlet oxygen ($\mathbf{O_2(a^1\Delta_g)}$), hydroxyl radical ($\mathbf{OH^{\bullet}}$) and hydrogen peroxide ($\mathbf{H_2O_2}$), which are known for their destructive mediated action of lipids, proteins and cell DNA. Singlet oxygen is the most active ROS with a lifetime of 40 minutes in ultrapure water, but with a short decay of action within microseconds after excitation in the presence of other transition metals and other radicals [6,7].

Reactive oxygen species are formed by electron's addition to O_2, which proceeds through a complex mechanism with evolution of superoxide anion radical (Eq.(1)). Intermediate chain reaction product, H_2O_2, which is a relatively good oxidant, undergoes two-electron reduction (Eq.(4)) to give OH^- (in basic solution) and H_2O (in acidic media) [8,9].

$$O_2 \xrightarrow{+e^-} O_2^{\bullet-} \quad (1)$$

$$2O_2^{\bullet-} + 2H^+ \longrightarrow H_2O_2 + O_2(a^1\Delta_g) \quad (2)$$

$$2O_2^{\bullet-} + 2H_2O \longrightarrow H_2O_2 + 2OH^- \quad (3)$$

$$H_2O_2 + 2e^- \longrightarrow 2OH^- \quad (4)$$

$$H_2O_2 + 2e^- + 2H^+ \longrightarrow 2H_2O \quad (5)$$

Oxidation of Tannins

It is known that tannins dissolved in water solution and exposed to air, within room temperature, could follow autooxidation reactions rapidly. Therefore, it is indicated to carefully manage tannins extraction, separation and their storage conditions [10,11].

Tannin polyphenols are a large class of compounds that could be divided into two general sub-classes: condensed tannins and hydrolyzable tannins. Grape seed tannins contain more predominantly condensed tannins, which contain polymers formed by condensation via C4→C8 carbon-carbon bond between catechin (epicatechin) monomer units, as showed in Figure 1 [1,12].

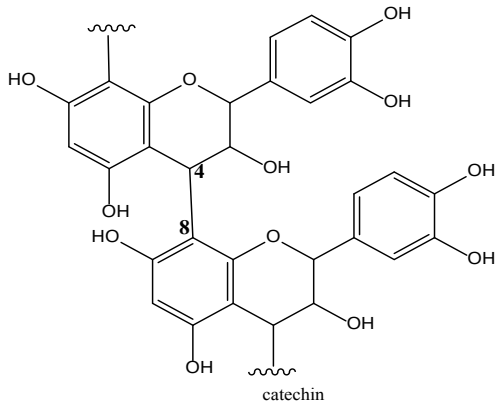

Figure 1. General enotannin structure [1].

Although oxidative cleavage of tannins involves a complex mechanism, several oxidation attempts have been investigated for monomer units in model solutions, like oxidation of quercetin, catechin and others flavanoids [13,14]. In Figure 2, it is represented the mechanism of H-abstraction and electron detachment from a quercetin molecule, in alkaline conditions [14].

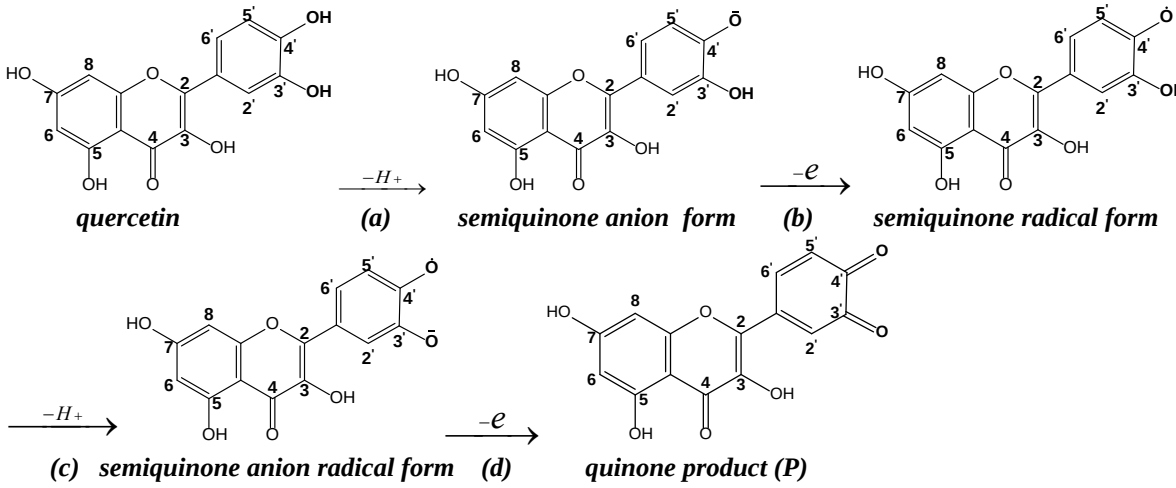

Figure 2. Schematic mechanism representation for quercetin autooxidation in alkaline conditions.

In order to elucidate the corresponding mechanism involved in these oxidation reactions, it is necessary the presence of several key-determinants in one's molecule structure, to be taken into account. The mechanism for the first H-abstraction from B-ring, which is a catechol moiety, is mainly due to the pKa values for C4'-OH and C3'-OH present in the B-ring, which are lower than other pKa of carbon-hydroxyl sites from resorcinol (A-ring) in positions C5-OH, C7-OH or from the heterocycle (C-ring) in position C3-OH. This makes B-ring to be more affordable for oxidation attack by physical quenching mechanism [14,15].

In a work by Bors et al., it is stipulated that three key-functional groups in the chemical structure of a polyphenol are the main cause of H-abstraction and electron donor afterwards, influenced by resonance structure's stabilization of the molecule: (i) the 3',4'-dihydroxy in the catechol B-ring configuration, which after the donation of a hydrogen atom gives the most stable semiquinone radicals; (ii) the double effect, of 2,3-double bond with the C4-carbonyl group in the C-ring, favours relocation of an electron from the B-ring phenoxy radical structure to resorcinol A-ring, and (iii) the combination of the 2,3-double(C2-C3) bond in C-ring and the hydroxyl group at C3 position [16,17].

The most close molecule structure for aforementioned main characteristics, which is related to the prooxidant nature, is considered quercetin (Figure 2) [17].

Quercetin is a unique chemical molecule with remarkable antioxidant activities, which is being considered as one of the most potent antiradical among other flavanoids. Due to the presence of dihydroxyl groups on B-ring and the combination of the double bond in C-ring, quercetin has been used in different experiments for the inhibiting of free oxygen, peroxynitrite, DPPH and ABTS radicals [18,19]. Thus, amplified antioxidant properties are characteristic for quercetin, its ability to exert prooxidant activities has been remarked for low concentration in solutions up to 2 μmol/L [20]. For this reason the toxicity of quercetin, upon DNA damage by promoting of superoxide anion radicals, when used *in vivo* should be analyzed very carefully [21].

Nevertheless, in order to describe the complex oxidation mechanism of tannins, it is necessary to identify products obtained after oxidation by advanced separation on columns with specific stationary phase, due to mixed nature of polarity of the compounds, highly instrumentation detection as mass spectrometry (ESI-MS, APCI-MS), NMR, MALDI and others.

Nowadays, modification and utilization of ecologically neglected tannins extracted from wine industry waste by-products represent a high potential for obtaining of new polyfunctional materials with amplified therapeutic efficiencies. Moreover, Lupascu T. and co-workers have identified remarkable antibacterial and antifungal properties exerted by the new product (Enoxil), obtained after oxidation of enotannins. After chromatographic separations and identification of compounds by mass spectrometry detector, it was revealed that oxidized tannins mixture contain lower molecular weight compounds, such as catechin monomers, quercetin, carboxylic and peroxy components [2,22].

Chemiluminescence detection- a promising tool

Chemiluminescence (CL) is considered a light's production system, induced by chemical reactions, that involves direct transformation of a chemical into electronic energy. This type of reaction belongs to the class of luminescence interactions based on the relaxation energy obtained after transition from excited state of the molecules to their ground state. This lead to a structural rearrangement at the molecule electronic levels, that in result show different physical and chemical properties compared to the ground state of the molecule. An effective CL reaction requires important components, described as follows: (i) chemiluminescent substrate molecule by emitting light after excitation, or transferring the energy to another molecule; (ii) an electron acceptor such as oxygen, when involved in an oxidation reaction; (iii) catalyst, which may be an enzyme or a metal ion [23]. General reactions that are involved in a chemiluminescence assay are represented by the following reactions (Eq.(6-7)):

$$T^{\bullet} \rightarrow T + h\nu \quad (6)$$

$$T^{\bullet} + A \rightarrow T + A^{\bullet} \text{ (CL signal produced after transferring the energy to another molecule)} \quad (7)$$

For the analysis and identification of reactive oxygen species, photoluminescence technique has been successful utilized. Baier J. and co-workers have measured luminescence of singlet oxygen at around 1.270 nm, but the signal obtained is ultra weak and very short in time (microseconds to one second) that needs highly advanced instrumentation [7]. To the contrary, by using exogenous photo-sensitizer, the luminescence could be enhanced and is explained by involvement of red-ox chemical reaction, which leads to a chemiluminescence signal response [6,10]. The appearance of chemiluminescence emission during chemical reactions is known for a long time and is closely related to the formation of free radical intermediates. Chemiluminescence was observed during the oxidation of polycyclic aromatic hydrocarbons, especially in the oxidation reaction by hydrogen peroxide upon a range of compounds such as amino acids, proteins, liver homogenates, riboflavin and polyphenols. In most of the chemiluminescence assays, it have been used oxidation reactions between a sensitizer (luminol, lucigen) and an oxidant specie (H_2O_2) present in alkaline solution, intended for the determination of antioxidant activities of natural flavanoids [23,24].

Chemiluminescence detection has been used for the identification and calibration of tannic acid [25], quercetin [26] and catechin [27]. In all these experiments, phenolic compounds with prooxidant activities are involved.

An enhancement of luminescence was observed after addition of quercetin in the CL, generation system Luminol/Carbonate buffer (pH=9.9), that was correlated to the ROS involved in the autoxidation of quercetin in alkaline aqueous solution. This enhancement was due to the existence of semiquinone radical anion form of quercetin in solution (Figure 2), that led to the superoxide radical anion by electron donation to oxygen molecule (Eq.(1)). Similar process of $O_2^{\bullet-}$ formation (see Eq.(11)) is involved in oxidation reaction of luminol (LumH). In result, more potent $O_2^{\bullet-}$ molecules, will interact with diazosemiquinine radical anion ($Lum^{\bullet-}$) and more content of luminol endoperoxide ($LumO_2^{2-}$) will be produced (see Eq.(12)). The following reactions (see Eq.(8-14)) describe the oxidation processes of initial luminol (LumH) to final product, (D^{2-}), obtained after heterocycle opening and elimination of N_2. Chemiluminescent signal ($h\nu$) occurs after transition of (D^{2-*}), in the lowest excited single state, to to the less vibrationally excited state (D^{2-}) [28].

$$LumH \xrightarrow{OH-} Lum^- \quad (8)$$

$$Lum^- \xrightarrow{-e-} Lum^{\bullet} \quad (9)$$

$$Lum^{\bullet} \xrightarrow{-H+} Lum^{\bullet-} \quad (10)$$

$$Lum^{\bullet-} \xrightarrow{O_2} Lum + O_2^{\bullet-} \quad (11)$$

$$Lum^{\bullet-} + O_2^{\bullet-} (\text{or } O_2(a^1\Delta_g)) \longrightarrow LumO_2^{2-} \quad (12)$$

$$LumO_2^{2-} \longrightarrow D^{2-*} (\text{the lowest excited single state}) + N_2 \quad (13)$$

$$D^{2-*} \longrightarrow D^{2-} (\text{less vibrationally excited state}) + h\nu,\ \lambda = 428\ nm \quad (14)$$

Fenton reaction

Fenton chemistry is widely used in scientific researches as source of free $OH^{\bullet}$ radicals. A special interest is accorded for Fenton type reactions and their importance in environmental science, as a catalytic oxidation mechanism for water pollutants removal [29,30]. In Eq.(15) is described the formation of $OH^{\bullet}$ radicals, which could be involved in further production of free radicals (Eq.(16)) [6].

$$Fe^{2+} + H_2O_2 \longrightarrow Fe^{3+} + OH^{\bullet} + OH^- \quad (15)$$

$$H_2O_2 + HO^{\bullet} \rightarrow O_2^{\bullet -} + H_3O^+ \text{ (in alkaline solutions)} \quad (16)$$

As have been mentioned, chemiluminescence analysis is a fast and reliable method for the determination of prooxidant/antioxidant potential of natural polyphenols. The goal of this work was to interpret the general aspects related to the autooxidation mechanism of low molecular polyphenolic compounds, obtained after depolymerization of enotannins, by using an enhanced chemiluminescence assay. In addition, it has been discussed the pathway of luminescent light's production after physico-chemical interaction of ROS with flavanoids, in mild alkaline solutions, in the presence of Fe^{2+} ions as catalyst.

Experimental

Apparatus

In this work Luminometer, Promega Glomax 20/20, USA, with photomultiplier tube (PMT) detector and spectral range between 350-650 nm, have been used. Luminescence sensitivity expressed as relative luminescence units (10^2-10^9, RLU, with an accuracy ±50). Relative luminescence units (a.u.) have been recorded as total sum of photon counts/10 seconds over the range 350-650nm.

Reagents

For these experiments have been used: Tris-EDTA buffer, pH 8.0 (BioUltra, 99% purity); oxidized tannins (Tox) were obtained by oxidation reactions of the enotannins of local origin, several concentrations of Tox in distilled water have been prepared, in the [Tox] range between 0.005-0.8% (g/100 mL H_2O); Moh'r salt solution (Fe^{2+} ion source, $[Fe^{2+}]$=0.001 mol/L) and distilled water. The motivation of the use Moh'r salt in these experiments, relay on the consideration that Fe(II) present in this salt is more resistant to oxidation than in ferrous sulphate ($FeSO_4$), due to the presence of acidifying ammonium ions.

Chemiluminescence assay

For the reference sample, in a microcentrifuge tube of 1.5 mL, 200 μL of Tox solution have been accurately transferred followed by the addition of 800 μL of Tris-EDTA buffer. The luminescence data have been collected in the Excel program, exactly after 10 seconds from initial mixing. In case of chemiluminescence signal enhancement, triggered by Fe^{2+} ions, 200 μL Tox solution have been transferred to 1.5 mL centrifuge tube, followed by simultaneously addition of 750 μL of Tris-EDTA buffer and 50 μL of Fe(II) solution (Mohr salt) with the data collection after the same 10 seconds.

Results and discussion

Although Tox represent a complex mixture of compounds obtained after tannin oxidation, for simplicity it has been treated as a whole chemical entity molecule in this work.

Occurrence of superoxide radical anion (Eq.(1)) is accomplished by the transition of an electron, released from semiquinone anion radical of Tox ($Tox^{\bullet -}$), to molecular oxygen, similar to the mechanism presented in Figure 2, (Eq. (17)). Furthermore, $O_2^{\bullet -}$ by proton's addition, led to the formation of hydrogen peroxide and oxygen singlet (Eq.(18)) [30,31]. As a consequence of polyphenol oxidation in mild to strong alkaline (pH 7.5-11.5) solutions, a weak chemiluminescent signal was exhibited. This yellow-green light, arises from a charge-transfer intramolecular character, which favours the ultrafast intermediary formation of the lowest excited state specie ($ToxQ^{2-}$*, Eq.(21)). Occurrence of intermediary peroxide dianion form ($ToxO_2^{2-}$, Eq.(20)) is due to the chemical type addition of O_2 ($a^1\Delta_g$) by flavonol (Tox) mainly responsible for oxygen attack on C-ring, with C4-oxy-group and C2-C3 double bond [32-35].

$$Tox^{\bullet -} - e \xrightarrow{O_2} P(\text{quinone}) + O_2^{\bullet -} \quad (17)$$

$$2O_2^{\bullet -} \xrightarrow{2H+} H_2O_2 + O_2(a^1\Delta_g) \quad (18)$$

$$2O_2^{\bullet -} + OH^{\bullet} \longrightarrow OH^- + O_2(a^1\Delta_g) \quad (19)$$

$$Tox + O_2(a^1\Delta_g)(O_2^{\bullet -}) \longrightarrow ToxO_2^{2-} \text{(intermediary peroxide dianion form, chemical addition)} \quad (20)$$

$$ToxOO_2^{2-} \longrightarrow ToxQ^{2-}* \text{ (lowest excited state)} \quad (21)$$

$$ToxQ^{2-}* \longrightarrow ToxQ^{2-} \text{ (quinone dianion form, less excited state)} + h\nu\ ,\ \lambda = 440 - 520nm \quad (22)$$

Lifetime of singlet oxygen, in protic media solutions, is from 1-200 μs depending on the solvent media used (ethanol, acetonitrile, acetone, DMSO). To the contrary, superoxide radical is extremely long-lived in alkaline media [36]. Therefore more content of $O_2^{\bullet-}$ present in alkaline solution catalyse the formation of the singlet oxygen, which by radiative deactivation of the excited state $O_2(a^1\Delta_g)$ would give $O_2(^3\sum_g^-)$ - in triplet ground state with a maximum at λ=635nm as shown in the following reaction (Eq.(23)) [37]:

$$2O_2(a^1\Delta_g)(a^1\sum_g^-) \longrightarrow 2O_2(^3\sum_g^-) + h\nu\,,\ \lambda = 635nm \quad (23)$$

Although this is the direct way of the photon's emission resulted after transition of excited state of oxygen singlet to its triplet ground state, this light is quite difficult to quantify. Nevertheless other indirect ways of light's emission could be also involved. In a work by Tournaire C. et al., it has been suggested that weak light has been observed after physical interaction of flavanol molecule with oxygen singlet (Eq.(24)). This was characterized by the energy transferred to a flavanol (Flv) molecule (Eq.(7)), resulted in the radiative deactivation of $O_2(a^1\Delta_g)$ (Eq.(23)). Afterwards, it follows the same processes as explained in reaction given by Eq.(6) with photon emission in the range of 420-520nm [38].

$$2O_2(a^1\Delta_g)(a^1\sum_g^-) + Flv \longrightarrow 2O_2(^3\sum_g^-) + Flv^* \quad (24)$$

The ability of polyphenols in reduction of Fe^{3+} ions (Eq.(15)) in aqueous solution, by a physical interaction between phenolate anion (Tox^-) and Fe^{3+} ions, would trigger so called "Fenton-like reactions", due to the indirect mechanism of reactions, which led to the formation of Fe^{2+} ions and resume the $OH^{\bullet}$ production (Eq.(15)) [6,39].

$$Tox^- + Fe^{3+} \longrightarrow Fe^{2+} + Tox^{\bullet-} \quad (25)$$

Combining the reactions described by the Eqs.(17-25), we would get a general view for the initiation, propagation and catalytic influence on the autooxidation reactions of polyphenols (Figure 3) [40].

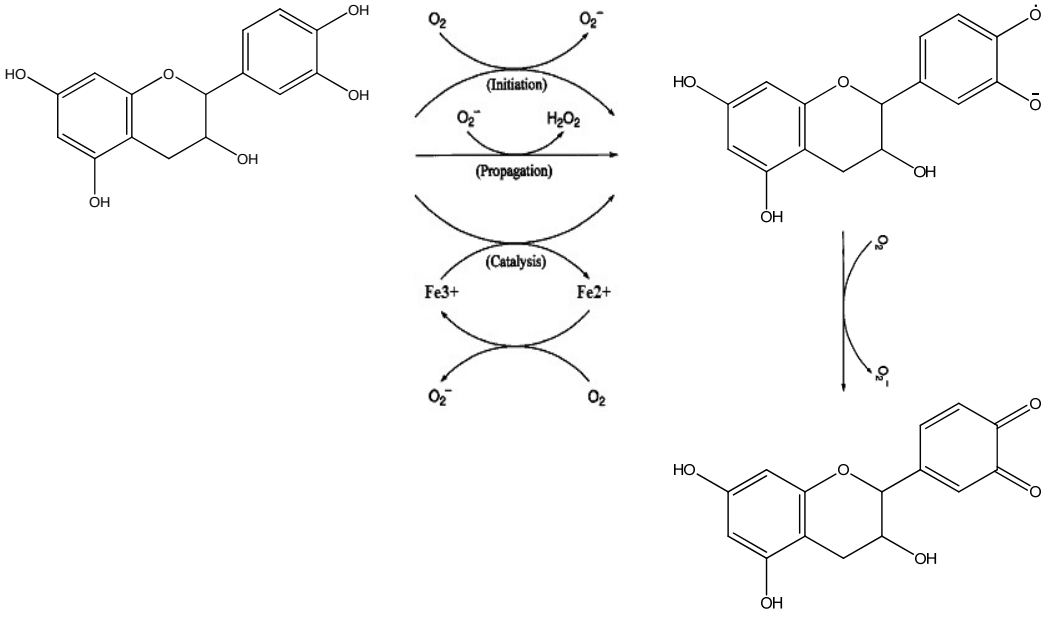

Figure 3. Mechanism of catechin's autooxidation in the presence of catalyst (adapted and modified according to [40]).

As have been mentioned, a weak luminescent light is formed by initiation of autooxidation reactions of polyphenols in mild to strong alkaline solutions advocated by the reactions described in Eq.(17-22). The interval characteristic for a weak luminescence is between $1 \cdot 10^2$-$1 \cdot 10^5$ (RLU, a.u.), while a high level intensity luminescence corresponds to the range between $1 \cdot 10^5$ - $1 \cdot 10^9$ (RLU, a.u.)

After mixing 200μL of polyphenols with 800 μL of Tris-EDTA, luminescent light have been measured exactly after 10 seconds, counting from the initial mixing. In Figure 4, it can be seen that weak light (max RLU=246 a.u.), is formed, which corresponds to the autooxidation reactions of Tox in mild alkaline solutions (Tris-EDTA, pH 8.0), increasing insignificantly by variation in Tox concentration (0.005-0.5, %).

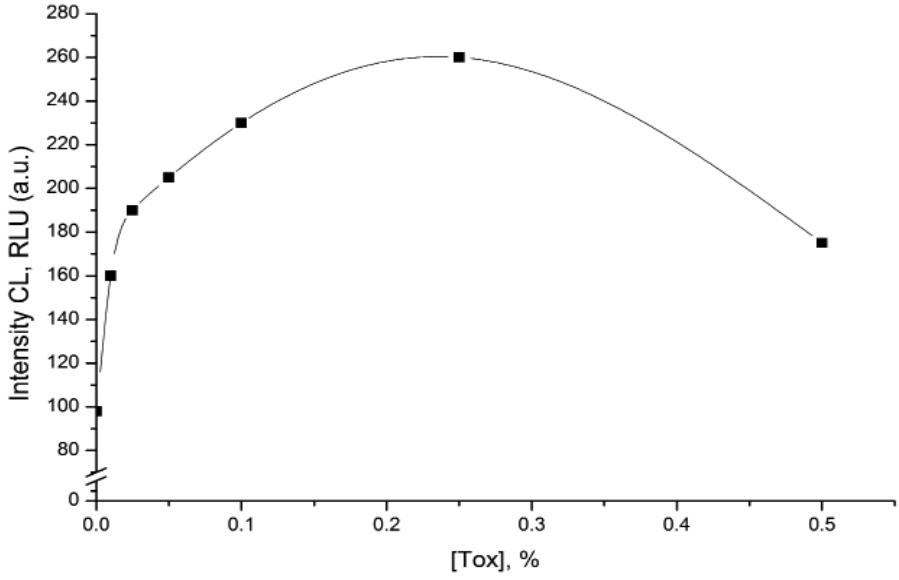

Figure 4. Chemiluminescent signal obtained in a CL generation system, Tox-Tris-EDTA pH 8.0, by increasing the Tox aqueous concentrations (%).

These results corroborates with the work by Slawinska D. and co-workers, where only a weak light was emitted, that has been interpreted as the sum of photon's distribution pattern over the range of 440-520 nm.

To the contrary by adding to the CL assay, Fe^{2+} ions, the luminescence light measured was almost 7 times higher as compared with a CL reaction without ferrous ions. In Table 1 it is presented the data obtained after CL light's measurement for Tox aqueous concentrations (0.005 - 0.1, %).

Table 1

Luminescence detection (RLU, a.u.) in a CL generation system, Tox/Tris-EDTA/Fe^{2+} for a range of Tox concentrations (0.005-0.1, %) obtained after 10 seconds from initial mixing.

Concentration of Tox, %	*RLU (a.u.) with Fe^{2+}*	*RLU (a.u.) without Fe^{2+}*
0.005	230±10	124±12
0.01	370±35	157±23
0.02	490±41	190±27
0.04	750±23	-
0.06	990±25	205±16
0.08	1235±38	-
0.1	1450±46	230±24

Note: all measurements have been done in triplicate

Interestingly that CL intensity (RLU, a.u.) is increasing linearly over the range of CL (200-2000, a.u.), with a linear regression (R^2=0.9994), which could be considered a confident result when a calibration curve should be obtained for the modified tannin (see Figure 5). However this increase is linearly only in the [Tox] $\geqq$ 0.1% (Figures 5 and 6). Further experiments are required for a deep analysis of inter-dependency conditions such as optimal concentrations of ferrous ions, detection of hydrogen peroxide content, specification of ROS species involved ($OH^{\bullet}$, $O_2^{\bullet-}$, O_2 ($a^1\Delta_g$) in oxidation mechanism, instrument's limit of detection and the interference by other chemical species that could influence the result.

Although the change in the concentration of Tox aqueous solutions is directly proportional to the increase in the chemiluminescent signal (Figure 5), in the case [Tox] $\geqq$ 0.25 % (g/100 mL H_2O) a decrease of the luminescent light have been noticed (Figure 6).

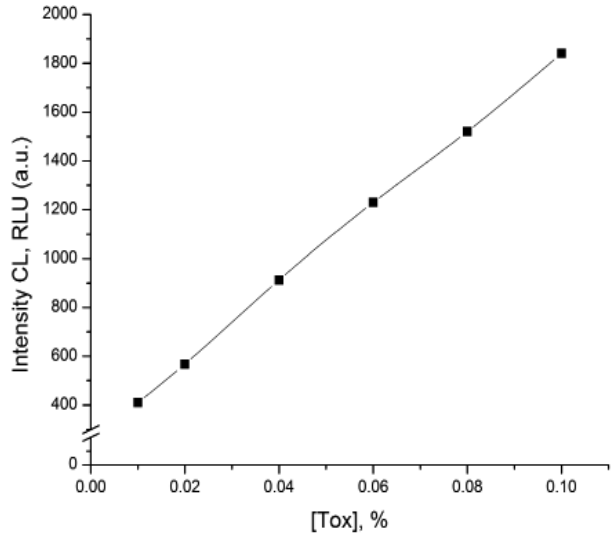

Figure 5. Decreasing luminescence versus increasing amount of [Tox] in a CL generation system, with Fe^{2+} ions.

This phenomena could explained by Tox participation in ROS production (Eqs.(17-25)), in the first place, for [Tox]<0.25 %, which is associated to the prooxidant activities exerted by polyphenols. At such lower concentration of Tox, it is believed that the rate of formation (R_f) [ROS] >> [Tox] with reduction properties available in the solution and will determine the formation of an oxidizing environment. Moreover, the reactions are mainly oriented to the initiation and propagation of chain reactions involving free radicals, which led to chemiluminescent light emission.

To the contrary, for [Tox] ≧ 0.25 %, antioxidant free radical scavenger reactions are more likely to occur. This could be explained by a predominant polyphenol proton-donation transfer to ROS free radicals, which will result in their inhibition.

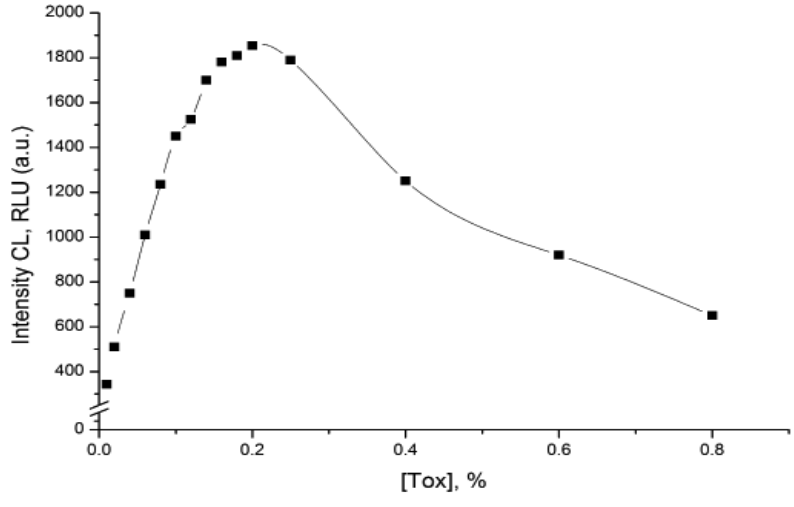

Figure 6. Decreasing luminescence versus increasing amount of [Tox] in a CL generation system, with Fe^{2+} ions.

According to this situation [Tox] ≧ 0.25 %, the prevalence in solution of Tox molecules, with proton-donor properties, would inhibit ROS in the first place. This environment could be characterized as a system with predominant reducing properties. This affirmation corroborate with our previous work, where for values of [Enoxil] ≧ 0.3% (g/100 mL H_2O) there is an increase of antioxidant activities (by 45%) compared to initial tannins, determined by $ABTS^{\bullet+}$ and DPPH assay [41].

Conclusions

In this work, it is described a general overview of autooxidation's reaction mechanism of polyphenols obtained after enotannin modification and chemiluminescence signal occurrence afterwards. Polyphenols in alkaline solutions are subject to autooxidation reactions, that could generate in result ROS (hydrogen peroxide, superoxide radical anion and oxygen singlet) by H-abstraction and proton-donor pathway. The catechol moiety on B-ring, in the flavanoid structure, is more susceptible for oxidation reactions by ROS through physical quenching, while chemical oxidation reactions are mainly involved on C-ring's, which has the oxy-group and carbon-carbon double bond. In this experiment, a light generation system has been developed, using oxidized tannin/Tris-EDTA/Fe^{2+} ions in the range of detection λ=360-650, and a detailed explanation of this light occurrence have been presented. It has been observed that addition of ferrous ions into the system, led to an enhancement of chemiluminescence light by Fenton-like reactions. The CL intensity was direct proportional to increasing Tox concentrations (0.005-0.1, %). It have been established, that for [Tox]<0.25 %, ROS formation is promoted, but for [Tox] $\geqq$ 0.25 %, free radical scavenger ability is enhanced and ROS formation was inhibited.

Due to a complex mixture of compounds obtained after tannin modification, further experiments are required for identification of components responsible for generation of active free radicals or for the antioxidant properties, respectively.

Acknowledgements

Author is thankful to Dr. Nina Timbaliuc for experimental assistance and supervisor Prof., Dr. Habilitate Tudor Lupascu for guidance and suggestions.

References

1. Kulciţki, V.; Vlad, P.; Duca, Gh. Investigation of grape seed proantocyanidins. Chemistry Journal of Moldova, 2007, 2(1), pp. 36-50.
2. Lupascu, T.; Duca, G.; Giurginca, M.; Vlad, P.; Lupascu, L.; Gromovoi, T.; Meghea, A. Natural Compounds with Antioxidant Properties. Key Engineering Materials, 2009, 415, pp. 25-28.
3. Muselík, J.; García-Alonso, M.; Martín-López, M.P.; Žemlička, M.; Rivas-Gonzalo, J.C. Measurement of antioxidant activity of wine catechins, procyanidins, anthocyanins and pyranoanthocyanins. International Journal of Molecular Sciences, 2007, 8(8), pp. 797–809.
4. Sengupta, P.K.; Kasha, M. Excited state proton-transfer spectroscopy of 3-hytdroxyflavone and quercetin. Chemical Physics Letters, 1979, 68(2–3), pp. 382–385.
5. Li, S.; Qian, L.; Zhu, Y.; Liu, M.; Gao, Y.; Ni, Y. Enhanced chemiluminescence of cerium(IV)-Tween 85 system and the analytical application. Luminescence, 2013, 28(6), pp. 948–953.
6. Ivanova, I.P. Mechanism of chemiluminescence in Fenton reaction. Journal of Biophysical Chemistry, 2012, 3(1), pp. 88–100.
7. Baier, J.; Maisch, T.; Maier, M.; Landthaler, M.; Baumler, W. Direct detection of singlet oxygen generated by UVA irradiation in human cells and skin. Journal of Investigative Dermatology, 2007, 127(6), pp. 1498–1506.
8. Duca, Gh. Homogeneous catalysis with metal complexes: fundamentals and applications. Springer Series in Chemical Physics: Germany, 2012, 480 p.
9. Foote, C.S. Active oxygen in chemistry. Springer series Structure Energetics and Reactivity in Chemistry: Netherlands, 1995, 342 p.
10. Tuominen, A.; Sundman, T. Stability and oxidation products of hydrolysable tannins in basic conditions detected by HPLC/DAD-ESI/QTOF/MS. Phytochemical Analysis, 2013, 24(5), pp. 424–435.
11. Poncet-Legrand, C.; Cabane, B.; Bautista-Ortín, A.-B.; Carrillo, S.; Fulcrand, H.; Pérez, J.; Vernhet, A. Tannin oxidation: intra- versus intermolecular reactions. Biomacromolecules, 2010, 11(9), pp. 2376–2386.
12. Hagerman, A.E.; Riedl, K.M.; Jones, G.A.; Sovik, K.N.; Ritchard, N.T.; Hartzfeld, P.W.; Riechel, T.L. High molecular weight plant polyphenolics (tannins) as biological antioxidants. Journal of Agricultural and Food Chemistry, 1998, 46(5), pp. 1887-1892.
13. Xu, G.; In, M.Y.; Yuan, Y.; Lee, J.; Kim, S. In situ spectroelectrochemical study of quercetin oxidation and complexation with metal ions in acidic solutions. Bulletin of the Korean Chemical Society, 2007, 28(5), pp. 889-892.
14. Janeiro, P.; Oliveira Brett, A. M. Catechin electrochemical oxidation mechanisms. Analytica Chimica Acta, 2004, 518(1-2), pp. 109–115.
15. Cren-Olivé, C.; Wieruszeski, J. M.; Maes, E.; Rolando, C. Catechin and epicatechin deprotonation followed by ^{13}C NMR. Tetrahedron Letters, 2002, 43(25), pp. 4545–4549.
16. Bors, W.; Michel, C.; Saran, M. Flavonoid antioxidants: rate constants for reactions with oxygen radicals. Methods in Enzymology, 1994, 234, pp. 420–429.
17. Abou Samra, M.; Chedea, V.S.; Economou, A.; Calokerinos, A.; Kefalas, P. Antioxidant/prooxidant properties of

model phenolic compounds: Part I. Studies on equimolar mixtures by chemiluminescence and cyclic voltammetry. Food Chemistry, 2011, 125(2), pp. 622–629.
18. Iacopini, P.; Baldi, M.; Storchi, P.; Sebastiani, L. Catechin, epicatechin, quercetin, rutin and resveratrol in red grape: Content, in vitro antioxidant activity and interactions. Journal of Food Composition and Analysis, 2008, 21(8), pp. 589–598.
19. Prior, R.; Wu, X.; Schaich, K. Standardized methods for the determination of antioxidant capacity and phenolics in foods and dietary supplements. Journal of Agricultural and Food Chemistry, 2005, 53(10), pp. 4290–4302.
20. Kolewski, P.; Siger, A.; Nogala-kałucka, M.; Polewski, K. Evaluation of antioxidant activity of alpha-tocopherol and quercetin during oxidation of phosphatidylcholine using chemiluminescent detection. Polish Journal of Food and Nutrition Sciences, 2009, 59(2), pp. 123–127.
21. Babich, H.; Schuck, A.G.; Weisburg, J.H.; Zuckerbraun, H.L. Research strategies in the study of the pro-oxidant nature of polyphenol nutraceuticals. Journal of Toxicology, 2011, 2011, pp. 1-12.
22. Lupascu, T.; Kulciţki, V.; Vlad, P.; Duca, Gh.; Nastas, R. Studies on the water solubilization processes of oenotannins and their physico-chemical properties. Chemistry Journal of Moldova, 2006, 1(1), pp. 74-80.
23. Roda, A.; Guardigli, M. Analytical chemiluminescence and bioluminescence: Latest achievements and new horizons. Analytical and Bioanalytical Chemistry, 2012, 402(1), pp. 69–76.
24. Roda, A.; Pasini, P.; Guardigli, M.; Baraldini, M.; Musiani, M.; Mirasoli, M. Bio- and chemiluminescence in bioanalysis. Fresenius Journal of Analytical Chemistry, 2000, 366(6-7), pp. 752–759.
25. Xie, C.; Cui, H. Detection of tannic acid at trace level in industrial wastewaters using a highly sensitive chemiluminescence method. Water Research, 2003, 37(1), pp. 233–237.
26. Lei, R.; Xu, X.; Yu, F.; Li, N.; Liu, H.W.; Li, K. A method to determine quercetin by enhanced luminol electrogenerated chemiluminescence (ECL) and quercetin autoxidation. Talanta, 2008, 75(4), pp.1068–1074.
27. Lee, J.M.; Karim, M.M.; Lee, S.H. Determination of catechin in aqueous solution by chemiluminescence method. Journal of Fluorescence, 2005, 15(5), pp. 735–739.
28. Brunmark, A.; Cadenas, E. Electronically excited state generation during the reaction of p-benzoquinone with H_2O_2: Relation to product formation: 2-OH- and 2,3-epoxy-p-Benzoquinone the effect of glutathione, Free Radical Biology and Medicine, 3(3), 1987, pp. 169-180.
29. Soon, A.N.; Hameed, B.H. Heterogeneous catalytic treatment of synthetic dyes in aqueous media using Fenton and photo-assisted Fenton process. Desalination, 2011, 269(1), pp. 1-16.
30. Gonta, M.; Duca, Gh.; Matveevici, V.; Mocanu L. The diminishing of the content of textile direct dyes and auxiliary compounds during their catalytic oxidation. Chemistry Journal of Moldova, 2014, 9(1), pp. 85-92.
31. Kruk, I.; Michalska, T.; Kładna, A. Luminescence in the oxidation of isoproterenol by the superoxide anion radical in dimethyl sulfoxide. Toxicological & Environmental Chemistry, 1998, 67(3-4), pp. 293–304.
32. Slawinska, D. Chemiluminescence and the formation of singlet oxygen in the oxidation of certain polyphenols and quinones. Photochemistry and Photobiology, 1978, 28, pp. 453–458.
33. Sengupta, B.; Reilly, S.M.; Davis D.E.; Harris, K.; Wadkins, R.M.; Ward, D.; Gholar, A.; Sengupta, H. Excited State Proton Transfer of Natural Flavonoids and Their Chromophores in Duplex and Tetraplex DNAs. The Journal of Physical Chemistry B, 2015, 119 (6), pp. 2546–2556.
34. Morales, J.; Günther, G.; Zanocco, A.L.; Lemp, E. Singlet oxygen reactions with flavonoids. a theoretical - experimental study. PLoS ONE, 2012, 7(7), pp. 1–8.
35. Mukherjee, T. Photo and radiation chemistry of quinones. Proceedings-Indian National Science Academy part A, 2000, 66(2), pp. 239-266.
36. Steeden, S.; Tosic, M.; Marjanovic, B.; Simicg, M.G. Flavonoids as Antioxidants. Journal of the American Chemical Society, 1994, 116(11), pp. 4846-4851.
37. Slawinska, D. Chemiluminescence in the peroxidation of tannic acid. Photochemistry and Photobiology, 1979, 30(1), pp. 71-80.
38. Tournaire, C.; Croux, S.; Maurette, M.T.; Beck, I., Hocquaux, M.; Braun, A.M.; Oliveros, E. Antioxidant activity of flavonoids: efficiency of singlet oxygen (1 delta g) quenching. Journal of Photochemistry and Photobiology B., Biology, 1993, 19(3), pp. 205–215.
39. Navas, D.; García Sánchez, F.; González García, J.A. Enhancement and inhibition of luminol chemiluminescence by phenolic acids. Journal of Bioluminescence and Chemiluminescence, 1995, 10(3), pp. 175–184.
40. Akagawa, M.; Shigemitsu, T.; Suyama, K. Production of hydrogen peroxide by polyphenols and polyphenol-rich beverages under quasi-physiological conditions. Bioscience, Biotechnology, and Biochemistry, 2003, 67(12), pp. 2632–2640.
41. Lupascu T.; Gonta A. Studies on the antioxidant activity of the compound Enoxil and its related forms. Chemistry Journal of Moldova, 2011, 6(2), pp. 58-64.

METHOD OF INFRARED SPECTRA REGISTRATION OF ACTIVATED CARBONS IN POTASSIUM BROMIDE PELLETS

Diana Shepel[a*], Tatiana Goreacioc[a,b], Tudor Lupascu[a], Mihail Filippov[a], Maria Rusu[a]

[a]*Institute of Chemistry of Academy of Science of Moldova, 3, Academiei str., Chisinau MD-2028, Republic of Moldova*
[b]*Institute of Ecology and Geography of Academy of Sciences of Moldova, 1, Academiei str., Chisinau MD-2028, Republic of Moldova*
[*]*email: dianashepel@gmail.com*

Abstract. This communication is devoted to the elaboration of a new optimal technique of infrared spectra registration of activated carbons in potassium bromide pellets. Authors investigated the dependence of the intensity of the least overlapping infrared bands of activated carbons on the conditions of preparation, recording of the spectrum, and the degree of homogenization with KBr.

Keywords: infrared spectroscopy, activated carbons, potassium bromide KBr pellets.

Received: February 2015/ Revised final: March 2015/ Accepted: March 2015

Introduction

Infrared (IR) spectroscopy has an important role in the study of the active carbon structure. In the study of carbons, research of pressed pellets with alkali metal halides is used for this purpose, as well as IR spectroscopy of attenuated total reflectance (ATR). Tabletting method has become the most popular method of obtaining IR spectra of active carbons [1-3]. However, errors may occur in the measurement of the intensity of the bands due to the inhomogeneous distribution of the sample in the pellet. When the sample is distributed unevenly in the pellet, the beam of the Fourier Transform Infrared (FTIR) spectrometer can fall on pure KBr regions with no test substance and this may lead to distortion of the measured intensities of the bands. The increase of voids caused by the inhomogeneous distribution of the test substance in the pellet leads to the decrease of recorded bands intensities and stronger bands decrease more significantly than weaker ones. Thus the so-called smoothing of the spectrum occurs.

The aim of this work was to study the dependence of the intensity of the least overlapping infrared bands of activated carbons on the conditions of preparation, recording of the spectrum, the degree of homogenization with KBr, as well as the elaboration of an optimal method of sample preparation as a pellet of active carbon homogenate with KBr for IR spectrum registration.

Experimental

The method of IR spectra registration of activated carbons in KBr pellets.

Amount of 0.40-0.50 mg of activated carbon was homogenized in an agate mortar with 300 mg of optically pure KBr, vacuumized for 5 min and pressed under 10 ton/cm^2 for 15 min. The area (S, cm^2) of the KBr pellet was 1.13 cm^2 (Zeiss standard). A light grey transparent pellet without visually noticeable grains was obtained. IR spectra were recorded on a PerkimElmer FTIR Spectrometer Spectrum 100, (2007) in the wave number range of 4000-400 cm^{-1}. Prior to the preparation of pellets and spectral analysis, the samples of carbons and KBr were dried and stored above anhydrous silica gel in an exicator. The optimal conditions of spectra recording were as follows: spectral resolution - 2 cm^{-1}, the scan number - 10, the number of automatic spectrum smooth - 2. Spectral data handling and baseline correction was carried out by the Spectrum software Version 6.2.0.0055 (2007). After the first registration of the spectrum the pellet was transferred quantitatively into a mortar and triturated (homogenized). The powder was repressed and IR spectrum was rerecorded. The operations of homogenization and IR spectrum registration were repeated until maximal stable values of absorption (A) were obtained. The IR spectrum was recorded using as control the same pellet made from pure ground potassium bromide.

Effects of various factors during the IR spectra registration in the KBr pellets have been examined on the example of a modified activated carbon AG-5ox (Table 1) obtained from a commercial sample of carbon AG-5. Activated carbon AG-5 was produced in granulated form from coal dust (coals mixture) and an adhesion agent by steam treatment at 850 - 950 °C [4]. Sample of AG-5ox has been prepared by oxidation of AG-5 with concentrated nitric acid as described in [5]. 0.480 mg of the active carbon sample AG-5ox was taken to prepare the KBr pellet according to the above-mentioned method. The concentration of AG-5ox was C = 0.425 mg/cm^2 and was held constant during the experiment.

Results and discussion

This communication described the method of sample preparation in the form of homogenate pellets of active carbon with KBr for recording the IR spectrum. The dependence of the intensity of the least overlapping infrared bands of activated carbons on the conditions of preparation, recording of the spectrum, and the degree of homogenization with potassium bromide has been investigated.

The recorded intensities of the IR bands depend on several factors:

1. Dependence on particle sizes. With all other conditions maintained equal, light scattering increases with the particle size in comparison with the wavelength. The particle size is comparable to the wavelength of the absorbed light in the ideal case. In the spectral region 4000 - 400 cm^{-1}, particle size 2.5 - 25 microns and particle size greater than 2.5 microns, the scattering of light decreases with increasing wavelength. The baseline correction method was used to compensate for the scattered light effect, consisting in the measurement of light absorption relative to a line drawn through the minima of the absorption (A) spectrum, respectively, through the transmittance (T,%) maxima.

2. Dependence on the uniformity of particle distribution in the KBr pellets. The recorded intensity of bands (A) depends not only on particle size but also on the equal distribution in the pellet. In the case of an uneven distribution of particles in the pellet, voids consisting of the pure KBr are formed between particles of analyzed sample, i.e. defects observed in the continuous distribution of particles. The increase in defects leads to the decrease of measured bands intensities, and this decrease is proportional to band intensity. The result is a so-called smoothing of the spectrum [6,7]. We have used techniques of consecutive sample homogenization with KBr to eliminate this defect. The pressed pellet has been reground and repressed consecutively several times to achieve constancy of the measured value A of the bands of varying intensity.

3. Homogenization of the mixture of investigated sample and KBr in an open atmosphere leads to moisture sorption. The bands of water absorbed by KBr appear in the spectrum ν(OH) at 3450 cm^{-1} and δ(HOH) at 1630 cm^{-1} [1, 8]. This absorption is compensated by the introduction of the control pellet of pure KBr in the reference beam of the spectrometer.

4. The measured value of absorption A depends on the weight of analyzed substance (g, mg) that is uniformly distributed over the area of the pellet (S, cm^2).

At a constant area of the pellet, any variation in the amount of KBr in the homogenate only leads to a change in the thickness of the pellet, but the quantity of the analyte projected in the beam onto the slit of the instrument is not changed. Thus the classic formula of the Lambert-Beer law for solid substance homogenized in the pellet with KBr has the form $K = A/C$. The K values (Eqs.(1) and (2)) of the intensities of the bands in the spectrum were compared.

$$C = g/S, \quad (1)$$

$$K = \frac{A \cdot S}{g}, \text{ cm}^2 \times \text{mg}^{-1}, \quad (2)$$

where A - measured absorbance (optical density); S - area of the pellet, cm^2; g – weight of the sample in the pellet, mg.

In order to compensate water absorption by the pellet during homogenization, the control pellet made from pure KB was placed in the beam of the FTIR spectrometer. The Carl Zeiss Company recommended a weight 300 mg of KBr on a standard area 1.13 cm^2 of a branded pellet to obtain sufficient firmness.

The results of investigations of the influence of various factors on the registration of the IR spectra of the modified activated carbon AG-5ox in KBr pellets are shown in Table 1.

Table 1

The dependence of optical density (A) of the least overlapping bands on the conditions of preparation and registration of the IR spectrum of the sample AG-5ox.

Conditions of spectrum registration	*Band$_1$*		*Band$_2$*		*Band$_3$*	
	ν_1, cm^{-1}	*$A_1 \cdot 10^3$*	*ν_2, cm^{-1}*	*$A_2 \cdot 10^3$*	*ν_3, cm^{-1}*	*$A_3 \cdot 10^3$*
Immediately after pressing	1711	415	1561	433	1101	457
In 20 hours	1717	428	1559	451	1096	474
Rotation of the pellet by 90°	1717	430	1560	454	1096	477

It was found that rotation of the pellet in the beam of the instrument didn't produce any changes. Consequently, the sample was uniformly distributed in the pellet. The spectrum of the sample in the pellet did not change after 20 hours, showing there was no interaction of the pressed AG-5ox with KBr during that time. No changes in the spectrum were observed after reapplying pressure on the uncrushed pellet during 3 hours.

The sample of AG-5ox was also used to investigate the dependence of the evenness of its distribution on the degree of homogenization in the KBr pellet (Table 2, Figure 1). After the first registration of the IR spectrum the pellet was subjected to repeated homogenization in a mortar, and another repressing. Pellet trituration in a mortar and pressing were repeated until stable values of absorption (A) were obtained.

Figure 1 shows the spectra of the AG-5ox sample as function of the degree of homogenization. Three least overlapping bands 1713 (C=O), 1560 (C=C), 1098 (C-C) cm^{-1} were chosen for quantitative characterization of the changes in the spectrum of AG-5ox during sample homogenization (Table 2). The first and second homogenizations

were insufficient to obtain a deeply embossed spectrum. The maximum and constant values of the IR bands intensities were achieved only after the third and fourth homogenizations. The increase in the homogenization degree made the spectra more relief and the latter reached a limit, which corresponded to previously reported data [1, 2, 6-8].

Table 2

The dependence of the IR bands intensities of modified activated carbon AG-5ox on the degree of homogenization.

Degree of homogenization	*Band*$_1$		*Band*$_2$		*Band*$_3$	
	ν_1, cm^{-1}	$A_1 \cdot 10^3$	ν_2, cm^{-1}	$A_2 \cdot 10^3$	ν_3, cm^{-1}	$A_3 \cdot 10^3$
1	1719	424	1567	449	1098	474
2	1714	464	1548	485	1097	519
3	1713	482	1548	514	1098	560
4	1713	489	1560	526	1099	574

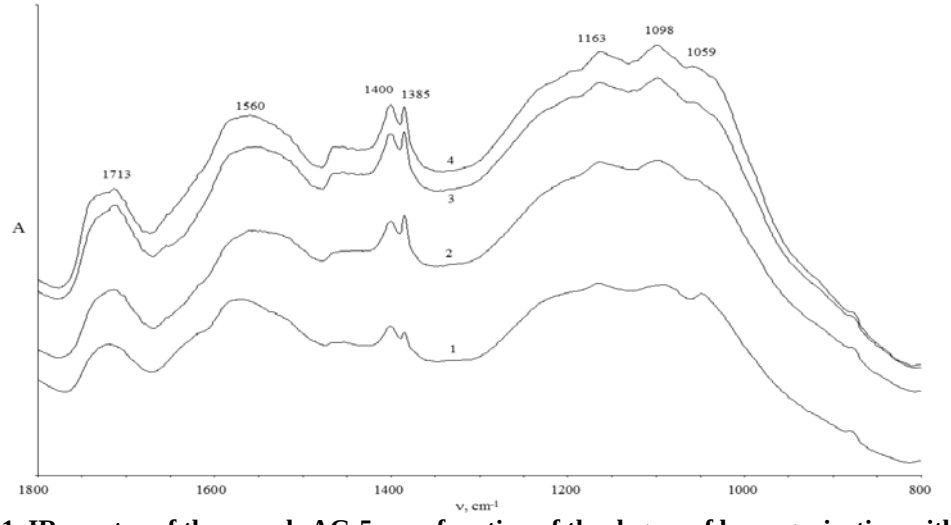

Figure 1. IR spectra of the sample AG-5ox as function of the degree of homogenization with KBr. The spectrum number corresponds to the degree of homogenization.

Conclusions

The investigation of the dependence of the optical density of the least overlapping bands in the IR spectrum of the activated carbon on the conditions of preparation and registration of the spectrum showed that the pressed sample of activated carbon was distributed evenly in the pellet and didn't suffer any changes after homogenization with KBr. An optimum technique for IR spectra registration of activated carbons in the KBr pellets has been proposed. The maximum and constant values of the intensities of the IR bands were achieved after the third and fourth homogenization of the KBr pellets.

References

1. Applied Infrared Spectroscopy. Edited by Kendall, D.N. Mir: Moscow, 1970, 376 p. (in Russian).
2. Roop, C. B.; Meenakshi, G. Activated Carbon Adsorption. A CRC Press Book. Taylor&Francis Group: New-York, 2005, pp. 22-34.
3. Cuhadaroglu, D.; Uygun, O.A. Production and characterization of activated carbon from a bituminous coal by chemical activation. African Journal of Biotechnology, 2008, 7(20), pp. 3703-3710.
4. GOST 20777-75. Granulated active carbon AG-5 (in Russian).
5. Goreacioc T. Oxidation and characterization of active carbon AG-5. Chemistry Journal of Moldova, 2015, 10(1), pp. 75-82.
6. Elliot, A. Infrared spectra and structure of polymers. Mir: Moscow, 1972, 160 p. (in Russian).
7. Tremblay, L.; Gagne, J.-P. Fast Quantification of Humic Substances and Organic Matter by Direct Analysis of Sediments Using DRIFT Spectroscopy. Analytical chemistry, 2002, 74(13), pp. 2985-2993.
8. Bellamy, L.J. The Infrared Spectra of Complex Molecules. Foreign Literature Publishing House: Moscow, 1963, 592 p. (in Russian).

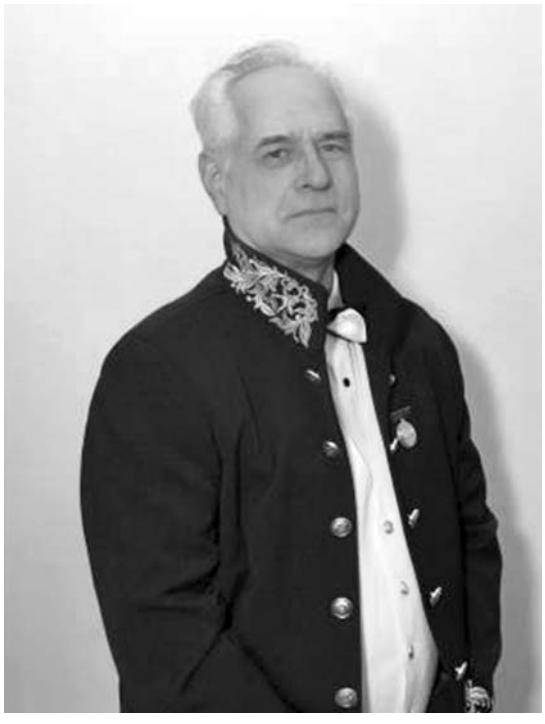

(20.12.1940 – 23.03.2015)

IN MEMORY OF ACADEMICIAN OF ACADEMY OF SCIENCES OF MOLDOVA PROFESSOR CONSTANTIN TURTA

Academician Constantin Turta, Doctor habilitate in chemistry, Professor, famous scientist, world-renowned chemist, Laureate of the State Prize of the Republic of Moldova, person of a exquisite culture and noble attitude, was born on December 20th 1940 in the village Buciusca, district of Rezina. After graduating the secondary school No.1 from town Rezina in 1956, he has successfully passed the entrance examinations, becoming a student of Faculty of Chemistry of State University of Chisinau. After graduating university in 1961, he is employed, as a researcher, in a military institute of Ministry of Defense of U.S.S.R. in the Saratov region, solving the problems of sorption and filtering substances. After 3 years, in 1964, he returns to Moldova, being employed as assistant at Department of General and Inorganic Chemistry at Polytechnic Institute of Chisinau.

In 1966 he enrolled in doctoral studies at the Institute of Chemistry of the A.S.M. and was delegated to pursue doctoral studies at the Institute of Physical Chemistry of A.S. U.S.S.R. (Moscow), where he works until April 1970. He has successfully presented his PhD thesis entitled “Studies of coordination compounds of iron with organic ligands by Mössbauer method” in 1971. At the Institute of Chemistry of A.S.M. he passed all scientific steps - from researcher to the head of laboratory.

Scientist Constantin Turta was a worldwide specialist in the field of bioinorganic and coordination chemistry. He became known in the scientific community by his fundamental pioneering work on the application of Mössbauer spectroscopy in inorganic and coordination chemistry.

Professor Turta developed the chemistry of homo- and heteropolynuclear clusters of iron (III), which allowed drafting new synthetic methods and preparing new physiologically active substances. A high appreciation have his works that are devoted to the synthesis and characterization of mixed valence iron (III) complexes, description of the dynamic phenomena, including dynamics of electron density in space and time, phase transition, elucidation of the factors influencing transition temperature and type of spin crossover, as well as the speed of electron transfer in the studied systems.

On the basis of Mössbauer spectroscopy a new method was developed and a class of substances was proposed to study the intermolecular electron transfer process.

International acknowledgment of founded by academician Constantin Turta scientific school is based on the polyvalent character of research, modern approach and argued presentation of conclusions, as well as well-documented elaborations and achievement of various projects within NATO, INTAS, CRDF, SCOPES, FP7 programs.

In the late 80s of last century Constantin Turta became recognized as a scholar of the highest authority in the application of Mössbauer spectroscopy in inorganic and coordination chemistry, as it was mentioned during the discussion of his habilitate thesis entitled "Dynamic effects in mono- and polynuclear complexes of iron with polydentate ligands (synthesis, structure, Mössbauer spectra and magnetic properties)" in the Institute of Physical Chemistry of A.S.U., Kiev, Ukraine.

In 1995 Mr. Constantin Turta was given the title of professor and elected as a corresponding member of A.S.M., subsequently becoming a titular member of A.S.M. (2010).

Due to steadiness and depth in the realization of scientific researches, scientific successes, but also his intelligence and verticality, authority of academician Constantin Turta in society had become emblematic, that is why his election in 2000 as general scientific secretary of A.S.M. was met as natural and necessary act.

Academician Constantin Turta is the author of over 550 scientific publications, including 200 published in prestigious international journals, 35 patents and a university handbook "Introduction to gamma resonance spectroscopy (Mössbauer spectroscopy)."

Professor Turta not only has lectured in universities from our country - Technical University, State University of Moldova, University of A.S.M., but also abroad, *e.g.* University "Gh. Asachi", Iasi, Romania; University of Tajikistan, Dushanbe; West University of Timisoara, Romania etc.

Under the tutorship of academician Constantin Turta 13 PhD and 2 Dr. habilitate theses were prepared and successfully discussed. He has actively contributed to the works of many international scientific forums with plenary communications and was one of the organizers, and from 2006 - President of Organizing Committee of the International Conference "Physical Methods in Coordination and Supramolecular Chemistry" that takes place every three years in Chisinau, and has a high visibility among scientists.

Merits of academician Constantin Turta were appreciated both by the scientific community and the government. He is Laureate of the State Prize of the Republic of Moldova, Knight of the Order "Labour Glory" and Medal "Dimitrie Cantemir" of the Academy of Sciences of Moldova.

Corresponding member Tudor Lupascu,
Director of the Institute of Chemistry of
Academy of Sciences of Moldova

Dr. habilitate Aculina Aricu,
Vice-director of the Institute of Chemistry of
Academy of Sciences of Moldova

Instructions for authors

Please follow these instructions carefully to ensure that the review and publication of your paper are as quick and efficient as possible. These notes may be copied freely. The electronic version of these notes is freely available for download on the web page of Chemistry Journal of Moldova (consult the section of the site **Instructions for authors** www.cjm.asm.md/author_instructions). Instruction notes and an example of manuscript formatting are available in the MS Word template file that can be found on the web page of Chemistry Journal of Moldova (www.cjm.asm.md).

Journal policy

"Chemistry Journal of Moldova. General, Industrial and Ecological Chemistry" seeks to publish experimental or theoretical research results of outstanding significance and timeliness in all fields of Chemistry, including Industrial and Ecological Chemistry. The main goal of this edition is strengthening the Chemical Society of Moldova, following development of research in Moldovan chemical institutions and promotion of their collaboration with international chemical community.

Fields of research:

1. Analytical chemistry
2. Ecological chemistry
3. Food chemistry
4. Industrial chemistry
5. Inorganic and coordination chemistry
6. Natural product chemistry and synthesis
7. Organic chemistry
8. Physical chemistry and chemical physics
9. Supramolecular chemistry

Publications may be in the form of *Short Communications, Full Papers* and *Review Papers*.

Short Communications should describe preliminary results of an investigation and for their significance are due to rapid communication. For this kind of publications, experimental confirmation is required only for the final conclusion of the communication. Maximum allowed length – 2 pages.

Full Papers should describe original research in chemistry of high quality and timeliness. Experimental work should be accompanied by full experimental details. Priority will be given to those contributions describing scientific work having as broad appeal as possible to the diverse readership. Maximum allowed length – 10 pages.

Review Papers are specially commissioned reviews of research results of topical importance. Maximum allowed length – 20 pages.

The language of submission is English, articles in other languages will not be considered. Papers are submitted on the understanding that the subject matter has not been previously published and is not being submitted elsewhere.

Authors must accept full responsibility for the factual accuracy of the data presented and should obtain any authorization necessary for publication.

The contents of papers are the sole responsibility of the authors, and publication shall not imply the concurrence of the Editors or Publisher.

All papers are sent to referees who advise the Editor on the matter of acceptance in accordance with the high standards required.

Referees' names are not disclosed, but their views are forwarded by the Editor to the authors for consideration.

Authors are strongly encouraged to suggest the names and addresses of suitable referees.

Journal conventions

Nomenclature

Authors will find the following reference books and websites useful for recommended nomenclature:

- IUPAC Nomenclature of Organic Chemistry; Rigaudy, J.; Klesney, S. P., Eds; Pergamon: Oxford, 1979.
- A Guide to IUPAC Nomenclature of Organic Compounds (Recommendations 1993); Panico, R.; Powell, W. H.; Richer, J. C., Eds; Blackwell Publishing: Oxford, 1993.
- http://www.acdlabs.com/iupac/nomenclature
- http://www.chem.qmul.ac.uk/iupac/

It is the responsibility of the author to provide correct chemical nomenclature.

X-ray crystallographic data

Prior to submission of the manuscript, the author should deposit crystallographic data for organic and metal-organic

structures with the Cambridge Crystallographic Data Centre (CCDC). The data, without structure factors, should be sent by e-mail to: deposit@ccdc.cam.ac.uk, as an ASCII file, in CIF format. CCDC deposition numbers (one per structure deposited) should be included with the following standard text in the manuscript: "CCDC-******" - contains the supplementary crystallographic data for this paper. These data can be obtained free of charge via http://www.ccdc.cam.ac.uk/conts/retrieving.html. Deposited data may be accessed by the journal and checked as part of the refereeing process. If data are revised prior to publication, a replacement file should be sent to CCDC.

Experimental

Authors should be as concise as possible in experimental descriptions. The experimental section must contain all the information necessary to guarantee reproducibility. An introductory paragraph containing information concerning solvents, sources of less common starting materials, special equipment, etc. should be provided. The procedures should be written in the past tense and include the weight, mmol, volume, etc. in brackets after the names of the substances or solvents. General reaction conditions should be given only once. The title of an experiment should include the chemical name and compound number of the product prepared: subsequently, these compounds should be identified by their number. Details of the work up procedure must be included. An experimental procedure is not normally required for known compounds prepared by a literature procedure; in such cases, the reference will suffice. For known compounds prepared by a novel procedure, comparative data together with the literature reference are required (e.g. m.p. and published m.p. with a reference to the latter).

Characterization of new compounds

All new compounds should be fully characterized with relevant physical and spectroscopic data, normally including compound description, m.p./b.p. if appropriate, IR, NMR, MS and $[a]_D$ values for enantiopure compounds. In addition, microanalyses should be included whenever possible. Under appropriate circumstances, and at the Editor's discretion, high resolution mass data may serve in lieu of microanalyses; in this case a statement must be included regarding the purity of the products and how this was determined [e.g. all new compounds were determined to be >95% pure by HPLC (or GLC or ^{1}H NMR spectroscopy)]. For compound libraries prepared by combinatorial methods, a significant number of diverse examples must be fully characterized (normally half of the members for libraries up to 40 compounds, 20 representative examples for bigger libraries). Resin-bound intermediates do not have to be fully characterized if acceptable characterization of released products is provided. No supplementary data are accepted in addition to the basic material.

Manuscript preparation

Please follow these guidelines for manuscript preparation. Please ensure that the required formats for text and figure submission are followed strictly.

General requirements

Manuscripts will be accepted only in electronic form in A4 format, orientation *Portrait*, one column layout, single-spaced, margins 2.15 cm on all sides. Ensure that each new paragraph is clearly indicated, using TAB at 1.25 pts.
Manuscript must be edited in Times New Roman font. Contributions should comprise an even number of pages. Authors are also kindly requested to adhere to the formatting instructions for font size and layout. Use the automatic page numbering function.

Please ensure that the required formats for text and figure submission are followed strictly. MS Word template can be found on the web page of Chemistry Journal of Moldova (www.cjm.asm.md). Use of this template is mandatory.

The manuscript should be compiled in the order depending on the paper type.

A theoretical or physicochemical paper normally contains the *Title, Authors, Affiliations, Abstract, Keywords,* a brief *Introduction* and formulation of the problem, an *Experimental* (or methodological part), *Results and discussion, Conclusions,* followed by *Acknowledgments* and *References.*

A paper devoted to synthesis contains the *Title, Authors, Affiliations, Abstract, Keywords, Introduction, Results and discussion, Conclusions, Experimental, Acknowledgments* and *References.*

Title

The title should be brief, specific and rich in informative words. Avoid the abbreviations where is possible. The title is in size 14 pt Bold (all capital letters).

Authors and affiliations

Include all authors in a single list. The style for the names is: first name, last name (full names, without initials). The names of the authors must be written in size 12 pt and separated by a comma.

Affiliations should be as detailed as possible and must include the country name and must be written in size 9 pt *Italic*. The corresponding author should be indicated with an asterisk, and contact details (e-mail, phone, fax) should be placed after nomination of affiliations. There should be only one corresponding author.

An example of formatting for authors and affiliations is available in the MS Word template that can be found on the web page of Chemistry Journal of Moldova (www.cjm.asm.md).

Abstract

Authors must include a short abstract of approximately four to six lines that states briefly the purpose of the research, the principal results and major conclusions. Compound numbers should not be mentioned in the abstract. The abstract body is 9 pt in size with the heading in Bold.

Keywords

Authors are expected to provide a maximum of 5 keywords, separated by a comma (10 pt, Normal). These keywords will facilitate database searching. Avoid general, plural terms and multiple concepts (avoid, for example, “and”, “of”).

Text

Text should be subdivided in the simplest possible way consistent with clarity. Headings should reflect the relative importance of the sections. The text body is 10 pt in size Times New Roman font with the heading in Bold. Ensure that all tables, figures and schemes are cited in the text in numerical order. The graphics and artworks should be integrated in the paper.

Trade names should have an initial capital letter, and trademark protection should be acknowledged in the standard fashion, using the superscripted characters TM and ® for trademarks and registered trademarks respectively (although not for words which have entered common usage, e.g. pyrex).

Authors are requested to draw attention to hazardous materials or procedures by adding the word CAUTION followed by a brief descriptive phrase and literature references if appropriate.

Abbreviations must be defined at the first mention in the text and used consistently thereafter.

SI units must be used throughout.

In order to avoid possible confusion between the numeral 1 (one) and the lower-case letter l (el), please use the capital letter L to express liter units.

Decimal numbers should be expressed using the point (do not use comma).

Experimental information should be as concise as possible, but it should contain all the information necessary to guarantee reproducibility.

Tables should be edited considering the requirements indicated below.

Tables should be centered and should occupy the full width of the page.

Table must fit in a size of a page A4, Portrait. Vertical lines should not be used.

If table transfers partially to the next page it should be mentioned on the next page that this is a continuation of the table and the headings must be indicated again.

All table columns should have a brief explanatory heading typed in *Italic* and where appropriate, units of measurement.

The punctuation at the end of the table title must be used.

All tables should be cited in the text, and numbered in order of appearance with Arabic numerals. Tables should be numbered sequentially—“Table 1”, “Table 2”, and should be cited in the text as “Table 1”, “Table 2”.

An example of Tables formatting is available in the MS Word template that can be found on the web page of Chemistry Journal of Moldova (www.cjm.asm.md).

Figures, *schemes* and *equations* must be cited in the text and numbered in order of appearance with Arabic numerals; other graphics should be placed at a particular position in the text but not specifically referenced.

Figures and *schemes* should normally be centered.

It is also more convenient for referees of the article if figures are placed as close as possible, and ideally after, the point where they are first mentioned in the text. Figures should be numbered sequentially—“Figure 1”, “Figure 2”, and should be cited in the text as “Figure 1”, “Figure 2”.

Each figure or scheme should have a concise caption describing accurately what figure depicts. Figure captions begin with the term Figure, followed by figure number, punctuation and figure title, all in Bold type. Also, use the punctuation at the end of the caption. We recommend placing figures and their captions in a table with no margins.

An example of Figures formatting is available in the MS Word template that can be found on the web page of Chemistry Journal of Moldova (www.cjm.asm.md).

Chemical structures must be edited using the following settings: font 7 pt Arial, chain angle 120°, bond spacing 20% of length, fixed length 0.43 cm, Bold width 0.056 cm, line width 0.016 cm, margin width 0.044 cm and hash spacing 0.062 cm. Compound numbers should be in Bold face.

Figures and schemes must be submitted in a very good resolution (but do not submit graphics that are disproportionately large for the content).

Figures will be printed in black and white. Color artwork will be available only in the electronic form of the published articles on the web page of Chemistry Journal of Moldova (www.cjm.asm.md). The quality of the figures must be such that they can be reproduced directly after size reduction and the numbers, letters, and symbols must be large enough to still be legible. Figures should be sent with the highest resolution possible (at least 300 dpi).

Figure and table titles must be typed in Bold and should appear below the figures and above the tables. If you are using previously published material please include the source in the form of reference citation at the end of the figure caption and/or table title.

Mathematical equations and formulas will be edited using Equation Editor or MathType (version 1999-2003). Quote them on the right side, between brackets. Equation must be cited in text as "Eq.(1)", "Eq.(2)".

$$\lambda = 2d \sin\left(\frac{\Theta}{2}\right) \qquad (2)$$

Please use size 10 pt and *Italic* for symbols, Bold face for vectors and normal fonts for standard functions (i.e. log, ln, exp) and subscripts (i.e. $//_{app}i$).

Large and complex chemical formulas should be presented in text as figures.

Please follow the IUPAC nomenclature for your chemical compound.

Conclusions

Concluding section will provide a summary of the main obtained results, formulated in a concise form. The author must not indicate the literature references in this section.

Acknowledgments

This is an optional section. The authors have to decide acknowledgement of certain collaborators, funds or programs who contributed in a way to the research described in the paper.

References

In the text, references should be indicated by Arabic numerals taken in square brackets, which run consecutively through the paper and appear before any punctuation; ensure that all references are cited in the text and vice versa.

References should be numbered in the text in the order they are cited [1]. Multiple consecutive references may be abbreviated as [2-5].

Do not cite references in the abstract.

References should be written in English only. If it's in a different language then the reference must be translated with an appropriate title in English. The original language must be indicated in round brackets.

Complete bibliographic information for all cited references is required. If abbreviated names of the journals are used then authors are expected to consult American Chemical Society guidelines (The ACS Style Guide; Dodd, J. S.; Solla, L.; Berard, P.M. Ed.: American Chemical Society: Washington, DC, 2006) or the policy of the cited journal.

All references must be edited in the same style.

Each reference should contain only one literature citation.

The following style must be used for all contributions:

Books:

1. Katritzky, A.R. Handbook of Organic Chemistry. Pergamon: Oxford, 1985, 200 p.
2. Wipke, W.T.; Heller, S.R.; Feldmann, R.J.; Hyde, E. Eds. Computer representation and manipulation of chemical information. John Wiley: New York, 1974, pp. 287–298.

Symposia volumes:

3. Bravo-Suárez, J.; Kidder, M.K.; Schwartz, V. Novel Materials for Catalysis and Fuels Processing. ACS Symposium Series; American Chemical Society: Washington, DC, 2013, vol. 1132, 400 p.

Translated journal papers:

4. Garaba, V. Problems of water supply in rural localities. Environment, 2005, 19, pp. 19-22 (in Romanian).
5. Magerramov, A.M.; Ramazanov, M.A.; Gadzhiyeva, F.V. Investigation of the structure and dielectric properties of nanocomposites based on polypropylene and zirconia nanoparticles. Surface Engineering and Applied Electrochemistry, 2013, 49(5), pp. 1-5 (in Russian).

Journal papers:

6. Shin, S.; Yoon, H.; Jang, J. Polymer-encapsulated iron oxide nanoparticles as highly efficient Fenton catalysts. Catalysis Communications, 2008, 10, pp. 178–182.

Patents:

7. Grant, P. Device for Elementary Analyses. USA Patent, 1989, No. 123456.

Theses:

8. Cato, S.J. Thermodynamic study of polymer solutions. Ph.D. Thesis, University of Florida, Florida, USA, 1987.

Legal regulations and laws, organizations:

9. EC Directive, Directive 2000/76/EC of the European Parliament and of the Council of 4 December 2000, on the incineration of waste, Annex V, Official Journal of the European Communities, L 332/91, 28.12.2000, Brussels.

Web references:

The full URL should be given in text as a citation, if no other data are known. It should be accompanied by a sentence indicating the explanation of the content. When you are indicating the URL you should remove the Hiperlink, this can be achieved by selecting the URL then click the right button of the mouse and chose from the menu *Remove Hyperlink.*

10. Spectral Database for Organic Compounds, SDBS. http://sdbs.db.aist.go.jp/sdbs/cgi-bin/cre_index.cgi.

Graphical Abstract

Authors must supply a graphical abstract at the time the paper is first submitted.

Graphical abstract will include *Title*, *Authors* and *Abstract body*.

The abstract body will summarize the contents of the paper in a concise form and it should not exceed 50 words. Carefully drawn chemical structures or figures are desired to be included, these will serve to illustrate the theme of the paper. Authors must supply the graphical abstract in a separate document. The graphics which are a part of the graphical abstract should be sent separately in its original format.

An MS Word template for the Graphical Abstract can be found on the web page of Chemistry Journal of Moldova (www.cjm.asm.md). Use of this template is mandatory.

Copyright guidelines

Upon acceptance of an article the copyright transfer will be automatic. This transfer will ensure the widest possible dissemination of information. If excerpts from other copyrighted works are included, the Author(s) must obtain written permission from the copyright owners and credit the source(s) in the article.

Submission of manuscripts

Please send your contribution as an e-mail attachment to:

Journal Editor, Academician Gheorghe DUCA
e-mail: *chemjm@asm.md* / *chemjm@gmail.com*

using Microsoft Word (Office 97 or higher for PCs) word processing soft.

Please prepare a file (allowed formats: *.doc or *.rtf) containing a short cover letter to the Editor, justifying why your article should appear in “Chemistry Journal of Moldova. General, Industrial and Ecological Chemistry”.

The manuscript with all schemes, figures, tables integrated in the text should be submitted in a separated document file.

Graphical abstract must be provided in a separated document file.

Authors should indicate the research field of their paper as well as the nature of contribution (Short Communication, Full Paper or Review Article) in their accompanying letters, along with their mailing address, daytime phone number and fax if available. Names and addresses of three potential referees are welcomed.

Authors will be notified by email if their contribution is received and accepted.

Proofs will be dispatched via e-mail and should be returned to the publisher with corrections as quickly as possible, normally within 48 hours of receipt.